Thermomechanical Processing of Structural Steels with Dilute Niobium Additions

Zhe Cui

Thesis submitted for the degree of Doctor of Philosophy

Department of Materials Science and Engineering
The University of Sheffield

September 2016

Abstract

In this thesis, the influence of various dilute Nb additions (0.005–0.02 wt%) on austenite microstructure evolution along thermomechanical processing, in terms of austenite recrystallisation and grain growth, were investigated using steels with three carbon content levels.

At the homogenisation temperature of 1250°C, all dilute Nb additions were dissolved in low carbon steels whereas the Nb dissolution limits for 0.4 wt% and 0.6 wt% C steels were 0.012 wt% and 0.08 wt%, respectively. Dilute Nb additions did not show significant influence on homogenised austenite grain size. The dramatic increase in C contents was more influential, which decreased the homogenised austenite grain size.

The influence of dilute Nb additions and C contents on dynamic recrystallisation behaviour was studied by rough rolling at high deformation temperature with low strain rate. The dilute Nb additions were found to increase the critical strain of dynamic recrystallisation whereas C contents showed no influence on the dynamic recrystallisation behaviour.

The austenite recrystallisation behaviour after finish rolling and after the holding period between finishing passes were studied by means of interrupted plane strain compression (PSC) tests and double hit PSC tests. It was found that with low Nb supersaturation, recrystallisation happened prior to Nb precipitation. Solute Nb in austenite delayed the onset of austenite recrystallisation through solute drag effect. With high Nb supersaturation, Nb precipitation occurred before the onset of recrystallisation which completely retarded austenite recrystallisation.

The austenite grain growth during the holding period between finish rolling passes was studied by the evolution of prior-austenite grain size before and after the 20s holding period at the highest finish rolling temperature (1050°C). There was no Nb precipitation found and the difference in austenite grain growth behaviour was

attributed to the solute drag effect from both Nb and C in solution. It was found that Nb in solution suppressed austenite grain growth. However, the effectiveness of solute Nb in suppressing austenite grain growth was affected by the C content.

Acknowledgement

I would like to express my sincere appreciation to my supervisor Dr Eric Palmiere, who constantly supported me throughout my PhD study. His guidance and encouragement on, not only my academic work, but also other aspects of life are invaluable. It is my pleasure to have worked with him.

My industrial supervisor Dr Jitendra Patel's guidance and support is greatly appreciated. It has been great meeting with him. His sharp understanding and intellectual opinions on the project and the whole steel industry always inspires me. What I have learned from him will certainly benefit my future career.

I would like to thank Companhia Brasileira de Metalurgia e Mineração (CBMM) and China Scholarship Council (CSC) for their generous financial support. Prof Bradley Wynne and Prof Panos Tsakiropoulos are appreciated for their advice and suggestions given in the viva for annual reports.

My appreciation goes to Dr Peter Kogul, Dr Peng Zeng, Dr Le Ma and Dr Cheryl Shaw in Sorby Centre for the training and technical help on Electron Microscopy and Microanalysis; Mr Dean Haylock and Dr Sarah Hinton for the training and help with the TMC machine; Mr Kyle Arnold, Dr Lisa Hollands, Mr Michael Bell and Mr Ian Watts for their day-to-day helps on various experimental works. Thank you all.

I am so blessed to meet many lovely colleagues and friends during these years. Special thanks goes to Mr Xingguang Liu, Ms Shasha Wu, Dr Feng Qian, Mr Matthew Lawes, Mr Pete Longbottom and Dr Fei Mo. I treasure all the moments we spend together and thank you for walking me through the hard days with your encouragement and genuine care. I also would like to thank my church family for their constant prayer and support.

Words fail to convey my deepest gratitude to my parents for their endless love and unconditional support. Without them, I could never reach this far.

Table of Contents

Table of Contents

Chapter 1 Introduction

1.1 Microalloyed steels

Microalloyed steel represents a group of steels containing a very small amount (typically 0.02–0.1 wt%) of microalloying elements, such as niobium (Nb), titanium (Ti) and vanadium (V). With properly designed thermomechanical processing, the microalloyed steels can obtain a combination of excellent properties such as high strength, high toughness, good weldability and low ductile to brittle transition temperature. These excellent properties enable end-users to advance their products and benefit from weight reduction, cost saving and others. Moreover, microalloyed steels are not only favoured by the end-users but also steelmakers. For some products, the cost for steel production is significantly reduced due to the elimination of any subsequent heat treatment process. Therefore, microalloyed steels have been widely used in a number of areas, including energy, automotive and structural applications since they were commercially launched in the 1960s.

The most well-known application of microalloying technology is the development of high strength pipeline steels, which is from grade X60 with a yield strength of around 420 MPa to grade X120 with a yield strength beyond 830 MPa, as shown in Figure 1-1 [1]. In addition to the precipitation hardening provided by fine precipitates, microalloying refines the microstructure through retardation of recrystallisation during thermomechanical processing to produce pipeline steel up to X80 [2]. Later, the application of accelerated cooling after thermomechanical processing provides the ability to control the microstructures after phase transformation. Low temperature transformation products, such as acicular ferrite and bainite etc., can be obtained, which further enhance the strength and toughness

of the steels as it is shown in Figure 1-1.

Compared with other microalloying elements, Nb has the most significant effect on retarding recrystallisation through solute drag and strain induced precipitation effects [3]. Numerous studies have been conducted to understand the effectiveness of Nb to retard austenite recrystallisation under the influence of variations in Nb content, deformation temperature, amount of strain, strain rate, and inter pass time, etc.

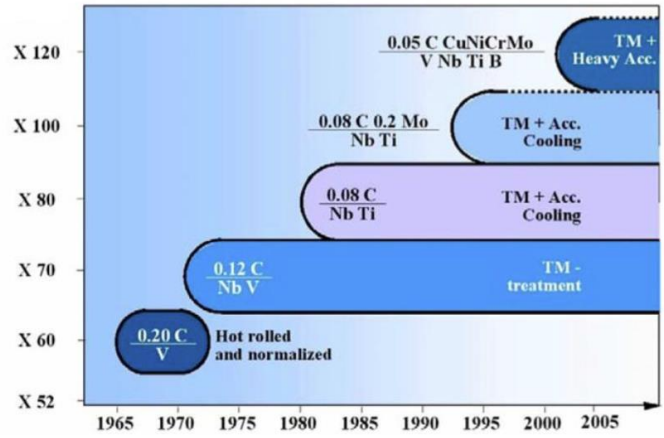

Figure 1-1 Evolution of pipeline steel development [1].

The vast majority of these studies have focused on the low carbon steel flat products. The research on the application of Nb microalloying addition to structural steel long products, such as sections, bars and beams etc., are very limited, especially in medium or high carbon steel long products. This is mainly because of the low solubility of Nb in medium and high carbon steels, hence the application of Nb in these steels is considered not as cost-effective as its application in low carbon steels.

Meanwhile, within the limited research studies [4–20], it has been reported that Nb additions provide benefits in reducing cost, due to the elimination of any following heat treatment, and improvement in mechanical properties of medium and high carbon steels. Using 0.02 wt% Nb, a successful product Niobras-200 rail steel was developed which provides great performance in heavy haul iron ore service [4]. Moreover, the 0.015 – 0.04 wt% Nb addition improves the on-field performance of

automotive engineering medium carbon steels, for fasteners and springs, etc. [5].

The successful metallurgical understanding and subsequent application of Nb microalloying in flat products could potentially be transferred to more extensive applications in structural long products.

1.2 Commercial opportunities and challenges

According to the statistics from the World Steel Association [21], structural steels, including sections, reinforcing bars and beams etc. account for 50% of the world steel production (around 770 million tons), as shown in Figure 1-2. A significant portion of these structural steels are plain carbon steels of medium and high carbon content.

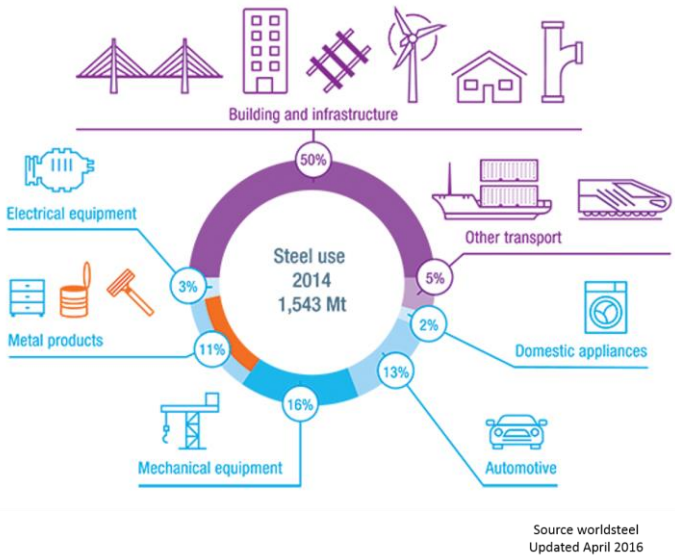

Figure 1-2 Statistics data of worldwide steel use in 2014 from World Steel Association [21].

Even though Nb solubility in steels with higher carbon contents (0.2-0.8 wt% C) is low, dilute amount of Nb (<0.02 wt%) can still be dissolved. The dissolved dilute Nb can potentially be used to improve the mechanical properties of steels. In the literature, there are numerous studies of the influence of Nb on grain growth and

recrystallisation behaviour of austenite under various processing parameters. However, almost all of these studies are focusing on typical amount of Nb (0.02-0.1wt% Nb) in low carbon steels. There is no systematic study on the influence of these dilute Nb additions on the recrystallisation and grain growth behaviour of steels, especially medium and high carbon steels.

There is anecdotal evidence of the beneficial effect from dilute Nb additions to the mechanical properties of structural steel long products. Therefore, there is a need for a detailed study in order to validate and quantify the influence of dilute Nb additions to the microstructure and properties of steels. Based on this, the optimal processing routes and/or alloy design can be proposed to best benefit from the dilute Nb additions. Considering the huge amount of plain carbon structural steel production around the world, successful implemention of dilute Nb additions in these products will generate great commercial opportunities.

This leads to the aim of this research.

1.3 Aim of the thesis

The aim of the current research is to investigate the influence of various dilute Nb additions (0.005 wt%, 0.01 wt% and 0.02 wt%) on the microstructural evolution of typical 0.08 wt%, 0.4 wt% and 0.6 wt% C structural steels during thermomechanical processing, so as to provide valuable information on designing proper steel composition and deformation parameters for tailored industrial application to best benefit from the dilute Nb additions.

The aim is elaborated by the main project objectives, as follows:

- To investigate the influence of dilute Nb additions on the austenite recrystallisation behaviour at various deformation temperatures and examine the retarding mechanisms.
- To investigate the influence of dilute Nb additions on the austenite grain growth behaviour between deformation passes.

- To investigate the influence of C content on the effectiveness of Nb in affecting recrystallisation and grain growth behaviours.
- To develop experimentally based semi-empirical equations to predict the influence of the dilute Nb additions on the austenite recrystallisation and grain growth behaviours.

Chapter 2 Literature Review

2.1 Physical metallurgy basis

2.1.1 Driving force for restoration processes - stored energy

When steels are deformed, most of the energy generated during the work is released by the means of heat dissipation. Only a small fraction, about 1-10% of the work, remains in the steel as stored energy [22]. New dislocations are continuously generated during deformation and some of them are trapped and incorporated by the existing dislocations to generate the new grain boundary areas. New dislocations are also generated within the grains. Therefore, the stored energy of the steel is increased. This leaves the deformed steel in an unstable state. Thermodynamically, the stored energy is the natural driving force for the restoration processes such as recovery and recrystallisation [23,24].

2.1.2 Restoration processes

Restoration processes, including recovery and recrystallisation, are the mechanisms through which the deformed steel try to restore the structures and properties from the high-energy unstable state after deformation to the low-energy stable state prior to deformation. The restoration processes can be dynamic (dynamic recovery or dynamic recrystallisation) or static (static recovery or static recrystallisation) depending on whether it happens concurrent with or after deformation [25]. The fact that the driving force for both of the processes is the stored energy of deformation makes recovery and recrystallisation competing processes. Recovery consumes the

stored energy, and leaves a smaller driving force for recrystallisation. In a similar way, recrystallisation reduces the dislocation density then restricts further recovery [22].

2.1.2.1 Recovery

Recovery, including dynamic and static recovery, is a process that occurs prior to recrystallisation characterised by the annihilation of point defects and relatively small reduction in dislocation density through continuous rearrangement of dislocations into low energy configurations. Humphrey *et al* [26] illustrated and summarised the various stages of recovery in a metal being plastically deformed, see Figure 2-1.

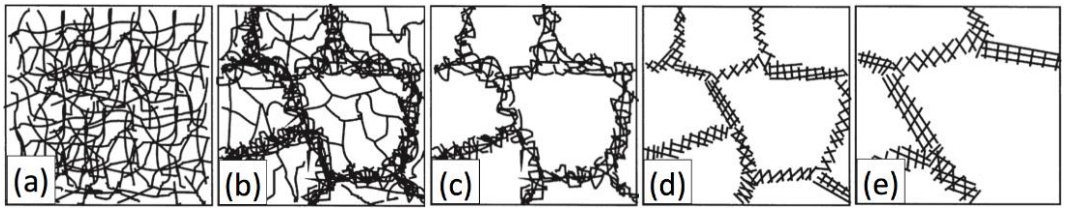

Figure 2-1 Schematic illustration of recovery process. (a) tangled dislocations after plastic deformation; (b) formation of cell structure; (c) dislocation annihilation within the cells; (d) formation of sub-grain structures; (e) growth of the sub-grains [26].

These events are achieved through thermally activated glide, cross-slip and climb of dislocations. The rate of dislocation cross-slip and climb, hence the extent of recovery, is decided by the stacking fault energy of the material [27].

The dislocations of high stacking fault energy materials could cross-slip and climb easily because of the short separation distance between them. Therefore, the fast cross-slip and climb of dislocations occur which balances the dislocations generated during continuous work hardening. Whereas, in low stacking fault energy materials, the large separation distance between partial dislocations makes it difficult to cross-slip and climb. As a result, rapid accumulation of stored energy could occur due to the little recovery of dislocations [27].

For austenite deformation of steel, the stacking fault energy is relatively low with the most commonly used value of about 75mJ•mm^{-2} [28,29]. Therefore, the contribution of recovery to the overall softening is limited.

The overall softening between passes is attributed to both recovery and recrystallisation. It is very hard to distinguish the softening percentage caused by each of them. Previous works [30–33] have reported that recovery accounts for up to 15-20% of the overall softening of austenite between passes. Later, 20% of overall softening is caused by recovery is adopted by other researchers [28,34,35].

2.1.2.2 Recrystallisation

Recrystallisation, including dynamic and static recrystallisation, is a process by which the deformed grains with a high dislocation density are consumed by newly formed grains with a low dislocation density.

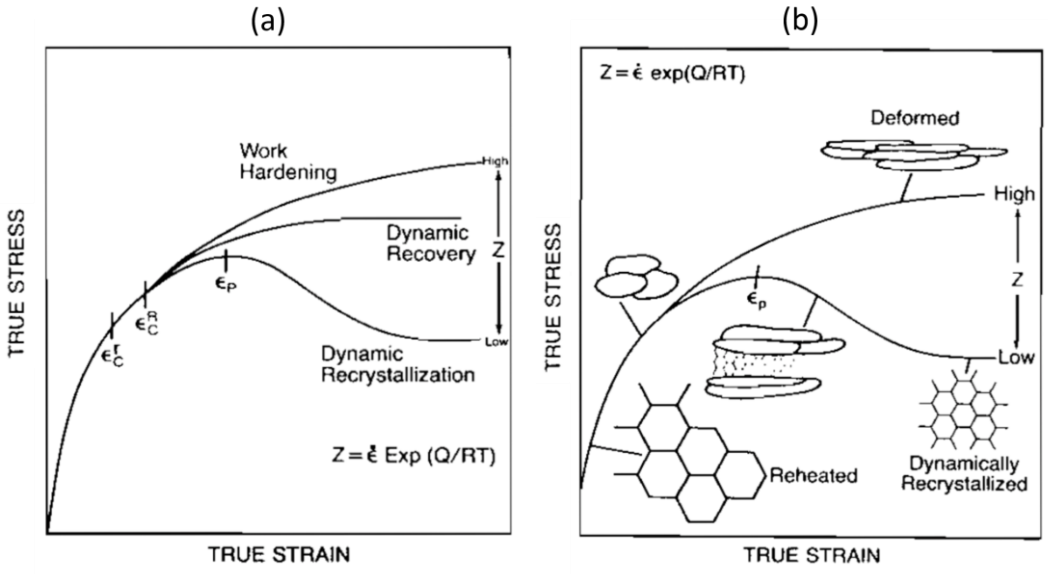

Figure 2-2 (a) Illustration of flow stress of austenite deformation and corresponding metallurgical phenomenon. (b) Evolution of austenite microstructure along deformation [36,37].

The flow behaviour of austenite during hot deformation is shown in Figure 2-2(a) and the corresponding evolution of austenite microstructure is shown in Figure

2-2(b). As it is shown, the flow curve and austenite microstructural behaviour are influenced by the Zener-Hollomon parameter Z, which is a temperature compensated strain rate [38,39]. The Zener-Hollomon equation is given as follows:

$$\mathrm{Z} = \dot{\varepsilon}\exp(\frac{Q}{RT}) \tag{2.1}$$

where $\dot{\varepsilon}$ is the strain rate, *R* is the ideal gas constant, *T* is the absolute temperature, *Q* is the activation energy for deformation.

For deformations with low Z value, the dislocations accumulate until the critical point where the dynamic restoration process happens. As it can be seen from Figure 2-2(a) before the critical strain for dynamic recovery (ε_c^r), the dislocation is accumulated through work hardening. Between the critical strain for dynamic recovery (ε_c^r) and recrystallisation (ε_c^R), dynamic recovery happens. Details have been discussed in Section 2.1.2.1. When the strain is higher than ε_c^R, dynamic recrystallisation happens with the new grains forming at high energy sites, i.e. grain/subgrain boundaries and deformation bands etc., concurrent with deformation. A mixed microstructure of dynamic recrystallised and elongated grains is obtained until the steady state region. At the steady state region, a balance is achieved between the generation and elimination of dislocations. An equiaxed but finer austenite microstructure is obtained in this region.

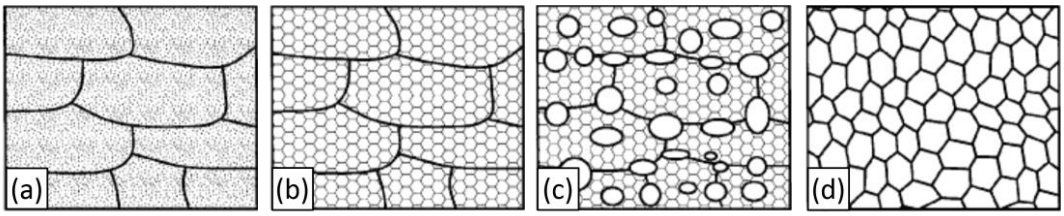

Figure 2-3 Schematic illustration of recrystallisation process; (a) deformed grains; (b) recovered grains; (c) partially recrystallised grains; (d) fully recrystallised grains [40].

For deformation with high Z value, little restoration happens and the deformed austenite microstructure with a high dislocation density is obtained. These microstructures possess high energy which can trigger static restoration processes. Static recrystallisation is a process which consists of formation of new grains and

their continuous growth [41]. After the incubation time, nucleation of new grain occur at the areas with high energy. Once the new grains with low dislocation density are nucleated, they grow continuously into the deformed grains until they are consumed [40]. An illustration of the recrystallisation process is shown in Figure 2-3.

The kinetics of static recrystallisation during isothermal annealing after deformation is described by the Johnson-Mehl-Avrami-Kolmogorov (JMAK) equation as following:

$$X_v = 1 - \exp[-Kt^n] \tag{2.2}$$

where X_v is the recrystallisation volume fraction, t is the time, n is JMAK exponent and K is a parameter associated with the nucleation rate $\dot{N}$, the growth rate $\dot{G}$ and shape factor f. The equation for K is given by:

$$\mathrm{K} = \frac{f\dot{N}\dot{G}^3}{4} \tag{2.3}$$

The recrystallisation fraction is plotted against the isothermal annealing time according to JMAK equation, as shown in Figure 2-4.

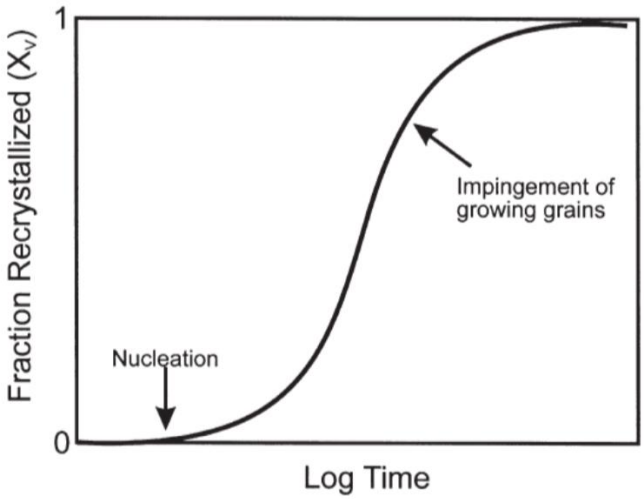

Figure 2-4 Typical recrystallisation kinetics during isothermal annealing after deformation [22].

2.2 Basis for thermomechanical processing of microalloyed steels

2.2.1 Strengthening mechanisms

The basic principle of thermomechanical processing is to achieve the desired mechanical properties by optimising the final microstructures through the control of deformation and transformation process.

A semi-empirical equation based on the expanded form of the well-known Hall-Petch equation [42] describes the contribution of different strengthening mechanisms to the yield strength of steel [43]:

$$\sigma_y = \sigma_0 + \Delta\sigma_s + \Delta\sigma_T + \Delta\sigma_P + \Delta\sigma_D + kd_f^{-\frac{1}{2}} \quad (2.4)$$

where σ_y is the yield stress, σ_0 is the instinctive strength of the iron lattice, $\Delta\sigma_s$ is the solid solution strengthening caused by both substitutional and interstitial atoms, $\Delta\sigma_T$ is the strengthening caused by texture effects, $\Delta\sigma_P$ is the precipitation strengthening, $\Delta\sigma_D$ is the dislocation strengthening. The last term represents the strengthening caused by grain boundaries, in which k is the parameter and d_f is the average ferrite grain size [44].

Among all the strengthening mechanisms, only grain refinement can improve both strength and toughness simultaneously, whereas the other strengthening mechanisms can only improve strength [43,45].

2.2.2 Conditioning of austenite

The main focus of thermomechanical processing of steel is to control the as-rolled austenite microstructure prior to transformation. The combination of the required as-rolled austenite microstructure and well-designed cooling process leads to the formation of optimal microstructures. The final transformed microstructures are controlled by some critical parameters, such as the as-rolled austenite grain

morphology, transformation temperature, cooling rate [46]. Generally, the finer grain size is achieved by the increasing number of ferrite nucleation sites and lower transformation temperature [47–51].

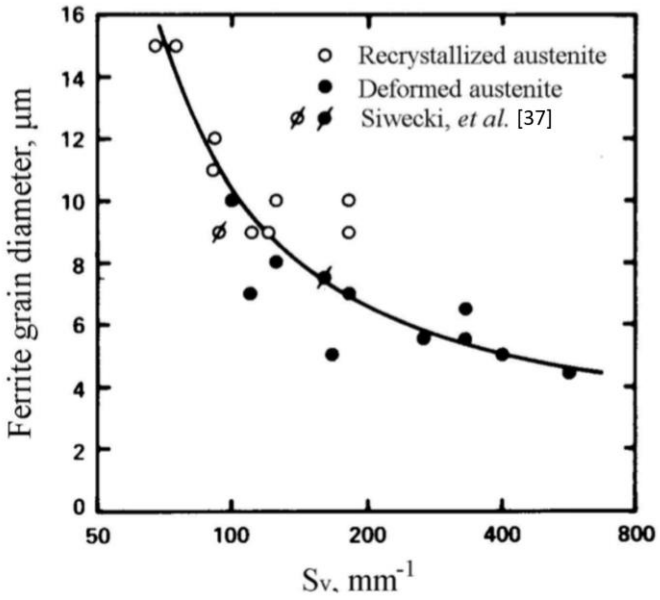

Figure 2-5 Ferrite grain sizes transformed from both recrystallised and unrecrystallised austenite with different S_v values [52,53]

The ferrite nucleation sites are found to be the near planar crystalline defects including grain boundaries and intragranular defects such as twin boundaries and deformation bands [53,54]. A parameter S_v has been defined as the total effective interfacial area per unit volume (with the unit of mm^2/mm^3 or mm^{-1}) of near planar crystalline defects [53]. Therefore, a large value of S_v directly contributes to the refinement of the transformed microstructures. Figure 2-5 shows the ferrite grain sizes transformed from recrystallised and unrecrystallised austenite with different S_v values. It is worth noting that, compared with the recrystallised austenite, unrecrystallised austenite has the tendency to lead to larger S_v values.

Palmiere *et al* [35] simulated the rolling passes in the industrial production of steel by isothermally deforming and holding the steels and then water quenching to room temperature to observe the different austenite condition. The austenite condition is related to two critical temperatures, $T_{5\%}$ and $T_{95\%}$, as shown in Figure 2-6.

$T_{5\%}$ and $T_{95\%}$ stands for the temperature at which 5% and 95% recrystallisation occur. They are used to indicate the onset and finish of recrystallisation. They are reviewed in Section 2.5.2.

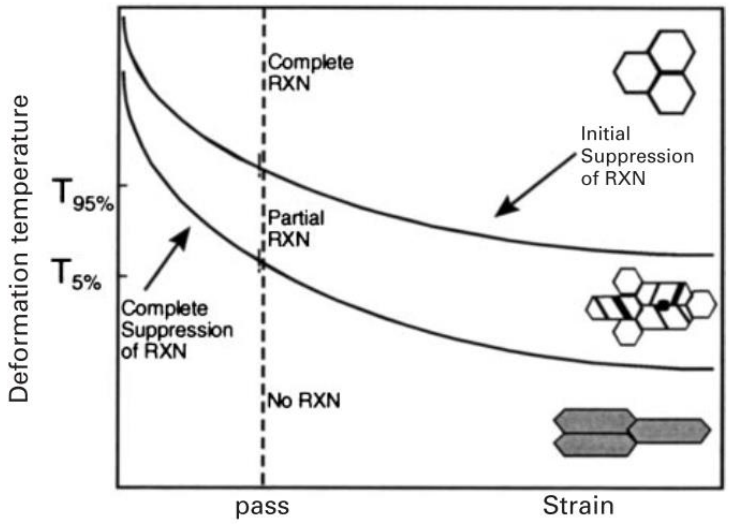

Figure 2-6 Illustration of different austenite microstructures obtained from deformation at various deformation temperatures with a constant strain [35].

When the austenite grains are in different conditions, different parameters contribute to the value of S_v. For all the deformation above $T_{95\%}$, the austenite microstructure is recrystallised completely, the increase of S_v only comes from the refinement of austenite grain size. The total effective interfacial area can be calculated using the following equation [55]:

$$Sv = 2/D_\gamma \tag{2.5}$$

where D_γ is the average grain size of the recrystallised austenite measured by linear intercept method.

Deformation below $T_{5\%}$ leads to the unrecrystallised austenite grains with the elongated and pancaked shapes. In this case, two contribution factors attribute to the increment of S_v as expressed by the following equation [43]:

$$Sv = Sv(GB) + Sv(DB) \tag{2.6}$$

where S_v(GB) is the contribution due to the grain boundaries, S_v(DB) is the

contribution from all the intragranular planar defects.

An equation of the S_v generated from the grain boundaries by Speich *et al* [53] is given as following:

$$S_v(\mathrm{GB}) = \frac{1}{D_\gamma'}(1 + R + \frac{1}{R}) \tag{2.7}$$

where D_γ' is the initial austenite grain size, R is the deformation reduction ratio (original thickness/final thickness).

The increment of the total interfacial area S_v contributed by the intragranular planar defects has been expressed by Ouchi *et al* [54] in the following equation:

$$S_v(\mathrm{DB}) = 0.63(\mathrm{Reduction} - 30)mm^{-1} \tag{2.8}$$

where the reduction is in percentage. It is worth noticing that any deformation less than about 30% cannot generate any deformation bands. Figure 2-7 shows the change of S_v value with increasing reduction, in which the contribution from both grain boundary and intragranular planar defects are clearly illustrated.

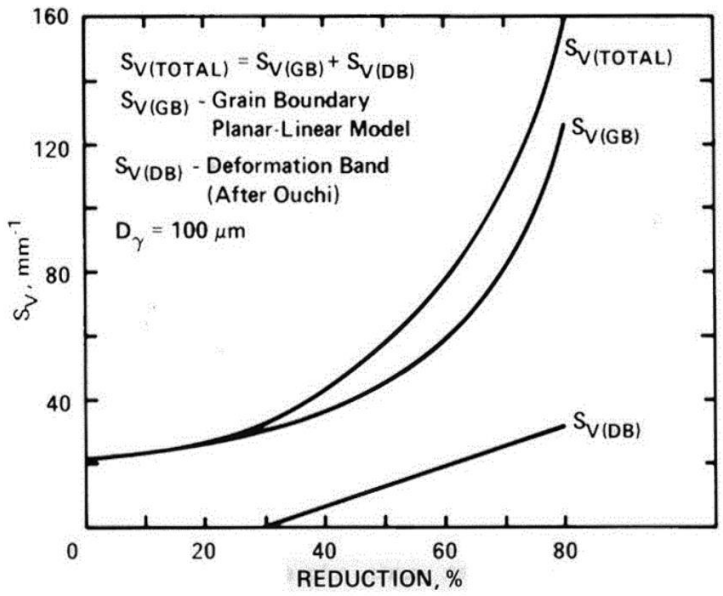

Figure 2-7 Contribution from grain boundary and intragranular planar defects to S_v [53].

Accordingly, the methods which can be used to achieve larger S_v value are as follows:

1) Refining initial austenite grain size before deformation;
2) Increasing the amount of deformation performed below $T_{5\%}$, to increase the grain boundary area per unit volume, i.e. pancaking the grains;
3) Increasing intragranular crystalline defects, e.g. deformation bands etc.

It is obvious that the initial austenite grain size and the extent of the reduction below $T_{5\%}$ are critical in achieving large S_v value [56]. In practice, the initial grain size refinement can be controlled by the reheating process and the repeated recrystallisation process by deformation above $T_{95\%}$. And both increase of grain boundary area and intragranular crystalline defects can be achieved by deformation performed below $T_{5\%}$. The more passes of deformation conducted below $T_{5\%}$, the higher will be the value of S_v. Through proper microalloying of the steels, $T_{5\%}$ can be greatly increased, by which more passes are enabled to perform below $T_{5\%}$ [57,58].

In the later Sections 2.4 and 2.5, the influence of microalloying elements on austenite grain growth behaviour and $T_{5\%}$ and $T_{95\%}$ after deformation are reviewed.

2.3 Microalloying elements

Microalloyed steels are designed to have better mechanical properties compared to the conventional plain carbon steels. Usually, the microalloyed steels contain small amounts (less than 0.1wt%) of microalloying elements such as niobium, titanium and vanadium [59–61]. The addition of these microalloying elements provides better strength and toughness through the refinement of the transformed products and strength through solid solution and/or precipitation strengthening. The extent of solid solution strengthening is highly related to the microalloying elements added. Furthermore, precipitation strengthening depends on the complicated precipitation

behaviour of microalloying elements under the specific thermomechanical processing routine.

2.3.1 Commonly used microalloying elements

2.3.1.1 Niobium

Nb has been used as a microalloying element in steel for decades. It has been widely accepted that small addition of Nb provides both grain refinement and precipitation strengthening [62,63]. Nb dissolves during reheating due to its high solubility in austenite at high reheating temperatures. However, at the deformation temperature, the solubility of Nb is much lower which gives Nb the potential to precipitate in the form of NbC, NbN or NbCN particles.

This leads to three benefits. First is the ability to form strain-induced precipitated during deformation of austenite. The strain-induced precipitation is very effective in retarding the recrystallisation of austenite. This leads to a higher S_v value and eventually grain refinement on the transformed products [64]. The rolling temperature for strain-induced precipitation to occur is generally between 1000 to 800°C [59,65], which is within the deformation temperature range for the finishing passes during hot rolling. Secondly, it increases the strength of the transformed products due to the solid solution and precipitation strengthening of Nb. The precipitation in ferrite can provide a strength increment of up to 100 MPa with normal processing routes and compositions [60,66]. Finally, Nb lowers the austenite transformation temperature [67,68]. At higher cooling rates, the amount of low temperature transformation products, e.g. acicular ferrite, bainitic ferrite, in Nb steels is reported to be larger [69].

2.3.1.2 Titanium

The main purpose of titanium addition is to form fine TiN precipitates. Since the solubility of TiN is so low in austenite even at high reheating temperatures, the fine

TiN particles form during solidification and will not dissolve during the subsequent heat treatment. Therefore, they provide inhibition on austenite grain coarsening throughout the rolling process [57]. With the Ti content less than 0.4 wt%, very little influence is shown on austenite recrystallisation and grain growth [59]. With higher Ti levels, Ti carbide or carbonitride could retard the recrystallisation and generate pancaked austenite microstructure [57]. However, with higher level of Ti, the impact toughness of the steel might be influenced due to the formation of coarse Ti precipitates during solidification [57].

2.3.1.3 Vanadium

V has a much higher solubility compared with Nb and Ti. It tends to fully dissolve in austenite and forms almost no precipitates. The lack of ability to precipitate in austenite makes it ineffective for retarding austenite recrystallisation. However, this makes V much more effective for precipitation strengthening by forming interphase precipitates during the transformation and ferrite precipitates after transformation [44,70,71].

At higher levels of V, retardation of austenite recrystallisation could be achieved. However, since V is an expensive alloying addition, the high level of V to create pancaked austenite is not economically attractive [57].

2.3.2 Solubility product

Using microalloying elements to design a steel product requires a good understanding of the behaviour of microalloying elements at various stage of the processing routine. As can be seen in the earlier sections the major influence of the microalloying elements comes from their precipitates, whether they are strain-induced precipitates which retard the recrystallisation process or they are the interphase precipitates which offer great precipitation strengthening. Precipitation happens only when two critical criteria are met [50]:

1) A critical supersaturation value of microalloying element is reached;

2) The microalloying element has substantial atomic mobility to diffuse.

The precipitation behaviour of microalloying elements are highly related with their solubility which is the amount of microalloying elements that can be dissolved in solid solution at any given temperature. And the solubility can be described by the solubility product.

The general form for a solubility product is given as following:

$$\log[\mathrm{M}][\mathrm{X}] = \mathrm{A} - \mathrm{B}/\mathrm{T} \tag{2.9}$$

where *M* is the content of microalloying element, e.g. Nb, Ti, V etc, in solid solution; *X* is the content of the non-metallic element, e.g. C and N, in solid solution; *A* and *B* are constants; *T* is the absolute temperature at which the elements fully dissolve.

Numerous studies have been done on the solubility of Nb in austenite. The reported solubility products of Nb is summarised in Table 2-1. The considerable difference between the solubility products can be attributed to the fact that each and every of the techniques used to obtain the solubility products has its own limitations and assumptions. The details are reviewed elsewhere [60,72].

Palmiere *et al* [72] has proposed a solubility product for stoichiometric NbC derived from data measured using an atom probe field ion microscope. The data was measured on a steel being reheated and quenched with composition of 0.08 wt% C, 1.5 wt% Mn, 0.08 wt% N and 0.02 wt% Nb.

$$\log[\mathrm{Nb}][\mathrm{C}] = 2.06 - 6700/\mathrm{T} \tag{2.10}$$

It is noteworthy that the comparison between this solubility product and several early solubility products shows that the early ones substantially underestimate the stability of Nb precipitates, hence the solubility temperature [72]. The solubility product has been used in other researches [35,73–75].

Table 2-1 Solubility products for NbC, NbN and NbCN systems in austenite

Product	Method	Reference
NbC System		
$Log[Nb][C]= 2.9 - 7500/T$	D	[76]
$Log[Nb][C]= 3.04 - 7290/T$	B	[76]
$Log[Nb][C]= 3.7 – 9100/T$	C	[77]
$Log[Nb][C]= 3.42 – 7900/T$	B	[78]
$Log[Nb][C]= 4.37 – 9290/T$	C	[79]
$Log[Nb][C]^{0.87}= 3.18 – 7700/T$	B	[80]
$Log[Nb][C]^{0.87}= 3.11 – 7520/T$	E	[76]
$Log[Nb][C]= 2.96 – 7510/T$	E	[76]
$Log[Nb][C]^{0.87}= 3.4 – 7200/T$	A	[76]
$Log[Nb][C]= 3.31 –7970/T+[Mn](1371/T – 0.9) - [Mn]^2(75/T – 0.0504)$	B	[81]
$Log[Nb][C]^{0.87}= 2.81 – 7019.5/T$	A	[82]
$Log[Nb][C]= 1.18 – 4880/T$	…	[83]
$Log[Nb][C]= 3.89 – 8030/T$	…	[83]
NbN System		
$Log[Nb][N]= 4.04 – 10230/T$	C	[84]
$Log[Nb][N]= 3.79 – 10150/T$	B	[80]
$Log[Nb][N] = 2.8 - 8500/T$	B	[78]
$Log[Nb][N] = 3.7 - 10800/T$	B	[68]
$Log[Nb][N]^{0.87} = 2.86 - 7927/T$	A	[82]
$Log[Nb][N] = 4.2 - 10000/T$	…	[83]
NbCN System		
$Log[Nb][C]^{0.24} [N]^{0.65}= 4.09 - 10500/T$	B	[76]
$Log[Nb][C + 12/14N] = 3.97 - 8800/T$	C	[85]
$Log[Nb][C + N] = 1.54 - 5860/T$	B	[76]
$Log[Nb][C]^{0.83}[N]^{0.14} = 4.46 - 9800/T$	B	[76]
$log[Nb][C+12/14N]=2\cdot26- 6770/T$	C	[86]

A: thermodynamic calculation; B: chemical separation and isolation of precipitate; C: carbon content analysis on Nb steels equilibrated with H_2-CH_4 atmosphere at different temperatures; D: hardness measurements; E: statistical treatment of previous solubility products.

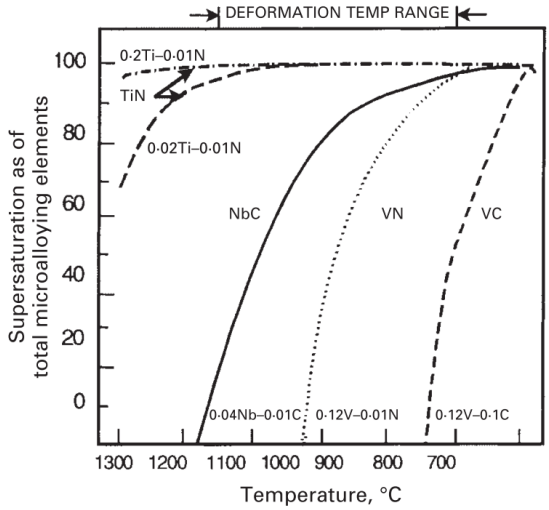

Figure 2-8 Precipitation potential of four common used microalloying systems [87].

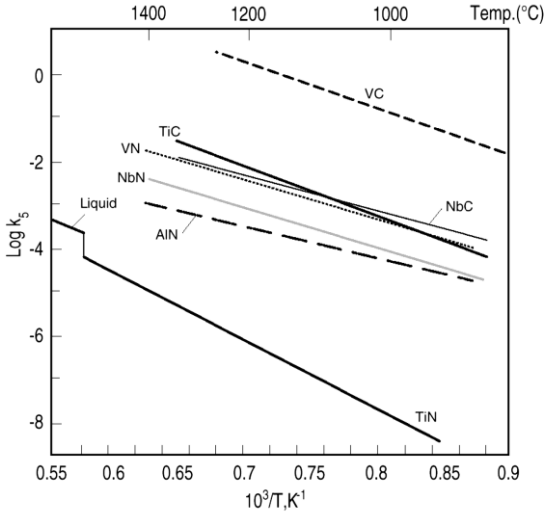

Figure 2-9 Solubility products of microalloying elements of their carbides and nitrides [88].

In Figure 2-8, the behaviours of several commonly used microalloying systems are illustrated. VC shows the highest solubility whereas TiN exhibits the lowest solubility in austenite, as shown in Figure 2-9. Each system has been reheated and cooled to various temperatures. The solubility of microalloying elements decrease as the temperature drops. At a critical temperature, the microalloying elements are saturated. They then become supersaturated when the temperature is lower than the critical temperature because of the difference between the amount of microalloying elements being dissolved after reheating and microalloying elements dissolution

limit in equilibrium condition at various temperatures. The degree of supersaturation is the potential for precipitation and it can be described by a factor, supersaturation ratio [35,89–96]. The supersaturation ratio is calculated by the solubility product of different microalloying elements at different temperatures using the following equation:

$$\mathrm{k} = \frac{[M][X]_{sol}}{10^{A-\frac{B}{T}}} \tag{2.11}$$

where *k* is the supersaturation ratio; *M* and *X* are the microalloying elements and non-metallic elements in solution after reheating; *A* and *B* are constants and *T* is the absolute temperature. The larger the supersaturation ratio, the larger the potential for precipitation to happen.

However, the supersaturation ratio is not the only factor that decides the precipitation potential, the ratio of precipitation forming solute atoms also plays an important role. Wadsworth *et al* [97] showed that when Nb and C wt% content in the steel is with the stoichiometry ratio of 7.8, the precipitation potential is the largest. Deviation from the stoichiometry ratio (hyper or hypo) results in a continuous decrease in the precipitation potential, see Figure 2-10.

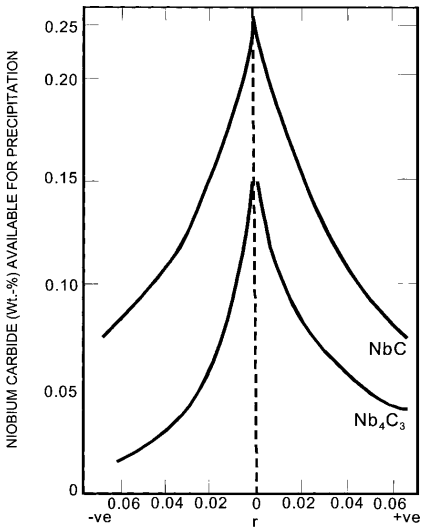

Figure 2-10 Niobium carbide available for precipitation at 923K (solution treatment at 1373K) as a function of extent of deviation from stoichiometry r. Positive r indicates C rich whereas negative r indicates Nb rich [97].

2.4 Grain growth during reheating

Grain growth happens in polycrystalline materials after the completion of recovery and recrystallisation to reduce grain boundaries areas, by which the internal energy of the system is further reduced. The grain boundaries are moved towards the respective centres of the curvature by the force difference on the grain boundaries. The grain boundary curvature is hence reduced [98]. The grain boundary movement leads to the elimination of smaller grains and growth of the larger grains with an increase of average grain sizes.

2.4.1 Driving force for grain growth

The grain growth behaviour of austenite grains has been intensively studied. For microalloyed steel production, avoiding any abnormal grain growth during the reheating stage is with great importance. This is because non-uniform austenite grains have been found to be hard to refine by subsequent rolling and it is very detrimental to the mechanical properties of the steel, toughness in particular [99].

The theory of grain growth is explained by Gladman [100,101]. He suggested the grain growth consists of two kinds of energy changes. First is the energy increase G_o caused by the expansion of the grain boundary of the growing grains. Second is the energy reduce G_s by the elimination of the shrinking grains [50]. The energy G_s and G_o are given by the following equations:

$$G_s = \frac{3\sigma}{2R_0} \tag{2.12}$$

$$G_0 = \frac{2\sigma}{R} \tag{2.13}$$

The net driving force is

$$\mathrm{G} = \frac{3\sigma}{2R_0} - \frac{2\sigma}{R} \tag{2.14}$$

where σ is the grain boundary energy, R_o is the mean radius of the grain and R is the radius of the growing grain. This shows that the grain radius being 4/3 larger than the mean grain radius is an essential for grain growth [50]. According to this, grain size distribution with good homogeneity is expected to have small or no grain growth. The grain growth tendency can be reduced by introducing drag forces on the austenite grain boundary movement. Solute drag and particle pinning are reported to be the two most important mechanisms [102–104].

2.4.2 Grain growth inhibition by particle pinning

When a moving grain boundary encounters a particle a part of the grain boundary is eliminated. To move the boundary away from the particle requires the eliminated grain boundary to be recreated which leads to an increase of the energy. This is the pinning force exerted on the moving grain boundary from the particles [50].

Gladman [105] proposed a model taking into consideration the elimination of small grains, the expending of growing large grains and the pinning force exerted by the particles. An equation was proposed showing the critical radius of the pinning particle:

$$r_c = \frac{6R_0 f}{\pi}\left(\frac{3}{2} - \frac{2}{z}\right)^{-1} \tag{2.15}$$

where R_o is the grain size, f is the precipitates volume fraction, z is the heterogeneity factor which is R/R_o the ratio of radii of the growing grains and pinned grains. Z value is observed to be in the range of $\sqrt{2}$ to 2 for grain growth [99,106]. Hence, for any grain size, a combination of particle volume fraction and particle size can suppress the grain growth.

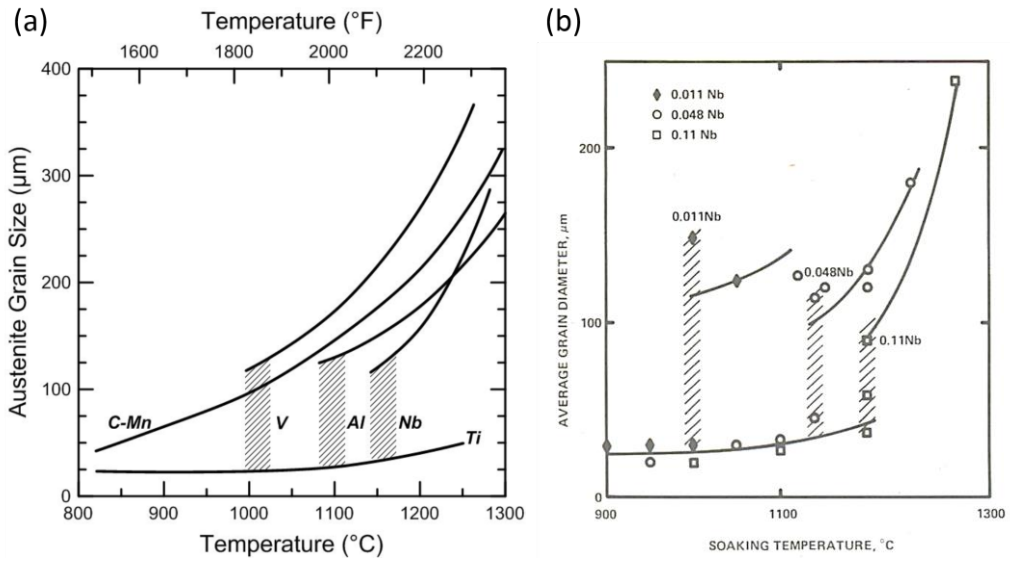

Figure 2-11 (a) Effect of various microalloying elements and reheating temperatures on the austenite grain size [107]. (b) Effect of Nb contents and reheating temperatures on the austenite grain size. Hatched area indicates the duplex grain sizes at the grain coarsening temperatures [99].

In order to retard austenite grain growth at high temperatures, it requires sufficient volume fraction of particles with the corresponding critical grain size. This can be achieved by adding the proper amount of microalloying elements into the steel. The undissolved second phase microalloying particles influence the migration of austenite grain boundaries due to the particle pinning theory explained above. The effect of various microalloying elements on austenite grain growth behaviour is shown in Figure 2-11. As it can be seen in Figure 2-11, the austenite grains of plain C-Mn steel shows continuously growth behaviour with the increase of the reheating temperature. The austenite grains gradually increase in size with a relative uniform equiaxed shape. However, microalloyed steels show discontinuous grain growth behaviour [72,105].

At lower reheating temperatures, the growth of austenite grains is pinned by the undissolved carbides or nitrides of the microalloying elements, e.g. NbCN, TiC or VN. When the reheating temperature reaches the critical grain coarsening temperature T_{GC}, hatched area in Figure 2-11, a small amount of grains grow abruptly producing a duplex microstructure [99,108–110]. This is because with the

increase of reheating temperature, the amount of microalloying elements dissolved increases [103,111]. This leads to the decrease in the volume fraction of the pinning particles. Hence some grains grow at the expense of the surrounding grains and the other grains remain being pinned. At reheating temperature higher than T_{GC}, the austenite grains show normal growth behaviour. This is because at this temperature, the vast majority of the precipitates are dissolved in solution. Hence, only a small amount of coarse and widely-spaced particles remains. They are ineffective in pinning the grain boundary movement [72,105].

Ti shows the strongest suppression force on grain growth of which the austenite grain growth is suppressed even above 1200°C, see Figure 2-11(a). The order of potential to suppress austenite grain growth is Ti>Nb>Al>V [107]. The potential to suppress is also highly related with the microalloying element concentration. As an example, Figure 2-11 (b) shows the increase of T_{GC} with the increasing amount of Nb [99].

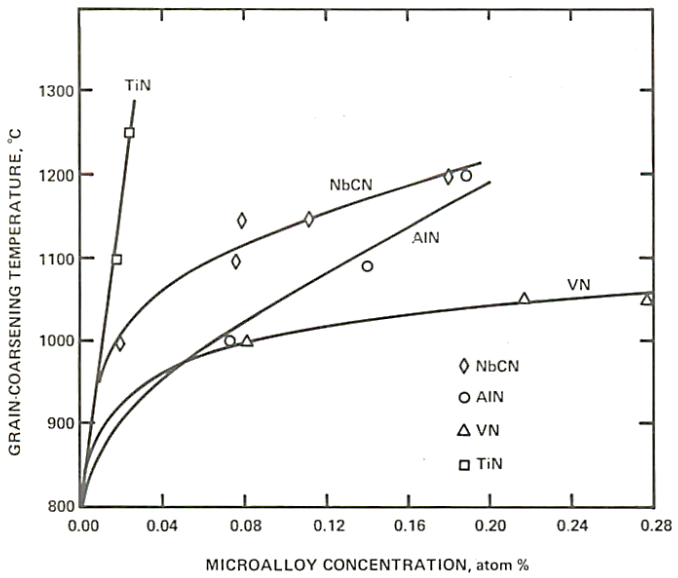

Figure 2-12 Effect of microalloying concentration of four kinds of microalloyed steels on the austenite grain coarsening temperature [99].

The grain coarsening temperature T_{GC} is the temperature above which discontinuous austenite grain growth occurs [47]. The effect of microalloying concentration of four kinds of microalloyed steels on T_{GC} was summarised by Cuddy *et al* in Figure 2-12

[99]. This nicely indicates the increase of T_{GC} with the increase of microalloying concentration in every kind of steels. However, it is lacking consideration of the influence from non-metallic elements C or N which interacts with the microalloying elements and decides the thermal stability of the precipitates [99,105,112]. To take the thermal stability of the precipitates into consideration, they compared T_{GC} with the dissolution temperature of the precipitates T_{DISS}. A linear relationship was found:

$$T_{GC} = A + BT_{DISS} \tag{2.16}$$

where *A* and *B* are constants dependent on the heat treatment histories of the steels. In Cuddy's other papers [3,113,114], he has reported that the T_{GC} is about 70-100°C lower than T_{DISS}. However, Palmiere *et al* [72] has reported that the solubility product Cuddy used has a tendency to underestimate the dissolution temperature by about 40-100°C. Using the solubility product he proposed in Equation 2.10, the calculated T_{DISS} is 107-150°C higher than the T_{GC}. This is much closer to the experimental determined difference between T_{DISS} and T_{GC} which is 100-200°C. Hence he developed an equation to predict the grain coarsening temperature T_{GC} from the dissolution temperature of the particles T_{DISS}, as following:

$$T_{GC} = T_{DISS} - 125°\text{C} \tag{2.17}$$

Accurate prediction on the T_{GC} and T_{DISS} is important to design the reheating practice. The choice of reheating temperature influences the amount of microalloying elements being dissolved, T_{GC} and initial austenite grain size. Reheating below T_{GC} avoids the intensive grain growth and improves the toughness and productivity. Whereas reheating above T_{DISS} dissolves all the microalloying elements and the potential to precipitate in austenite and/or ferrite during the following processing is greatly improved [115].

2.4.3 Grain growth inhibition by solute drag

The grain boundary migration under a fixed driving force will be influenced by the

solute atoms when they are attached to the grain boundary. Many studies have been conducted on the theory of solute drag [116,117]. Cahn [116] reported that with the increase of solute levels the grain growth rate decreases. The solute atoms will exert influences on the grain boundary energy per unit volume, isothermal grain growth law exponent and the boundary mobility at unit concentration solute. So each solute influences the grain growth rate with its own specific extent.

The driving pressure *(P)* for grain boundary migration to occur when solute is existed can be expressed by the combined Cahn-Lucke-Stuwe (CLS) theories [116,118,119]:

$$\mathrm{P} = (\mathrm{V}/\mathrm{M}) + [\alpha C_o V/(1 + \alpha\alpha' V^2) \tag{2.18}$$

where V is the grain boundary velocity, M is the boundary mobility, C_o is equilibrium solute level and α and α' are constants depending on the model used.

With high boundary velocities, the solute atoms cannot keep up with the moving boundary. The boundary breaks away from the solute atmosphere. In this case, the first term in the Equation 2.18 dominates, therefore the solute atoms only exert a very weak effect to slow the boundary migration. Conversely, the second term of Equation 2.18 represents the case of low driving force and low boundary velocities. With low boundary velocities, the solute atoms may diffuse with the boundary and tend to drag the boundary back to its equilibrium position. Hence the boundary mobility is considerably slowed by the solute.

The influence of solute drag effect on austenite grain growth has been studied by many researchers [74,120–123]. Fu *et al* [120,121] compared modelling results considering only pinning effect or both pinning and solute drag effect with the experimental results at various temperatures, as shown in Figure 2-13. It can be seen that both pinning effect and solute drag effect play an important role in retarding austenite grain growth. The solute drag effect reduces with the increase of temperature as the grain boundary gradually break away from the solute atmosphere.

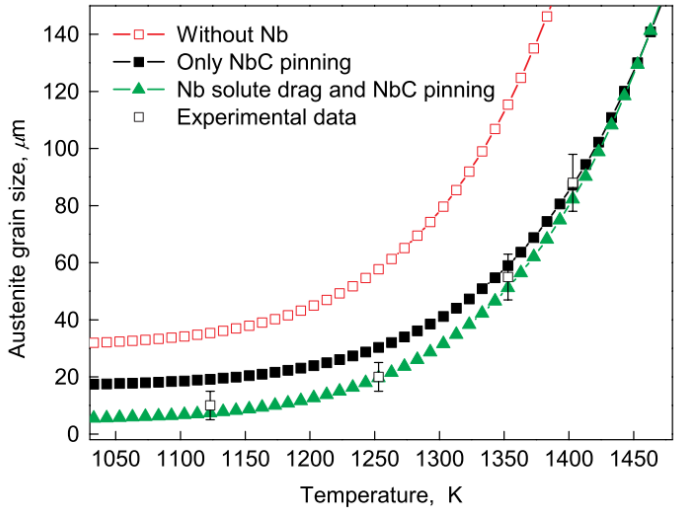

Figure 2-13 Comparison between the calculated austenite grain size and the experimental data at various temperatures [120].

2.5 Grain refinement during thermomechanical processing

2.5.1 Metallurgical processes happening during thermomechanical processing

Thermomechanical processing of microalloyed steels includes reheating to dissolve the microalloying elements, rough rolling in the full recrystallisation region ($T_{def} > T_{95\%}$), finish rolling in the full unrecrystallisation region ($T_{def} < T_{5\%}$) and subsequent cooling. The microstructural evolution and the metallurgical processes happening along thermomechanical processing is illustrated in Figure 2-14.

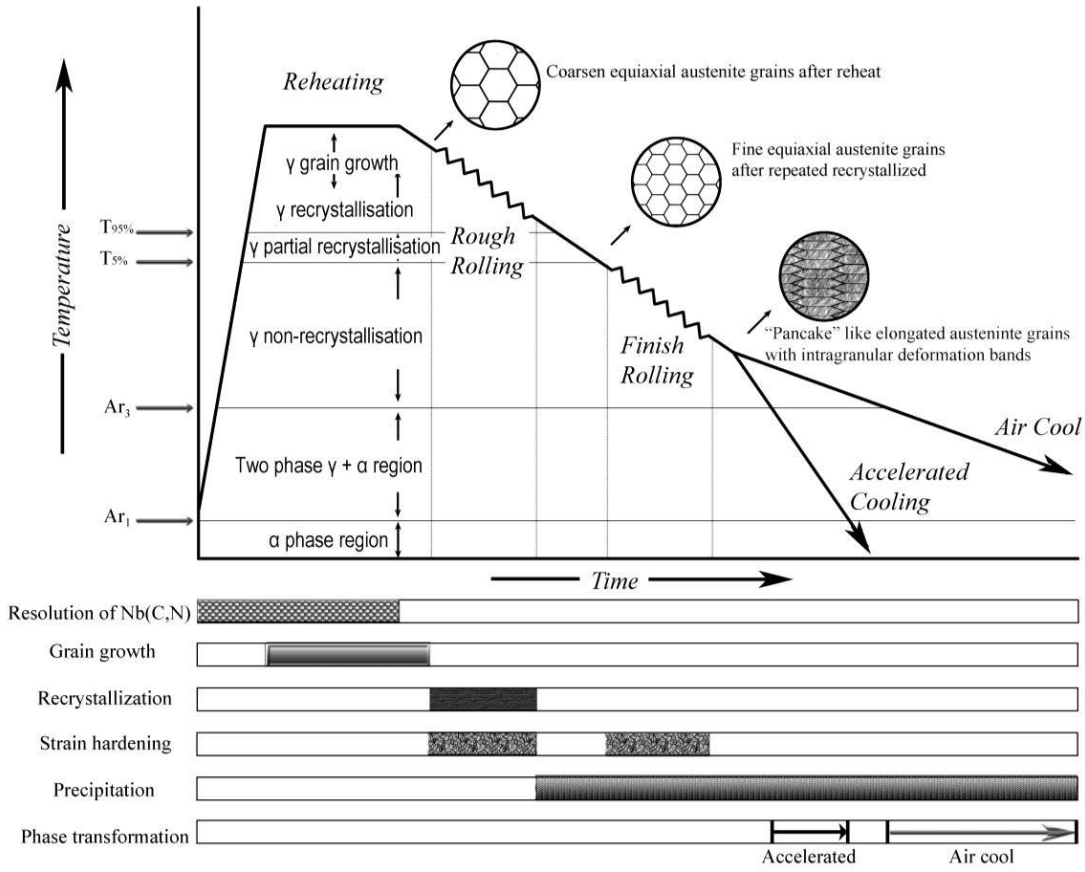

Figure 2-14 Schematic illustration of the stages of thermomechanical processing and metallurgical mechanisms taking place during these processes [124].

2.5.2 Critical temperatures $T_{5\%}$ and $T_{95\%}$

2.5.2.1 Definition of $T_{5\%}$ and $T_{95\%}$

$T_{5\%}$ and $T_{95\%}$ are the temperatures at which 5% and 95% recrystallisation has occurred for a given holding period [58,125]. $T_{5\%}$ is used to indicate the temperature under which no recrystallisation happens for a given holding period. And $T_{95\%}$ represents the temperature under which the recrystallisation fraction can no longer complete during the given holding period. Both $T_{5\%}$ and $T_{95\%}$ are dependent on alloy composition [59,108] and deformation parameters [59,90,126,127]. $T_{5\%}$ is roughly 30-70°C below $T_{95\%}$ depending on different steels and processing parameters [35,128].

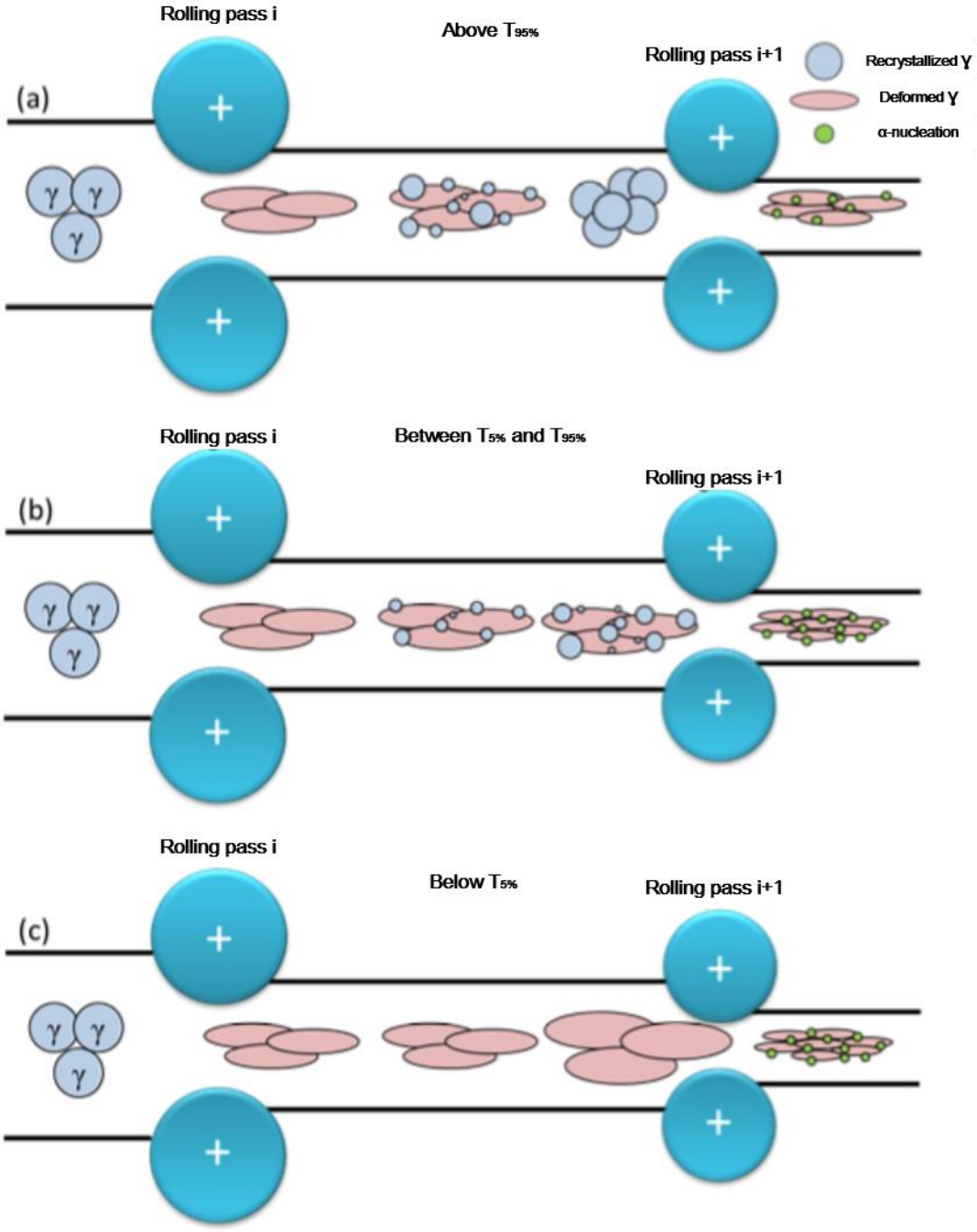

Figure 2-15 Illustration of deformation (a) above $T_{95\%}$ where complete recrystallisation happens between rolling pass i and i+1; (b) between $T_{5\%}$ and $T_{95\%}$ where partial recrystallisation occur between rolling pass i and i+1; (c) below $T_{5\%}$ where no recrystallisation happens between rolling pass i and i+1; Adapted from [51].

It can be seen in Figure 2-6 that if the deformation is performed above $T_{95\%}$, fully recrystallised microstructure is obtained. No recrystallisation happens when the steel is deformed below $T_{5\%}$. And partially recrystallisation happens when the deformation is conducted between $T_{5\%}$ and $T_{95\%}$. An illustration of austenite microstructure evolution when the steel is deformed at temperature above $T_{95\%}$ and $T_{5\%}$ is shown in Figure 2-15.

There is no doubt that $T_{5\%}$ and $T_{95\%}$ are among the most important parameters during thermomechanical processing of microalloyed steels. A thorough understanding of their role and the factors that can influence them is important to optimise production process and to achieve the required properties more efficiently.

2.5.2.2 Influence of microalloying elements on $T_{5\%}$ and $T_{95\%}$

In practice, the most important role that microalloying elements play is their influence on the recrystallisation stop temperature $T_{5\%}$. A classic graph proposed by Cuddy [58] shows the effect of different microalloying elements and its contents to the $T_{5\%}$ temperature. It is clearly shown that $T_{5\%}$ is raised by all of these elements, in which Nb shows the most profound influence. This can be explained with the help of Figure 2-8. Due to the difference in solubility, Ti precipitates before deformation and V does not precipitate until the end of deformation.

The mechanisms of microalloying elements to raise $T_{5\%}$ is explained through the interaction between precipitation and recrystallisation in Section 2.5.5.

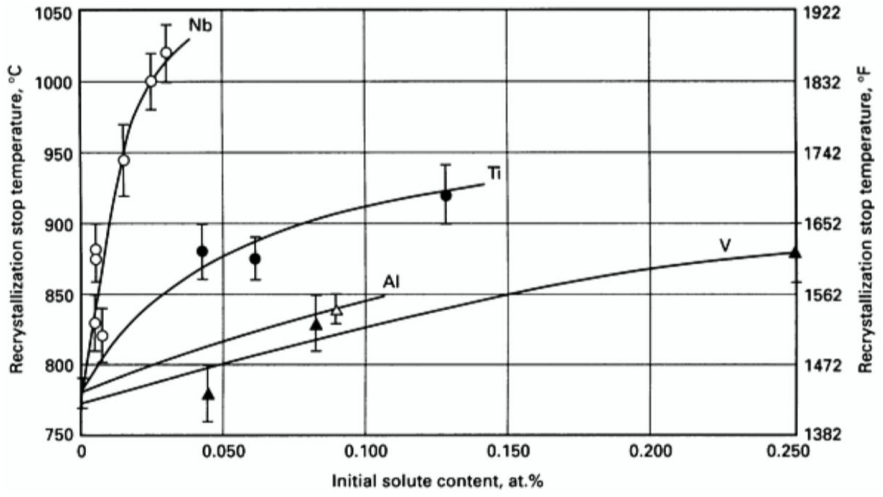

Figure 2-16 Influence of different elements and its contents on recrystallisation stop temperature on a steel with 0.07 wt% C, 1.4 wt% Mn and 0.25 wt% Si. Deformation per pass 10-15% [58].

2.5.2.3 Determination of $T_{5\%}$ and $T_{95\%}$

$T_{5\%}$ and $T_{95\%}$ can be determined by various methods. The most commonly used methods are direct microstructure observation [35,122,124,129], empirical determination [90,130,131] multi-deformation testing [90,95,130–136], interrupted deformation testing [28,35,51,63,137–142] and rolling mill data logs [128,131].

(a) Empirical determination

Using empirical equations to predict the $T_{5\%}$ can be useful to design the rolling process to produce steels with required mechanical properties, especially in the cases when the laboratory tests are not available.

Boratto *et al* [130] proposed a well-known equation to estimate $T_{5\%}$ as a function of the chemical composition.

$$T_{5\%} = 887 + 464\mathrm{C} + \left(6445\mathrm{Nb} - 644\sqrt{\mathrm{Nb}}\right) + \left(732\mathrm{V} - 230\sqrt{\mathrm{V}}\right) + 890\mathrm{Ti} + 363\mathrm{Al} - 357\mathrm{Si} \quad (2.19)$$

where *C, Si, Al, Ti, Nb* and *V* are contents of the elements in weight percent of the steel. It is well known that $T_{5\%}$ can alter dramatically with different deformation

parameters. However, the influence of the deformation is not considered in Boratto's equation. Another equation is developed by Bai *et al* [90], in which the influence of strain is taken into consideration.

$$T_{5\%} = \beta e^{-0.36\varepsilon} \tag{2.20}$$

where β is a composition-dependent coefficient and ε is the pass strain. For the steels and stains used by Bai *et al* [90], the coefficient β is reported to be 1078°C, 1088°C and 1103°C.

The empirical equations may be used to estimate the $T_{5\%}$ for the steels used in these particular studies. However, due to their empirical nature their ability to accurately predict $T_{5\%}$ for any steels with chemical compositions or deformation parameters outside these studies is dubious.

(b) Multi-deformation testing

The multi-deformation testing consists of performing consecutive deformations with certain interval between passes while the steel is cooled with a selected cooling rate. The strain, stress and temperature for each pass is recorded. The mean flow stress (MFS) for each pass is calculated by dividing the area below the stress-strain curve for each pass by the corresponding strain [90,95,130–136]. Then a curve representing the evolution of MFS with the change of the inverse of temperature is generated. The $T_{5\%}$ which illustrates the inhibition of recrystallisation is determined by the changing point of the slope of MFS curve. An example is shown as following:

Figure 2-17 (a) shows the stress strain curve of a multi-deformation testing simulating a 23 passes plate rolling process with a 20s interval time and 1°C/s cooling rate. The change of stress with the increase of strain is divided into four regions as indicated in Figure 2-17. And the determination of the four regions is better interrupted with the help of the MFS curve shown in Figure 2-17 (b).

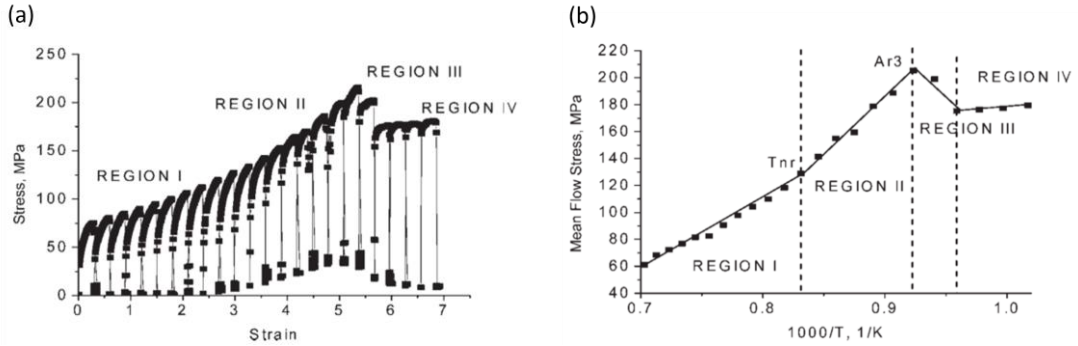

Figure 2-17 a) Stress-strain curve from a multi-deformation test on a low carbon microalloyed steel. b) Mean flow stress evolution against inverse of absolute temperature [140].

In region I the deformation is conducted at high temperature where complete recrystallisation happens between passes and no strain is accumulated. The stress increases is only caused by the decrease of deformation temperature. In region II, the increase in the stress is faster than that of region I, which means besides temperature drop another mechanism is contributing to the stress increment. This is because recrystallisation is being inhibited between passes and the strain is accumulated. In region III, the MFS drops significantly and this indicates the transformation of austenite to ferrite. In region IV, the stress starts to increase again indicating the deformation of ferrite.

$T_{5\%}$ is the intersection point between region I and II. However, the $T_{5\%}$ point is not intersected by two straight lines. It has been reported that near the $T_{5\%}$ point, the two lines are actually curved which give a gradual transition from region I to region II [51]. And this is because of the existence of deformation in the partially recrystallised region between $T_{95\%}$ and $T_{5\%}$. The strain starts to accumulate in the partially recrystallised region but the accumulation is not as fast as it in the fully unrecrystallised region. Hence there is a gradual transition near $T_{5\%}$ point.

$T_{5\%}$ is dependent on the interval time as it decides whether it has enough time for precipitation to happen and inhibit the recrystallisation. So the interval time should be chosen carefully based on the rolling process to be simulated. It is also worth mentioning that even though the strain, strain rate, cooling rate and interval time

between passes changes continuously in industrial production. These parameters need to be kept constant when this method is used. Any change of these parameters between passes could generate false transition data [51].

(c) Double-hit deformation testing

The double-hit deformation test is designed to measure the softening fraction of austenite under the prescribed interval time between the two passes. The double-hit deformation test consists of dissolving microalloying elements back into solution by reheating, fast cooling the steel to the deformation temperature, deformation with the chosen deformation parameters (i.e. strain, strain rate), unload and holding isothermally for the given interval time, deforming the steel again using the same deformation parameters. After deformation, the flow stress curve is recorded and analysed to measure the softening fraction of austenite during the interval time [33,35,60,63,139,143].

The softening fraction is calculated by analysing the flow curves generated from the two deformation passes. After the first deformation, the amount of softening during the interval time alters the shape of the flow curve of the second deformation. If 100% softening happens, the two flow curves are identical. If no softening happens, the second curve matches the extrapolation from the flow curve of the first deformation.

As reviewed in the earlier Section 2.1.2.1, the overall softening fraction caused by recovery in austenite is approximately 15-20% [30–33]. Any deformation leading to overall softening less than 20% is conducted below $T_{5\%}$.

The four main methods used in the literature to analyse the flow curve data are summarised in Figure 2-18 [35,51,63,137–142].

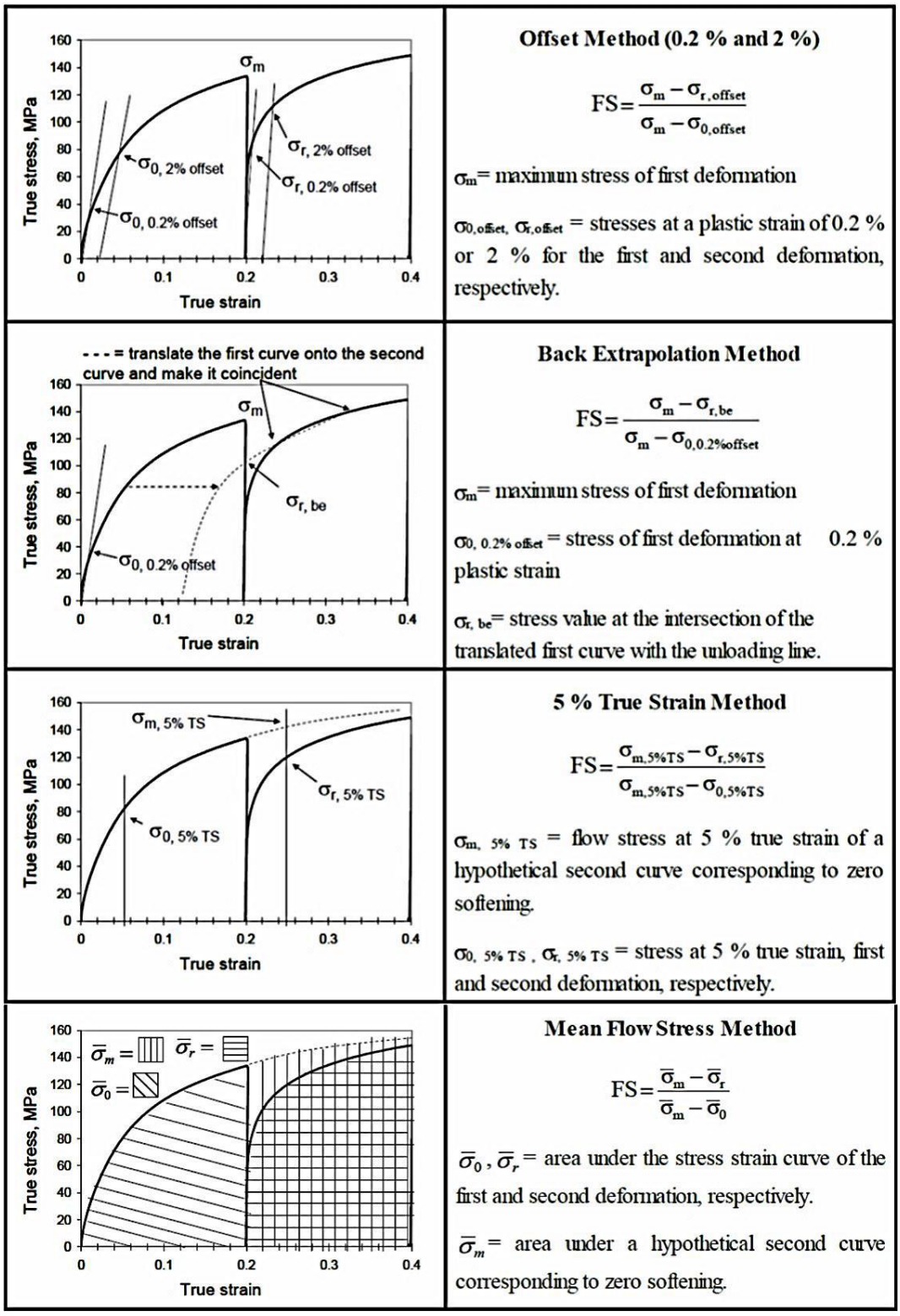

Offset Method (0.2 % and 2 %)

$$FS = \frac{\sigma_m - \sigma_{r,offset}}{\sigma_m - \sigma_{0,offset}}$$

σ_m= maximum stress of first deformation

$\sigma_{0,offset}$, $\sigma_{r,offset}$ = stresses at a plastic strain of 0.2 % or 2 % for the first and second deformation, respectively.

Back Extrapolation Method

$$FS = \frac{\sigma_m - \sigma_{r,be}}{\sigma_m - \sigma_{0,0.2\%offset}}$$

σ_m= maximum stress of first deformation

$\sigma_{0,\ 0.2\%\ offset}$ = stress of first deformation at 0.2 % plastic strain

$\sigma_{r,\ be}$= stress value at the intersection of the translated first curve with the unloading line.

5 % True Strain Method

$$FS = \frac{\sigma_{m,5\%TS} - \sigma_{r,5\%TS}}{\sigma_{m,5\%TS} - \sigma_{0,5\%TS}}$$

$\sigma_{m,\ 5\%\ TS}$ = flow stress at 5 % true strain of a hypothetical second curve corresponding to zero softening.

$\sigma_{0,\ 5\%\ TS}$, $\sigma_{r,\ 5\%\ TS}$ = stress at 5 % true strain, first and second deformation, respectively.

Mean Flow Stress Method

$$FS = \frac{\bar{\sigma}_m - \bar{\sigma}_r}{\bar{\sigma}_m - \bar{\sigma}_0}$$

$\bar{\sigma}_0$, $\bar{\sigma}_r$ = area under the stress strain curve of the first and second deformation, respectively.

$\bar{\sigma}_m$ = area under a hypothetical second curve corresponding to zero softening.

Figure 2-18 Summary of the four common methods to determine the softening fraction from the flow curves of a double-hit deformation test [140].

2.5.3 Deformation in fully recrystallised region ($T_{def} > T_{95\%}$)

2.5.3.1 Conventional Rough rolling process

When slab comes out from reheating furnace or continuous casting machine, it will first enter the rough rolling mill to be rough rolled. There are two purposes for the rough rolling. The first is simply to reduce the thickness of the steel to the required value ready to be finish rolled. Large reductions can be achieved because of the low mill loads required due to the high rolling temperature. The second is to obtain the uniform austenite structure with the finest possible grain size at the end of the rough rolling stage. Since the deformation happens above the $T_{95\%}$, complete recrystallisation happens between passes. Hence, during rough rolling, the fine austenite microstructure is obtained through repeated recrystallisation.

Uniformity of austenite microstructure at the end of rough rolling is of great importance. To ensure that complete recrystallisation occurs between passes of rough rolling, a critical strain or minimum reduction (15-20%) is widely reported [48,57,125]. This critical strain is influenced by the initial austenite grain size. The larger the initial grain size the higher the critical strain is required for complete recrystallisation.

In practice, many researchers [3,57,114,125] have discovered that the influence of the initial austenite grain size to the final recrystallised austenite grain size at the end of rough rolling is minor. This is because the recrystallised austenite grain size tends to converge after several passes regardless of the initial grain sizes, as can be seen in Figure 2-19. Hence there is a limit degree of refinement which can be achieved through rough rolling [3,57,114,125]. Within the capabilities of conventional rolling mills, the finest austenite grain size has been reported to be about 15μm [46].

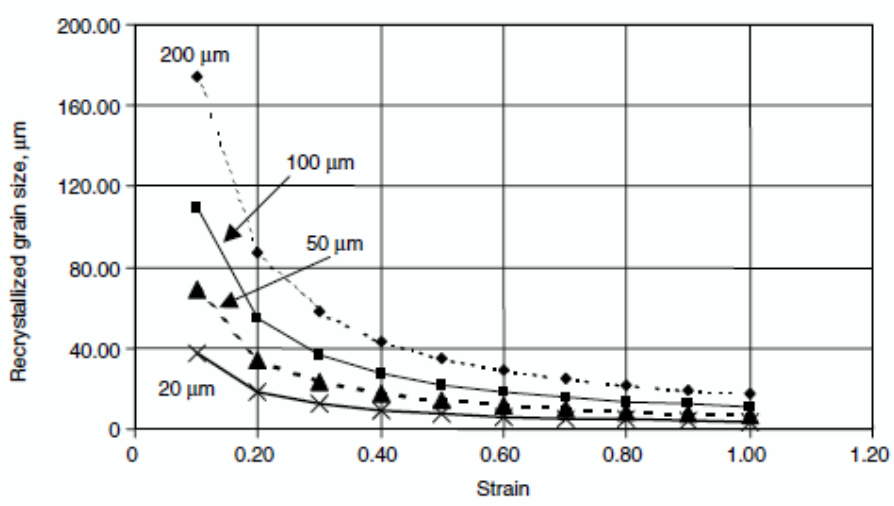

Figure 2-19 Influence of different initial austenite grain size to the final recrystallised austenite grain size at the end of rough rolling [57].

2.5.3.2 Recrystallisation controlled rolling (RCR)

The recrystallisation controlled rolling (RCR) process consists of repeated recrystallisation of austenite and the inhibition of austenite grain growth. There are two essential features for the steels designed to use for RCR. The first one is that they need to have a low $T_{95\%}$ to make sure that all the passes needed will be performed within the fully recrystallised region, even if there is a large temperature drop from reheating furnace to the temperature of the final finish pass. For example, for wide plate rolling, a temperature drop of about 300-400°C is expected. The second requirement is the pre-existing inhibition system to suppress the grain boundary motion. The pinning force needs to be weak enough to allow static recrystallisation to happen and yet large enough to suppress the austenite grain growth between passes [60].

The difference in austenite behaviour between steels subjected to CHR (conventional hot rolling) and RCR is illustrated schematically in Figure 2-20. The difference between CHR and RCR is the grain growth inhibitor. In CHR, the advantage of grain refinement through repeated recrystallisation is negated due to the rapid grain growth after recrystallisation. However, in RCR a finer austenite microstructure will be

achieved because of the existence of the ideal magnitude pinning force on grain growth [50,60].

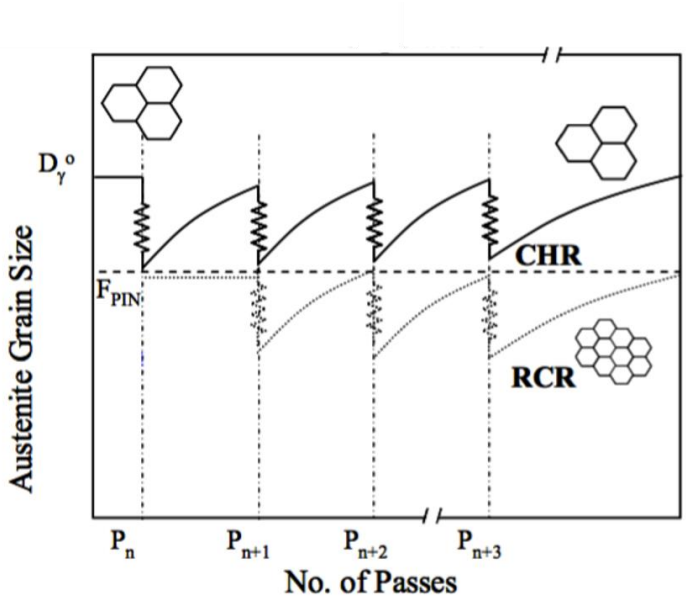

Figure 2-20 Grain size evolution along different processing routes. CHR: conventional hot rolling. RCR: recrystallisation controlled rolling [50,60].

The V-Ti-N microalloyed steels have been reported to be suitable for RCR processing [110,115,144,145]. Precipitated TiN provides grain growth pinning force with the ideal magnitude and V(CN) precipitates provides ferrite strengthening during final cooling. Nb-Mo system is also been developed [50] to use for RCR processing. In this Nb-Mo system, the force to retard austenite grain growth consists of two parts, the pinning force from the undissolved Nb(CN) during reheating and the solute drag force from the molybdenum segregated on the grain boundaries.

Because of the existence of the inhibition force on grain growth, in RCR processing, the finish rolling can be conducted with much higher onset temperature. This leads to smaller mill loads and shorter interval time between rough rolling and finish rolling (3mins for RCR and 8mins for CHR) which ultimately increased the productivity [146].

2.5.4 Deformation in partially recrystallised region ($T_{5\%} < T_{def} < T_{95\%}$)

When the deformation temperature is between $T_{5\%}$ and $T_{95\%}$, the recrystallisation of austenite starts but cannot finish during the interval time between passes. Therefore, there is tendency for the austenite to have a duplex microstructure consisting of fine recrystallised grains and coarse deformed original grains [3,35,89,113,114,147].

There might be two reasons for the occurrence of the partially recrystallised region. First is that the pinning force provided by the precipitates are too small to fully retard recrystallisation. The second is that the distribution of precipitation is too localised [114].

Ideally, it is important to make sure that no deformation is performed in the partially recrystallised region. This is because once the duplex microstructure is created, it cannot be removed by any further deformation [114]. They will eventually be transformed into duplex ferrite microstructure which is detrimental for the mechanical properties of the steel, especially for those applications where both strength and toughness are very important [147]. An example is given in Figure 2-21. Cuddy [48] showed the duplex austenite microstructure after deformation in the partially recrystallised region and the corresponding duplex ferrite microstructure.

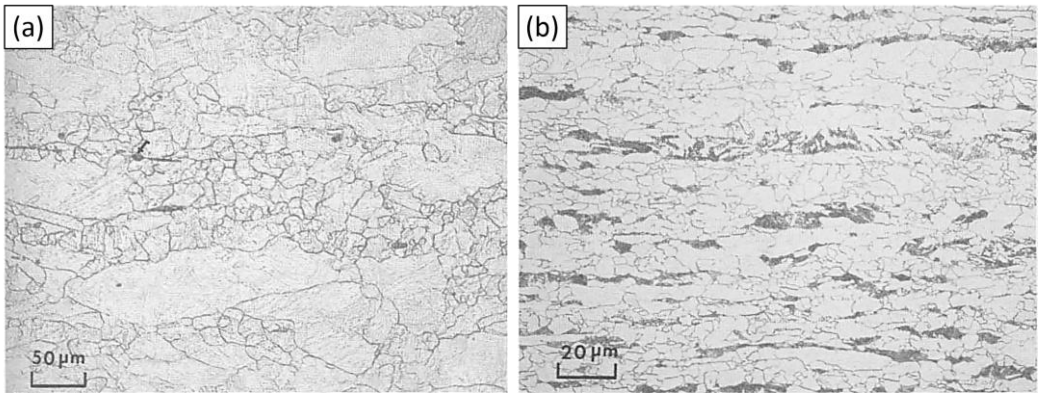

Figure 2-21 a) Duplex austenite microstructure after deformation in partially recrystallised region b) The corresponding transformed ferrite microstructure [48].

2.5.5 Deformation in fully unrecrystallised region ($T_{def} < T_{5\%}$)

2.5.5.1 Effects of Nb solute or precipitation on austenite recrystallisation

As reviewed above, the existence of microalloying elements raise the $T_{5\%}$ of steels. The reasons that microalloying addition causes the suppression of austenite recrystallisation has drawn great interest from many researchers. The mechanisms have been reported to be solute drag effect, strain-induced precipitation effect or the combined action of the two.

From early researches [81,148], it has been reported that the solute drag effect of microalloying elements could retard the recovery and recrystallisation of austenite, which shifts the recrystallisation-temperature-time (RTT) diagram to longer times compared with the plain carbon steel, as shown in Figure 2-22 [148]. Such a retardation on recrystallisation of austenite is of great importance because it provides the possibility for the recrystallisation and precipitation curves to intersect. Precipitation then happens before recrystallisation which holds the unrecrystallised austenite microstructures even further. The effectiveness of solute drag on retarding the recrystallisation is Nb > Ti > Mo > V [81,93,104].

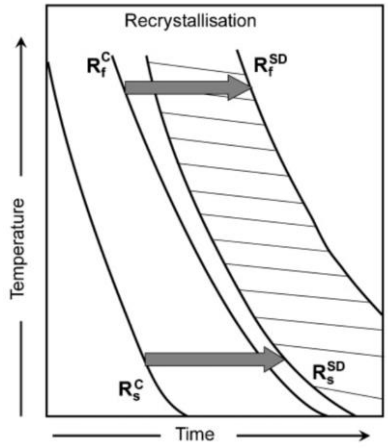

Figure 2-22 Interaction between recrystallisation and solute drag effect. R_s is recrystallisation start curve; R_f is the recrystallisation finish curve; C stands for plain carbon steel; SD stands for solute drag effect. Adopted from [148]

Solute drag effect provided by Nb in solution is limited and it can only suppress the recrystallisation to certain extents [81,89,93,104,125,139,148,149]. A much greater retarding force is the pinning force provided by the strain-induced fine Nb(CN) particles if precipitation occurs prior to or at the early stage of recrystallisation [93].

Nb in solution before deformation is necessity to retard recrystallisation [149]. If the precipitation happens before deformation, i.e. the Nb(CN) is existing before deformation, there is almost no pinning effect [149]. This is because of the high heterogeneity in the distribution of strain-induced precipitates. The preferred site for strain-induced precipitation to happen is the high dislocation density regions, i.e. grain/subgrain boundaries and deformation bands, where the precipitation density is much higher. Hence a stronger retardation force is provided [139]. A good illustration is shown in Figure 2-23 [85]. The distribution of strain-induced precipitate is highly localised. After those areas are occupied by Nb(CN) precipitates general precipitation in the matrix of unrecrystallised austenite happens. In order to have strain-induced precipitation, a critical level of Nb supersaturation ratio needs to be reached [89,93].

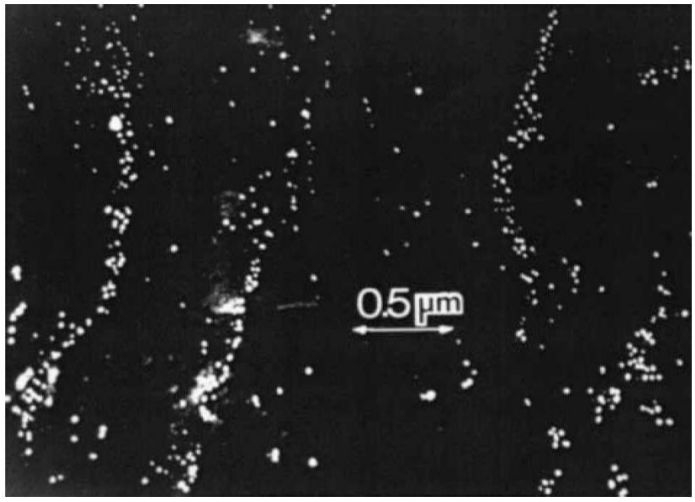

Figure 2-23 Strain-induced precipitation of NbCN in austenite steel containing 0.09 wt% C and 0.07 wt% Nb. Sample being reheated to 1250°C, then rolled (25%) and held at 950°C, followed by air cooling to room temperature [85].

2.5.5.2 Interaction between precipitation and austenite recrystallisation

With the help of a generalised recrystallisation-precipitation-temperature-time (RPTT) diagram, Hansen *et al* [93] explained the interaction between the two competing process, precipitation and recrystallisation, see Figure 2-24. T_{sol} is the lowest temperature Nb(CN) particles are fully dissolved in austenite. T' is the temperature below which precipitation and recrystallisation complete. T_R is the temperature below which Nb precipitation happens before austenite recrystallisation. Also in Figure 2-24, R_s' and R_f' stands for the start and finish of recrystallisation of plain carbon steel. R_s and R_f are the start and finish of recrystallisation of Nb steel. P_s' and P_s'' are the hypothetical precipitation curves for deformed and undeformed austenite.

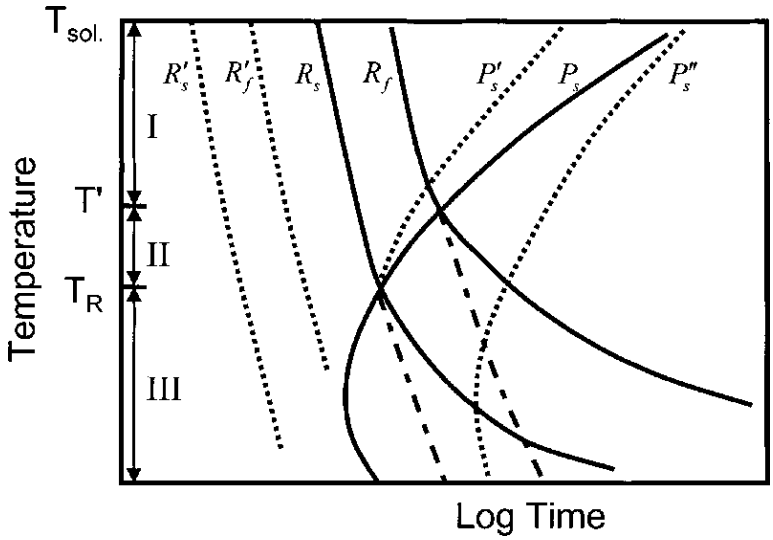

Figure 2-24 Recrystallisation-Precipitation-Temperature-Time (RPPT) diagram illustrating the interaction between niobium solute, precipitation and recrystallisation [93,139].

In region I, the recrystallisation is completed before the onset of precipitation. However, the austenite grains are refined though recrystallisation which may cause an acceleration of the onset of precipitation. Hence the actual start of precipitation P_s is between P_s' and P_s''.

In region II, precipitation happens after the partial recrystallisation. Deformation in this area needs to be avoided as discussed in Section 2.5.4.

In region III, precipitation happens before the start of the recrystallisation. The pinning force of precipitation further suppress the onset of recrystallisation to longer times.

2.5.5.3 Quantitative explanation on recrystallisation suppression by precipitation pinning effect

The mechanism of recrystallisation nucleation is widely accepted to be the strain-induced boundary migration [93,150–152]. The austenite grains with low dislocation density will bulge into the high dislocation density grains. The driving force for recrystallisation is considered to be the dislocation density difference between adjacent subgrains [152]. The quantitative driving force is given by the following equation:

$$F_{RXN} = \frac{\mu b^2 \Delta\rho}{2} \tag{2.21}$$

where μ is the austenite shear modulus, b is the Burgers vector and $\Delta\rho$ is the dislocation density change. The values of μ, b and $\Delta\rho$ has been experimentally measured and used in some studies on thermomechanical processing of austenite [32,93,113,139]. The driving force for recrystallisation has been found to be approximately of the order of 20MN•m^{-2} [37,72,139].

In order to retard recrystallisation, the pinning force provided by the strain-induced precipitates must be larger than the recrystallisation driving force. The pinning force can be calculated using the following equation:

$$F_{PIN} = 4r\sigma N_s \tag{2.22}$$

where r is the radius of precipitate particles, σ is the interfacial energy of austenite grain boundary and N_s is the number of particles per unit area.

Three different models have been proposed to calculate N_s. These are rigid boundary

[103], flexible boundary [113] and subgrain boundary [93] models. The subgrain model of Hansen *et al* [93] has been reported to be the most realistic model [35,37,139]. The pinning force is given by:

$$F_{PIN} = \frac{3\sigma f_v l}{2\pi r^2} \tag{2.23}$$

where, σ is the interfacial energy of austenite grain boundary, f_v the is the volume fraction of precipitate particles, l is the size of the subgrains and r is the radius of precipitate particles.

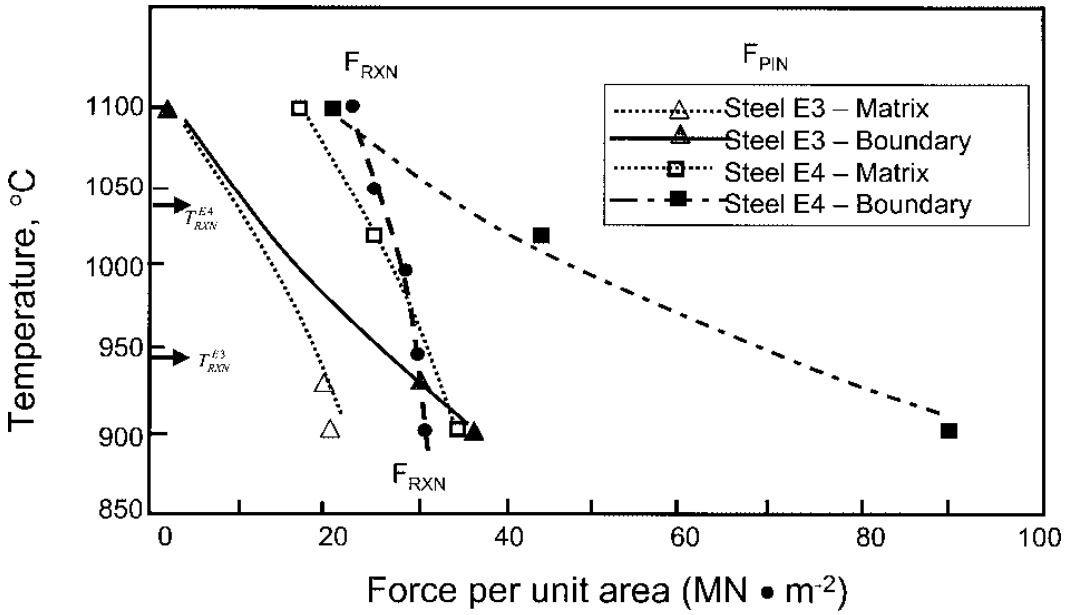

Figure 2-25 Comparison between F_{RXN} and F_{PIN} at various deformation temperatures; E3: 0.08 wt% C, 1.45 wt% Mn, 0.02 wt% Nb; E4: 0.08 wt% C, 1.45 wt% Mn, 0.09 wt% Nb [35].

In the study by Palmiere *et al* [35], the volume fractions and grain sizes of the precipitate particles were measured separately on austenite grain/subgrain boundaries and in the grain matrix. The result in Figure 2-25 shows that the pinning forces at the grain boundaries are much larger than the driving force for recrystallisation. This explains well that the suppression of recrystallisation is because of the high pinning force on the grain boundaries. This is particularly obvious when comparing F_{REX} and F_{PIN} at 10°C below the $T_{5\%}$ temperature as shown

in Figure 2-25. For example, for E4 F_{PIN} at the grain boundaries is about 19MN•m^{-2} greater than F_{REX}, whereas the F_{PIN} in the matrix is approximately 1 MN•m^{-2} less than F_{REX}. For E3 F_{PIN} in the matrix is well less that F_{REX} but F_{PIN} at grain boundaries is similar with the F_{REX}. Palmiere *et al* [35] explained that this is because the efficiency of the extraction replica technique cannot reach 100% as well as the difficulty in detecting particles smaller than 2nm. This caused the calculated F_{PIN} to be smaller than the actual F_{PIN}.

2.6 Microalloying application on long products

Nowadays, the application of microalloying concept to low carbon flat rolled steel products has been widely accepted and used in the steel industry. Comparatively, its application in long products has been much limited. Especially Nb microalloying in long products containing higher carbon content (>0.2wt %) has been in debate for a long time caused by its limited solubility in austenite. However, considering the successful application of microalloying in flat rolling products, this lack of application in long products offers significant opportunities to design new steel to meet more rigorous requirements, e.g. anti-seismic grade rebars or heavy haul rail steels [6,7].

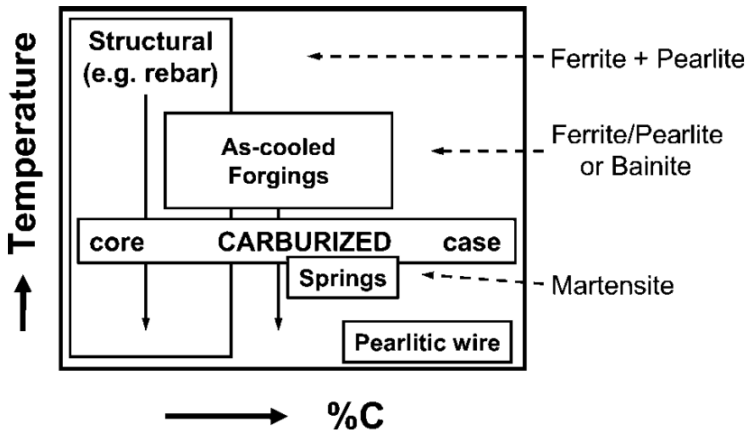

Figure 2-26 Processing window for different long products application which have the potential to benefit from microalloying addition [7].

For long product applications, the design of alloying and corresponding processing routine is based on the specific needs, e.g. mechanical properties or section size and shape of each application [7]. Figure 2-26 shows the substantial differences in microstructures, processing temperature and carbon content of long product application. A brief review of the development and application of microalloyed long products is given in the following section [7].

2.6.1 Application examples

2.6.1.1 Reinforcing bars (Rebars)

Rebar is a vital element in concrete structure to offer the tensile strength it requires to perform in its service. To ensure the successful performance of reinforced concrete in more serious situations, e.g. earthquake resistance or corrosion resistance, has continuously raised the requirement for rebars.

In the early 70s, a technique called Tempcore [153] was developed and used to produce high strength rebars. The bar is partially water quenched immediately after rolling to form a layer of martensite on the surface. During the following cooling, the martensite layer is self-tempered by the residual heat in the core. Therefore, the outer layer provides high strength and the core provides high toughness. However, the obvious drawback of the Tempcore rebar is that the yield strength is heavily depended on the martensite outer layer. If damaged, the load or cracking will transfer to the weaker core [7,8].

More recently, microalloying has been applied to produce multiple grades of high strength rebars with strength up to 600MPa. Compared to Tempcore rebars, the microalloyed rebar shows optimized strength and ductility, better weldability due to the relatively lower carbon levels and improved fatigue properties [6–8].

Nb and V microalloyed rebars have been developed by direct cooling after thermomechanical processing [8,9]. V is added into a standard 20MnSi base rebar steel with different N contents. The strength contribution from different

strengthening mechanisms are illustrated in Figure 2-27. A small increase in the grain size contribution is observed in both microalloyed steel due to the V addition. The main increase in strength is attributed to the precipitation strengthening. With a higher precipitation potential from the high N steel, an even larger precipitation strengthening contribution is observed.

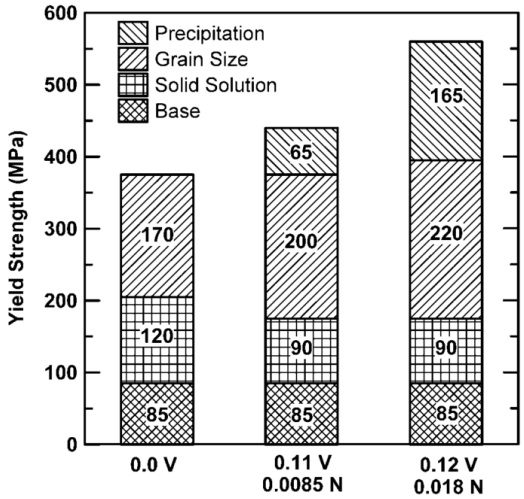

Figure 2-27 Contribution of each strengthening mechanisms to the base rebar from V additions [7].

Hashimoto *et al* [9] studied the influence of Nb addition on the properties of a rebar steel with composition of 0.25C-1.2Mn-0.5Si. It is reported that the reheating temperature is a critical factor because it determines the degree of Nb dissolution, hence the precipitation potential in the following process.

Most recently, Wright [8] reported a commercially launched Nb microalloyed high strength rebar with excellent properties of 626MPa yield stress, 752MPa tensile stress and 24.5% elongation.

2.6.1.2 Rail steels

Since 1850s when railroad traffic started, various rail steels and sections have been developed for the purposes of communication and industrial needs. Recently, due to the increasing requirement on load capacity and speeds of the railroads, the rail

steels has to offer better mechanical properties. The key mechanical properties for rail steels are the wear resistance and contact rolling fatigue resistance [10,11]. Nb provides austenite grain refinement which transfers to smaller interlamellar spacing and colony size of pearlite, because of this the ductility of the rail steels improves which increase the resistance to rail head damage [4].

Early work on Nb microalloyed rail steels with 0.015-0.047 wt% Nb exhibited continuously improved mechanical properties with the increase of Nb contents [12]. Later, Singh *et al* [13] found that a 40MPa increase in tensile strength can be achieved through refinement of pearlite colony size and interlamellar spacing without harming the weldability. Using Nb as a grain refiner, a successful product Niobras-200 rail steel was developed with the composition of 0.75 wt% C, 0.8 wt% Si, 1.0 wt% Mn and 0.02 wt% Nb. Niobras-200 possesses a high tensile strength of approximately 1100MPa and it provides great performance in heavy haul iron ore service [14]. A recent work on the basis of the heavy haul rail steel with increased Nb content (up to 0.073 wt %) has shown that the finest austenite grain size of 7.2um is achievable. And the best fracture toughness which is approximately 50MPa•$m^{1/2}$ is obtained when the Nb content is about 0.05 wt% [15].

2.6.1.3 Wire rods

Nb delays the pearlite transformation hence refines the interlamellar spacing and colony size of pearlite [16]. Jansto [154] evaluates the influence of Nb from 0.02-0.12 wt%, Nb and V combinations and V up to 0.092 wt% and finds the best ductility and interlamellar spacing occur with the addition of 0.02 wt% Nb where the interlamellar spacing is 72nm with a corresponding 45% reduction in area. The Nb addition even improves the interlamellar spacing and properties of the V microalloyed steels.

2.6.1.4 Other applications

Successful application of Nb microalloyed beam has been reported [17]. The

toughness of the beam is significantly improved through the grain refinement of Nb and the special designed cooling practice during the production. With the composition of 0.1 wt% C, 1.4 wt% Mn, 0.025-0.035 wt% Nb the Charpy impact strength energy was doubled compared to a V microalloyed steel with similar base steel composition at every testing temperature. Singh *et al* [18] reported that the application of microalloying elements (0.057-0.072 wt% Nb, 0.11-0.13 wt% V and 0.15-0.20 wt% Mo) on steels for the coach and wagon wheels led to increments of up to 100MPa yield strength, 50MPa tensile strength and 4.5% elongation. Jansto [19] found that on the base of a conventional spring steel (Grade SAE 9259), the fracture toughness increased slightly from 27MPa•$m^{-1/2}$ to 29 MPa•$m^{-1/2}$ with 0.1 wt% V. A larger increment was observed (from 29 MPa•$m^{-1/2}$ to 36 MPa•$m^{-1/2}$) with an additional 0.035 wt% Nb.

2.6.2 Economic Benefits

The increase in mechanical properties from using microalloying elements in long products provides not only better performance of the final products but also the reduction of the cost for both manufacturers and end users. Because of the improvement in machinability of Nb microalloyed wire rods, the operational cost was reduced by 10-15% per tonne [20]. Due to the elimination of the heat treatment process, application of Nb microalloyed steel to produce the heavy equipment ball mill led to a 7% ($3000USD) operational benefit [6].

In terms of cost benefits for the end users, replacing the conventional spring steel with the NbVMo microalloyed spring steel led to a 15% reduction of the steel used. And yet the lighter spring offered a 27% increase in fatigue toughness [20]. Resulting from the increase of mechanical properties of the Nb microalloyed rebar, the amount of rebar needed to provide the same strength was halved [8].

Chapter 3 Experimental Methods

In this chapter, the experimental equipment and methods used to achieve the aims of this project are explained. The following is a brief overview explaining the aims and objectives of various experiments.

The steels used were lab-cast steels with chemical compositions focusing on the difference in C and Nb contents. This was so that the influence from dilute Nb contents can be evaluated with each carbon content, and the influence from different C contents can also be investigated. Solution treatment was performed to simulate the reheating furnace operation in order to obtain homogenised austenite microstructure before the deformation. The influence of C and Nb contents on the homogenised austenite microstructure could also be captured.

In order to investigate the influence of dilute Nb contents to austenite recrystallisation and grain growth behaviours, a processing route was designed based on a rebar processing routine provided by CBMM Technology Suisse [155]. The experimental processing route included a pass of rough rolling and two identical passes of finish rolling with a holding time of 20s.

Analysis was performed on the rough rolling flow stress curves to investigate the critical strain for dynamic recrystallisation of steels with different Nb contents. This analysis, in combination with the investigation on prior-austenite recrystallisation behaviour at the end of rough rolling, was aimed to understand the influence of dilute Nb contents on dynamic recrystallisation.

Analysis of the recrystallisation behaviour at the end of finish rolling was performed in order to study the influence of solute Nb to the recrystallisation behaviour at various deformation temperatures. Investigating the prior-austenite microstructure at

the end of the holding period was intended to aid understanding and Nb retarding mechanism (solute drag / precipitation pinning) on austenite microstructure evolution during the holding period. TEM analysis was performed on selective samples to study the precipitation behaviour of NbC; this was conducted so that the dominant retarding mechanism on recrystallisation during the holding period for various samples could be determined. In order to validate the microstructural analysis after the holding period, austenite fractional softening behaviour was investigated by analysing the flow stress curves of the double hit finish rolling PSC tests.

The austenite grain size evolution during the holding period was studied by analysing the prior-austenite grain size prior and after the holding period, which was intended to understand the influence of Nb and C on austenite grain growth behaviour.

The experimental methods and analytical techniques are explained in details as following:

3.1 Materials

3.1.1 Materials chemical compositions

In order to study the influence of dilute Nb addition on the austenite recrystallisation and grain growth behaviour during thermomechanical processing, the chemical elements other than Nb of the steels used in this project were strictly controlled to be the same, so that the influence of the compositional differences from other elements was eliminated. Therefore, the steels were vacuum induction melted and lab-cast at the Swinden Technology Laboratory of Tata Steel. After casting, the steels were homogenised at 1200°C for 2 hours and hot rolled at the rolling temperature of 1100°C to plates with 25mm thickness.

The chemical compositions of the steels used in this study are shown in Table 3-1. Three dilute Nb concentrations are focused on, which were 0.005, 0.01 and 0.02

wt%. In order to study not only the influence of different dilute Nb concentrations but also their influence on steels with different carbon contents, the Nb were added into steel samples with three carbon contents. As can be seen in Table 3-1 that the steels used were one low carbon steel containing 0.08wt% carbon, two medium carbon steels containing 0.4 and 0.6 wt.% carbon respectively. For the purpose of comparison, a reference steel with no Nb additions was made for each of the carbon compositions. Therefore, 12 steels in total were used in this study.

The first column of Table 3-1 shows the codes designed for the steels. They are used to distinguish different samples throughout the thesis. The code composed of two parts. The first half is the carbon concentration and the second part is the Nb concentration of the samples. For example, 8C20Nb stands for the steels containing 0.08 wt% of carbon and 0.02 wt% of Nb.

Table 3- 1 Chemical compositions of steels used in this study (wt%)

	Code	C	Si	Mn	P	S	N	Nb
Low Carbon Steel (0.08C)	8C0Nb	0.086	0.20	0.98	<0.01	<0.003	<0.007	-
	8C5Nb	0.085	0.19	1.00	<0.01	<0.003	<0.007	0.005
	8C10Nb	0.078	0.17	0.98	<0.01	<0.003	<0.007	0.01
	8C20Nb	0.080	0.18	0.98	<0.01	<0.003	<0.007	0.02
Medium Carbon Steel (0.4C)	40C0Nb	0.38	0.20	1.00	0.018	0.007	0.008	-
	40C5Nb	0.38	0.21	0.99	0.018	0.007	0.007	0.003
	40C10Nb	0.39	0.20	1.00	0.016	0.008	0.005	0.008
	40C20Nb	0.38	0.20	1.00	0.016	0.007	0.005	0.017
Medium Carbon Steel (0.6C)	60C0Nb	0.60	0.20	1.00	0.014	0.007	0.007	-
	60C5Nb	0.60	0.20	1.00	0.015	0.007	0.007	0.003
	60C10Nb	0.59	0.19	1.01	0.012	0.007	0.007	0.007
	60C20Nb	0.60	0.20	1.02	0.013	0.007	0.006	0.018

3.1.2 Materials solution treatment and machining for PSC samples

The heat treatment temperature of 1250°C and heat treatment time of one hour were chosen to dissolve most of the precipitation of Nb elements back into solution and to homogenise the microstructures and Nb distribution in the reheated steels. The reheating temperature was chosen due to its common usage in steel industries. After the steels were received, a section was cut from each of the steel plates using a large sectioning saw.

For the low carbon steels, solution treatment was commenced on the bulk steel before machining. The sections of the low carbon steels were put into a preheated and calibrated muffle furnace at a temperature of 1250°C in argon atmosphere for one hour. After the heat treatment, the steel plate was taken out from the furnace and quenched in an ice water tank immediately. By doing this, the condition of the homogenised austenite microstructures was frozen and retained. The homogenised austenite can later be re-established in very short holding time at the homogenisation temperature 1250°C in the TMC machine prior to deformation. The solution treated steel sections were sent to a local machining company to be machined into standard PSC samples. The dimensions of the standard PSC sample are 60mm in length, 30mm in width and 10mm in thickness.

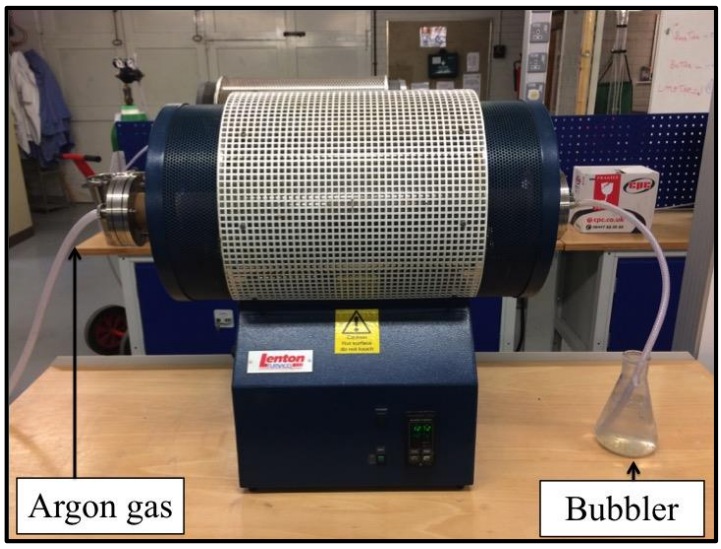

Figure 3- 1 Tube furnace setting up used for heat treatment

The medium carbon steels possessed very high hardness (above 590HV) after quenching, which exceeded the capacity of the local machining company. Hence the steel sections were sent to be machined into PSC samples prior to the solution treatment. A tube furnace was used to give better control of the temperature and protection from the oxidation of the PSC samples. The tube furnace used was shown in Figure 3-1. Before the heat treatment, calibration was conducted using a K type thermocouple. The furnace was preheated to 1250°C and two samples were placed in the middle of the furnace by a steel stick. The furnace was sealed on both ends and argon gas was passed through the furnace to protect the sample from oxidation. A bubbler was placed at the end to ensure the argon flow was sufficient. The samples would reach the temperature of 1250°C in 5 minutes. Then the samples were held another hour for the solution treatment. The samples were pulled out immediately after solution treatment into a bucket with ice water to be quenched. Finally, after being dried, the samples were homogenised and made ready for the deformation experiments.

3.2 Thermomechanical Compression (TMC) machine and Plane Strain Compression (PSC) tests

3.2.1 Thermomechanical compression (TMC) machine

In this study, all the deformation tests were performed on a very precise physical deformation simulator, which is the Thermomechanical Compression (TMC) machine at The University of Sheffield. The TMC machine was specially designed and produced by Servotest Ltd to simulate deformation processes with great control of the deformation parameters including deformation temperature, strain, strain rate, holding period between passes, heating rate, cooling rate etc [156]. All these parameters are fully controlled and recorded by the specially designed computer software. TMC machine is a powerful machine with great capacity to simulate most kinds of deformations. The technical specifications of TMC machine are shown in

Table 3-2.

Figure 3-2 shows the structure of TMC machine with the important components labelled. Figure 3-3 shows the standby position of a PSC sample held in the robot arms before the start of a PSC test. Figure 3-4 is a sketch illustration of the structure of the TMC and deformation components within the test furnace. The functions of these components are brief explained.

As can be seen in Figure 3-2, on top of the machine there are six hydraulic accumulators. Three of them are used for low pressures and the others are for high pressures [157]. They provide the force to move the main actuator. The movement of the actuator driven by the hydraulic accumulators performs the deformation.

Table 3- 2 Specifications of TMC machine

	Machine specifications
Actuators	Servo hydraulic
Maximum strain	2
Maximum strain rate	150~200/s
Maximum deformation temperature	1200°C
Maximum load	500kN
Machine stiffness	410kN/mm
Maximum FTTU heating temperature	1300°C
Quench start time	<0.5 second
Cooling methods	Force air, mist and water quench
Inert gas atmosphere	None – Natural air atmosphere
Temperature control and measurement	Up to 3 thermocouples

The hydraulic accumulators are supported by the crosshead. The crosshead is a large beam that can be moved vertically along the stainless steels beams. By moving the crosshead, the upper part of the machine can be set into an ideal position when

different tools are used, i.e. PSC or axisymmetric tools.

The deformation components are the pair of PSC tools in the test furnace as shown in Figure 3-4. The deformation section on the tool is rectangular with the width of 15mm and length of 100mm. The tools are made of an M22 nickel-based superalloy. It is strong enough at high temperatures to provide the loads required for hot deformation.

The bottom tool is fixed by four bolts onto the bottom post, which is mounted into the 500kN load cell on the base of the machine [158]. The upper tool is the moving tool which controls all the deformation parameters such as displacement, velocity etc. The movement of the upper tool is operated by the hydraulic system depending on the requirement from the tests.

The wedge is a mechanical stop component whose thickness is different along the horizontal direction. The stop distance can be adjusted by moving the wedge horizontally. The main actuator is raised to leave enough space before each deformation. There two reasons for this. Firstly, in the test furnace, leaving the clearance for the sample to be moved within the tools. Secondly, leaving substantial distance for the main actuator to obtain the required velocity by accelerating when it makes contact with the sample [157]. When the main actuator is raised, the wedge actuator moves the wedge automatically to the pre-defined position according the requested strain, thus the required strain will not be surpassed. Another important function of the wedge is to protect the TMC machine. If any unexpected failure of the system happens during the tests, the wedge will protect the tools from coming together with large load, hence to avoid any potential damage to the machine.

The fast thermal treatment unit (FTTU) is for the heat treatment of the sample. As can be seen in Figure 3-2 that the FTTU is positioned right in front of the test furnace. There are two sets of induction coils on the top and bottom of the FTTU to give stable and accurate heating to the sample. Different kinds of cooling units, i.e. forced air unit and water quench unit, are also embedded in the FTTU. Through the controlling software, the cooling units can be used separately (air blasting or water

quench) or combined (mist cooling) to cool the sample with great accuracy. A thermocouple is inserted into the sample to control the temperature.

The deformation and heat treatment during passes are conducted separately in the test furnace and FTTU. The robot arms are used to carry the sample in and out FTTU and test furnace. During simulation, multi-pass deformation is often used. The robot arms need to hold the sample firmly throughout the tests. However, during tests, a number of things could cause the sample to drop off from the robot arms when the sample is moving between the test furnace and FTTU. A detailed discussion of this is presented in the Appendix I.

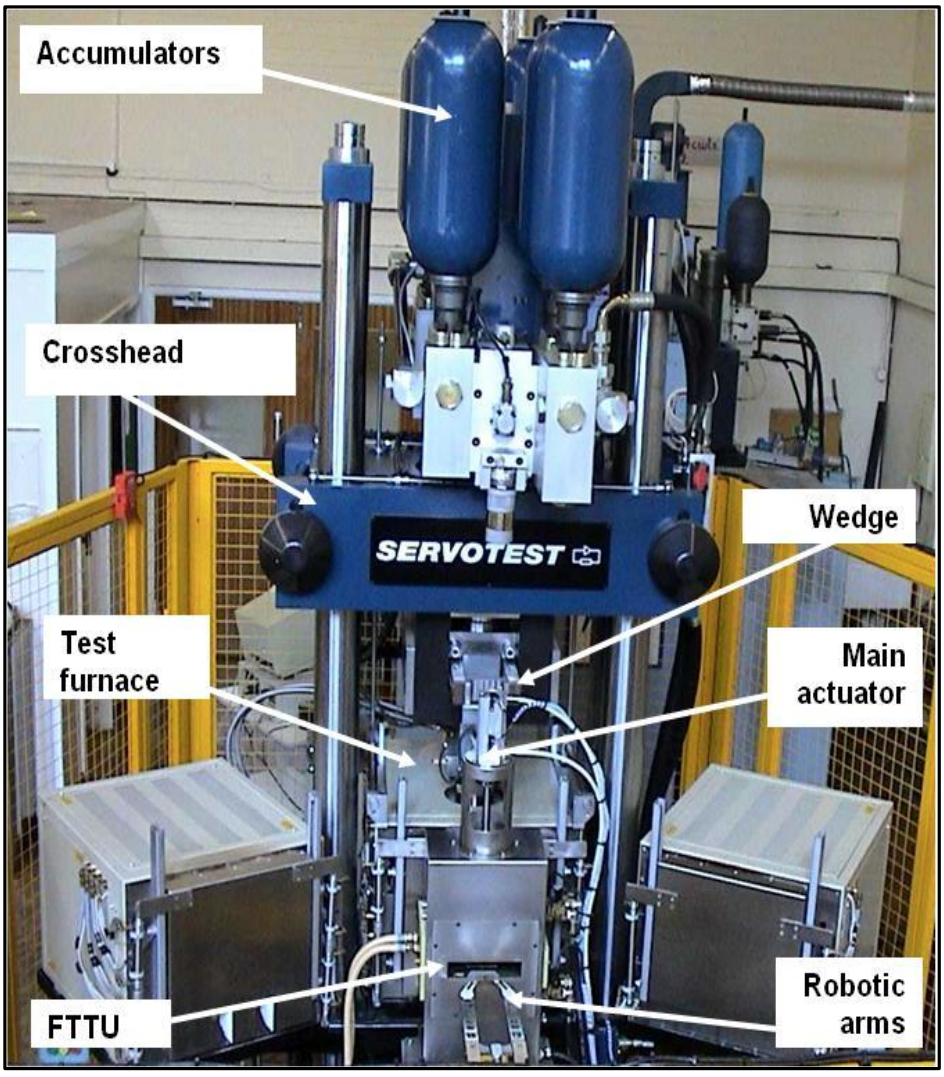

Figure 3- 2 Structures of the components on TMC machine [157,158].

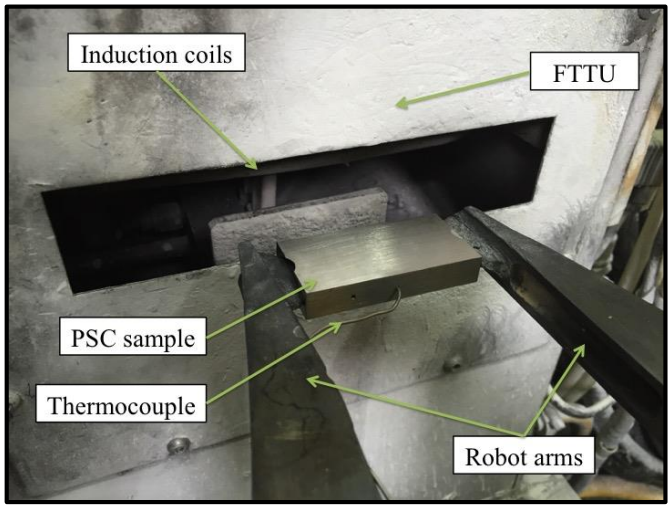

Figure 3- 3 Standby position of a PSC sample on the robot arms before testing.

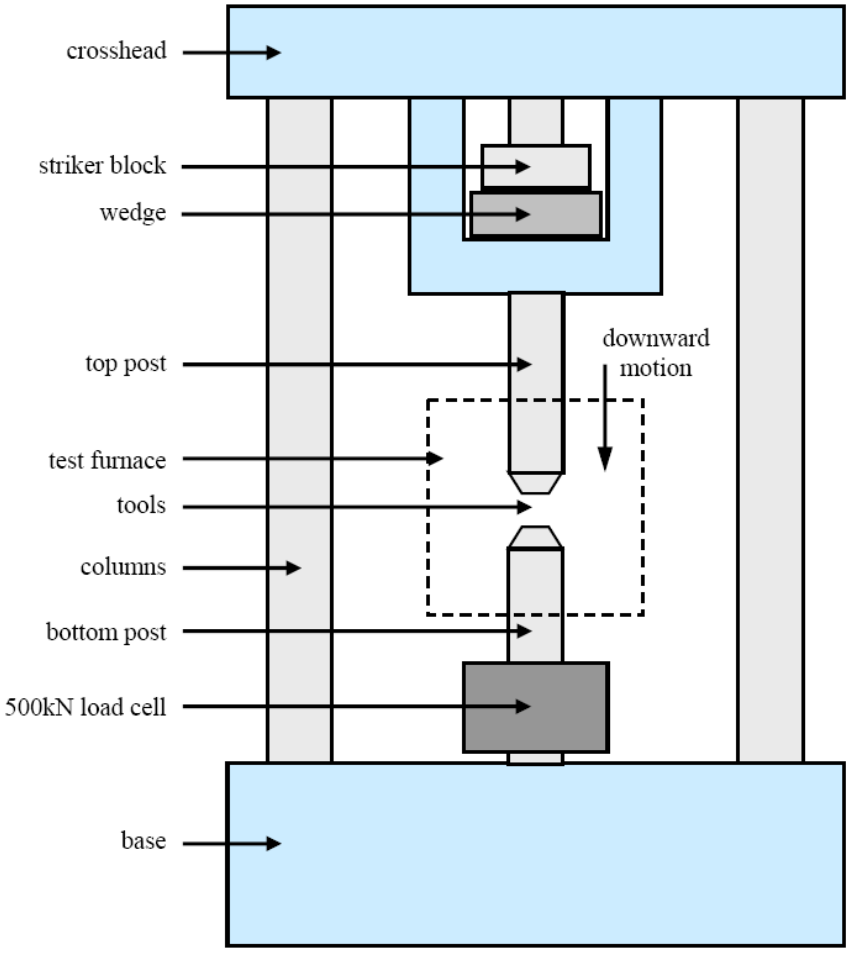

Figure 3- 4 Sketch illustration of the components within the test furnace [158].

3.2.2 Plane strain compression (PSC) Test

Reliable simulations of deformation processes on not only steels but also all kinds of metals are required by industry and academia. The microstructure evolution and flow stress data can be used to refine the deformation process, to generate models or to conduct systematic scientific research. The Several kinds of tests including laboratory rolling mill [48,159], plane strain compression (PSC) tests [160,161], axisymmetric compression [162,163] and torsion tests [137,164] are reported to be used in simulating hot deformation of metals.

3.2.2.1 PSC test and samples

Sketch illustrations of PSC test is shown in Figure 3-5. As can be seen the deformation area, which is defined by the width of the tools (15mm), is narrower compared with the width of the PSC sample (60mm). This leaves two undeformed areas on both sides of the tool. Those areas restrict the breath spread of the deforming sample into the minimal. The breadth spread is then compensated using the method proposed in the good practice guide [156].

These features of the PSC test make it the most suitable simulation with good control of the processing parameters to the rolling process; hence the rationale for the PSC test being used in this research. More detailed PSC sample dimensions are shown in Figure 3-6.

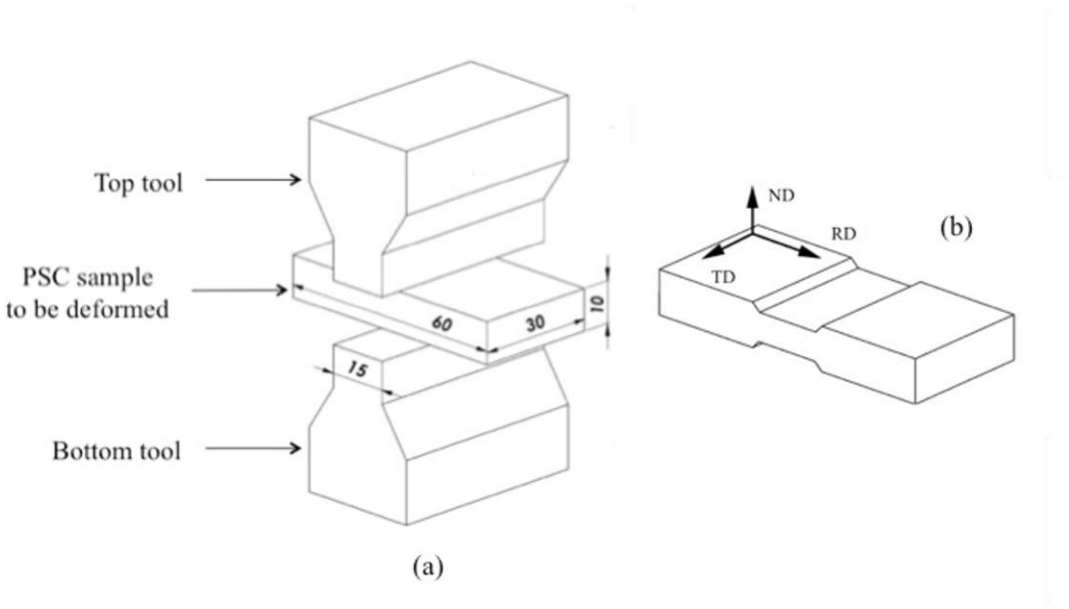

Figure 3- 5 Sketch illustrations of details of plane strain compression (PSC) test (a) illustration of PSC test and sample position relative to the tools (b) illustration of deformed PSC sample

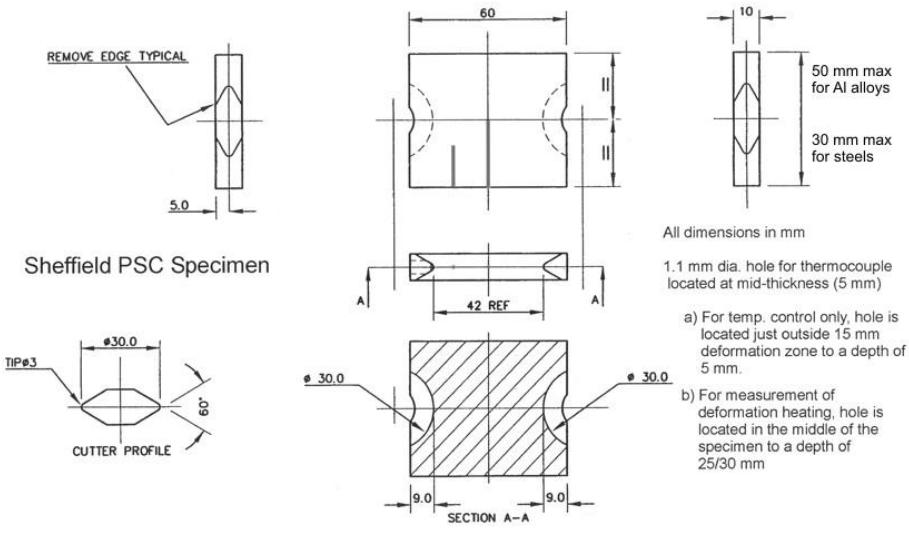

Figure 3- 6 PSC sample dimensions [165].

3.2.2.2 Test furnace temperature setting for PSC test

Before heating the test furnace up to the set temperature, the tools are cleaned and carefully aligned. This is essential for a successful PSC test. The tools are required to be heated up to a temperature just below the minimum deformation temperature so that the tools are harder than the sample and yet the temperature of the sample will not be strongly influence by contacting the tools. Due to the distance between the tools and the heating elements, there is always a temperature discrepancy of about 30°C. Therefore, a higher furnace temperature is normally set to reach the required temperature for the tools. For example, the lowest deformation temperature of the PSC test is 950°C. The ideal tools temperature is about 940°C. So the test furnace temperature is set to 970°C.

3.2.2.3 Machine condition preparation before PSC test

After the set temperatures for the furnace and the tools are reached, several essential checks need to be done to make sure the TMC machine is in a good condition for a successful PSC test.

First, a zero offset process to adjust the distance between the bottom and up tools is needed because of the thermal expansion of the posts and tools at high temperature. The zero offset process is required before each PSC tests in order to eliminate any possible discrepancy induced by the deformation.

Second, the pathway of the sample needs to be checked to be clear. In order to avoid the sample hitting the tools or the sample becoming twisted or dropping off, the sample position relative to both up and bottom tools should be adjusted carefully.

Finally, a thin layer of boron nitride needs to be sprayed on both sides of the sample. The boron nitride acts as lubricant and anti-welding agent between the sample and PSC tools during the high temperature deformation.

After these essential checks and settings, the TMC machine is in a positive position

for a successful PSC test. The design of PSC test deformation parameters will be explained in the following section.

3.3 Deformation processing routes of the PSC tests

Based on the processing routine of a rebar production provided by CBMM Technology Suisse [155], the deformation route used in this study was designed. The processing route is schematically illustrated in Figure 3-7.

As can be seen in Figure 3-7, the deformation route comprises of two kinds of rolling, rough rolling and finish rolling, which possess different rolling parameters and temperatures. At the beginning of the deformation route, the sample is heated to the homogenisation temperature 1250°C at the heating rate of 10°C/s. The sample was held at 1250°C for 120s to recover the homogenised microstructure which was frozen by direct quenching into ice water. The sample was then fast cooled to the rough rolling temperature, which was 1100°C. Immediately after the temperature became stable, the rough rolling was conducted with the strain of 0.3 and strain rate of 0.2/s. After rough rolling, the sample was fast cooled to the finish rolling temperatures. There were three finish rolling temperatures used in this study which were 1050°C, 1000°C and 950°C. There were two passes for the finish rolling. The deformation parameters for the two finish passes were exactly the same. The finish rolling was conducted with strain of 0.2 and strain rate of 2/s. During two finish passes, a 20s isothermal holding period was chosen to representative the interval time between passes in the industry production.

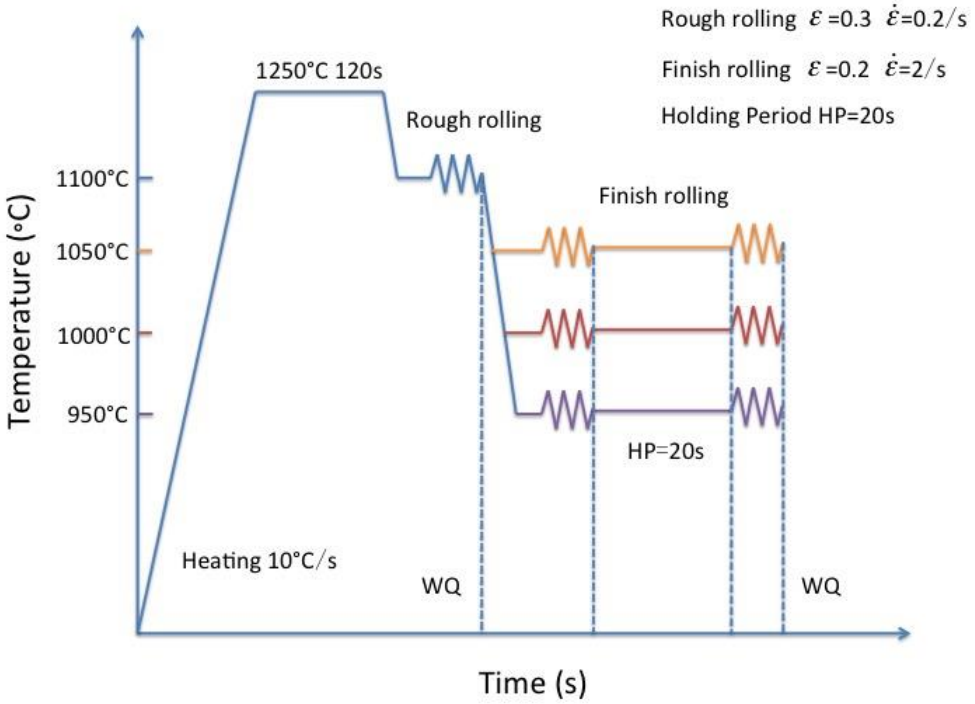

Figure 3- 7 Processing routes designed base on the rolling data of rebar production provided by CBMM Technology Suisse.

Interrupted quench was performed at different stages of the processing route as shown in Figure 3-7. Immediate quenching was conducted after rough rolling, after first finish rolling, after holding period and after second finish rolling. By doing this, the austenite microstructure at different stage of the process were revealed. And the influence of dilute Nb additions to the austenite microstructure evolution along the processing were investigated.

3.4 Data logging and analysis techniques

3.4.1 Data logging for flow curves

During every PSC test, data including sample temperature, displacement, velocity of the ram and load of the machine were recorded by the TMC machine with great

detail. The frequency of recording can be set by the user from 20kHz at the maximum to 5Hz at the minimum. After deformation, the raw data can be made into a special type of file, MUS file. The MUS file can be edited and analysed in Microsoft Excel spreadsheet to generate the required curves, in this case the flow curves of the PSC tests. A good practice guidance [156] was used to analyse the raw data and generate the flow curves.

3.4.2 Fractional softening behaviour

The two finish rolling passes shown in Figure 3-7 were designed to measure the percent fractional softening of austenite during the 20s isothermal holding period at various finish rolling temperatures. After the first finish rolling, the sample was unloaded and held at the corresponding finish rolling temperature for 20s. Then the second finish rolling was conducted followed by immediate water quenching of the sample.

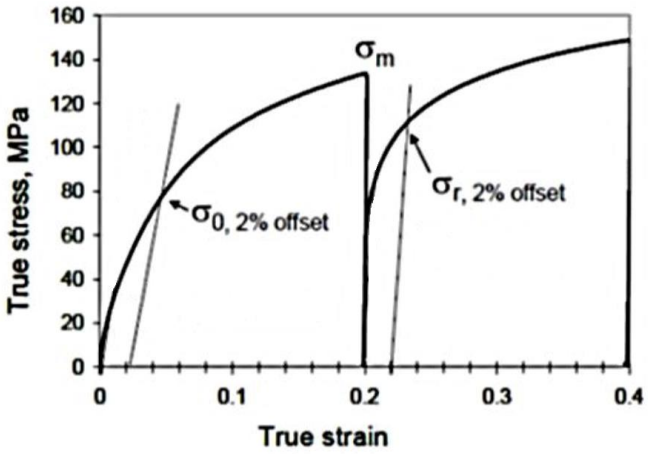

Figure 3- 8 Schematic of flow stress curves of the double-hit finish rolling. The values of stress with 2% plastic strain for the first and second finish rolling are σ_0 and σ_r. σ_m is the maximum stress for the first finish rolling.

The fractional softening of austenite for each of the steels being finish rolled at various temperatures were measured based on the 2% offset method depicted in Figure 3-8. The amount of fraction softening was calculated by:

$$FS = \frac{\sigma_m - \sigma_r}{\sigma_m - \sigma_0} \quad (3.1)$$

where σ_0 and σ_r are the values of stress with 2% plastic strain for the first and second finish rolling; σ_m is the maximum stress for the first finish rolling.

3.4.3 Optical microscopy

3.4.3.1 Sample preparation

All the PSC samples were cut using an abrasive sectioning machine on the position shown in Figure 3-9. The final cut which cut off the interest areas was performed on the Iso-Met 5000 precise sectioning machine. The sample was cut using a slower cutting speed with a finer blade, so that any possible damage to the quenched microstructure due to the heat generated during cutting by the large abrasive sectioning machine was eliminated.

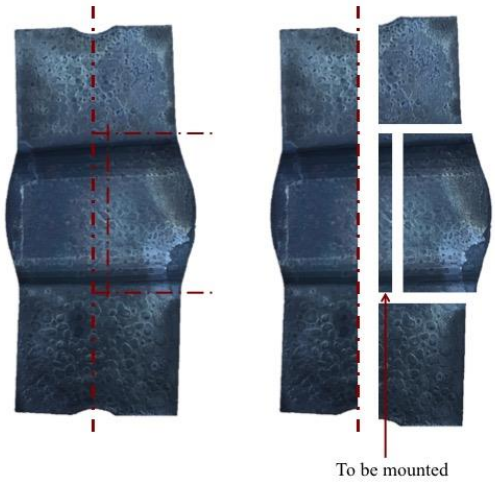

Figure 3- 9 Illustration of sectioned PSC sample for hot mounting

Then the piece of sample with the interest areas was mounted into Bakelite using the mounting press. The identity of sample was engraved on the back of the Bakelite to distinguish different samples.

The mounted samples were then manually ground using silicon carbide grinding papers to remove the scratches. 120, 240, 400, 800 and 1200 grids grinding papers

were used in the increasing order.

After grinding, the samples were polished using diamond suspension from 6μm to 1μm on different fine polishing clothes to avoid interact contaminations. The final polish was conducted using Silco colloidal silica of 0.05μm to obtain a stretch free surface for etching.

3.4.3.2 Etching

In order to study the microstructural evolution of austenite, clearly revealing the prior-austenite grain boundaries is critical. A number of different methods were tried including using 75% saturated picric acid aqueous solution with several drops of HCl and 25% Teepol [165], saturated picric acid ethyl/aqueous solution with 20 drops of HCl and 20 drops of Teepol [166], Villella solution (saturated picric ethyl solution with 5ml HCl) [167,168], 2-4% nital solution [169] etc. on both as quenched samples and tempered samples (490°C for 24 hours in argon atmosphere to segregate phosphorus to the prior-austenite grain boundaries to help etching). However, the results from these methods were unsatisfactory. The etched microstructures were not clear enough for any quantitative metallographic measurement and analysis.

It can be noted that in this work, numerous samples need to be etched and analysed. Therefore, a successful etching method on the as quenched samples is much preferred for the purpose of saving time. After a huge amount of trial and error efforts, a new technique using saturated picric acid aqueous solution with a new wetting agent was discovered. The solution preparation procedure is explained as following:

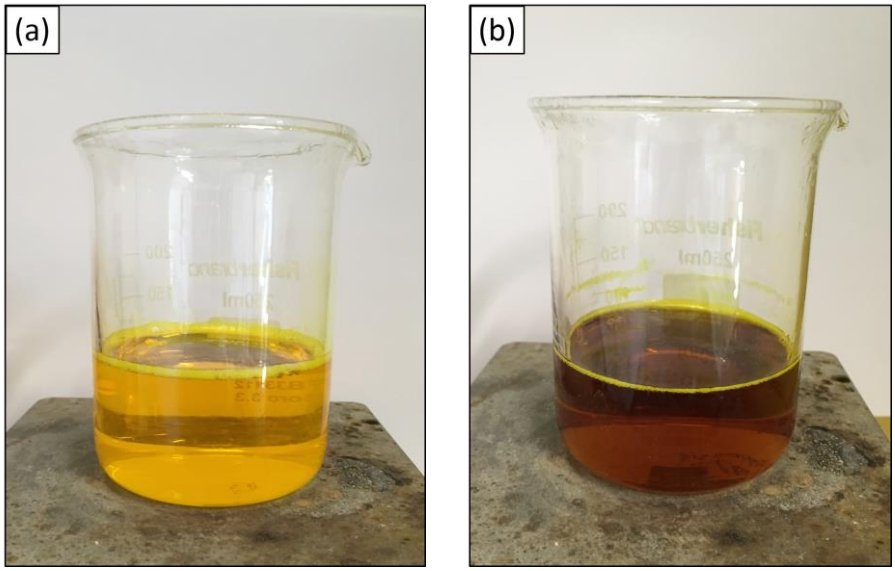

Figure 3- 10 Colour difference between fresh made and matured picric acid aqueous solution. After dissolved, the wetting agent left a foam ring on the surface of the solution near the beaker. (a) yellow fresh made picric acid aqueous solution (b) light brown matured picric acid aqueous solution after dummy etchings.

The solution was made by dissolving powder picric acid into 100ml distilled water at 80°C. The solution was kept stirring while the powder picric acid was added into the solution until a little bit of picric acid powder was remained undissolved, which indicated the solution was made saturated at 80°C. 3-6 drops of concentrated HCl (37%) was added into the solution. After gently stirred the solution to evenly dissolve the HCl, 1 gram of the wetting agent was added and dissolved into the solution. The new wetting agent found in this study was sodium dodecyl sulphate. The solution temperature was kept between 80-90°C by placing the solution beaker onto a temperature controlling hot plate.

However, at this stage, the condition of the solution was defined as an ‘unmatured’ condition, which was not yet ready for etching prior-austenite grain boundaries. In order to mature the solution, three ground and polished dummy samples were immersed into the solution for 5 minutes each. After the dummy etchings were done, the solution showed darker colour (light brown) compared with yellow colour the solution possessed when they were fresh made. The colour difference can be clearly distinguished in Figure 3-10. Then the solution was matured and ready to etch.

The samples were immersed into the solution at 80-90°C. The etching sample was kept still in the solution for 2-4.5 minutes, i.e. no swabbing by cotton or vibrating in an ultrasonic bath. After etching, the sample was washed by running water and cleaned by wet cotton. The etched samples were sprayed with isopropanol, dried immediately under a hot air blower and checked with an optical microscope. The under-etched and over-etched samples were re-ground from 1200 grit grinding paper, then re-polished and re-etched. The well-etched samples were stored in a desiccator and ready for the optical microscopy analysis.

A mechanism of this new etching technique is proposed and discussed in Appendix II. Crucial influential factors such as wetting agent, solution concentration etc. are also discussed.

3.4.3.3 Optical microscopy analysis

Optical microscope was used to provide the evidence of microstructural evolution of austenite. Optical microscopy provides the ability for low magnification observation, which reveals the microstructure over a large area. After etching, the images of prior-austenite microstructures of all the homogenised samples and the deformed PSC samples were taken and analysed on the Polyvar Met and Nikon Eclipse LV150 microscopes.

For deformed PSC samples, the strain distribution is heterogenetic in the deformation zone. Therefore, it is important to observe the microstructures of the samples from the areas in which the local strain is of interest. Mirza and Sellars [170] conducted finite element analysis to model the strain distribution in the deformation zone of a steel sample being deformed in PSC test, as it is shown in Figure 3-11. Using their result, the microstructures throughout this project were taken within the blue square area (see Figure 3-11) in which the local strain is equivalent to the strain applied. Quantitative metallographic analysis such as prior-austenite grain size and percent recrystallisation measurements was made on these images.

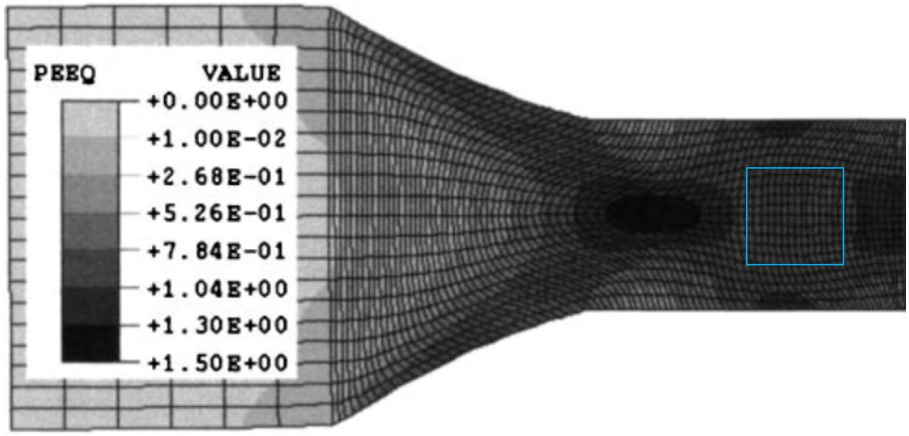

Figure 3-11 Finite element analysis showing strain distribution of a steel sample being deformed in PSC test at strain rate of $10s^{-1}$ at 1000°C to the strain of 1. [170]

(a) Grain size measurement

In the case of grain size measurement, there are several software programmes available to measure the grain size automatically. In this study, the manual linear intercept method (ASTM E112) [171,172] was used to eliminate the possible errors, which could be caused by the use of such software programmes. Several random placed but equally spaced lines were drawn on the images. The lines were sufficiently spaced to make sure that no grain was crossed more than once. The grain boundaries crossed by each line was counted and recorded. The data were used to calculate the average prior-austenite grain sizes in both rolling direction and transversal direction. The prior-austenite grain aspect ratio were calculated by the ratio of prior-austenite grain sizes in rolling direction to that of transversal direction. In order to obtain reliable results, at least 40 lines were calculated for each test condition.

For each line *i*, prior-austenite grain size for the line L_i was calculated by dividing the total lengths of the lines by the number of prior-austenite grain boundaries crossed. These prior-austenite grain sizes were summed, and divided by the total number of lines to get the average prior-austenite grain size $\bar{L}$. Then the standard deviation of the measurement were calculated using the following equation.

$$s^2 = \frac{\sum(Li-\bar{L})^2}{n-1} \quad (3.2)$$

where s is the standard deviation for the measurement, L_i is the prior-austenite grain size of line i, $\bar{L}$ is the average prior-austenite grain size and n is the number of lines.

From the standard deviation, the standard error were calculated using

$$S(\bar{L}) = \frac{s}{\sqrt{n}} \quad (3.3)$$

Then the 95% confidence limit were calculated using the relevant t-value (Table 3-3). Therefore, the average prior-austenite grain size with 95% confidence limits were expressed in the form as following:

$$\bar{L} \pm (t_{95n-1})S(\bar{L}) \quad (3.4)$$

Table 3-3 Values of *t* for 95% confidence limits ($t_{(95, n-1)}$) as a function of the number of degrees of freedom, *v = n-1*

v	$t_{(95, n-1)}$
20	2.086
25	2.060
30	2.042
40	2.021
60	2.000
120	1.98
∞	1.96

(b) Percent recrystallisation measurement

In order to calculate the percent recrystallisation of prior-austenite under different deformation conditions, point counting method (ASTM E562) [172,173] was used in this study. Point counting method is a method based on calculating the fraction of points falls in the interested microstructure, recrystallised prior-austenite in this study. This could be used for fraction of different phases or recrystallisation fraction calculation. In this method, a random grid composing horizontal and vertical lines

was placed on the image. Sufficient distance between two adjacent points was left so that the same grain was not counted more than once. The number of intersection points of the horizontal and vertical lines was counted and the fraction of them was calculated. At least six images were used to give a reliable result for each of the test condition.

Taking either horizontal or vertical lines, assessing the locations where the intersections of the grid were located. Each point was assigned a value, 1 if the point was in recrystallised prior-austenite, 0 if the point was not and 0.5 if the point was on the boundary. The total of each line was calculated. For each line, *i*, the point fraction P_{pi} was calculated by dividing the total by the number of points per line. These point fractions were summed and divided by the total number of lines to get the average percent recrystallisation $\bar{P}_p$. The standard deviation of the measurement were calculated using the following equation,

$$s^2 = \frac{\sum(P_{pi} - \overline{P_p})^2}{n-1} \tag{3.5}$$

where *s* is the standard deviation for the measurement, P_{pi} is the point fraction of line *i*, $\bar{P}_p$ is the average percent recrystallisation and *n* is the number of lines.

From the standard deviation, the standard error were calculated using

$$S(\bar{P}_p) = \frac{s}{\sqrt{n}} \tag{3.6}$$

Then the 95% confidence limit were calculated using the relevant t-value (Table 3-3). Therefore, the percent recrystallisation with 95% confidence limits were expressed in the form as following:

$$\bar{P}_p \pm (t_{95n-1})S(\bar{P}_p) \tag{3.7}$$

3.4.4 Electron microscopy

3.4.4.1 Carbon extraction replicas

In order to study the precipitation behaviour of the Nb additions, transmission electron microscopy (TEM) was used to capture the morphology of the Nb precipitates. A carbon extraction replica method [174,175] was used so as to avoid the complexity of the as-transformed matrix substructure on the identification and analyses of the precipitates. The carbon extraction replica process is illustrated in Figure 3-12.

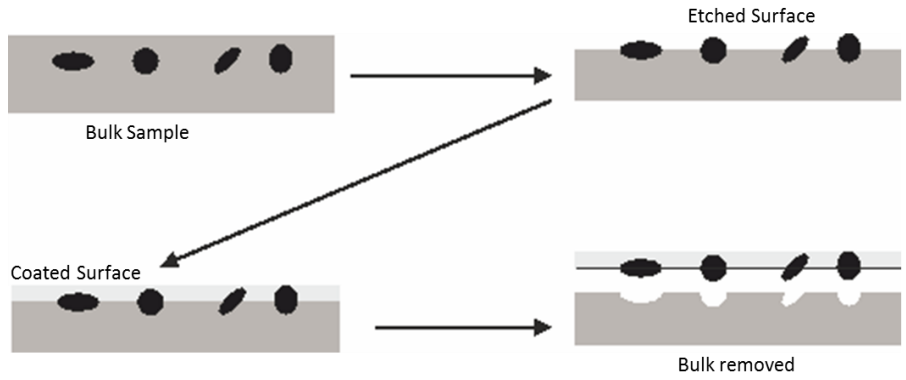

Figure 3-12 Schematic illustration of carbon extraction replica process [174].

The sample was cut, mounted, ground and polished as explained in Section 3.4.3.1. Extra care was given here to make sure the good scratch free finishing surface to ensure the sample to be evenly etched. After polishing, the sample was lightly etched using 2% nital solution. Then the sample was cleaned by Teepol and running water to make sure that the solution was completely removed from the sample. The sample was then immersed into isopropanol and ultrasonic cleaned for three minutes to remove any possible pollution. Finally, the sample was dried and stored in a desiccator and ready for the carbon coating.

A very thin layer of carbon was evaporated and deposited on the surface of the sample using the Speedivac carbon coating machine in Sorby Centre. After carbon

coating, in order to avoid the carbon film from the unwanted area of the sample and the surface of the Bakelite being peeled off, a layer of varnish was coated on those areas. This ensured the carbon films were peeled off from the interested area.

Square grids of about $2mm^2$ were scratched using a knife on the surface of the sample. Then the sample was carefully immersed into 10% nital solution. After several minutes, bubbles started to form on the surface of the sample, which showed the carbon film was lifted from the matrix. Then the sample was removed into a wide baker with methanol. The square carbon film was collected on a 400 mesh copper grid with 3 mm diameter.

3.4.4.2 Transmission electron microscopy

TEM was used in this work to study the nanoscale precipitates including the precipitation size distribution, density and composition of the precipitates. The TEM observation, including precipitation observation and TEM-EDS, were conducted on FEI Tecnai at 200kV and JEOL 2010F at 200kV.

The TEM images of precipitates captured from carbon extraction replica were used to study the precipitate size distribution and number density. ImageJ analysis software could be used to analyse the precipitation. However, due to the fine precipitation size, the distinction of the precipitate particles was poor. Therefore, in order to have accurate measurement, manual measurement was conducted on the precipitates.

Chapter 4 Results

The results of this project are presented following the austenite microstructure evolution along the thermomechanical processing route. The as homogenised prior-austenite microstructures before deformation are presented in Section 4.1. Then, the flow stress curves from thermomechanical processing and the fractional softening of various steels are shown in Section 4.2. After that, the prior-austenite microstructures after rough rolling (Section 4.3), finish rolling (Section 4.4) and isothermal holding period of 20s (Section 4.5) are illustrated. Additionally, the precipitation morphology of NbC precipitates are reported. Finally, the influence of Nb on the austenite grain growth behaviour during the isothermal holding is illustrated.

Before explaining the prior-austenite microstructures, it is easier to state here that there was no proeutectoid ferrite in any of the steels. Fully martensitic microstructure was observed after water quenching in all cases.

4.1 As-homogenised microstructure

The main objective for homogenisation treatment at 1250°C for 1 hour was to eliminate the influence of deformation and dissolve most of the NbC precipitates back into solid solution, in order to obtain a fully recrystallised microstructure with evenly distributed Nb element.

The prior-austenite microstructures after homogenisation for 8C, 40C and 60C steels are shown in Figure 4-1, Figure 4-2 and Figure 4-3, respectively. Equiaxed recrystallised prior-austenite grains were observed in each of the steels. The

prior-austenite grain sizes of the homogenised steels were calculated and summarized in Table 4-1.

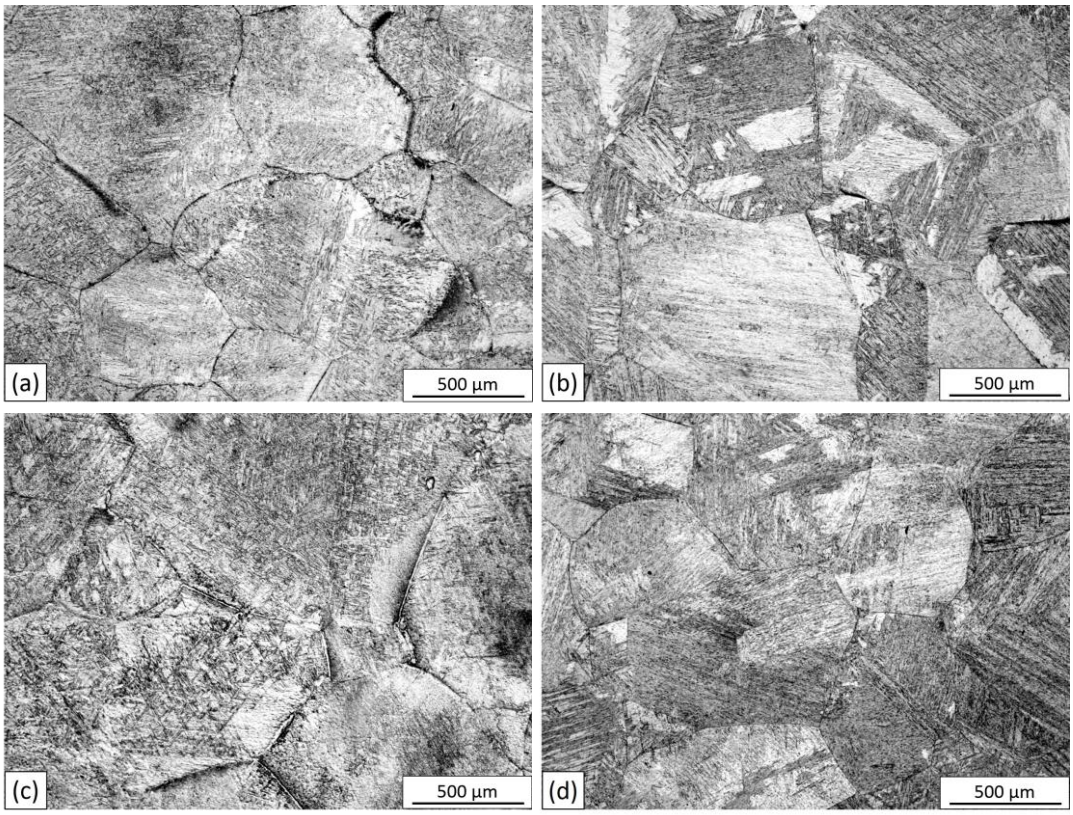

Figure 4-1 Prior-austenite microstructures of 8C steels after homogenisation at 1250°C for 1 hour followed by immediate water quenching. (a) 8C0Nb; (b) 8C5Nb; (c) 8C10Nb; (d) 8C20Nb.

A complete comparison between homogenised prior-austenite grain sizes for all the steels is shown in Figure 4-4. Within each carbon content, no obvious influence from Nb contents to prior-austenite grain size was observed after homogenisation. For example, the homogenised prior-austenite grain sizes of 8C0Nb, 8C5Nb, 8C10Nb and 8C20Nb steels were 633.7±56.5µm, 627.2±60.6µm, 618.8±65.3µm and 607.6±70.8µm, respectively.

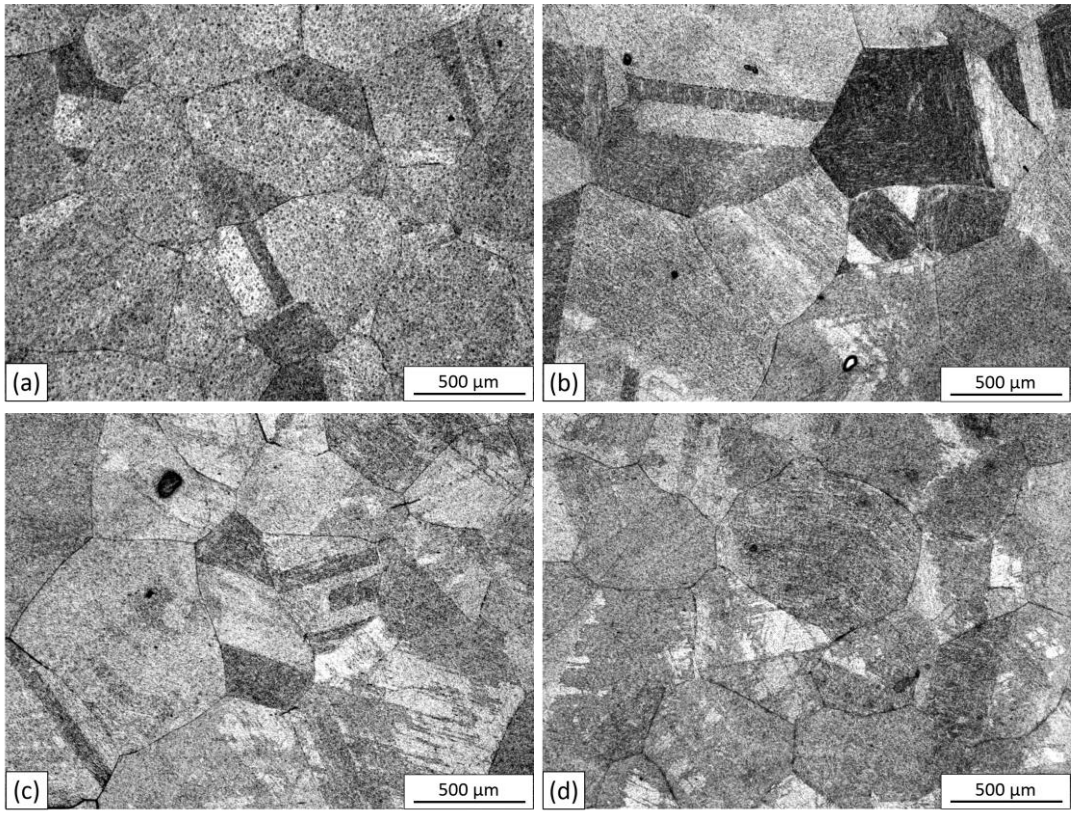

Figure 4-2 Prior-austenite microstructures of 40C after homogenisation at 1250°C for 1 hour followed by immediate water quenching. (a) 40C0Nb; (b) 40C5Nb; (c) 40C10Nb; (d) 40C20Nb.

The homogenised prior-austenite grain size was found to be finer with the increasing C contents. For example, the prior-austenite grain sizes for the plain carbon steels 8C0Nb, 40C0Nb and 60C0Nb were 633.7±56.5µm, 523.3±58.5µm, and 442.0±31.8µm. Similar observations were also found in 5Nb, 10Nb and 20Nb steels, see Table 4-1 and Figure 4-4.

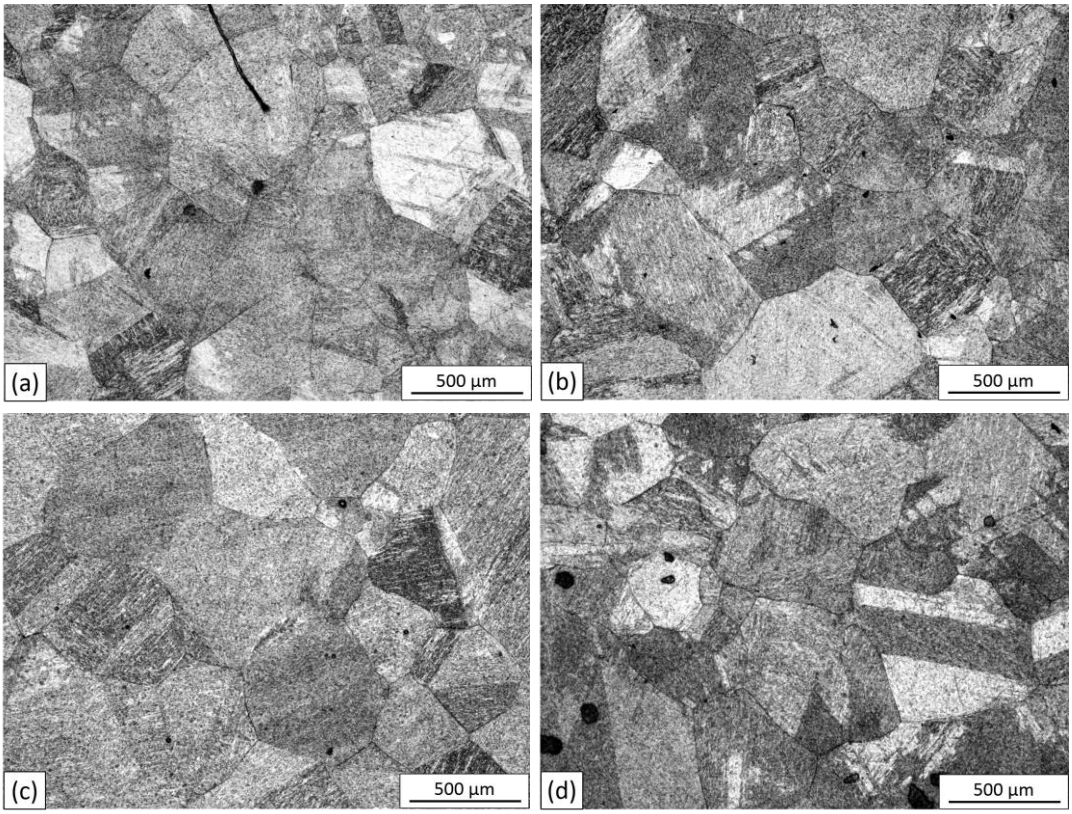

Figure 4-3 Prior-austenite microstructures of 60C steels after homogenisation at 1250°C for 1 hour followed by immediate water quenching. (a) 60C0Nb; (b) 60C5Nb; (c) 60C10Nb; (d) 60C20Nb

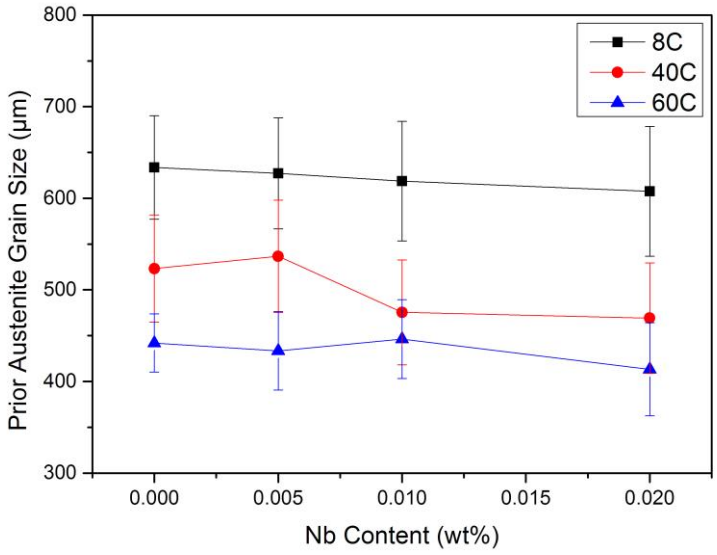

Figure 4-4 Evolution of homogenised prior-austenite grain sizes as a function of Nb contents. Error bars indicate the 95% confidence limits of the measurements. Carbon contents are shown in legend.

Table 4-1 Average prior-austenite grain sizes for homogenised and quenched steels (μm)

	0Nb	5Nb	10Nb	20Nb
8C	633.7±56.5	627.2±60.6	618.8±65.3	607.6±70.8
40C	523.3±58.5	536.7±61.4	475.5±57.3	469.2±60.3
60C	442.0±31.8	433.5±42.9	446.3±43.0	413.3±50.7

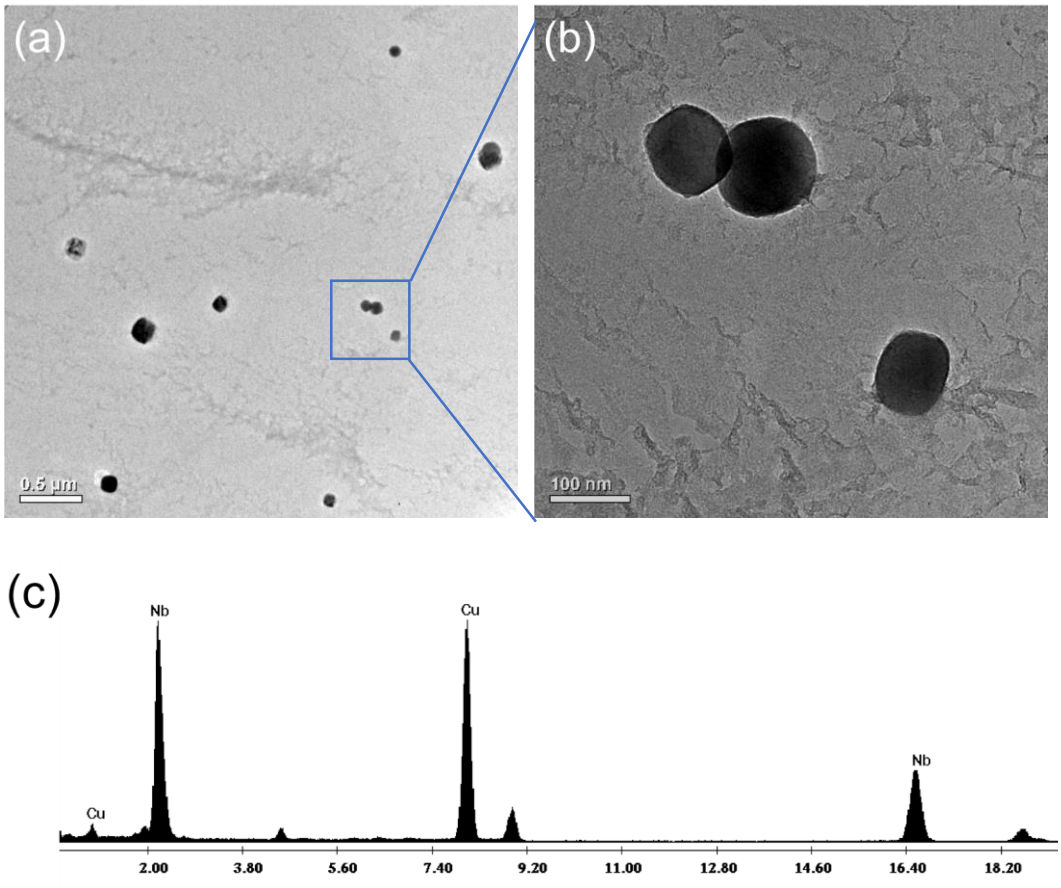

Figure 4-5 TEM bright field image of undissolved NbC precipitates in 40C20Nb steel after homogenisation at 1250°C for 1 hour followed by direct quench. (a) Low magnification image of the undissolved precipitates. (b) High magnification image of the precipitates. (c) EDS spectra from precipitates in (b).

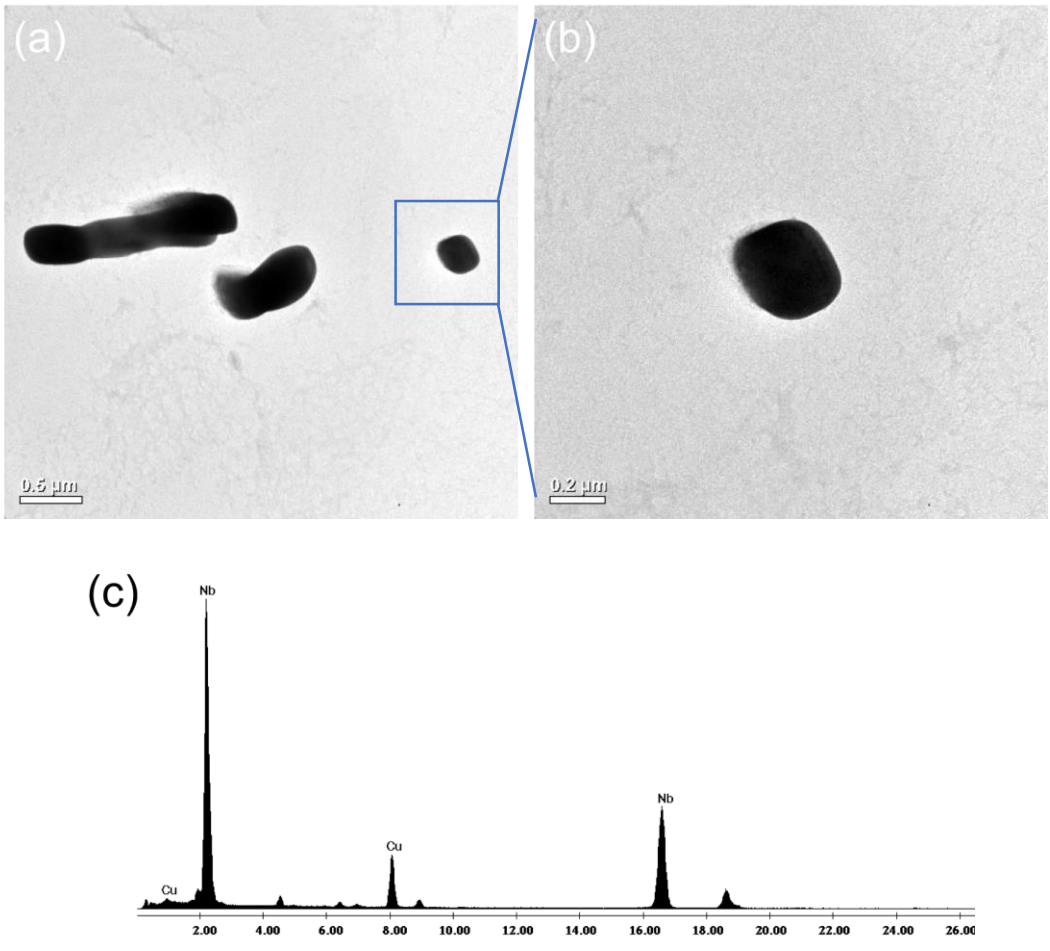

Figure 4-6 TEM bright field image of undissolved NbC precipitates in 60C20Nb steel after homogenisation at 1250°C for 1 hour followed by direct quench. (a) Low magnification image of the undissolved precipitates. (b) High magnification image of the precipitates. (c) EDS spectra from precipitates in (b).

As discussed in Section 2.3.2 the solubility product is influenced by both C and Nb contents. Variation in C contents influence the Nb dissolution behaviour. Using the solubility product proposed by Palmiere *et al* [72] (Equation 2.10), the temperatures for Nb to be fully dissolved were calculated, as shown in Table 4-2. The full dissolution temperatures for all but two steels are below the homogenisation temperature 1250°C. The temperature of full dissolution for 40C20Nb and 60C20Nb steels are 1305°C and 1392°C. Therefore, the 0.02wt% Nb in 40C20Nb and 60C20Nb steels are expected to be partially dissolved.

Table 4-2 Calculated Nb dissolution temperatures for all steels (°C)

	0Nb	5Nb	10Nb	20Nb
8C	-	967	1032	1116
40C	-	1068	1196	1305
60C	-	1123	1236	1392

Homogenised and quenched 8C20Nb, 40C20Nb and 60C20Nb steels were examined under the TEM. No undissolved particle was found in 8C20Nb steel indicating the complete dissolution of the 0.02wt% Nb. Large particles were found in 40C20Nb and 60C20Nb steels after homogenisation, as shown in Figure 4-5 and Figure 4-6. EDS data show that the particles were Nb-rich. The particles are believed to be NbC which were not dissolved during homogenisation resulting from the reduction in Nb solubility due to the substantial increase in C contents from 0.08wt% to 0.4wt% and 0.6wt%. This behaviour is consistent with the solubility product calculation.

4.2 Flow behaviours

In this section, the von Mises equivalent stress-strain curves of all steels after one pass rough rolling at 1100°C with strain of 0.3 and strain rate of 0.2/s and two-pass finish rolling at 1050°C with strain of 0.2 and strain rate of 2/s are shown.

Between the two finish rolling, the steel was held isothermally for 20s. The flow curves of the two identical finish rolling were then used to calculate the fractional softening during the 20s holding period at various finish rolling temperatures. In combination with the microstructural observation, the fraction softening results of various steels during the isothermal holding was later used to understand the influence of dilute Nb on the softening behaviour.

4.2.1 Flow behaviours of 8C steels

Figure 4-7, Figure 4-8 and Figure 4-9 show the flow stress of 8C steels being deformed at the finish rolling temperature of 1050°C, 1000°C and 950°C.

At 1050°C (Figure 4-7), the first and second finish rolling for all four 8C steels show the same shape, which suggests that almost complete softening happened in all four 8C steels during the 20s isothermal holding period at 1050°C.

Figure 4-8 shows the flow curves of three-pass rolling with the finish rolling temperature of 1000°C. The flow curves for 8C0Nb, 8C5Nb and 8C10Nb show similar behaviours whereas 8C20Nb show slightly higher stress indicating less softening.

The difference in softening behaviour becomes more obvious at the low rolling temperature 950°C. With the increase of Nb content, the stresses for the second finish rolling continuously increase (Figure 4-9).

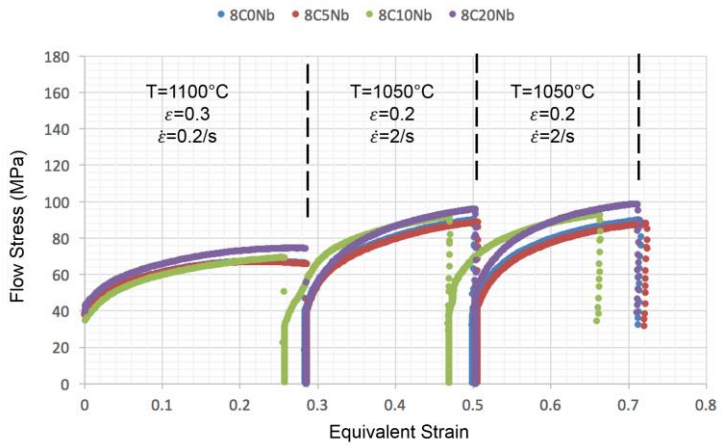

Figure 4-7 von Mises equivalent stress-strain curves of 8C steels after one rough rolling at 1100°C and two finish rolling at 1050°C.

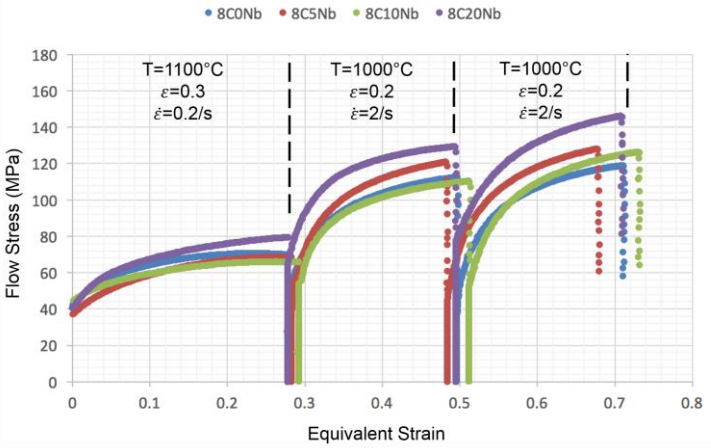

Figure 4-8 von Mises equivalent stress-strain curves of 8C steels after one rough rolling at 1100°C and two finish rolling at 1000°C.

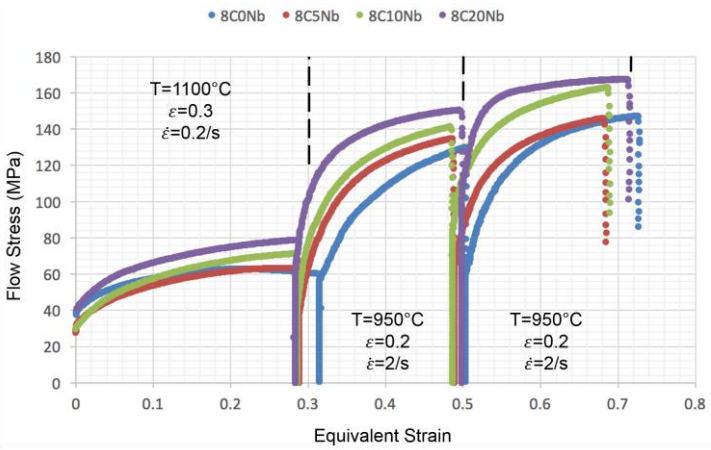

Figure 4-9 von Mises equivalent stress-strain curves of 8C steels after one rough rolling at 1100°C and two finish rolling at 950°C.

Using the 2% offset method explained in Chapter 3, the percent fractional softening during the 20s holding period at various finish rolling temperatures was calculated and plotted in Figure 4-10. At 1050°C, around 90% softening happened for all 8C steels. No obvious difference was introduced from Nb additions. The influence of Nb addition became more obvious at the lower temperature 1000°C and 950°C. Increasing Nb addition led to less softening. For instance, at 950°C the percent fraction softening reduced continuously from 97.5% to 19.7% with Nb content increased from 0% to 0.02wt%.

For microalloying steels 8C5Nb, 8C10Nb and 8C20Nb, less softening occurred with the decrease of rolling temperature. For example, the percent fractional softening for 8C20Nb dropped from 91.5% to 63.5% to 19.7% when the rolling temperature reduces from 1050°C to 1000°C to 950°C.

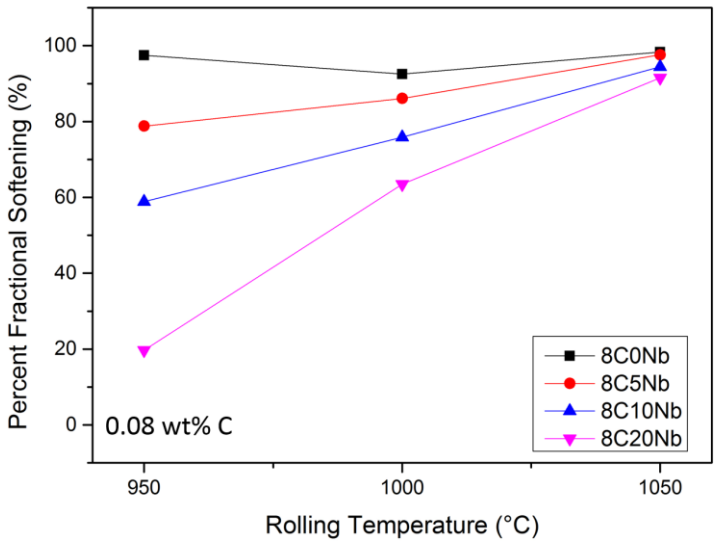

Figure 4-10 Austenite percent fractional softening of 8C steels calculated from corresponding flow curves.

4.2.2 Flow behaviours of 40C steels

Figure 4-11, Figure 4-12 and Figure 4-13 show the von Mises equivalent stress-strain curves of 40C steels after being rolled with the same processing routine at various finish rolling temperatures. According to the flow curves, the percent fractional softening was calculated and plotted in Figure 4-14.

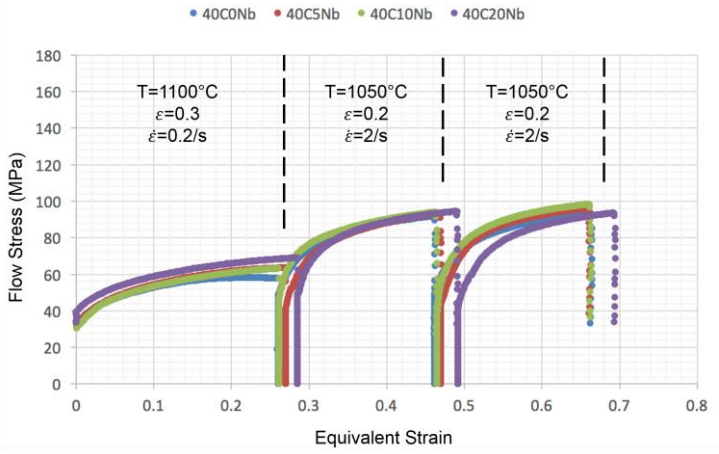

Figure 4-11 von Mises equivalent stress-strain curves of 40C steels after one rough rolling at 1100°C and two finish rolling at 1050°C.

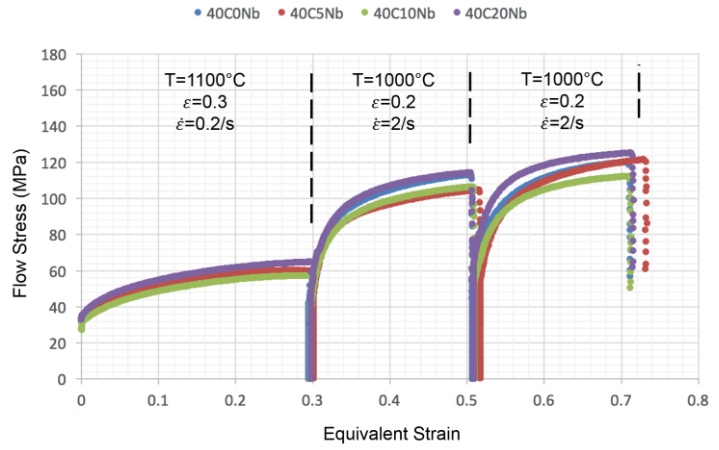

Figure 4-12 von Mises equivalent stress-strain curves of 40C steels after one rough rolling at 1100°C and two finish rolling at 1000°C.

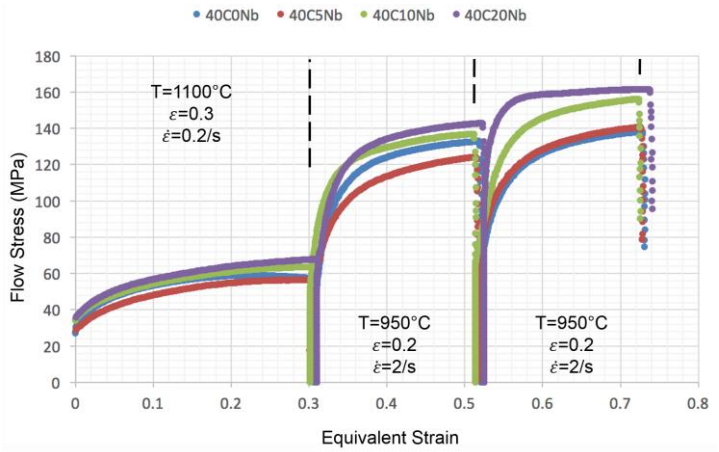

Figure 4-13 von Mises equivalent stress-strain curves of 40C steels after one rough rolling at 1100°C and two finish rolling at 950°C.

Similar to the softening behaviour of 8C steels, 40C steels showed almost complete softening at the finish rolling temperature of 1050°C. The percent fractional softening reduced with the increase of Nb content at the finish rolling temperature of 1000°C and 950°C. All the microalloyed steels showed less fractional softening with the decrease of rolling temperature.

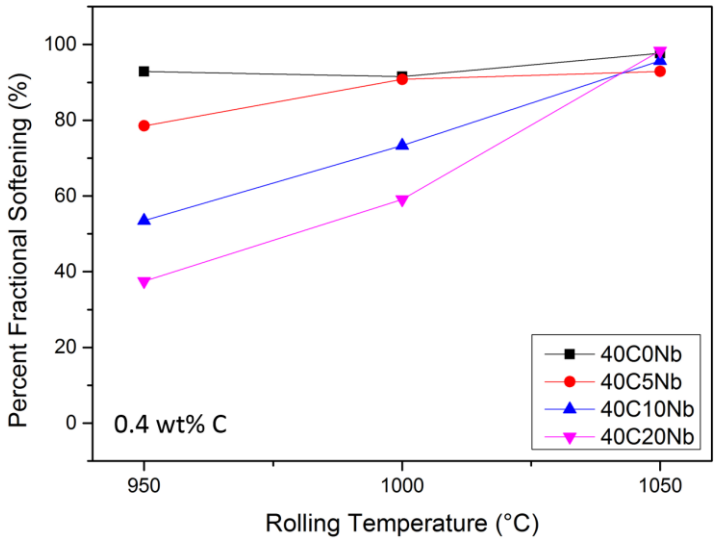

Figure 4-14 Austenite percent fractional softening of 40C steels calculated from corresponding flow curves.

4.2.3 Flow behaviours for 60C steels

The von Mises equivalent stress-strain curves of the 60C steels being rolled at the finish rolling temperatures of 1050°C, 1000°C and 950°C are shown in Figure 4-15, Figure 4-16 and Figure 4-17, respectively. And the calculated percent fractional softening is shown in Figure 4-18.

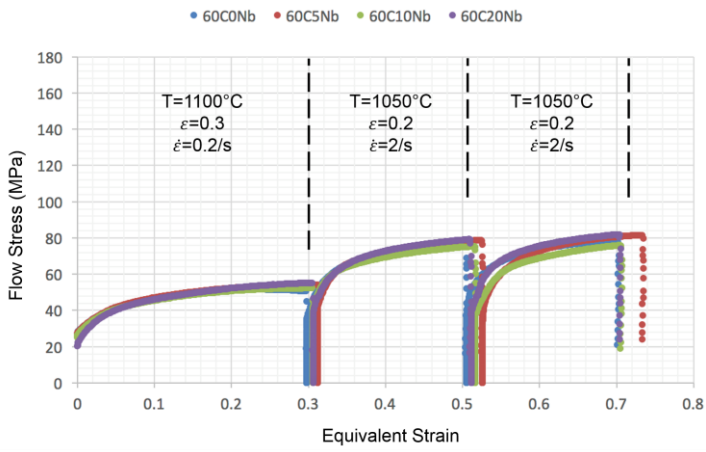

Figure 4-15 von Mises equivalent stress-strain curves of 60C steels after one rough rolling at 1100°C and two finish rolling at 1050°C.

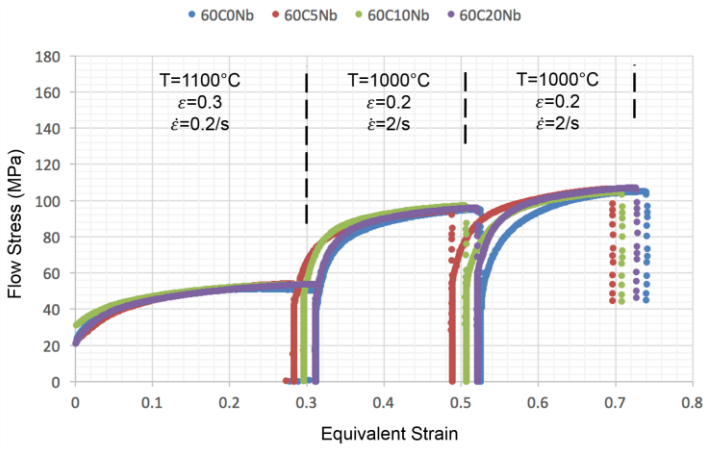

Figure 4-16 von Mises equivalent stress-strain curves of 60C steels after one rough rolling at 1100°C and two finish rolling at 1000°C.

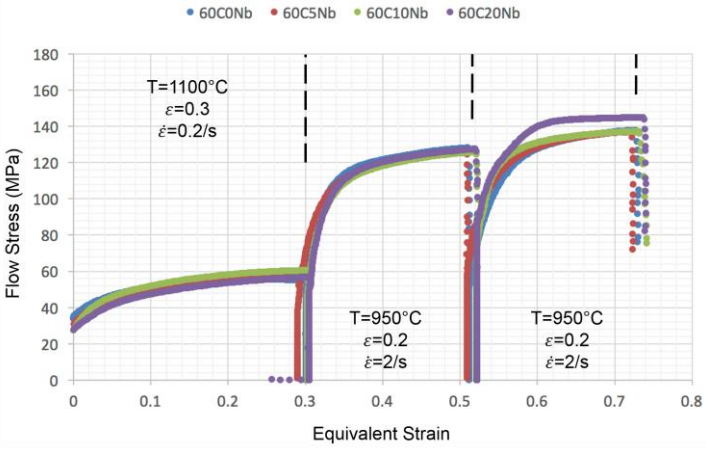

Figure 4-17 von Mises equivalent stress-strain curves of 60C steels after one rough rolling at 1100°C and two finish rolling at 950°C.

Again, compared with 8C and 40C steels, softening behaviour of 60C steels showed a similar trend with the change of Nb contents and finish rolling temperatures. Steels with higher Nb content showed less fractional softening at rolling temperatures of 1000°C and 950°C. At 1050°C, all steels showed almost complete softening. For any microalloyed steels, less softening was found at lower finishing rolling temperatures.

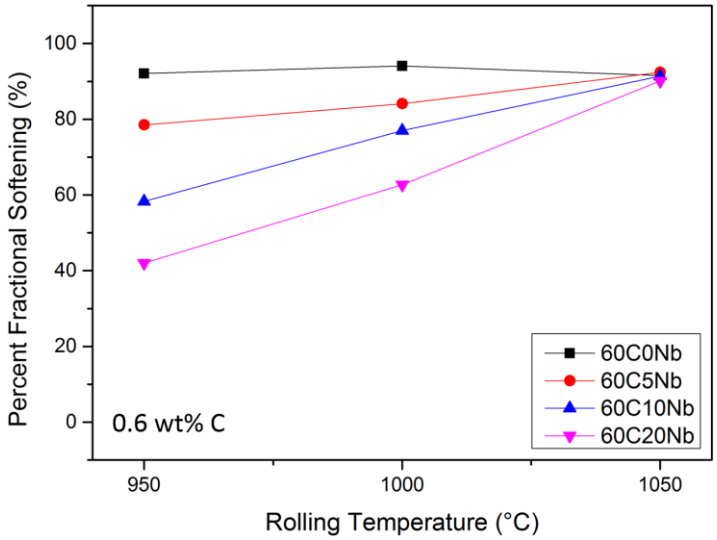

Figure 4-18 Austenite percent fractional softening of 60C steels calculated from corresponding flow curves.

It is worth noticing that in steels with all three carbon contents, the flow stress curves for rough rolling showed a plateau of steady state (microalloyed steels) or a drop in stress (plain carbon steels). This indicated that dynamic recrystallisation happened during rough rolling. Whereas for finish rolling, the flow stress curves in all cases showed continuous work hardening. Dynamic recrystallisation did not happen during finish rolling.

4.3 Prior-austenite microstructures after rough rolling

The rough rolling was conducted at 1100°C at a strain rate of 0.2/s with a strain of 0.3 (Figure 4-19). The prior-austenite microstructures for 8C, 40C and 60C steels quenched at the end of rough rolling are shown in Figure 4-20, Figure 4-22 and

Figure 4-24. For all 12 cases, partially recrystallised prior-austenite microstructures were obtained. This is due to the occurrence of dynamic recrystallisation during rough rolling. The recrystallisation process was not finished at the end of rough rolling which resulted in the partially recrystallised prior-austenite microstructures.

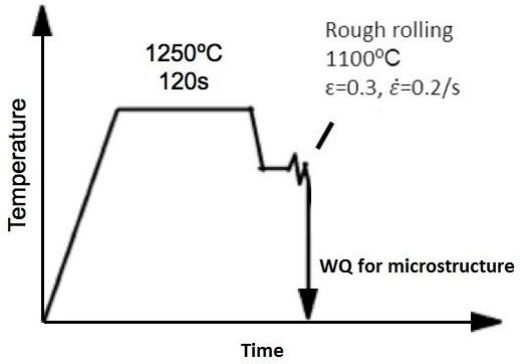

Figure 4-19 Illustration of water quenching performed at the end of rough rolling for microstructural observation.

The percent recrystallisation of prior-austenite microstructures after rough rolling was calculated using the point counting method and summarized in Table 4-3. The influence of Nb on the percent recrystallisation of 8C, 40C and 60C steels were plotted in Figure 4-21, Figure 4-23 and Figure 4-25. The percent recrystallisation of prior-austenite was decreased with the increase of Nb contents in steels with all three carbon contents.

A comparison between percent recrystallisation of all steels after rough rolling is presented in Figure 4-26, in which the influence of C on the recrystallisation behaviour was discovered. For 0Nb, 5Nb and 10Nb steels, similar percent recrystallisation was found for steels with all three C contents. For example, the percent recrystallisation for 8C5Nb, 40C5Nb and 60C5Nb are 71.3±3.3%, 67.7±3.4% and 67.0±3.4%. For 20Nb steels the percent recrystallisation was slightly increased with increasing C content. This is because the incomplete dissolution of the 0.02wt% Nb after homogenisation for the higher C content steels (40C and 60C). The higher the C content, the lower amount of Nb was dissolved. Since the Nb addition reduced the recrystallisation, the lower Nb dissolution resulted in higher percent recrystallisation.

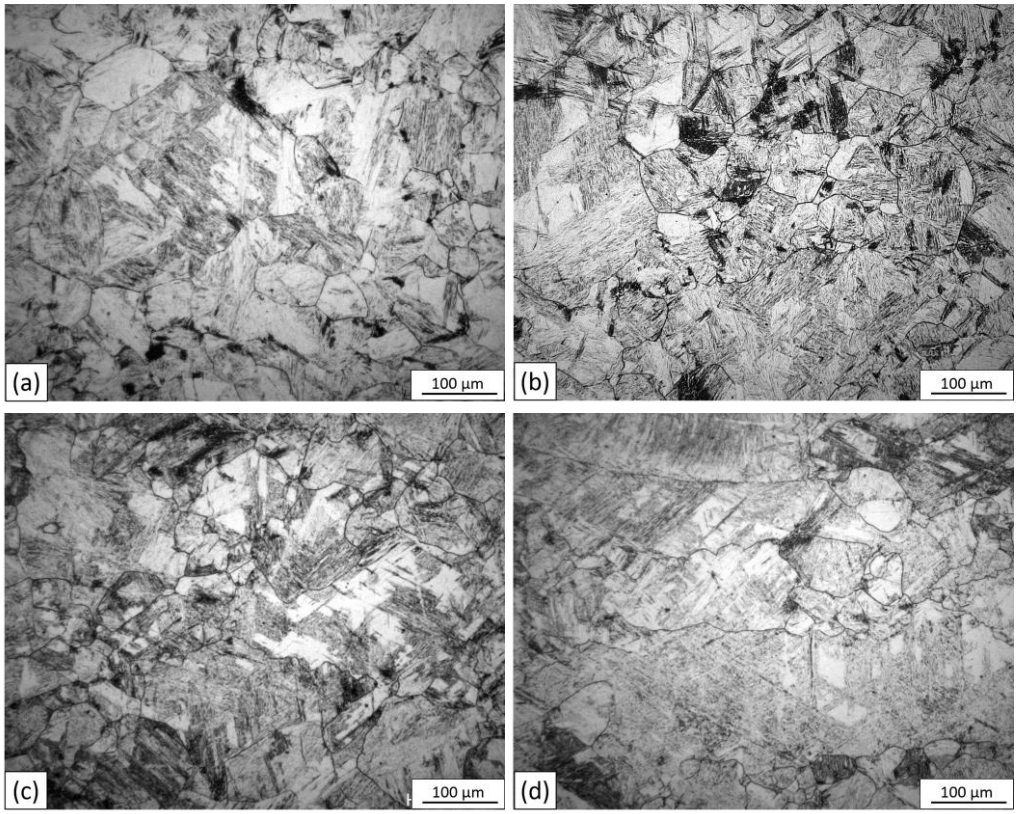

Figure 4-20 Prior-austenite microstructures of 8C steels after rough rolling and water quenching. (a) 8C0Nb; (b) 8C5Nb; (c) 8C10Nb; (d) 8C20Nb.

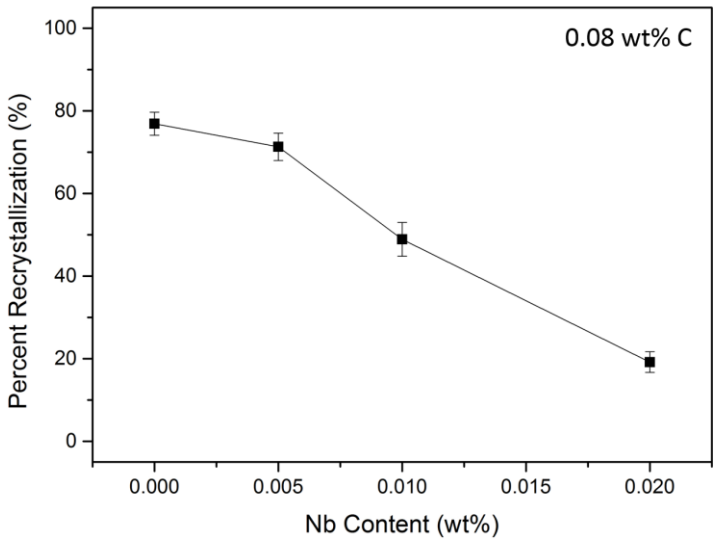

Figure 4-21 Evolution of percent recrystallisation of 8C steels after rough rolling and water quenching as a function of Nb contents. Error bars indicates the 95% confidence limits of the measurements.

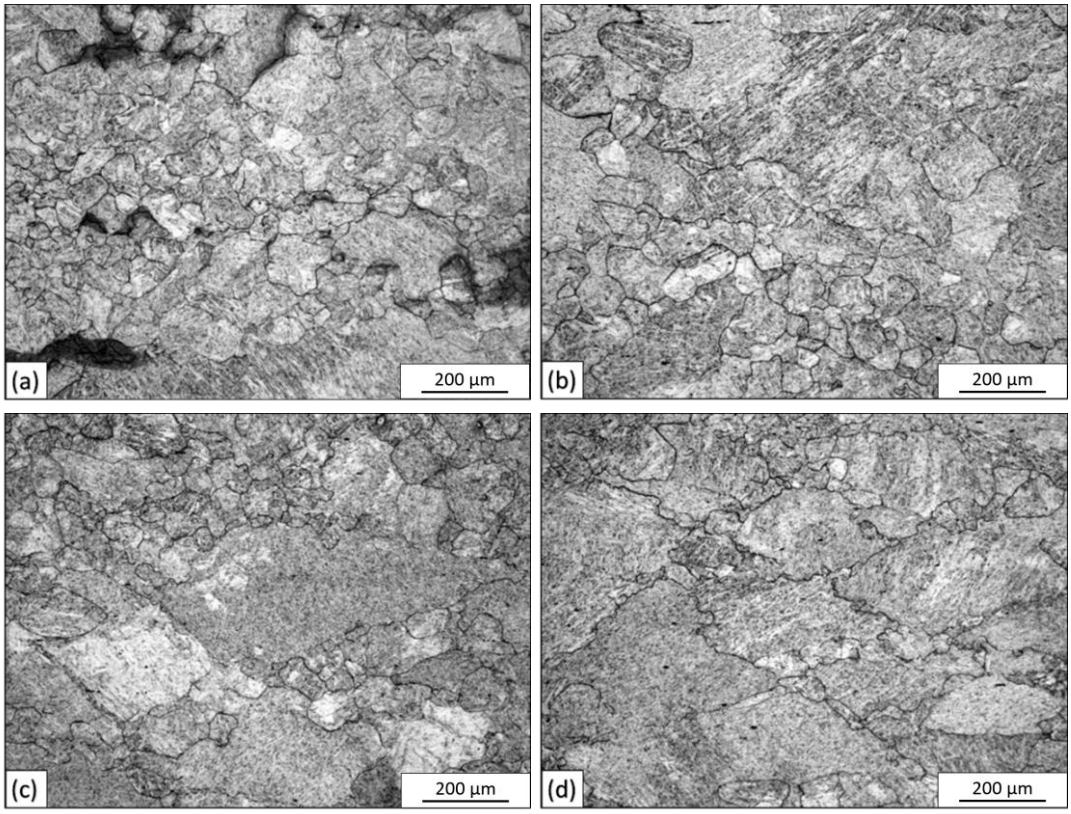

Figure 4-22 Prior-austenite microstructures of 40C steels after rough rolling and water quenching. (a) 40C0Nb; (b) 40C5Nb; (c) 40C10Nb; (d) 40C20Nb.

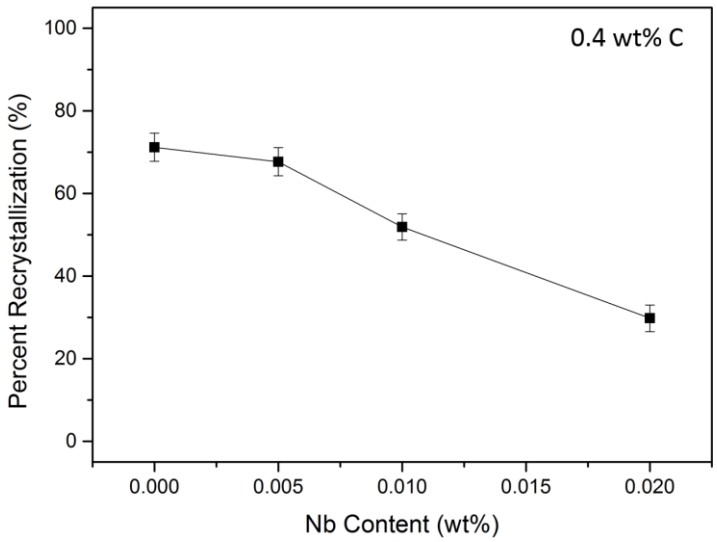

Figure 4-23 Evolution of percent recrystallisation of 40C steels after rough rolling and water quenching as a function of Nb contents. Error bars indicates the 95% confidence limits of the measurements.

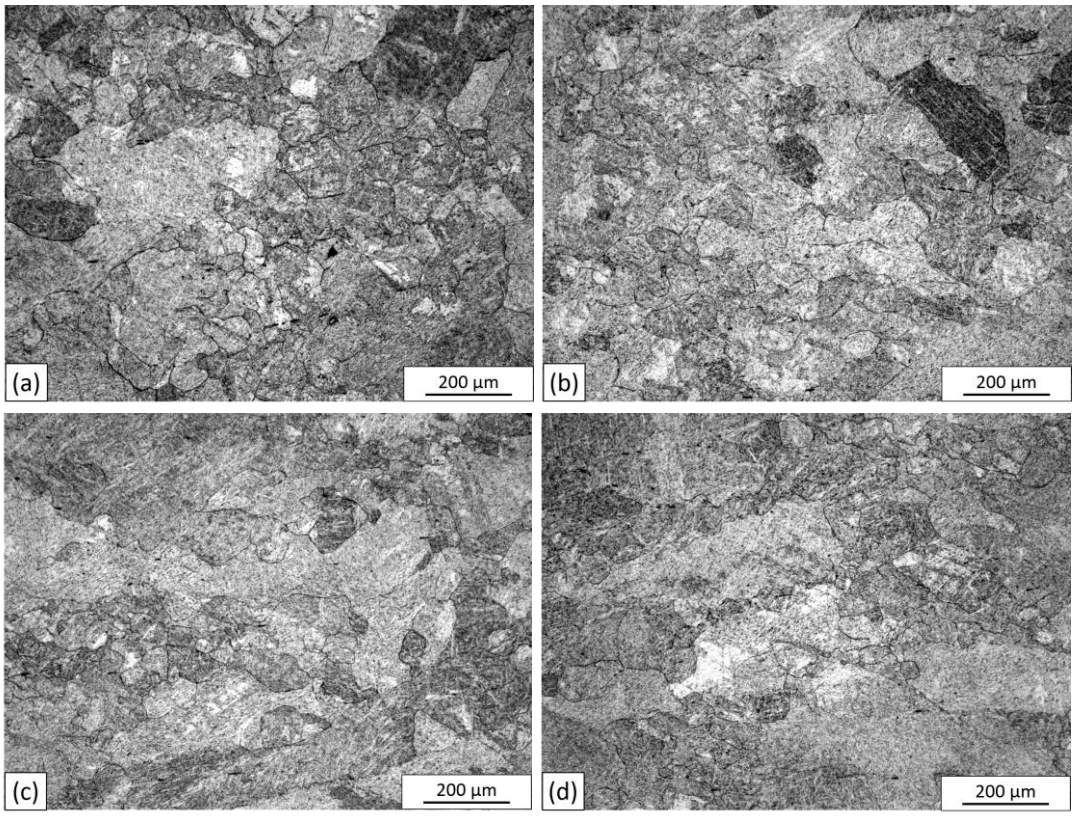

Figure 4-24 Prior-austenite microstructures of 60C steels after rough rolling and water quenching. (a) 60C0Nb; (b) 60C5Nb; (c) 60C10Nb; (d) 60C20Nb.

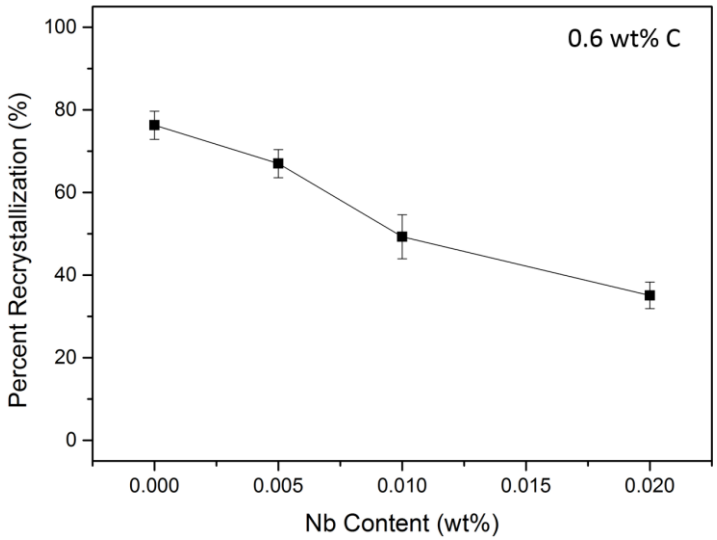

Figure 4-25 Evolution of percent recrystallisation of 60C steels after rough rolling as a function of Nb contents. Error bars indicates the 95% confidence limits of the measurements.

Table 4-3 Percent recrystallisation for steels after rough rolling and water quenching (%)

	0Nb	5Nb	10Nb	20Nb
8C	76.9±2.5	71.3±3.3	48.9±4.1	19.2±2.2
40C	71.2±3.4	67.7±3.4	51.9±3.2	29.8±3.2
60C	76.3±3.4	67.0±3.4	49.3±5.3	35.1±3.2

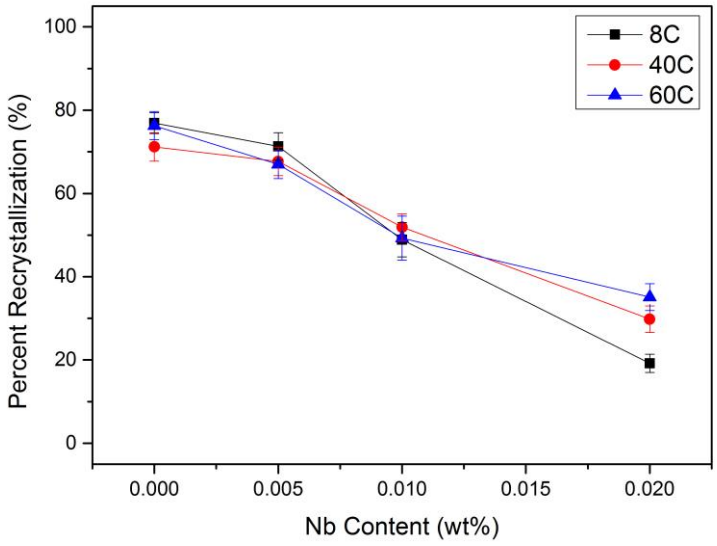

Figure 4-26 Comparison between influences of Nb on percent recrystallisation after rough rolling in steels with various carbon contents. Carbon contents are shown in the legend.

4.4 Prior-austenite microstructures after finish rolling at different finish rolling temperatures

After rough rolling, the steels were fast air cooled to the finish rolling temperatures, which were 1050°C, 1000°C and 950°C. The finish rolling was performed at a strain rate of 2/s with a strain of 0.2. Immediately after finish rolling, the steels were water quenched, as shown in Figure 4-27. The prior-austenite microstructures of the steels are shown below.

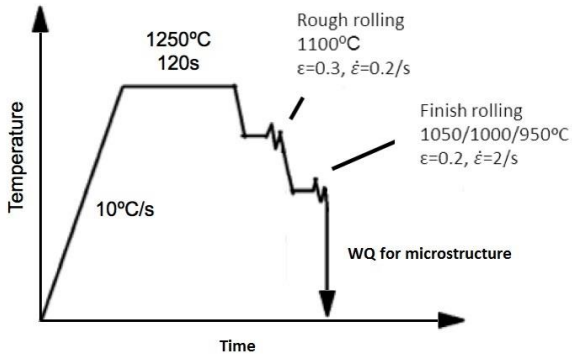

Figure 4-27 Illustration of water quenching performed at the end of finish rolling for microstructural observation

4.4.1 Prior-austenite microstructures of 8C steels after finish rolling at different finish rolling temperatures

The microstructures of 8C steels immediately quenched after finish rolling at the finish rolling temperature of 1050°C, 1000°C and 950°C are shown in Figure 4-28, Figure 4-29 and Figure 4-30, respectively.

The prior-austenite percent recrystallisation for all the 8C steels were calculated and summarized in Table 4-4. Figure 4-31 shows the evolution of percent recrystallisation as a function of Nb contents after finish rolling at different finish rolling temperatures. Figure 4-32 shows the change of prior-austenite percent recrystallisation as a function of finish rolling temperatures with different Nb contents.

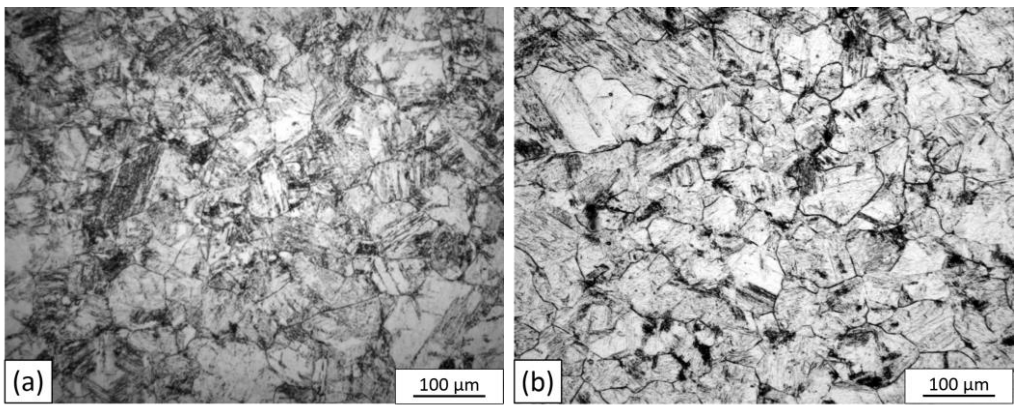

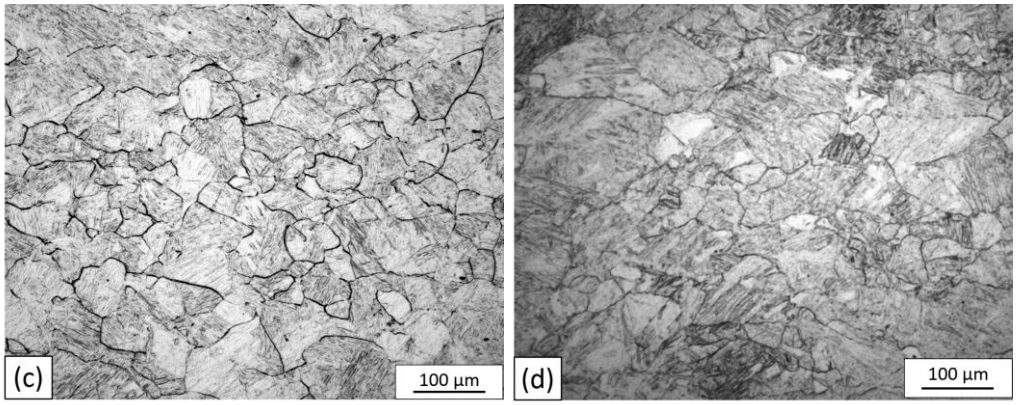

Figure 4-28 Prior-austenite microstructures of 8C steels after finish rolling at 1050°C followed by water quenching. (a) 8C0Nb; (b) 8C5Nb; (c) 8C10Nb; (d) 8C20Nb.

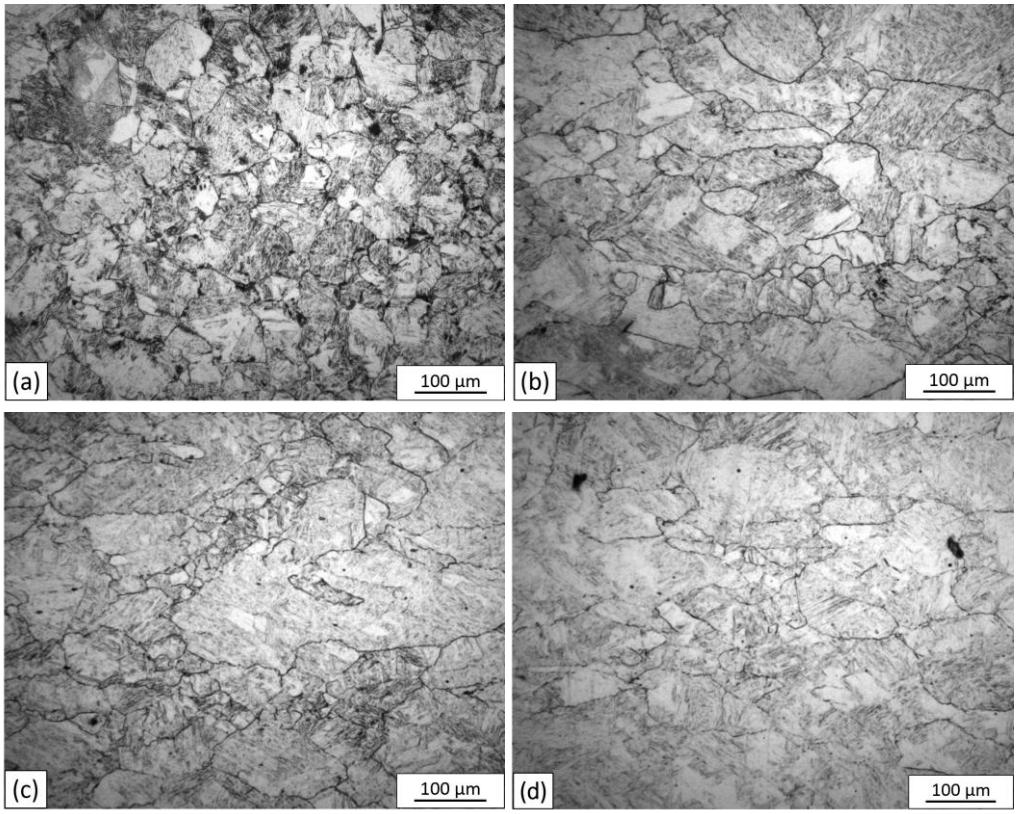

Figure 4-29 Prior-austenite microstructures of 8C steels after finish rolling at 1000°C followed by water quenching. (a) 8C0Nb; (b) 8C5Nb; (c) 8C10Nb; (d) 8C20Nb.

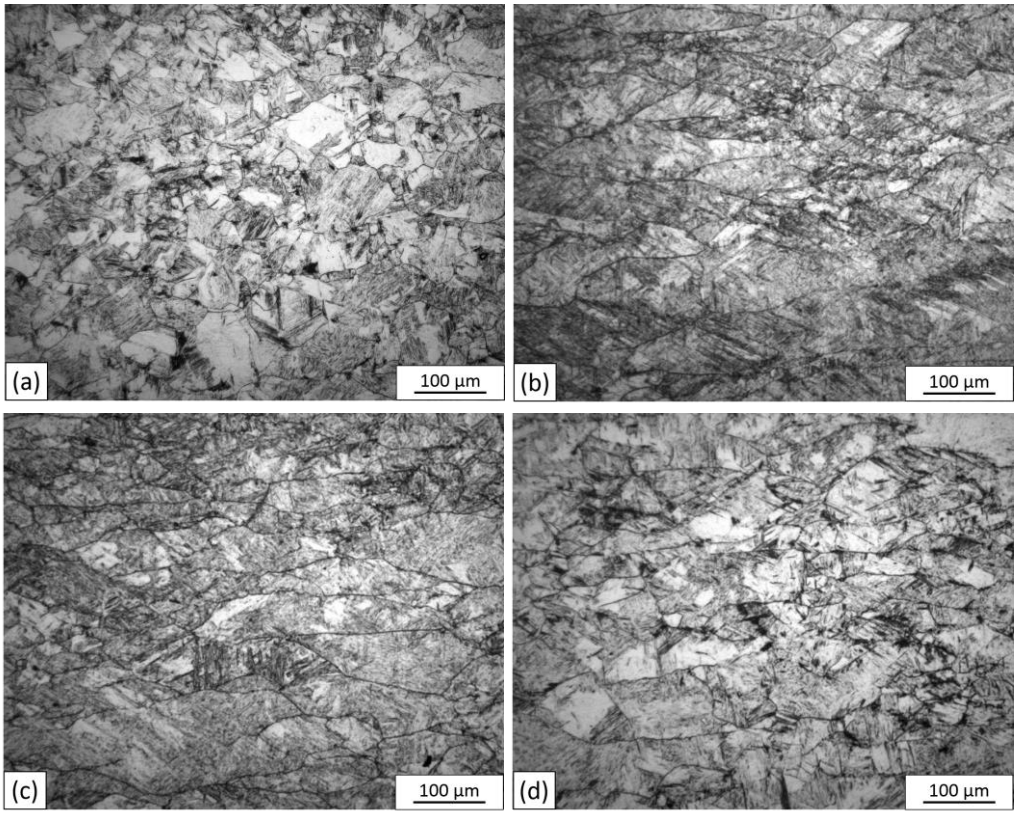

Figure 4-30 Prior-austenite microstructures of 8C steels after finish rolling at 950°C followed by water quenching. (a) 8C0Nb; (b) 8C5Nb; (c) 8C10Nb; (d) 8C20Nb.

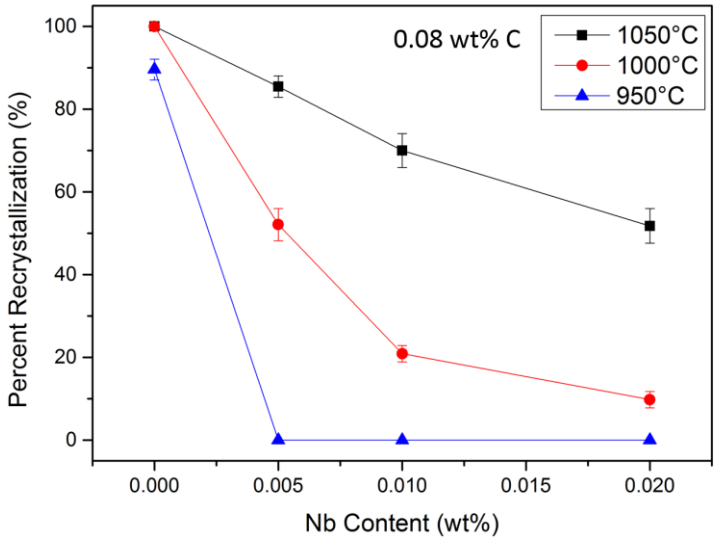

Figure 4-31 Evolution of percent recrystallisation of 8C steels after finish rolling as a function of Nb content. Error bars indicates the 95% confidence limits of the measurements. Finish rolling temperatures are shown in the legend.

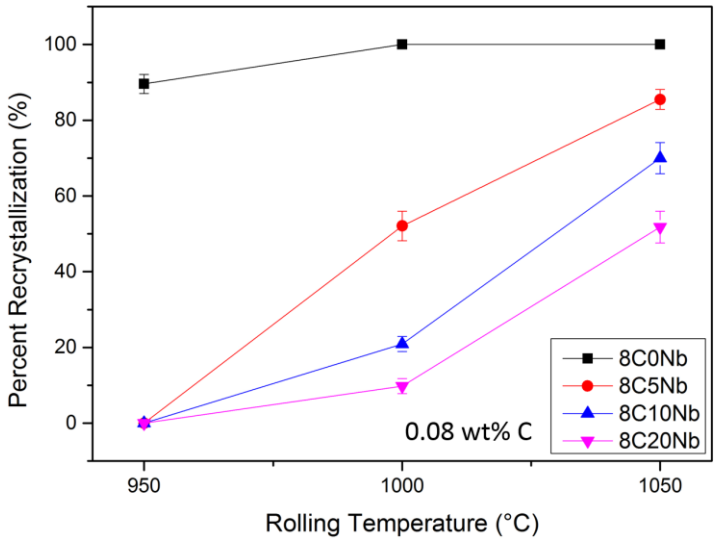

Figure 4-32 Evolution of percent recrystallisation of 8C steels after finish rolling as a function of finish rolling temperatures. Error bars indicates the 95% confidence limits of the measurements. Nb contents are shown in the legend.

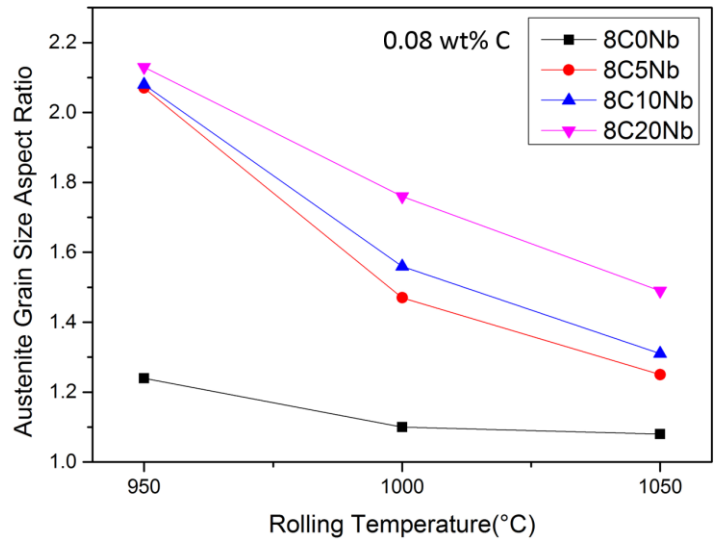

Figure 4-33 Evolution of prior-austenite grain size aspect ratio of 8C steels after finish rolling as a function of finish rolling temperatures. Nb contents are shown in the legend.

Table 4-4 Prior-austenite percent recrystallisation of 8C steels after finish rolling at different finish rolling temperatures (%)

	8C0Nb	8C5Nb	8C10Nb	8C20Nb
1050°C	100	85.5±2.6	70.0±4.1	51.8±4.2
1000°C	100	52.1±3.9	20.9±2.0	9.8±2.0
950°C	89.6±2.5	0	0	0

Table 4-5 Prior-austenite grain sizes of 8C steels after finish rolling at different finish rolling temperatures (μm)

	1050°C		1000°C		950°C	
	RD	TD	RD	TD	RD	TD
8C0Nb	61.9±4.3	57.4±3.4	47.1±2.3	42.7±2.1	47.5±3.3	38.2±2.3
8C5Nb	67.9±3.4	54.2±2.1	79.7±6.5	54.1±4.3	127.7±12.2	61.8±3.6
8C10Nb	74.6±5.0	56.8±2.5	83.0±7.8	53.1±3.3	128.3±9.8	61.8±3.4
8C20Nb	87.7±7.5	58.7±4.1	92.0±11.2	52.4±3.9	125.8±13.8	59.2±2.9

As it can be seen from Figure 4-31 and Figure 4-32, Nb addition delayed recrystallisation at all rolling temperatures. At 1050°C (Figure 4-28), the reference plain carbon steel 8C0Nb showed a fully recrystallised microstructure after finish rolling. All the Nb microalloyed steels showed partially recrystallised microstructures. The percent recrystallisation decreased from 85.5% to 70.0% and 51.8% with Nb content increasing from 0.005wt% to 0.01wt% and 0.02wt%.

At 1000°C (Figure 4-29), a similar but stronger retarding effect on recrystallisation was observed from the Nb additions. The percent recrystallisation for 8C0Nb, 8C5Nb, 8C10Nb and 8C20Nb steels were 100%, 52.1%, 20.9% and 9.8%, respectively.

At the rolling temperature of 950°C (Figure 4-30), the plain carbon steel 8C0Nb showed 89.6±2.5% recrystallised prior-austenite microstructure. The Nb addition showed a strong retarding effect on recrystallisation at 950°C, all three microalloyed

steels showed fully unrecrystallised microstructures.

The prior-austenite grain sizes were calculated using the linear intercept method and summarized in Table 4-5. The prior-austenite grain size aspect ratios were calculated and plotted in Figure 4-33. For 8C0Nb reference steel, the recrystallised prior-austenite grain size was decreased with the decreasing temperature. For all the Nb microalloyed steels, the transversal direction prior-austenite grain size was fairly constant with the change of rolling temperature. However, the degree of prior-austenite grain elongation on the rolling direction was substantially increased at lower deformation temperatures.

Comparing Figure 4-32 and Figure 4-33, it was found that the fully recrystallised prior-austenite had a grain size aspect ratio of approximately one (8C0Nb at 1050°C and 1000°C). When the recrystallisation was not completed, the degree of elongation on the rolling direction continuously increased with the decrease of percent recrystallisation, which led to an increase in the prior-austenite grain size aspect ratio. The fully unrecrystallised prior-austenite showed an aspect ratio of around 2.1 (see 8C5Nb, 8C10Nb and 8C20Nb at 950°C). These results shows good agreement with previous studies [28,35,124,134].

4.4.2 Prior-austenite microstructures of 40C steels after finish rolling at different finish rolling temperatures

Figure 4-34, Figure 4-35 and Figure 4-36 show the prior-austenite microstructures of 40C steels after finish rolling at the rolling temperature of 1050°C, 1000°C and 950°C, respectively.

The prior-austenite percent recrystallisation for all the 40C steels after finish rolling were calculated and summarized in Table 4-6. The change of percent recrystallisation with Nb contents and finish rolling temperature were plotted in Figure 4-37 and Figure 4-38.

The recrystallisation behaviour of 40C steels after finish rolling was similar to that of 8C steels. As it is shown in Figure 4-37 and Figure 4-38, at all rolling temperatures,

the percent recrystallisation decreased with the increase of the Nb content. However, the influence of Nb addition to the percent recrystallisation was affected by different finish rolling temperatures. At 1050°C, percent recrystallisation reduced gradually from 100% recrystallisation of the reference steel 40C0Nb to 83.3%, 76.2% and 63.5% with the Nb addition of 0.005wt%, 0.01wt% and 0.02wt%.

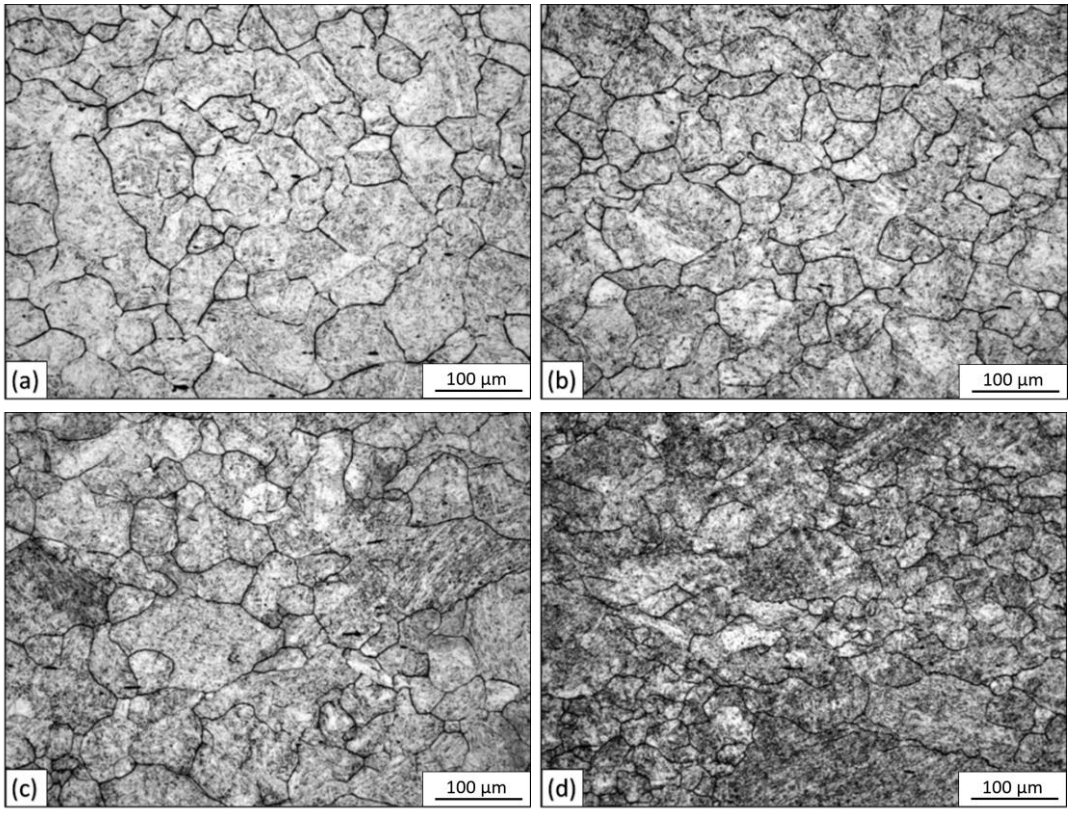

Figure 4-34 Prior-austenite microstructures of 40C steels after finish rolling at 1050°C followed by water quenching. (a) 40C0Nb; (b) 40C5Nb; (c) 40C10Nb; (d) 40C20Nb.

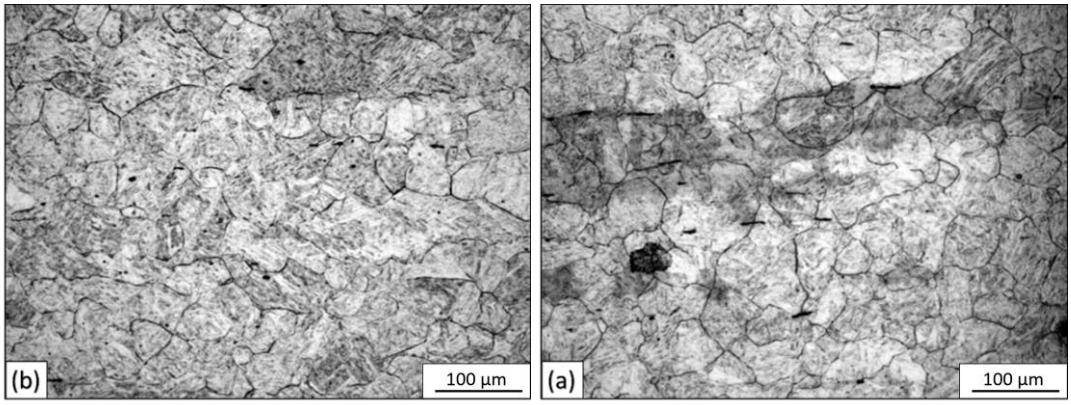

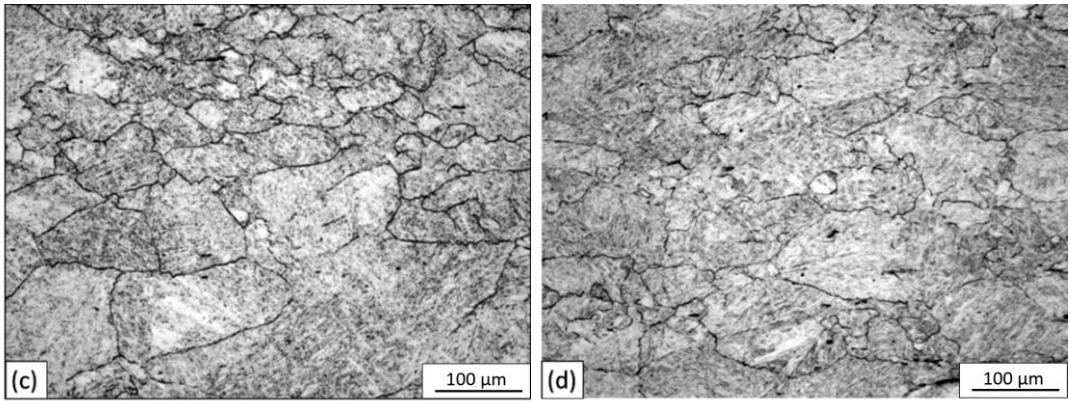

Figure 4-35 Prior-austenite microstructures of 40C steels after finish rolling at 1000°C followed by water quenching. (a) 40C0Nb; (b) 40C5Nb; (c) 40C10Nb; (d) 40C20Nb.

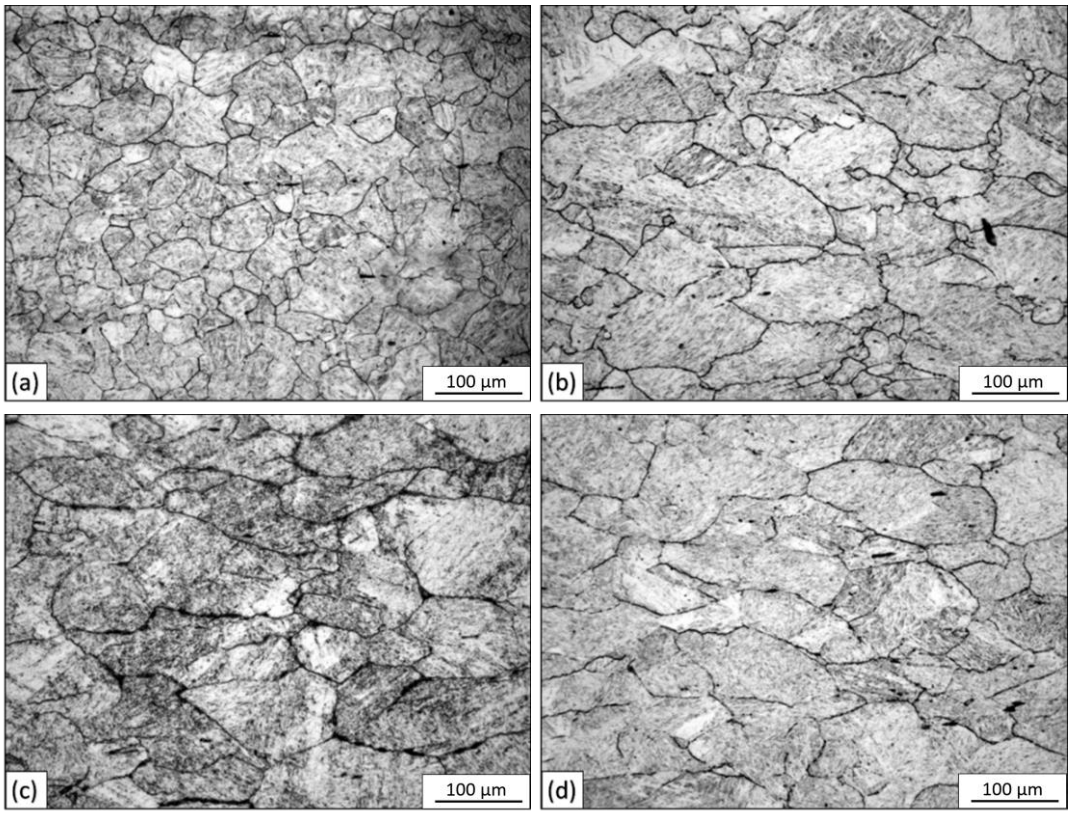

Figure 4-36 Prior-austenite microstructures of 40C steels after finish rolling at 950°C followed by water quenching. (a) 40C0Nb; (b) 40C5Nb; (c) 40C10Nb; (d) 40C20Nb.

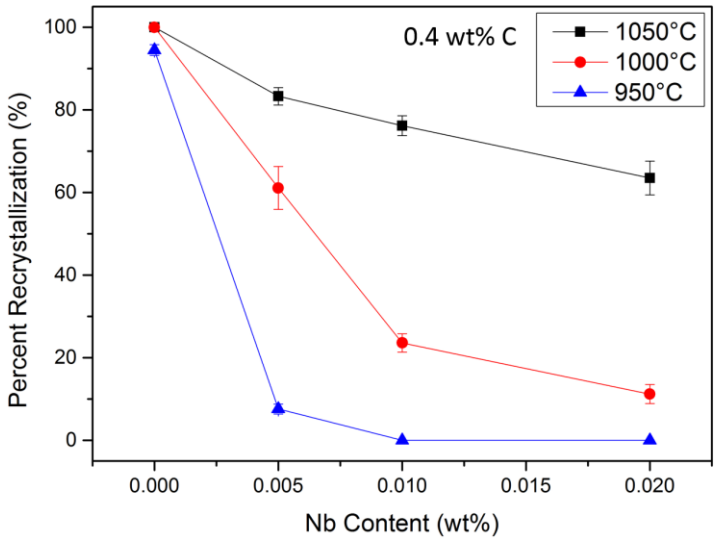

Figure 4-37 Evolution of percent recrystallisation of 40C steels after finish rolling as a function of Nb contents. Error bars indicates the 95% confidence limits of the measurements. Finish rolling temperatures are shown in the legend.

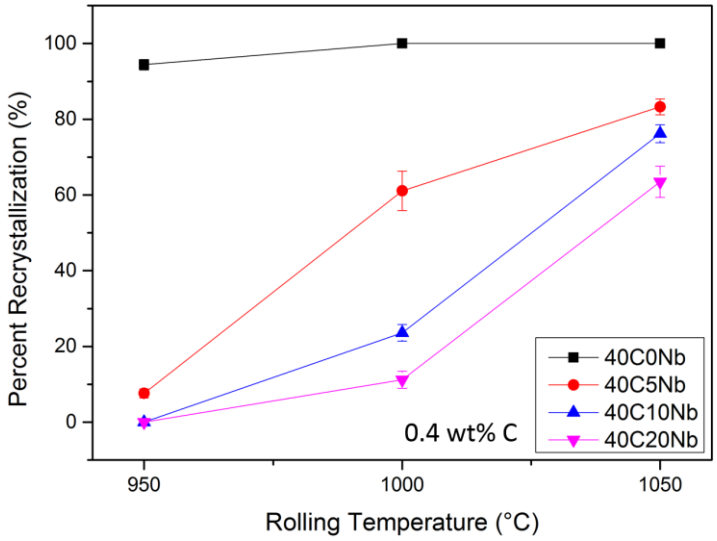

Figure 4-38 Evolution of percent recrystallisation of 40C steels after finish rolling as a function of finish rolling temperatures. Error bars indicates the 95% confidence limits of the measurements. Nb contents are shown in the legend.

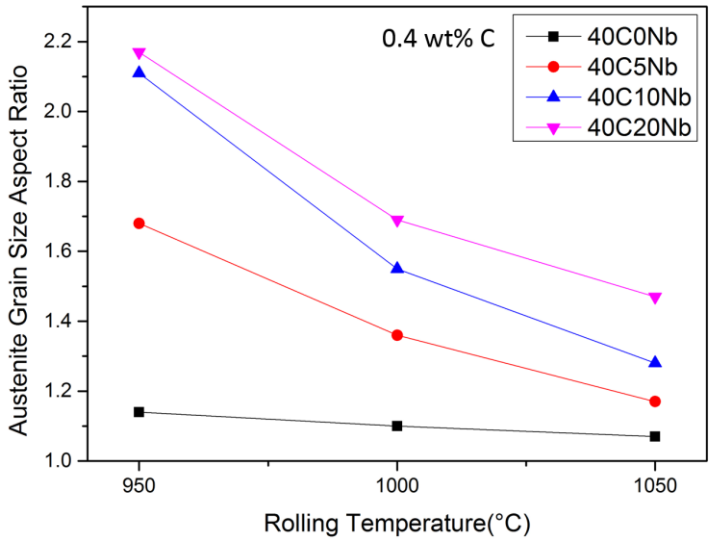

Figure 4-39 Evolution of percent recrystallisation of 40C steels after finish rolling as a function of finish rolling temperatures. Error bars indicates the 95% confidence limits of the measurements. Nb contents are shown in the legend.

Table 4-6 Prior-austenite percent recrystallisation of 40C steels after finish rolling at different finish rolling temperatures (%)

	40C0Nb	40C5Nb	40C10Nb	40C20Nb
1050°C	100	83.3±2.1	76.2±2.4	63.5±4.1
1000°C	100	61.1±5.2	23.6±2.2	11.2±2.3
950°C	94.4±1.4	7.6±1.2	0	0

Table 4-7 Prior-austenite grain sizes of 40C steels after finish rolling at different finish rolling temperatures (μm)

	1050°C		1000°C		950°C	
	RD	TD	RD	TD	RD	TD
40C0Nb	51.5±1.4	48.2±1.4	46.2±2.7	42.0±1.8	42.3±2.6	37.1±1.5
40C5Nb	54.5±2.6	46.3±2.6	60.6±4.8	44.4±2.1	86.4±9.0	51.3±3.0
40C10Nb	57.4±4.1	44.7±2.4	82.2±11.6	52.9±3.1	119.3±9.2	56.6±4.2
40C20Nb	65.6±8.1	44.6±3.6	91.8±10.2	54.2±3.5	122.5±9.6	56.3±3.4

When the finish rolling temperature was 1000°C, the recrystallisation of the reference steel 40C0Nb steel was completed after finish rolling. Compared with finish rolling temperature of 1050°C, the percent recrystallisation of 40C5Nb, 40C10Nb and 40C20Nb steels reduced to 61.1%, 23.6% and 11.2%, respectively.

The most profound influence was found at the lowest rolling temperature 950°C. For the reference steel 40C0Nb, the recrystallisation process was nearly finished with a percent recrystallisation of 94.4±1.4%. Only 7.6±1.2% of the prior-austenite grains were recrystallised for the 40C5Nb steel. Even stronger retardation on recrystallisation was found in both 40C10Nb and 40C20Nb steels in which a fully unrecrystallised microstructure was shown.

The prior-austenite grain sizes for all 40C steels deformed at the three finish rolling temperatures were calculated and listed in Table 4-7. The prior-austenite grain aspect ratios were also calculated and plotted in Figure 4-39. The fully recrystallised prior-austenite microstructures had an aspect ratio of approximately 1.0, and the fully unrecrystallised prior-austenite microstructures had an aspect ratio of approximately 2.1. All the partially recrystallised microstructures had aspect ratios between 1.2 and 2.0 with a decreased ratio with increasing percent recrystallisation. This showed good consistency with observation of 8C steels and previous works [28,35,124,134].

4.4.3 Prior-austenite microstructures of 60C steels after finish rolling at different finish rolling temperatures

After finish rolling at 1050°C, 1000°C and 950°C, the prior-austenite microstructure of 60C steels are shown in Figure 4-40, Figure 4-41 and Figure 4-42, respectively.

The prior-austenite percent recrystallisation for all 60C steels after being rolled at various different rolling temperatures was calculated and summarized in Table 4-8. The influence of Nb contents and finish rolling temperatures on the prior-austenite recrystallisation are shown in Figure 4-43 and Figure 4-44.

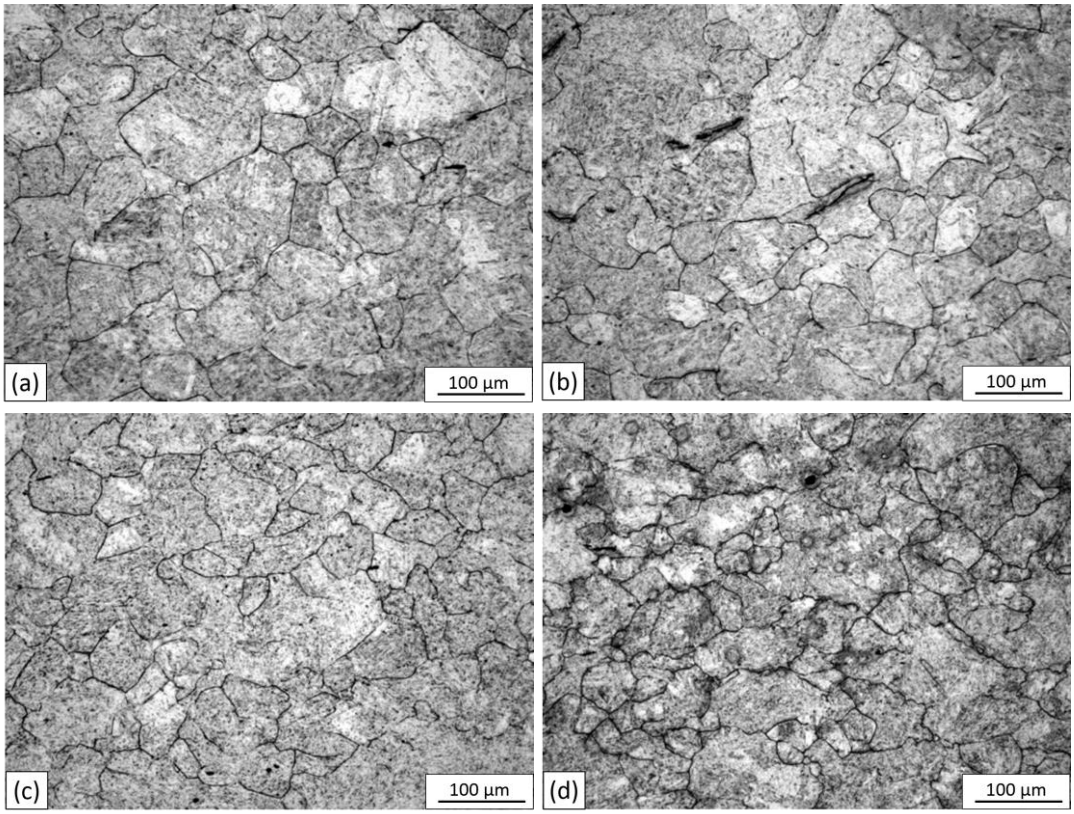

Figure 4-40 Prior-austenite microstructures of 60C steels after finish rolling at 1050°C followed by water quenching. (a) 60C0Nb; (b) 60C5Nb; (c) 60C10Nb; (d) 60C20Nb.

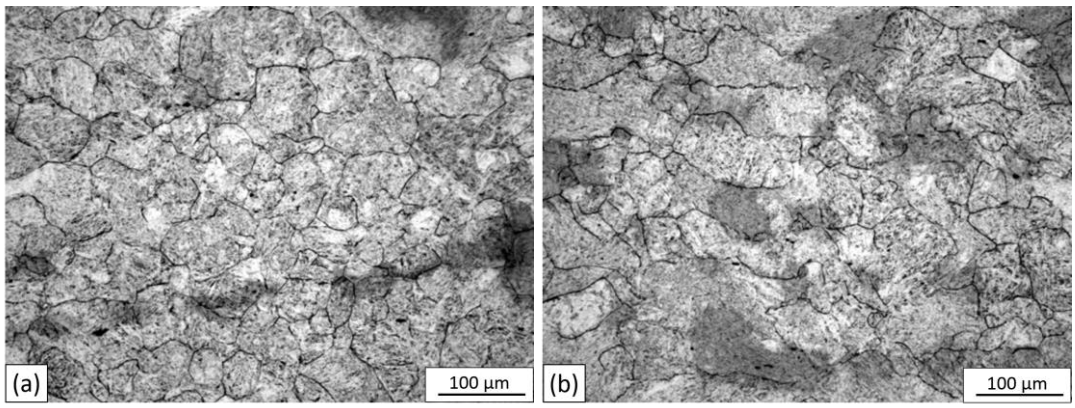

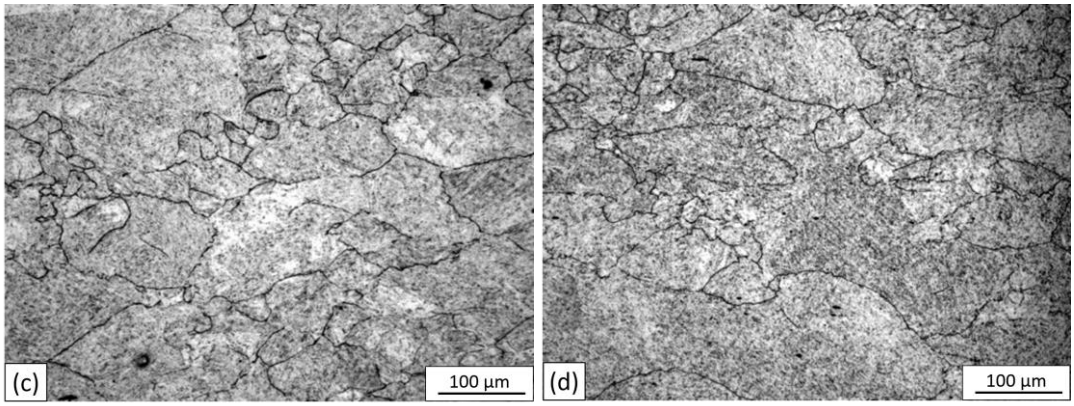

Figure 4-41 Prior-austenite microstructures of 60C steels after finish rolling at 1000°C followed by water quenching. (a) 60C0Nb; (b) 60C5Nb; (c) 60C10Nb; (d) 60C20Nb.

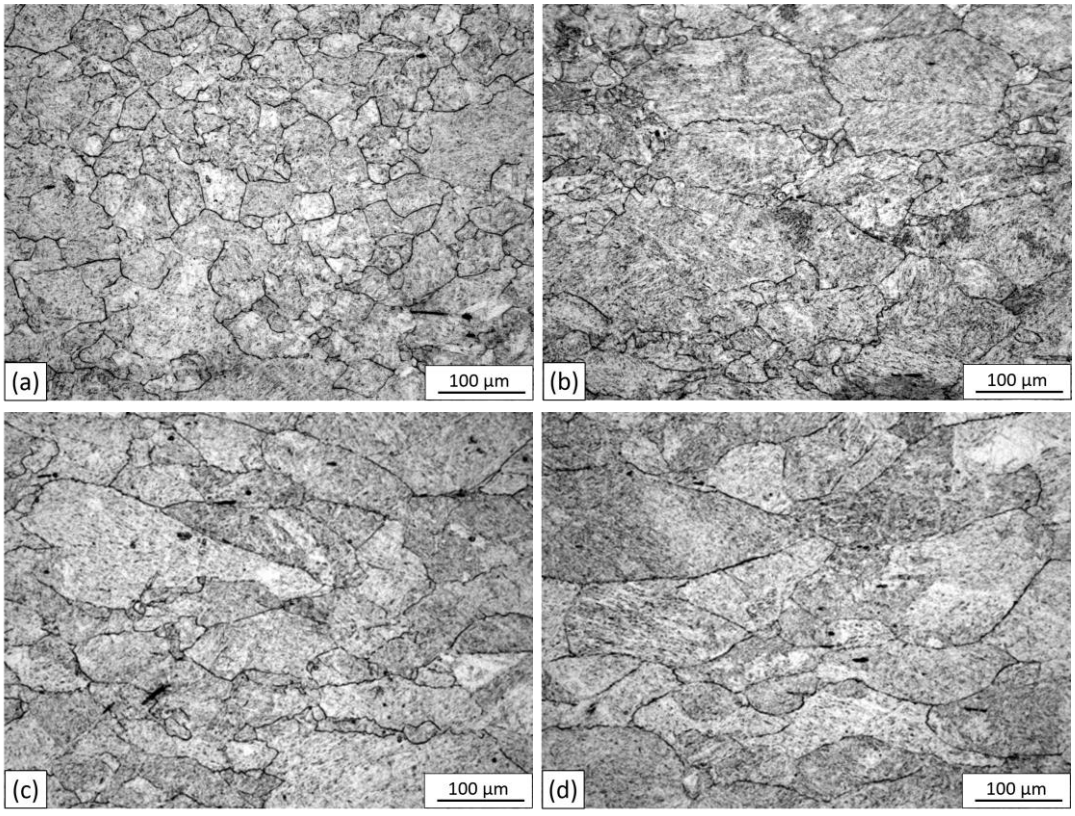

Figure 4-42 Prior-austenite microstructures of 60C steels after finish rolling at 950°C followed by water quenching. (a) 60C0Nb; (b) 60C5Nb; (c) 60C10Nb; (d) 60C20Nb.

Figure 4-43 shows the evolution of percent recrystallisation for all 60C steels after finish rolling as a function of finish rolling temperatures and Nb contents. Again similar to 8C and 40C steels, it can be clearly seen that the percent recrystallisation

reduced gradually with the increase in Nb content at all the finish rolling temperatures. However, the extent of the influence of Nb addition to the recrystallisation behaviour was strongly dependent on the finish rolling temperature.

At the finish rolling temperature of 1050°C, a large fraction of the prior-austenite grains was recrystallised for all 60C steels. The reference steel, 60C0Nb, showed a fully recrystallised microstructure. The Nb microalloyed steels showed partially recrystallised microstructure due to the retarding force on recrystallisation exerted by the Nb addition. With the increase of Nb addition from 0.005wt% to 0.01wt% and 0.02wt%, the percent recrystallisation of the steels dropped from 82.6±2.6% to 72.1±2.3% and 65.2±3.3%, respectively (Figure 4-43).

When the finish rolling was conducted at 1000°C, the reference steel 60C0Nb was fully recrystallised. 60C5Nb steel showed a gentle decrease on the percent recrystallisation from 82.6±2.6% to 65.4±3.1% due to the drop on finish rolling temperature from 1050°C to 1000°C. However, 60C10Nb steel showed a more dramatic decrease in the recrystallisation compared with 60C5Nb steel. Comparing the percent recrystallisation of 0.01wt% Nb steels at finish rolling temperature of 1050°C and 1000°C, a large decrease from 72.1±2.3% to 24.6±2.4% was observed. This indicated that the finish rolling temperature plays an important role on the extent of the retarding force provided by the Nb addition. For 60C20Nb steel, the recrystallisation was further retarded. Only 13.1±2.8% of the prior-austenite grains were recrystallised.

At the finish rolling temperature of 950°C, the reference steel 60C0Nb showed a nearly fully recrystallised prior-austenite microstructure. The percent recrystallisation for 60C0Nb was 87.6±1.9%. For the Nb steels, all the Nb steels showed more profound retarding force on recrystallisation at the finish rolling temperature of 950°C. The dramatic decrease in percent recrystallisation from 87.6±1.9% to 9.1±1.6% happened even only 0.005wt% of Nb was added. A further decrease of percent recrystallisation was showed in the 60C10Nb steel, with 4.2±1.0% of prior-austenite grains recrystallised. When the Nb content was increased to 0.02wt% (60C20Nb), fully unrecrystallised prior-austenite microstructure was obtained which

indicated the full retardation of recrystallisation at the finish rolling temperature of 950°C.

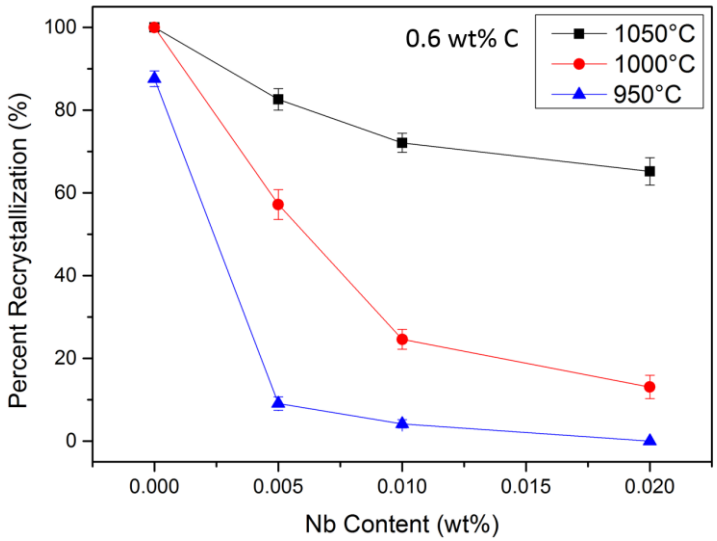

Figure 4-43 Evolution of percent recrystallisation of 60C steels after finish rolling as a function of Nb contents. Error bars indicates the 95% confidence limits of the measurements. Finish rolling temperatures are shown in the legend.

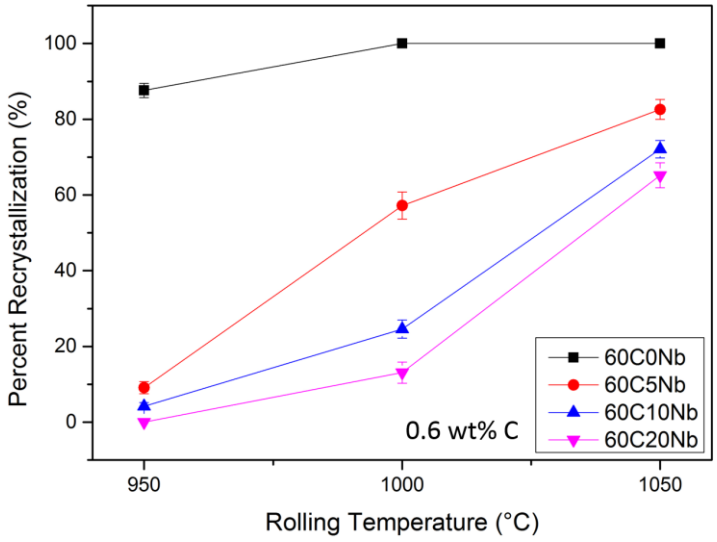

Figure 4-44 Evolution of percent recrystallisation of 60C steels after finish rolling as a function of finish rolling temperatures. Error bars indicates the 95% confidence limits of the measurements. Nb contents are shown in the legend.

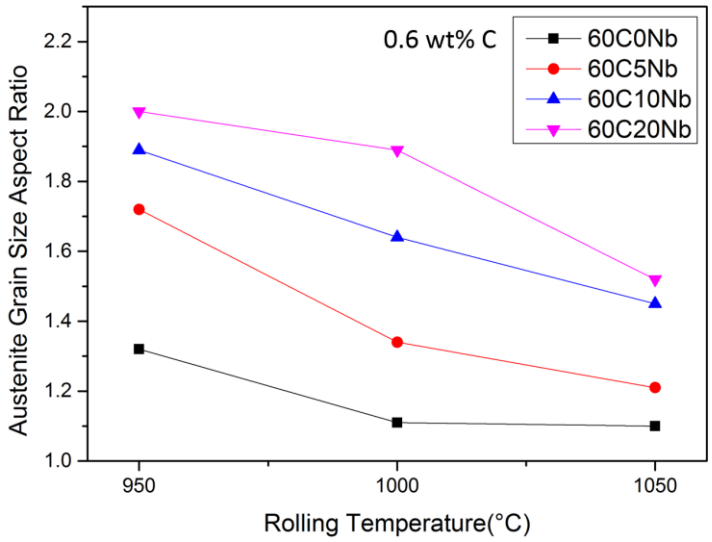

Figure 4-45 Evolution of prior-austenite grain size aspect ratio of 60C steels after finish rolling as a function of finish rolling temperatures. Nb contents are shown in the legend.

Table 4-8 Prior-austenite percent recrystallisation of 60C steels after rough rolling and finish rolling at different finish rolling temperatures (%)

	60C0Nb	60C5Nb	60C10Nb	60C20Nb
1050°C	100	82.6±2.6	72.1±2.3	65.2±3.3
1000°C	100	57.2±3.6	24.6±2.4	13.1±2.8
950°C	87.6±1.9	9.1±1.6	4.2±1.0	0

Table 4-9 Prior-austenite grain size of 60C steels after rough rolling and finish rolling at different finish rolling temperatures (μm)

	1050°C		1000°C		950°C	
	RD	TD	RD	TD	RD	TD
60C0Nb	58.0±3.3	50.6±2.9	47.1±3.1	42.3±3.4	55.4±6.9	42.1±2.4
60C5Nb	60.3±5.6	49.8±4.1	63.5±8.3	47.4±4.5	103.9±11.8	60.3±5.0
60C10Nb	64.3±7.7	44.3±3.3	78.7±13.6	47.9±3.4	110.0±6.9	58.1±3.6
60C20Nb	71.2±5.7	46.9±2.5	96.5±17.8	51.1±4.3	121.5±6.3	60.6±2.7

The prior-austenite grain sizes for all the 60C steels rolled at three finish rolling temperatures were calculated and listed in Table 4-9.

According to the grain sizes, the prior-austenite grain aspect ratios were calculated and plotted in Figure 4-45. Comparing the evolution of prior-austenite recrystallisation behaviour (Figure 4-44) and prior-austenite grain aspect ratio (Figure 4-45) with finish rolling temperature, it was found that the fully recrystallised prior-austenite microstructures had a grain size aspect ratio of approximately 1.0, and the fully unrecrystallised prior-austenite microstructures had a grain size aspect ratio of about 2.0. For the partially recrystallised microstructures, the grain size aspect ratio was between 1.2 and 1.9. It showed an increasing aspect ratio with decreasing percent recrystallisation. Similar results have been reported by other researchers [28,35,124,134].

4.4.4 Comparison of prior-austenite microstructures after finish rolling between steels with various C contents

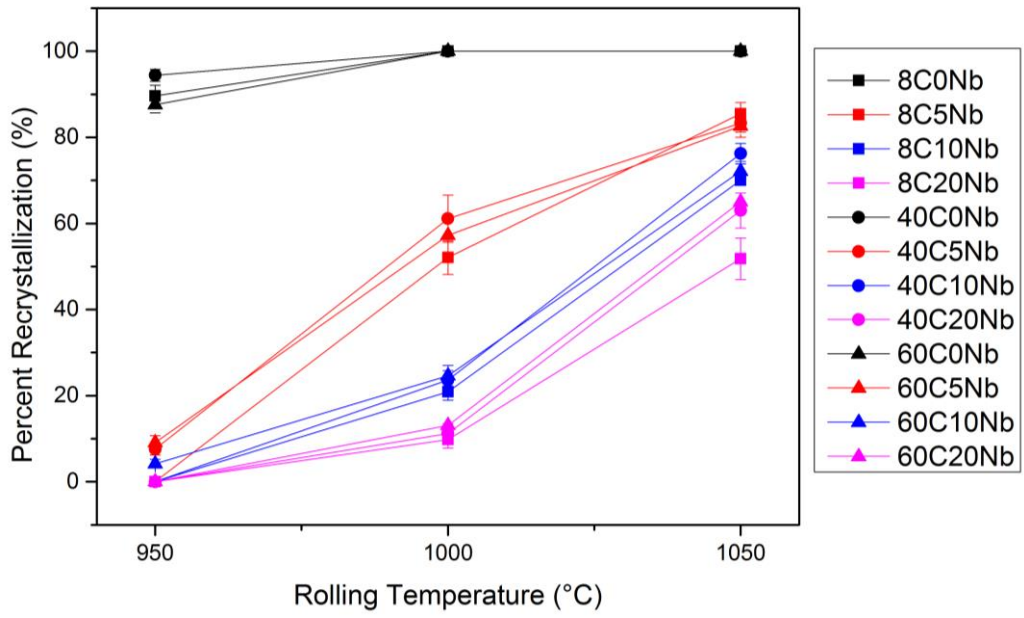

Figure 4-46 Comparison of percent recrystallisation of all steels after finish rolling and water quenching. Symbols for various steels are shown in the legend.

In order to illustrate the influence of C on the effectiveness of Nb in retarding the recrystallisation, a comparison of percent recrystallisation of all the steels after finish rolling are shown in Figure 4-46. Steels with the same Nb but different C contents were plotted in the same colour. For example, 8C5Nb, 40C5Nb and 60C5Nb were shown in red. It can be seen that data points with the same colour, i.e. same Nb but different C contents, had almost the same percent recrystallisation. There was no obvious influence observed from the change in C content.

The only exception was 20Nb steels being rolled at 1050°C, a slightly smaller percent recrystallisation was observed in 8C20Nb steel compared with 40C20Nb and 60C20Nb steels. This might be attributed to the higher Nb in solution after homogenisation in 8C20Nb.

4.5 Prior-austenite microstructures after the isothermal holding period of 20s at different finish rolling temperatures

In order to represent the rolling conditions during industrial production, an isothermal holding was performed to simulate the interpass time. For structural steels, the rolling process can be different for different shapes (bar, section etc) and dimensions of the final products. It also varies in different plants. Therefore, a general holding time of 20s was chosen in this study.

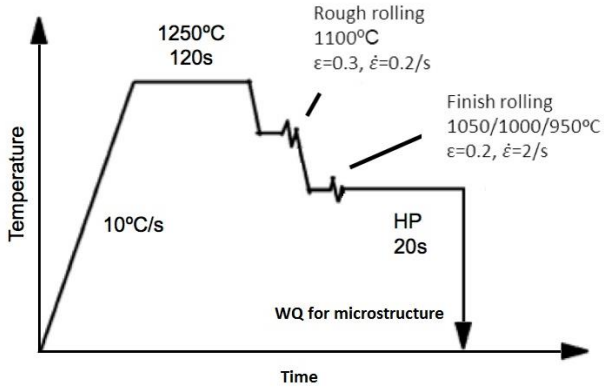

Figure 4-47 Illustration of water quenched performed at the end of isothermal holding period of 20s for microstructural observation.

After rough rolling (at 1100°C, strain rate of 0.2/s and strain of 0.3) and finish rolling (at 1050°C/1000°C/950°C, strain rate of 2/s and strain of 0.2), the steels were isothermally held at the corresponding finish rolling temperature for 20s. At the end of the isothermal holding, the steels were water quenched to investigate the prior-austenite microstructure (Figure 4-47).

4.5.1 Prior-austenite microstructures of 8C steels after the isothermal holding period of 20s at different finish rolling temperatures

The prior-austenite microstructure of 8C steels after finish rolling and the 20s isothermal holding period at various rolling temperatures are shown in Figure 4-48, Figure 4-49 and Figure 4-50.

As it is shown in Figure 4-48, all 8C steels showed fully recrystallised microstructure after the holding period of 20s at the rolling temperature of 1050°C.

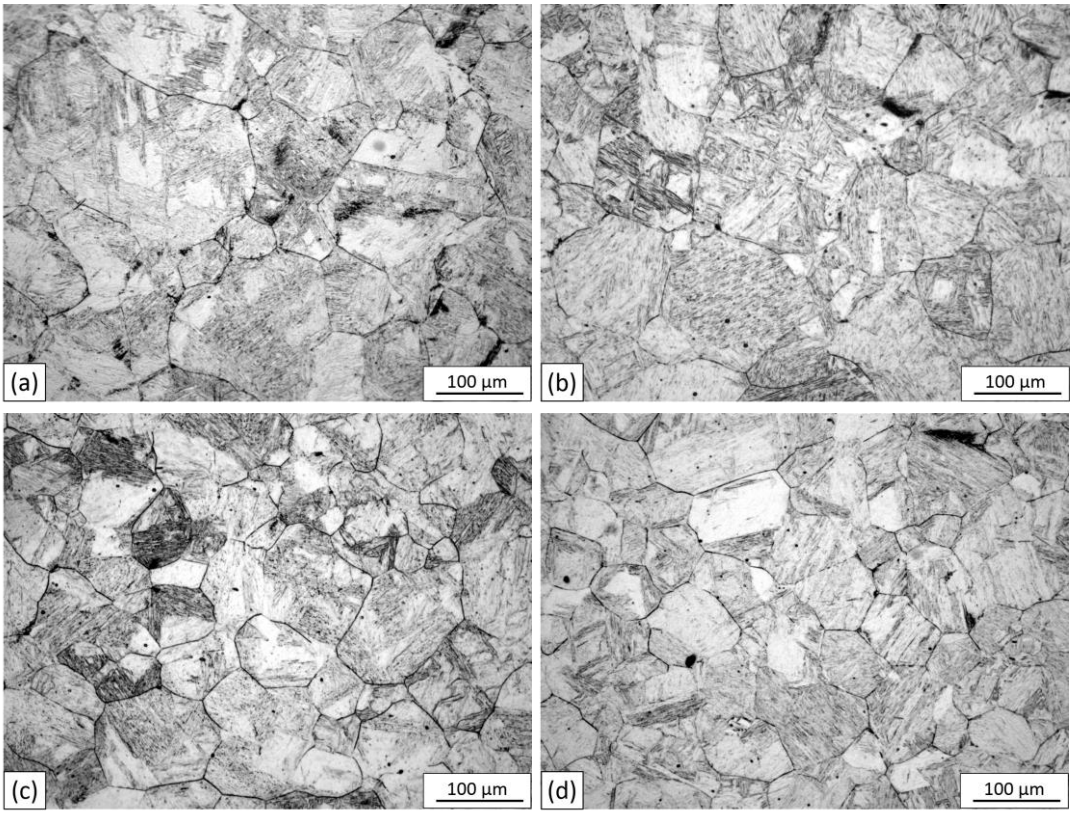

Figure 4-48 Prior-austenite microstructures of 8C steels after 20s holding period at 1050°C followed by water quenching. (a) 8C0Nb; (b) 8C5Nb; (c) 8C10Nb; (d) 8C20Nb.

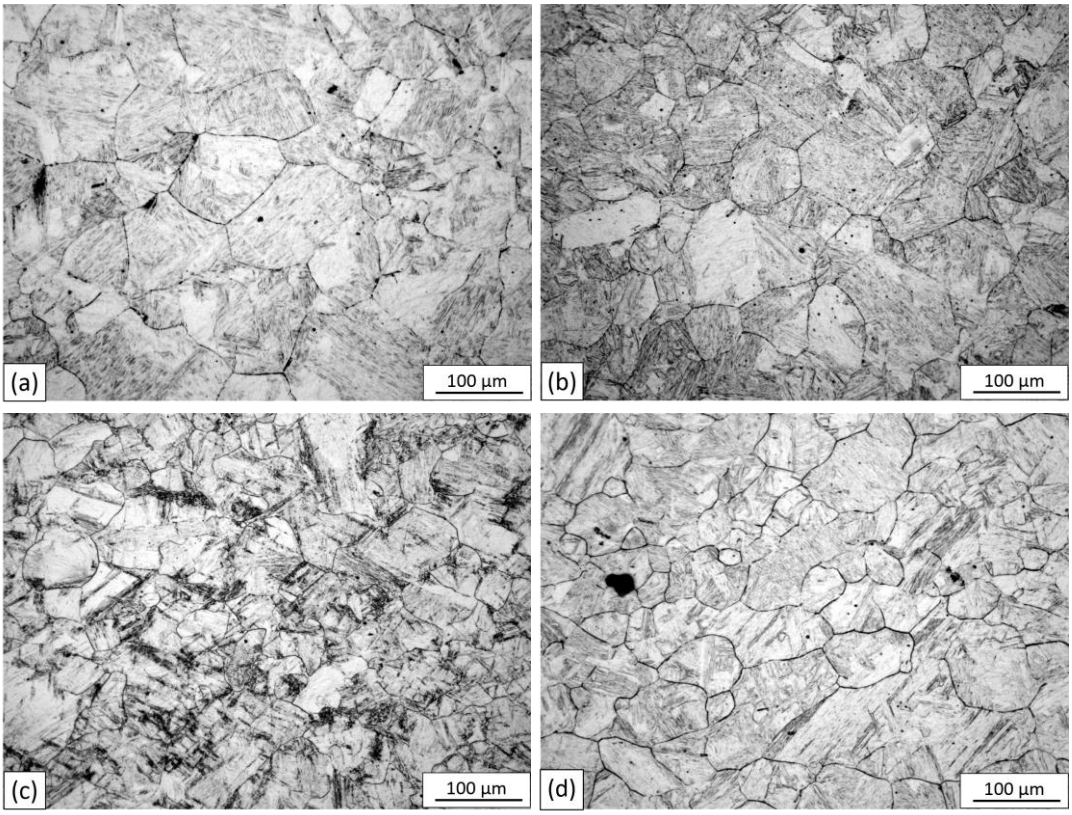

Figure 4-49 Prior-austenite microstructures of 8C steels after 20s holding period at 1000°C followed by water quenching. (a) 8C0Nb; (b) 8C5Nb; (c) 8C10Nb; (d) 8C20Nb.

With the rolling temperature of 1000°C (Figure 4-49), recrystallised microstructures were observed in 8C0Nb, 8C5Nb and 8C10Nb. For the higher Nb steel 8C20Nb, a partially recrystallised microstructure was revealed.

When 8C steels were held at finish rolling temperature of 950°C (Figure 4-50), various microstructures were shown. For the reference steel 8C0Nb and the low Nb steel 8C5Nb, fully recrystallised microstructures were found. 8C10Nb steel was partially recrystallised. For 8C20Nb steels, no recrystallisation was observed. The recrystallisation process was completely retarded by the 0.02wt% Nb addition.

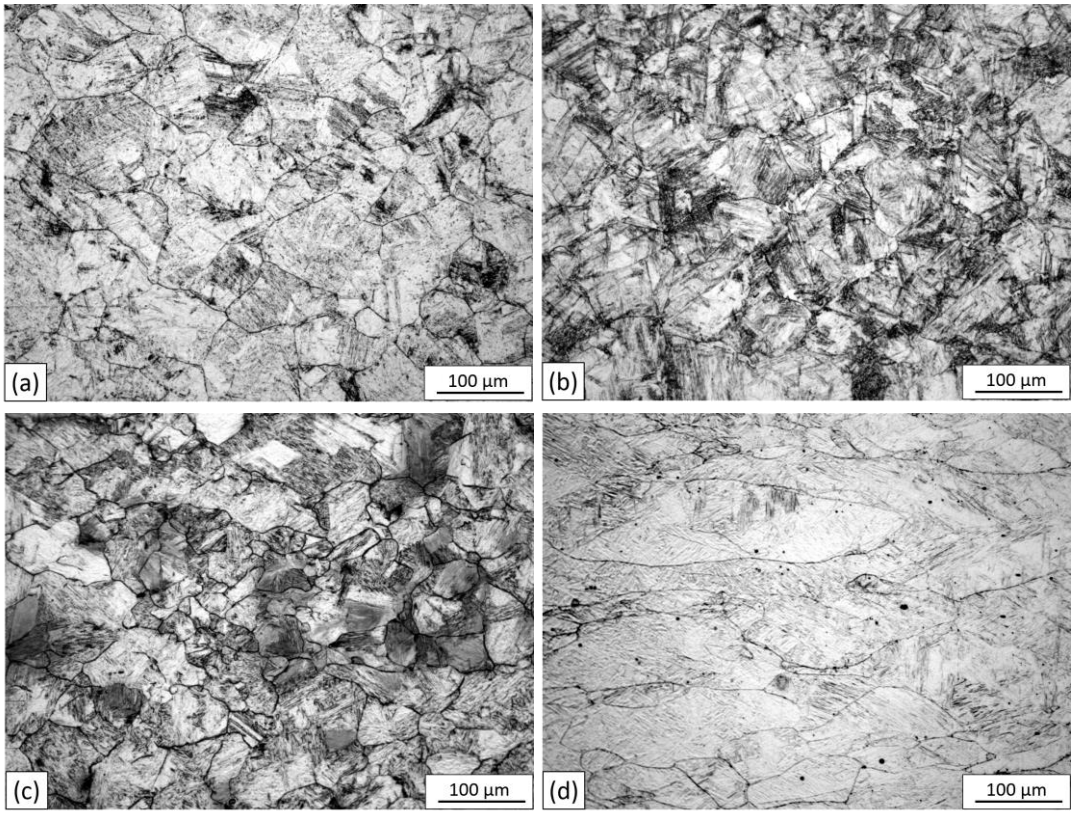

Figure 4-50 Prior-austenite microstructures of 8C steels after 20s holding period at 950°C followed by water quenching. (a) 8C0Nb; (b) 8C5Nb; (c) 8C10Nb; (d) 8C20Nb.

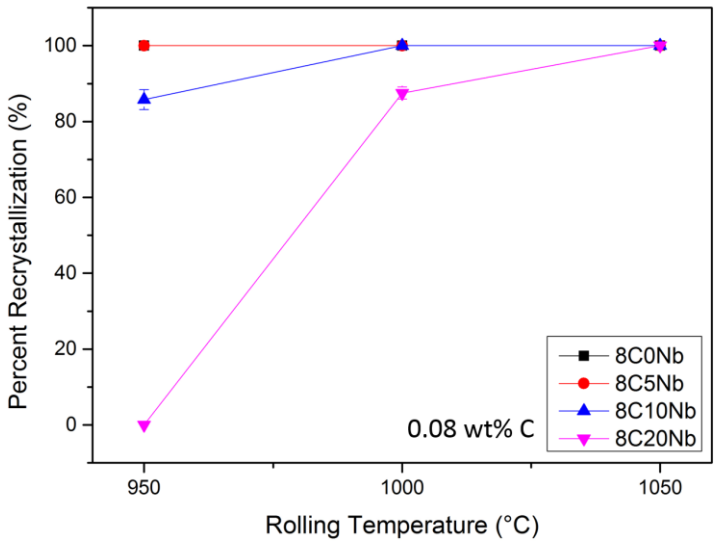

Figure 4-51 Evolution of percent recrystallisation of 8C steels after the isothermal holding period of 20s as a function of finish rolling temperatures. Error bars indicates the 95% confidence limits of the measurements. Nb contents are shown in the legend.

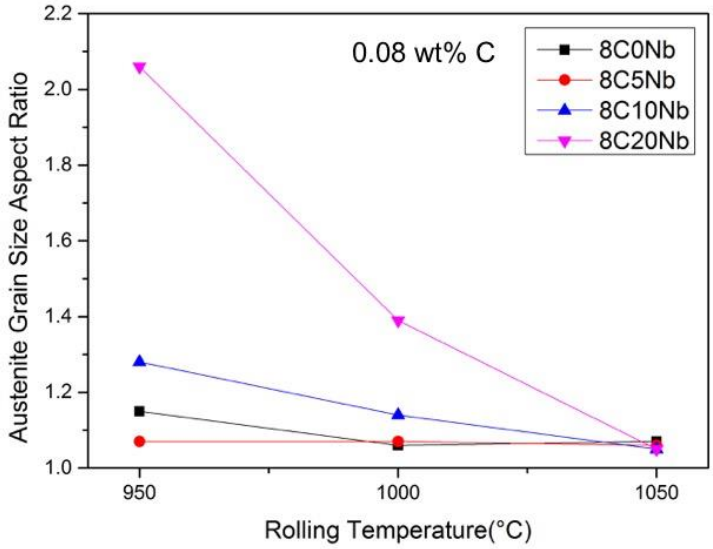

Figure 4-52 Evolution of prior-austenite grain aspect ratio of 8C steels after the isothermal holding period of 20s as a function of finish rolling temperatures. Nb contents are shown in the legend.

Table 4-10 Prior-austenite percent recrystallisation of 8C steels after the isothermal holding period of 20s at different finish rolling temperatures (%)

	8C0Nb	8C5Nb	8C10Nb	8C20Nb
1050°C	100	100	100	100
1000°C	100	100	100	87.5±1.6
950°C	100	100	85.8±2.6	0

Table 4-11 Prior-austenite grain size of 8C steels after the isothermal holding period of 20s at different finish rolling temperatures (μm)

	1050°C		1000°C		950°C	
	RD	TD	RD	TD	RD	TD
8C0Nb	95.2±3.2	88.8±3.2	75.7±4.1	71.2±3.6	56.3±3.1	48.8±2.4
8C5Nb	83.4±2.9	78.9±2.4	60.4±3.0	56.6±4.7	46.9±2.5	44.0±2.2
8C10Nb	71.8±2.8	68.2±2.6	56.5±3.1	49.7±2.6	49.6±4.6	39.9±3.2
8C20Nb	64.8±3.0	61.5±2.7	63.3±3.4	45.7±2.1	120.8±12.9	58.5±7.4

The percent recrystallisation of all 8C steels after the 20s holding period at three rolling temperatures were calculated and summarised in Table 4-10. The same data was used to plot Figure 4-51.

As it is shown in Figure 4-51, the full recrystallisation in reference steel 8C0Nb was obtained after isothermal holding at all three rolling temperatures, which was as expected due to the lack of retarding force for recrystallisation. Like the reference steel 8C0Nb, 8C5Nb also showed a fully recrystallised microstructure due to the small retarding force provided by the low Nb content (0.005wt %).

For 8C10Nb steel, complete recrystallisation was observed at the rolling temperature of 1050°C and 1000°C. At 950°C, the recrystallisation cannot be completed. A partially recrystallised microstructure with percent recrystallisation of 87.5±1.6% was obtained. Compared with complete recrystallisation of 8C5Nb at rolling temperature of 950°C, a stronger retarding force is found due to the higher Nb content.

Not surprisingly, the strongest retarding force on recrystallisation was found in 8C20Nb. Recrystallisation was completed after isothermal holding at the high rolling temperature 1050°C. When the rolling temperature was reduced to 1000°C, the percent recrystallisation was decreased to 85.8±2.6%. At the lowest rolling temperature 950°C, the recrystallisation was completely retarded. The reasons for different recrystallisation behaviour will be discussed Chapter 5.

The prior-austenite grain size for all the 8C steels were calculated and summarised in Table 4-11. According to the grain size, the grain size aspect ratios were calculated and plotted in Figure 4-52. The relationship between aspect ratio and the percent recrystallisation behaviour showed good consistency compared with results in Section 4.3 and previous works.

4.5.2 Prior-austenite microstructures of 40C steels after the isothermal holding period of 20s at different finish rolling temperatures

Figure 4-53 shows the prior-austenite microstructures of 40C steels after the holding period of 20s at the finish rolling temperature of 1050°C. It is clear that all the steels showed a fully recrystallised microstructure with equiaxed prior-austenite grains.

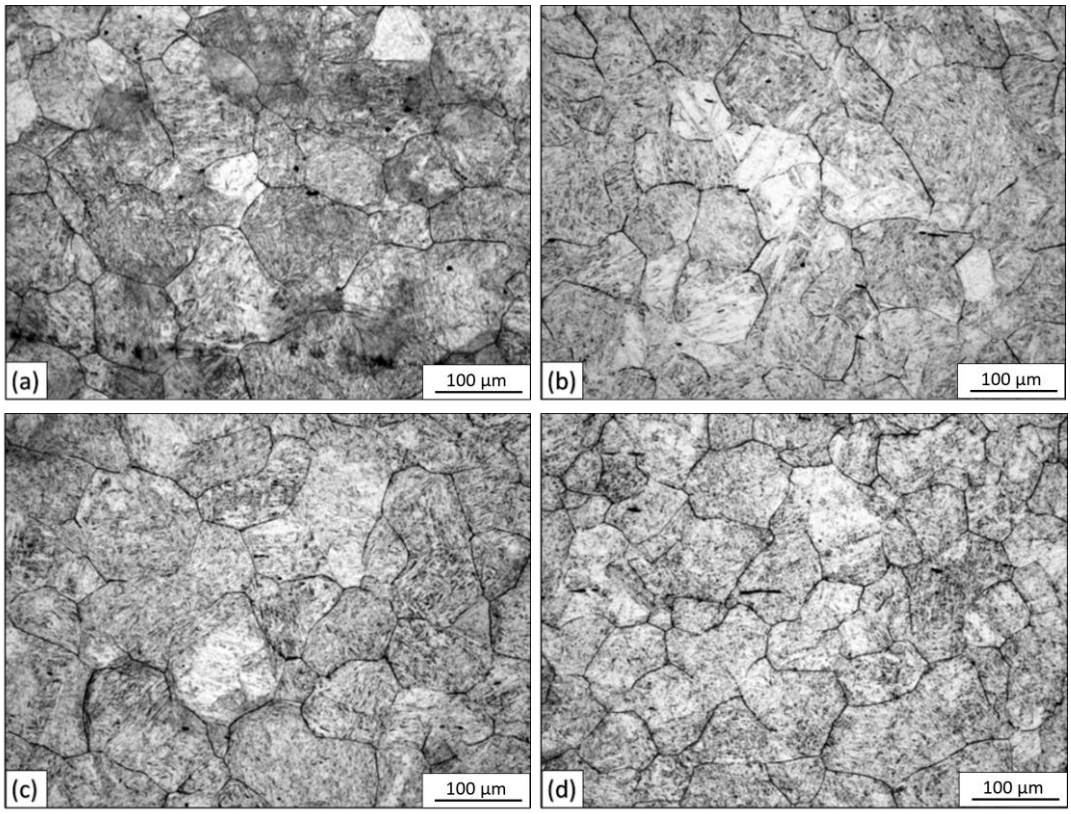

Figure 4-53 Prior-austenite microstructures of steels after 20s holding period at 1050°C followed by water quenching. (a) 40C0Nb; (b) 40C5Nb; (c) 40C10Nb; (d) 40C20Nb.

After isothermal holding at 1000°C, fully recrystallised microstructure with equiaxed prior-austenite grains was observed in 40C0Nb, 40C5Nb and 40C10Nb steels. However, for the steel 40C20Nb, a partially recrystallised microstructure was observed which indicated the recrystallisation was not completed during the 20s holding period.

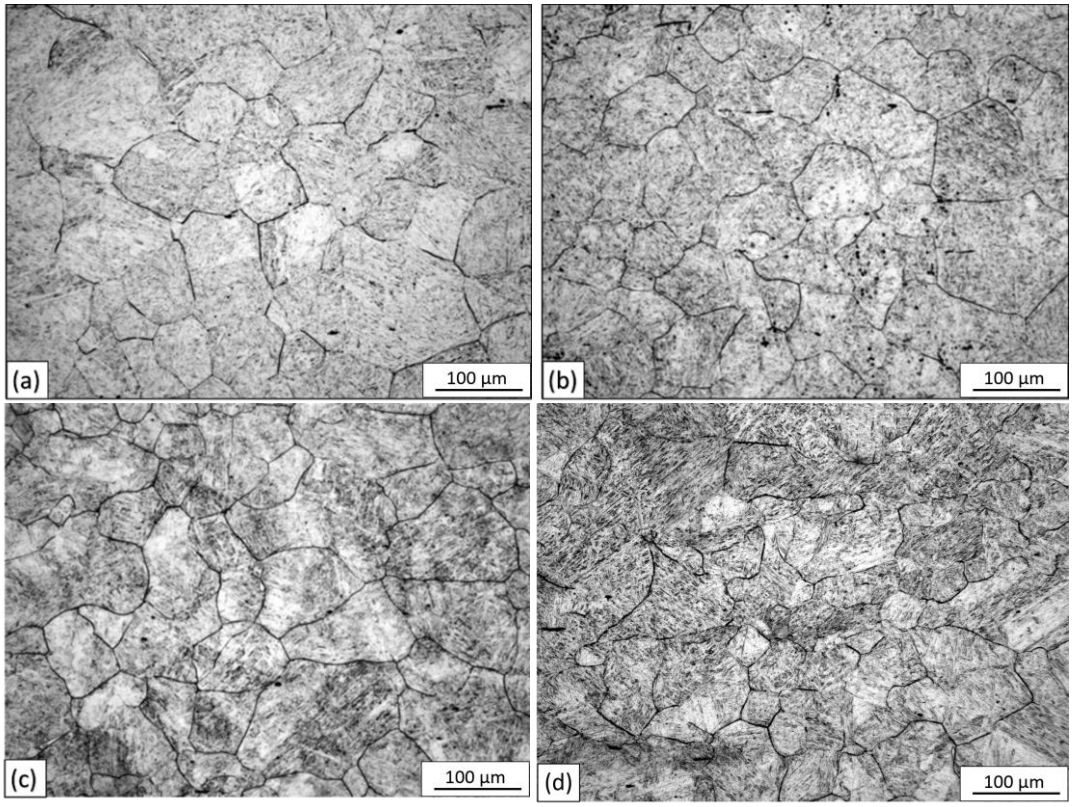

Figure 4-54 Prior-austenite microstructures of steels after 20s holding period at 1000°C followed by water quenching. (a) 40C0Nb; (b) 40C5Nb; (c) 40C10Nb; (d) 40C20Nb.

When the finish rolling and isothermal holding temperature was reduced to 950°C, only reference steel 40C0Nb and 40C5Nb steel showed a fully recrystallised microstructure. The recrystallisation in 40C10Nb and 40C20Nb steels were not finished during the 20s isothermal holding period at 950°C. From the microstructures, 40C20Nb steel showed a lower percent recrystallisation compared with the 40C10Nb steel. This indicated that the higher Nb content provided a stronger retarding force for static recrystallisation during the isothermal holding period.

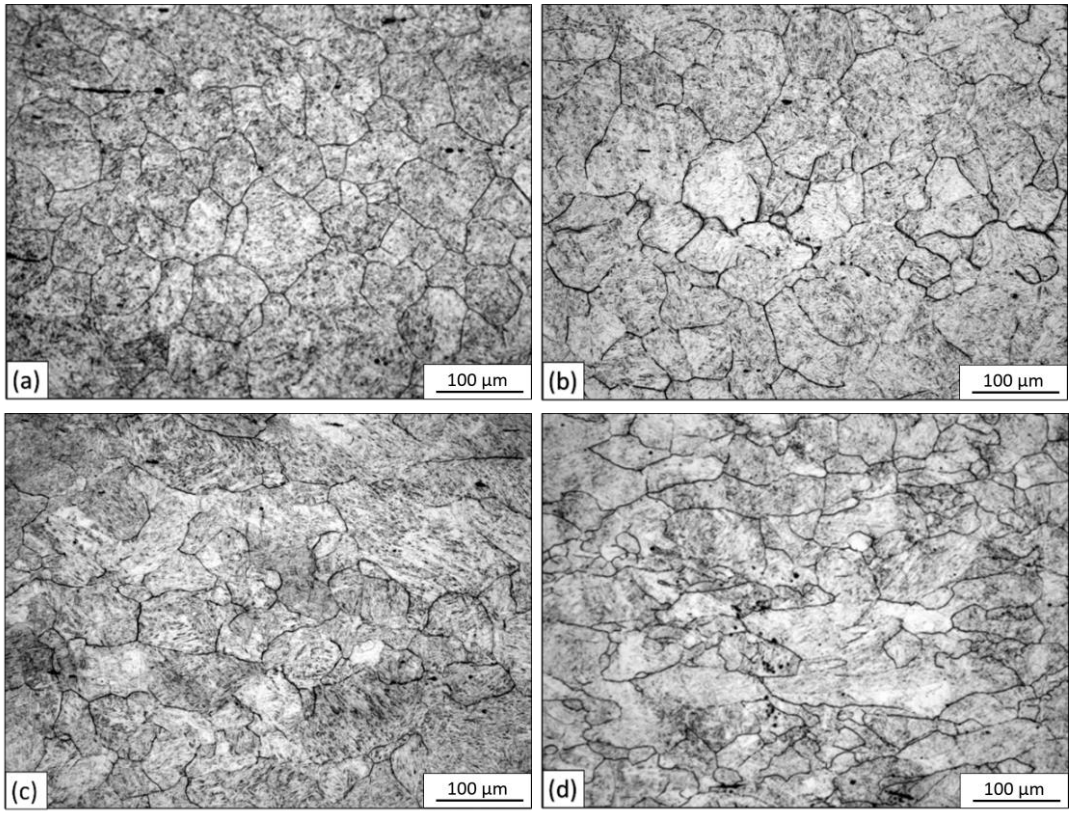

Figure 4-55 Prior-austenite microstructures of steels after 20s holding period at 950°C followed by water quenching. (a) 40C0Nb; (b) 40C5Nb; (c) 40C10Nb; (d) 40C20Nb.

The percent recrystallisation of all 40C steels after finish rolling and the isothermal holding period of 20s were calculated and plotted as a function of finish rolling temperatures and Nb contents in Figure 4-56.

For the steel 40C5Nb, full recrystallisation was reached after the 20s holding period at all three finish rolling temperatures. It showed the same recrystallisation behaviour with the reference steel 40C0Nb. The influence of 0.005wt% Nb to the recrystallisation during the holding period was rather small.

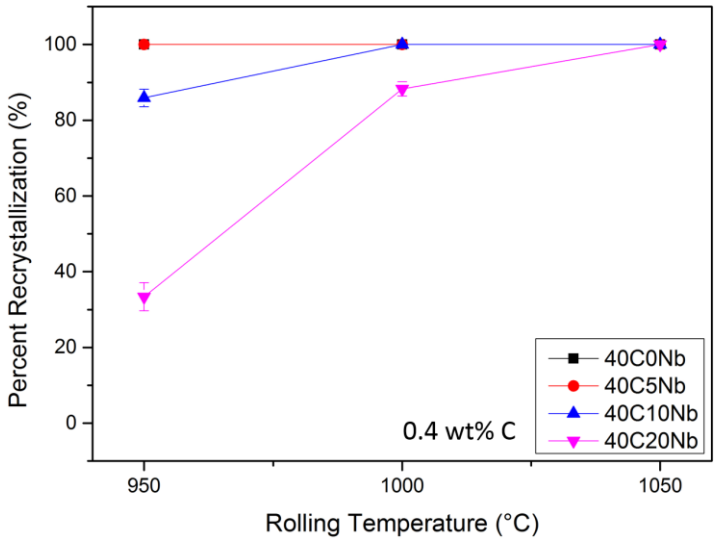

Figure 4-56 Evolution of percent recrystallisation of 40C steels after the isothermal holding period of 20s as a function of finish rolling temperatures. Error bars indicates the 95% confidence limits of the measurements. Nb contents are shown in the legend.

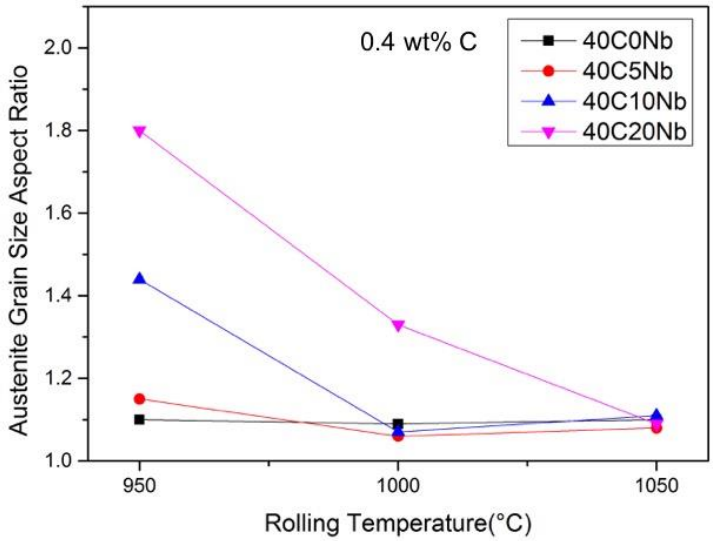

Figure 4-57 Evolution of prior-austenite grain aspect ratio of 40C after the isothermal holding period of 20s as a function of finish rolling temperatures. Nb contents are shown in the legend.

Table 4-12 Prior-austenite percent recrystallisation of 40C steels after the isothermal holding period of 20s at different finish rolling temperatures (%)

	40C0Nb	40C5Nb	40C10Nb	40C20Nb
1050°C	100	100	100	100
1000°C	100	100	100	88.3±1.9
950°C	100	100	85.9±2.3	33.4±3.7

Table 4-13 Prior-austenite grain size after the isothermal holding period of 20s at different finish rolling temperatures (μm)

	1050°C		1000°C		950°C	
	RD	TD	RD	TD	RD	TD
40C0Nb	76.1±3.7	69.0±3.0	67.9±2.8	62.1±2.7	56.4±1.9	51.3±2.0
40C5Nb	73.7±2.1	68.2±2.7	63.1±3.6	60.8±2.1	57.5±3.1	49.8±4.0
40C10Nb	72.4±3.0	65.0±2.7	60.5±2.8	56.5±2.3	68.0±7.8	47.3±5.8
40C20Nb	60.6±1.7	55.6±2.0	68.9±5.8	51.8±3.1	89.8±8.6	49.9±4.6

For 40C10Nb steel, at finish rolling temperatures of 1050°C and 1000°C, the recrystallisation was completed after 20s holding period. However, at the finish rolling temperature of 950°C, the Nb retarded the recrystallisation process and complete recrystallisation was not reached. A percent recrystallisation of 88.3±1.9% was obtained.

For the steel 40C20Nb, fully recrystallised prior-austenite microstructure was only obtained at a finish rolling temperature of 1050°C. The percent recrystallisation of 40C20Nb after the holding period was decreased from 100% at 1050°C to 84.6% at 1000°C and 33.4% at 950°C.

The prior-austenite grain sizes for all 40C steels were calculated and listed in Table 4-13. In Figure 4-57, the evolution of the prior-austenite grain aspect ratio as a function of finish rolling temperature and Nb contents is shown. The fully recrystallised microstructure has an aspect ratio of about 1.1. The aspect ratio changes with the percent recrystallisation in a reciprocal fashion. The behaviour of prior-austenite grain aspect ratio matches well with the evolution of percent recrystallisation in Figure 4-56.

4.5.3 Prior-austenite microstructures of 60C steels after the isothermal holding period of 20s at different finish rolling temperatures

The prior-austenite microstructures of all 60C steels after the isothermal holding period of 20s at the finish rolling temperature of 1050°C are shown in Figure 4-58. The equiaxed prior-austenite grains, which indicated the fully recrystallised microstructure, were revealed in all four 60C steels.

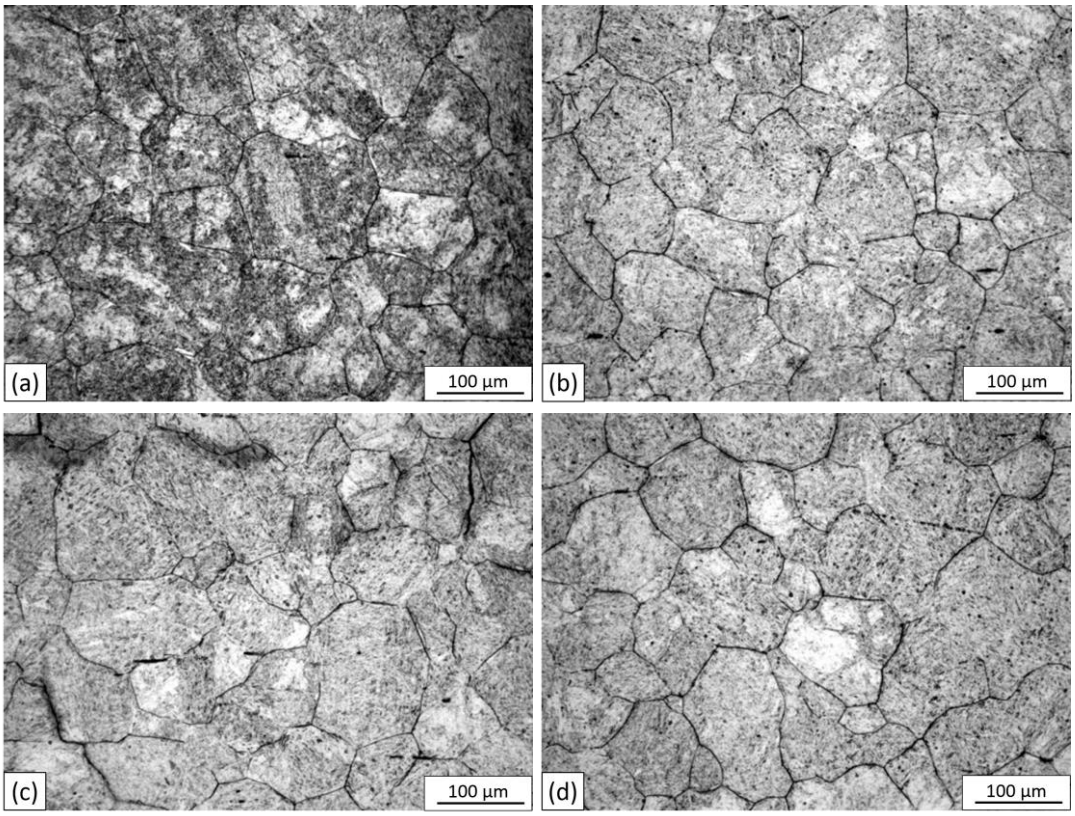

Figure 4-58 Prior-austenite microstructures of 60C steels after the 20s isothermal holding period at 1050°C followed by water quenching. (a) 60C0Nb; (b) 60C5Nb; (c) 60C10Nb; (d) 60C20Nb.

As can be seen in Figure 4-59, when the steels were finish rolled and isothermally held at 1000°C, fully recrystallised microstructure with equiaxed prior-austenite grains were obtained in the reference steel 60C0Nb and the low Nb content steels 60C5Nb and 60C10Nb. However, the recrystallisation was not finished during the

20s holding period for 60C20Nb steel. Partially recrystallised prior-austenite microstructure was revealed for the 60C20Nb steel.

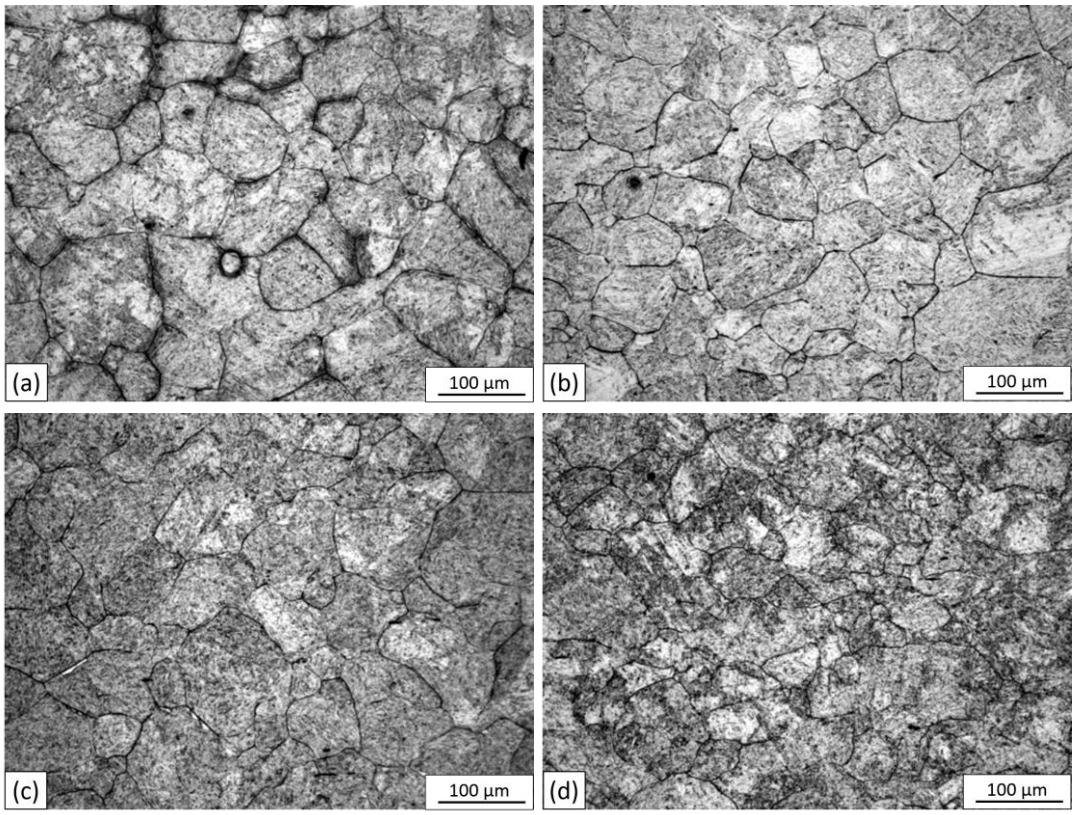

Figure 4-59 Prior-austenite microstructures of 60C steels after the 20s isothermal holding period at 1000°C followed by water quenching. (a) 60C0Nb; (b) 60C5Nb; (c) 60C10Nb; (d) 60C20Nb.

When the finish rolling and isothermal holding temperature was reduced to 950°C, the fully recrystallised microstructures were only revealed in the reference steel 60C0Nb and the low Nb steel 60C5Nb. 60C10Nb and 60C20Nb steels showed partially recrystallised microstructures. As can be seen in Figure 4-60, the percent recrystallisation of 60C10Nb steel was higher than that of 60C20Nb. Higher Nb content provided a stronger retarding force.

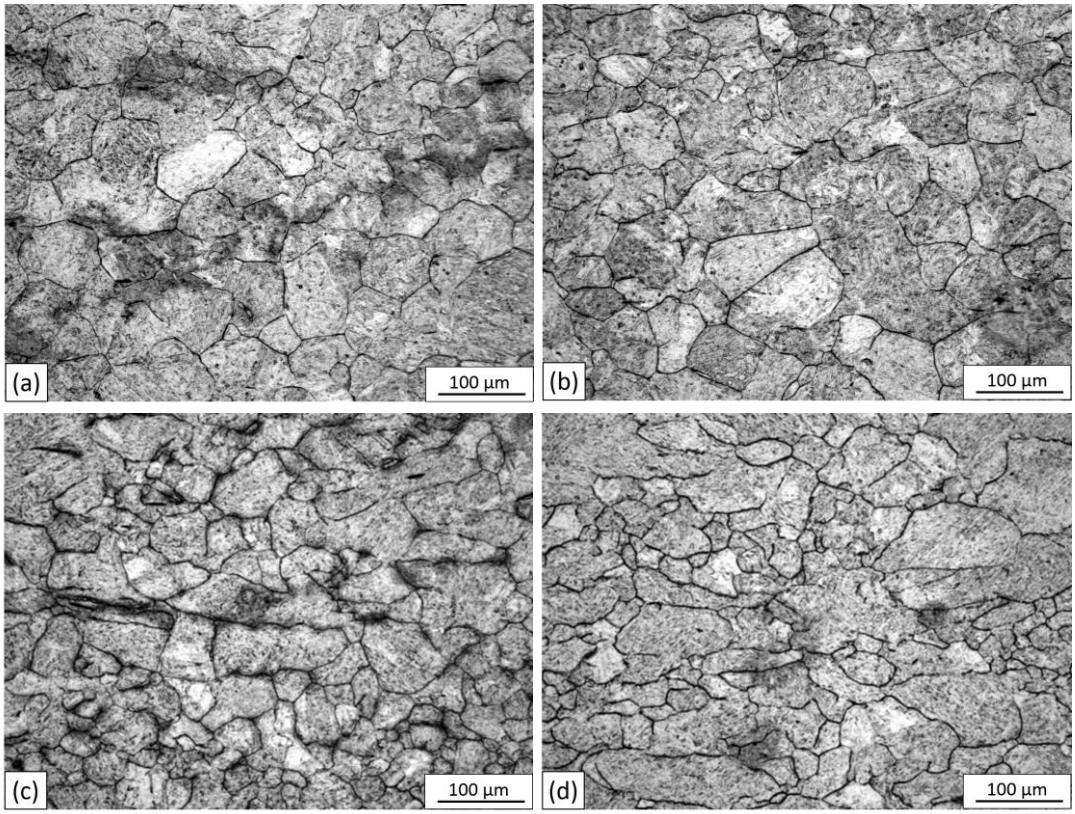

Figure 4-60 Prior-austenite microstructures of 60C steels after the 20s isothermal holding period at 950°C followed by water quenching. (a) 60C0Nb; (b) 60C5Nb; (c) 60C10Nb; (d) 60C20Nb.

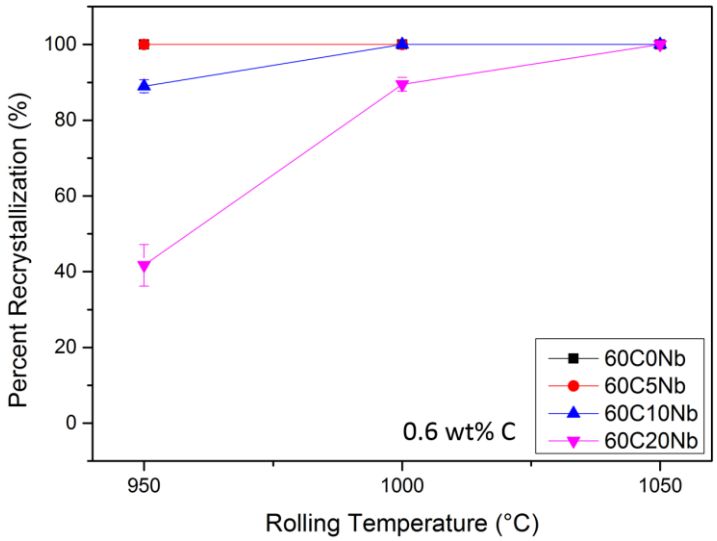

Figure 4-61 Evolution of percent recrystallisation of 60C steels after the isothermal holding period of 20s as a function of finish rolling temperatures. Error bars indicates the 95% confidence limits of the measurements. Nb contents are shown in the legend.

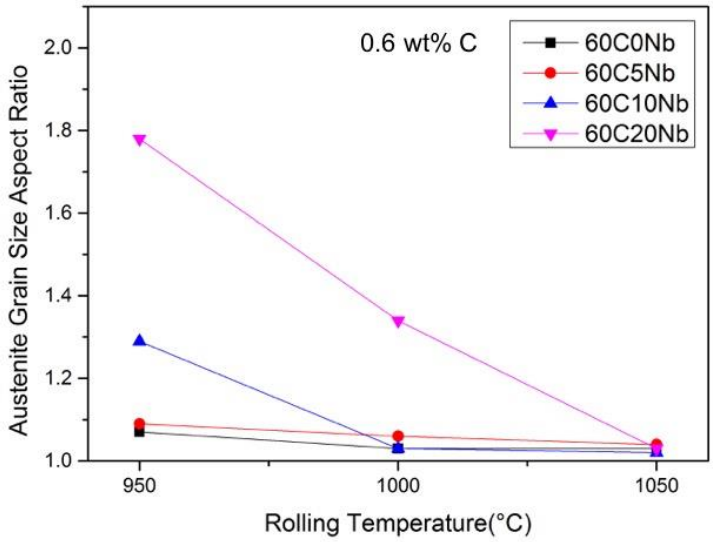

Figure 4-62 Evolution of prior-austenite grain aspect ratio of 60C steels after the isothermal holding period of 20s as a function of finish rolling temperatures. Nb contents are shown in the legend.

Table 4-14 Prior-austenite percent recrystallisation of 60C steels after the isothermal holding period of 20s at different finish rolling temperatures (%)

	60C0Nb	60C5Nb	60C10Nb	60C20Nb
1050°C	100	100	100	100
1000°C	100	100	100	89.5±1.8
950°C	100	100	89.0±1.7	41.7±5.5

Table 4-15 Prior-austenite grain size of 60C steels after the isothermal holding period of 20s at different finish rolling temperatures (μm)

	1050°C		1000°C		950°C	
	RD	TD	RD	TD	RD	TD
60C0Nb	77.3±2.3	74.9±3.1	69.2±2.3	67.4±2.5	52.9±2.4	49.3±1.5
60C5Nb	75.4±3.2	72.6±3.0	68.7±2.7	64.6±3.3	51.0±3.2	46.7±2.8
60C10Nb	74.5±2.4	72.7±2.8	65.7±3.3	63.8±2.5	57.0±5.0	44.3±4.1
60C20Nb	73.9±2.9	71.9±5.2	69.5±3.3	51.7±2.5	91.3±16.0	51.2±6.5

Figure 4-61 shows the percent recrystallisation of all 60C steels after the isothermal holding period of 20s as a function of finish rolling temperature and Nb content.

Similar to the reference steel 60C0Nb, recrystallisation was completed after the 20s holding period for 60C5Nb steel at all three finish rolling temperatures. This shows that the addition of 0.005wt% Nb did not influence the recrystallisation behaviour after the 20s holding period at the three rolling temperatures used in this study.

For the steel 60C10Nb, the recrystallisation was completed after the 20s holding period at higher finish rolling temperatures of 1050°C and 1000°C. However, at the low finish rolling temperature of 950°C, the completion of recrystallisation was not obtained. The percent recrystallisation for 60C10Nb was 89.0±1.7% after the 20s holding period at 950°C.

Fully recrystallised prior-austenite microstructure was only observed in 60C20Nb steel at the high finish rolling temperature 1050°C. The percent recrystallisation of 60C20Nb steel after the 20s holding period is 89.5±1.8% and 41.7±5.5% at finish rolling temperature of 1000°C and 950°C, respectively.

The prior-austenite grain sizes for all the 60C steels after isothermal holding were calculated and summarized in Table 4-15. The prior-austenite grain size aspect ratio was calculated and plotted in Figure 4-62. Again, consistent with the observation in 8C and 40C steels, the fully recrystallised microstructure possessed an aspect ratio of approximately 1.1. Prior-austenite grain aspect ratio increased with the decrease of the percent recrystallisation.

4.5.4 Comparison of prior-austenite microstructures after the isothermal holding period of 20s between steels with various C contents

As can be seen in Figure 4-63, a comparison of prior-austenite percent recrystallisation between all steels after the 20s isothermal holding period is shown.

The most significant difference caused by C contents in prior-austenite recrystallisation behaviour after the 20s holding period was found between the 20Nb steels being deformed and held at 950°C. Because of the relatively high Nb contents

and low rolling temperature, Nb precipitation happened during the isothermal holding. Variation in C contents influenced the Nb content in solution after homogenisation, hence further influence on the precipitation behaviour during the isothermal holding. The NbC precipitation morphology is shown in Section 4.7.

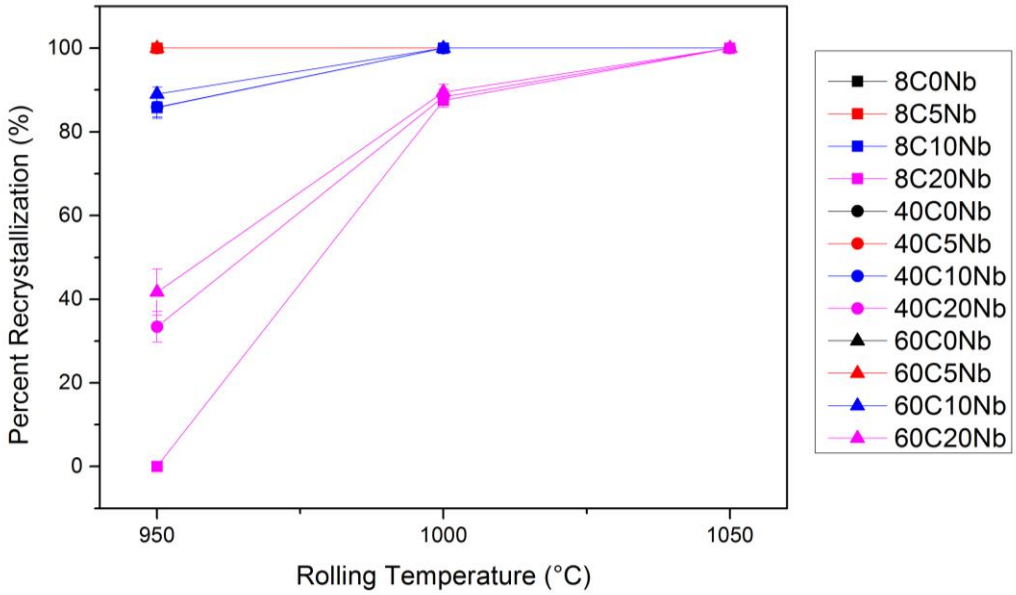

Figure 4-63 Comparison of percent recrystallisation of all steels after the 20s isothermal holding period at various finish rolling temperature. Symbols for various steels are shown in the legend.

For all the other steels, the precipitation did not happen. Solute drag effect from Nb was the main mechanism to influence recrystallisation behaviour. The variation in C contents did not seem to have any obvious influence on the percent recrystallisation after the holding period.

The detailed discussion of the influence of Nb solute drag and precipitation pinning effect on austenite recrystallisation behaviour during the isothermal holding period is presented Chapter 5.

4.6 Relationship between percent recrystallisation and prior-austenite grain size aspect ratio

As it has been shown in Section 4.4 and 4.5, the prior-austenite grain size aspect ratio was corresponding to the percent recrystallisation of prior-austenite. Therefore, the percent recrystallisation for all the samples after finish rolling and after the holding period are plotted against its corresponding prior-austenite grain size aspect ratios, as shown in Figure 4-64.

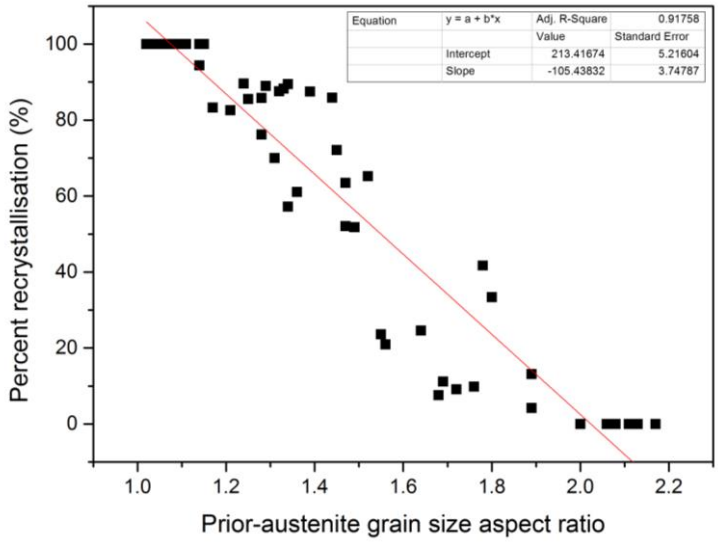

Figure 4-64 Relationship between percent recrystallisation and prior-austenite grain size aspect ratio with the strain of 0.2.

The percent recrystallisation shows a linear relationship with the prior-austenite grain size aspect ratio. When the prior-austenite were fully recrystallised, the prior-austenite microstructure consisted of equiaxed prior-austenite grains. Therefore, the prior-austenite grain size aspect ratio was around unity. With the reduction of the percent recrystallisation, the degree of pancaking increased which resulted in an increase in the prior-austenite grain size aspect ratio. When there was no recrystallisation, the aspect ratio reached the highest value which was around 2.1 for the deformation strain of 0.2. The result shows good consistency with previous studies [28,35,124,134].

It is worthy noticing that the corresponding percent recrystallisation value for an aspect ratio value is changing with the amount of deformation strain.

4.7 Precipitation behaviour

In order to explain the difference in recrystallisation behaviour of the 20Nb steels after the 20s isothermal holding period, the precipitation behaviour was studied using TEM.

Carbon extraction replicas were investigated to determine the composition, size and number density of the precipitates. Figure 4-65 (a) shows the TEM bright field image of precipitates in 8C20Nb steel. A high magnification image of a precipitate is shown in Figure 4-65 (b). Figure 4-65 (c) shows the EDS spectra from the precipitate in (b). The frequency distribution of the NbC particle sizes is shown in Figure 4-65 (d).

Corresponding to Figure 4-65, the TEM data of precipitates in 40C20Nb and 60C20Nb steels are shown in Figure 4-66 and Figure 4-67, respectively.

It was found that the precipitation distribution was highly localised in all three steels. As reviewed in Section 2.5.5.1, the preferred site for strain-induced precipitation is at the grain/subgrain boundary. The precipitation in the matrix happen much slower than the precipitation at the grain boundary. Because of the dilute Nb content, the supersaturation was very small even at the low rolling temperature 950°C. Therefore, the driving force for precipitation was small which led to a low concentration of precipitates. Due to the localised distribution of precipitates, it was believed that the precipitates observed were all in the vicinity of prior-austenite grain boundaries.

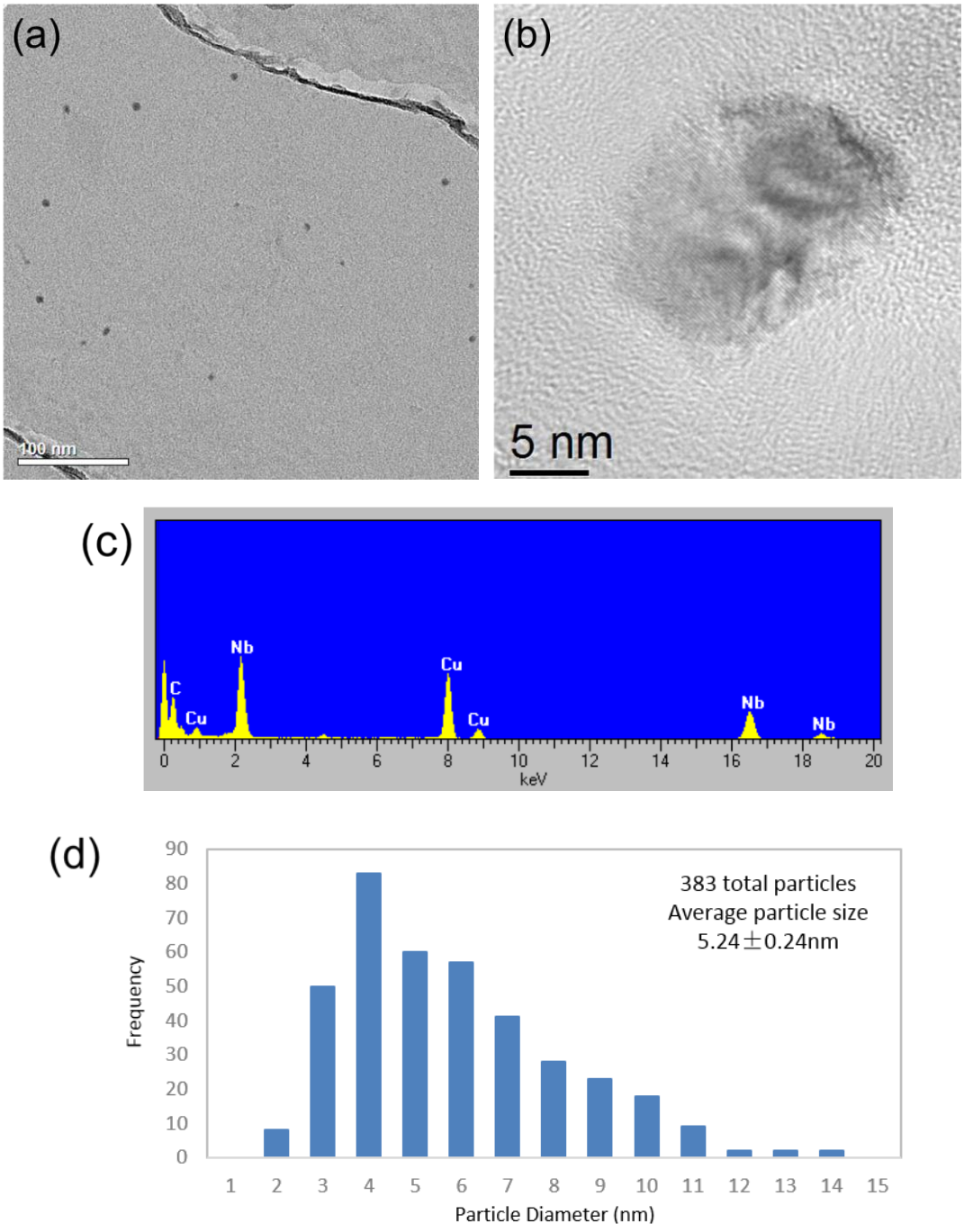

Figure 4-65 TEM bright field image of strain-induced precipitates of 8C20Nb steel quenched after the isothermal holding period of 20s at finish rolling temperature of 950°C. (a) Low magnification of precipitates. (b) High magnification of a precipitate. (c) EDS spectra from precipitate in (b). (d) Frequency distribution of the NbC particle size.

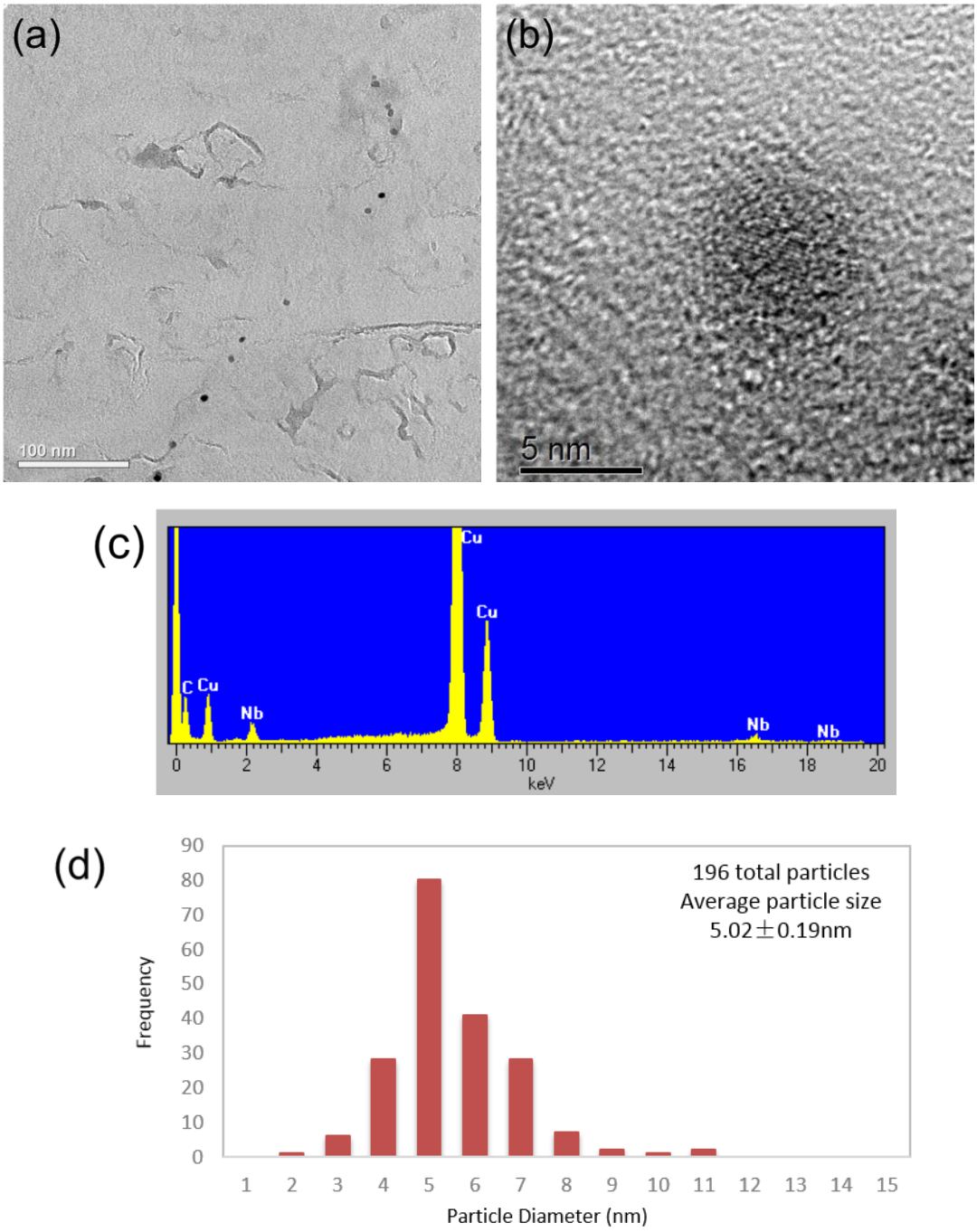

Figure 4-66 TEM bright field image of strain-induced precipitates of 40C20Nb steel quenched after the isothermal holding period of 20s at finish rolling temperature of 950°C. (a) Low magnification of precipitates. (b) High magnification of a precipitate. (c) EDS spectra from precipitate in (b). (d) Frequency distribution of the NbC particle size.

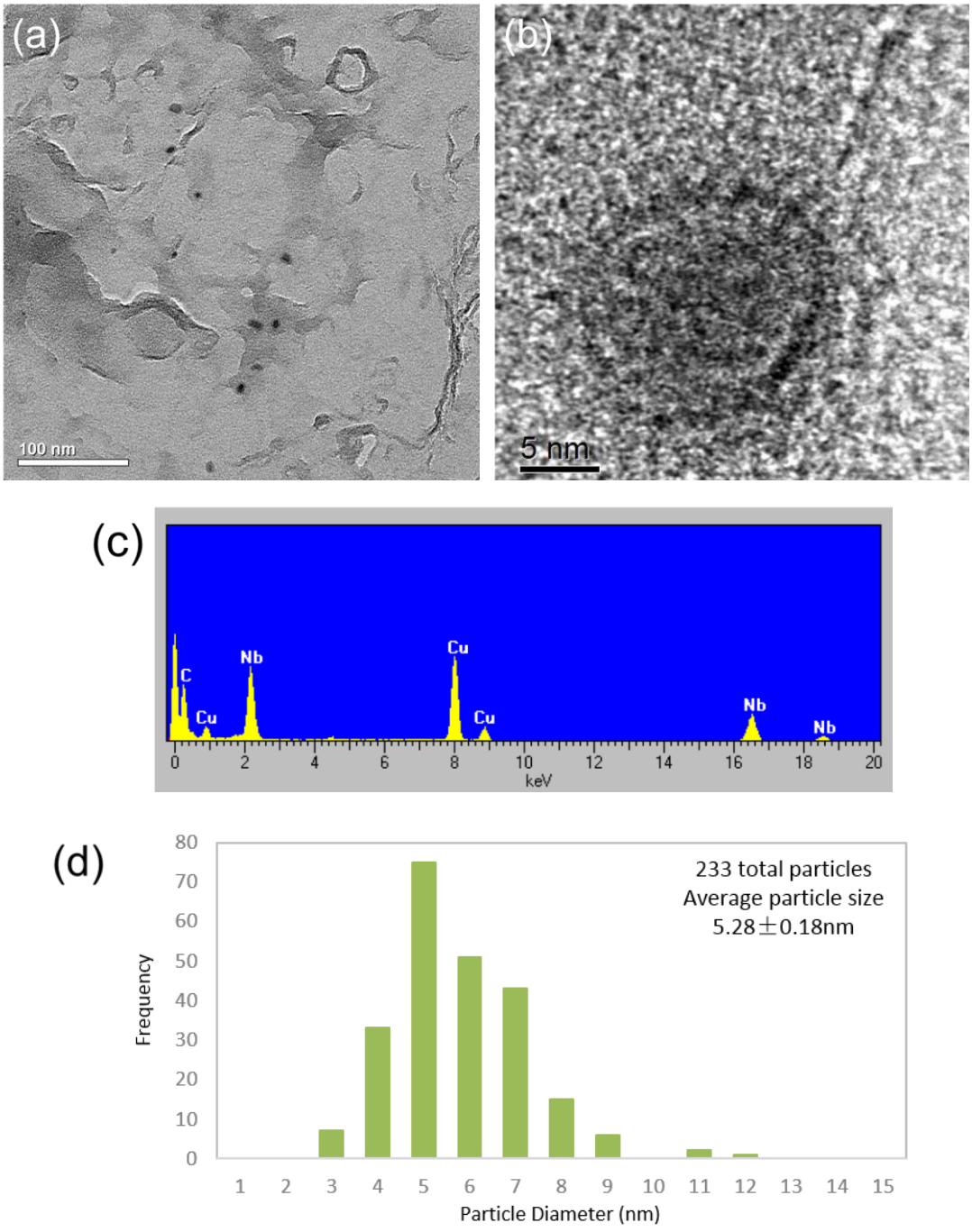

Figure 4-67 TEM bright field image of strain-induced precipitates of 60C20Nb steel quenched after the isothermal holding period of 20s at finish rolling temperature of 950°C. (a) Low magnification of precipitates. (b) High magnification of a precipitate. (c) EDS spectra from precipitate in (b). (d) Frequency distribution of the NbC particle size.

The number density of the three 20Nb steels were calculated and shown in Figure 4-69. It can be seen clearly that with the increase of carbon contents, the precipitate number density reduced. This observation was attributed to the influence of C on the dissolution behaviour of Nb during homogenisation. Details are discussed further in Section 5.4.3.

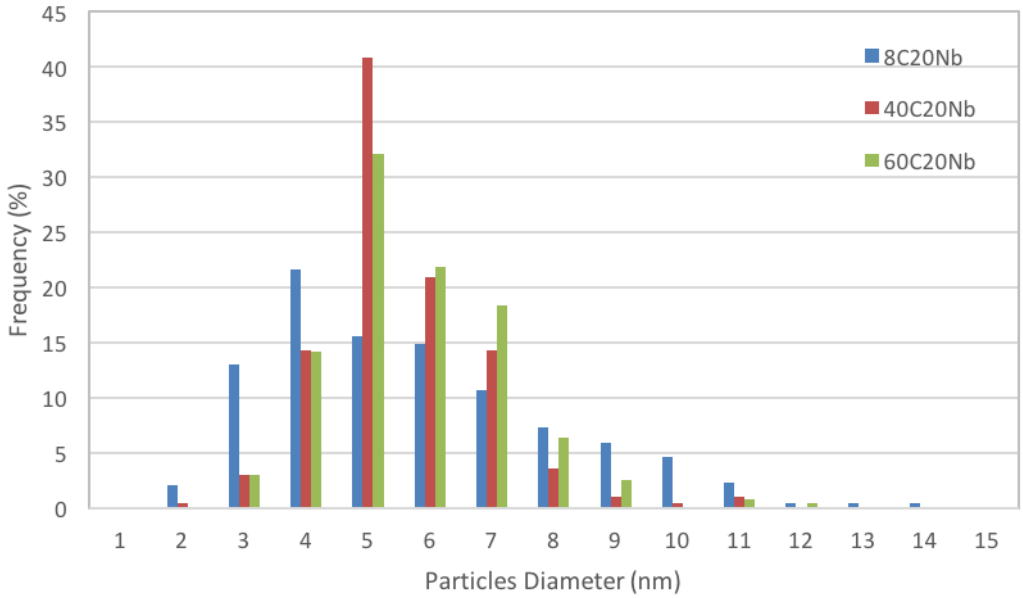

Figure 4-68 Frequency distribution of the NbC particle size in three 20Nb steels quenched after the isothermal holding period of 20s at finish rolling temperature of 950°C.

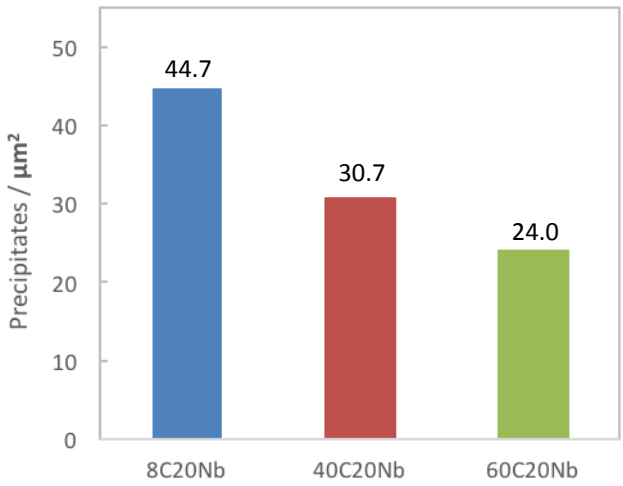

Figure 4-69 Number densities of precipitates from 20Nb steels quenched after the isothermal holding period of 20s at finish rolling temperature of 950°C.

4.8 Austenite grain growth behaviour during the 20s isothermal holding period at the finish rolling temperature

During the 20s holding period, some steels finished recrystallisation due to the large driving force and small retarding force for recrystallisation, see Figure 4-63. After the completion of recrystallisation, the austenite grains in these steels continue to grow before they were water quenched at the end of the holding period. In order to investigate the influence of Nb on the austenite grain growth behaviour, the prior-austenite grain sizes for all recrystallised steels after isothermal holding were compared as follows.

4.8.1 Austenite grain growth behaviour of 8C steels

The evolution of recrystallised prior-austenite grain sizes of 8C steels as a function of Nb contents after the 20s holding period at different finish rolling temperatures is shown in Figure 4-70.

The Nb addition showed clear refinement on prior-austenite grain size on all three deformation temperatures. At 1050°C, the prior-austenite grain size of reference steel 8C0Nb showed a substantial growth from 61.9±4.3μm (after finish rolling) to 95.2±3.2μm (after isothermal holding) during the 20s holding period. The prior-austenite grain size was continuously refined with the increase of Nb contents. The prior-austenite grain size for 8C5Nb, 8C10Nb and 8C20Nb at the end of the 20s isothermal holding period were 83.4±2.9μm, 71.8±2.8μm and 64.8±3.0μm, respectively.

Consistent with the observation at 1050°C, the Nb additions showed a retarding force on austenite grain growth during the 20s holding period at 1000°C. The prior-austenite grain sizes reduced from 75.7±4.1μm (8C0Nb) to 60.4±3.0μm (8C5Nb) and 56.5±3.1μm (8C10Nb). 8C20Nb did not complete the recrystallisation.

At 950°C, the prior-austenite grain size was reduced from 56.3±3.1μm to 46.9±2.5μm with 0.005wt% Nb addition.

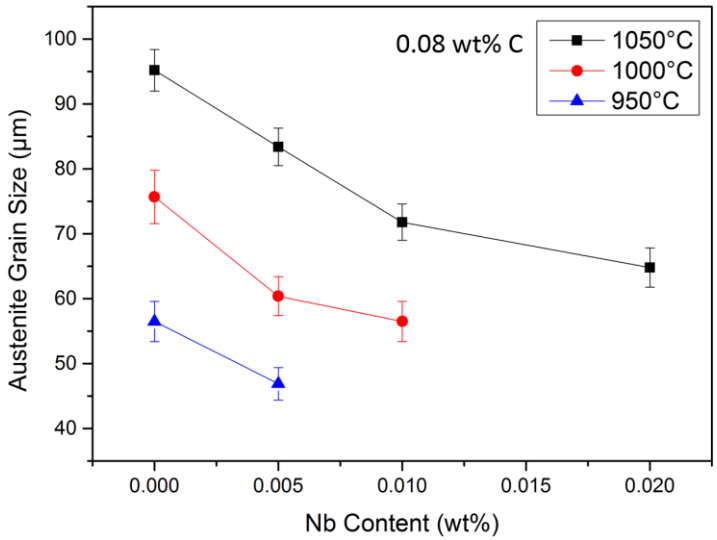

Figure 4-70 Evolution of recrystallised prior-austenite grain sizes of 8C steels after the isothermal holding period of 20s as a function of Nb contents. Finish rolling temperatures are shown in the legend.

4.8.2 Austenite grain growth behaviour of 40C steels

The grain size of the recrystallised prior-austenite grains of 40C steels after the 20s holding period at all three finish rolling temperatures were plotted in Figure 4-71.

The grain size of 40C5Nb and 40C10Nb steels were 73.7±2.1μm and 72.4±3.0μm, respectively. Both grain sizes showed no difference with the reference steel 40C0Nb whose grain size was 76.1±3.7μm. This indicates that Nb content lower than 0.01wt% did not have a noticeable influence on the austenite grain growth at 1050°C. However, for the 40C20Nb steel, a clear refinement in the prior-austenite grain size was observed. It can be seen from Figure 4-71 and Table 4-3 that a decrease of prior-austenite grain size from 76.1±3.7μm (40C0Nb) to 60.6±1.7μm (40C20Nb) was obtained. It seems that a critical value of Nb content need to be reached to slow the austenite grain growth. For 40C steels used in this study, the critical Nb content to retard austenite grain growth was between 0.01wt% to 0.02wt% at the isothermal holding temperature of 1050°C.

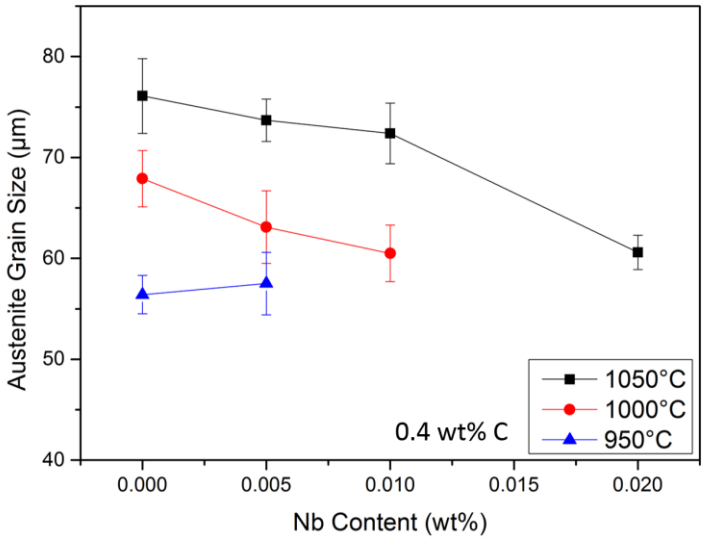

Figure 4-71 Evolution of recrystallised prior-austenite grain sizes of 40C steels after the isothermal holding period of 20s as a function of Nb contents. Finish rolling temperatures are shown in the legend.

For the finish rolling temperature of 1000°C, recrystallisation was not finished for 40C20Nb steel. Similar to what happened when the finish rolling temperature was 1050°C, the 0.005wt% Nb did not show any influence on the austenite grain growth behaviour. The prior-austenite grain size was 63.1±3.6μm for 40C5Nb steel. It was nearly the same with 67.9±2.8μm for the reference steel 40C0Nb. 40C10Nb showed a prior-austenite grain size of 60.5±2.8μm. When compared with the grain size of the reference steel only a small refinement was observed, the refinement in prior-austenite grain size was not significant taking into account of the 95% confidence limits.

When the finish rolling and isothermal holding temperature was reduced to 950°C, only 40C5Nb and the reference steel 40C0Nb completed recrystallisation. Their prior-austenite grain sizes were 56.4±1.9μm and 57.5±3.1μm, respectively. No austenite grain size refinement was found with 0.005 wt% Nb at 950°C.

4.8.3 Austenite grain growth behaviour of 60C steels

Figure 4-72 shows the prior-austenite grain size of all the fully recrystallised 60C steels after the isothermal holding period of 20s.

As presented in Section 4.4 all the 60C steels were fully recrystallised after the isothermal holding period of 20s at 1050°C. The prior-austenite grain sizes are 77.3±2.3μm, 75.4±3.2μm, 74.5±2.4μm and 73.90±2.9μm for 60C0Nb, 60C5Nb, 60C10Nb and 60C20Nb steels, respectively. No measurable difference in prior-austenite grain size was obtained with various Nb additions.

Recrystallisation was not completed for 60C20Nb steel during the isothermal holding period of 20s at the finish rolling temperature of 1000°C. The prior-austenite grain sizes were 69.2±2.3μm, 68.7±2.7μm and 65.7±3.3μm for 60C0Nb, 60C5Nb and 60C10Nb, respectively. Similar to the observation at 1050°C, the Nb addition did not show any noticeable influence on the austenite grain growth behaviour during the isothermal holding period.

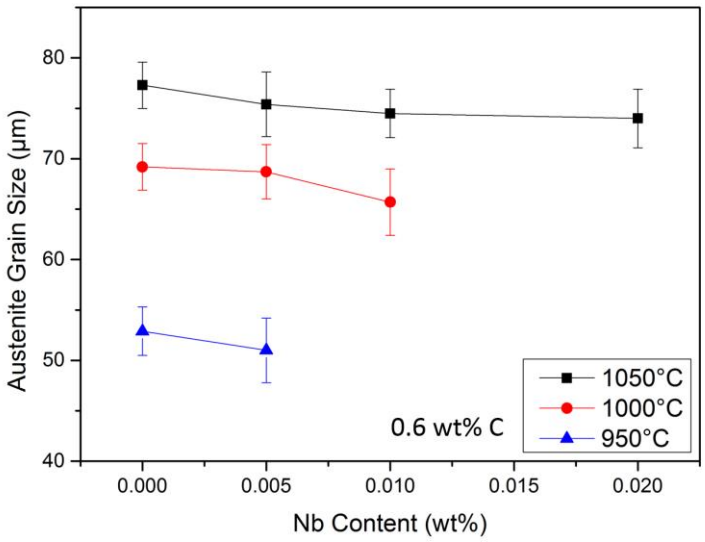

Figure 4-72 Evolution of recrystallised prior-austenite grain size of 60C steels after the isothermal holding period of 20s as a function of Nb contents. Finish rolling temperatures are shown in the legend.

Recrystallisation only completed in 60C0Nb and 60C5Nb steels when the steels were finish rolled and isothermally held at 950°C. Their prior-austenite grain sizes were 52.9±2.4μm and 51.0±3.2μm, respectively. Again, no refinement of prior-austenite grain size was observed.

Chapter 5 Discussion

In this Chapter, the experimental results are discussed and compared with work in the literature.

The choice of solubility product is briefly discussed in Section 5.1. In Section 5.2 and 5.3, the influence of Nb and C contents on rough rolling and finish rolling behaviour is shown. During 20s isothermal holding period after finish rolling, recrystallisation behaviour is interpreted in association with Nb precipitation behaviour in Section 5.4. The influence of Nb on the austenite grain growth behaviour during the 20s holding period is illustrated in Section 5.5. The influence from the strain accumulation on the rolling load to the rolling mills is discussed in Section 5.6. Finally, the possible industrial application is discussed in Section 5.7.

5.1 Solubility product

As reviewed in Section 2.3.2, the solubility products in the literature show considerable differences due to the inevitable assumptions or limitations for each of the techniques used to obtain the solubility product. Therefore, choosing a solubility product which best describes the solubility of Nb is important to interpret the results, especially in this study where the C content changes dramatically.

Two of the solubility products were chosen and compared. The first one was the widely-used equation proposed by Irvine [86], and the second one was the equation proposed by Palmiere [176]. In his work, the data is measured by a more advanced atom probe ion microscope (APFIM) and the solubility product is reported to be perhaps the most accurate [60]. The equations are given as following:

Irvine [86]: $$Log[Nb]\left[C+\frac{12}{14}N\right]=2.26-\frac{6770}{T} \quad (5.1)$$

Palmiere[176]: $$Log[Nb]\left[C+\frac{12}{14}N\right]=2.06-\frac{6700}{T} \quad (5.2)$$

where *[Nb]*,*[C]* and *[N]* is the element in wt% and *T* is the absolute temperature.

The Nb dissolution limited at the homogenisation temperature (1250°C) was calculated using both equations and summarized in Table 5-1. As it can be seen for the 8C steels, the calculated solubility limitations from both equations are higher than the highest Nb content in this study (0.02 wt%). And for 60C steels, the Nb content in the 60C20Nb steel is beyond the calculated solubility limits. Undissolved Nb particles are expected after homogenisation and are experimentally confirmed in Figure 4-6.

Table 5-1 Nb dissolution limitation at the homogenisation temperature of 1250°C

	Max Nb (wt%)	Irvine's equation (wt%)	Nb dissolution percentage (%)	Palmiere's equation (wt%)	Nb dissolution percentage (%)
8C	0.020	0.076	100%	0.057	100%
40C	0.017	0.017	100%	0.012	71%
60C	0.018	0.011	61%	0.008	44%

For 40C steels, the calculated solubility limits from the two equations showed considerable difference which was used to validate the equations. The chemical composition of the steels used is shown in Table 3-1. The actual Nb content in 40C20Nb steel is 0.017 wt%. Irvine's equation suggests at 1250°C, 0.017 wt% Nb (100%) can be dissolved in solution which is contrary to the experimental observation. In Figure 4-5, the existence of the substantial undissolved Nb particles is clearly shown. In contrast, Palmiere's equation predicted that only 0.012wt% Nb (71%) can be dissolved, which was consistent with the experimental observations.

Therefore, in this study, Palmiere's solubility product was used. The solubility limit was calculated and illustrated in Figure 5-1. The supersaturation ratios of Nb at various deformation temperatures were calculated accordingly in later sections.

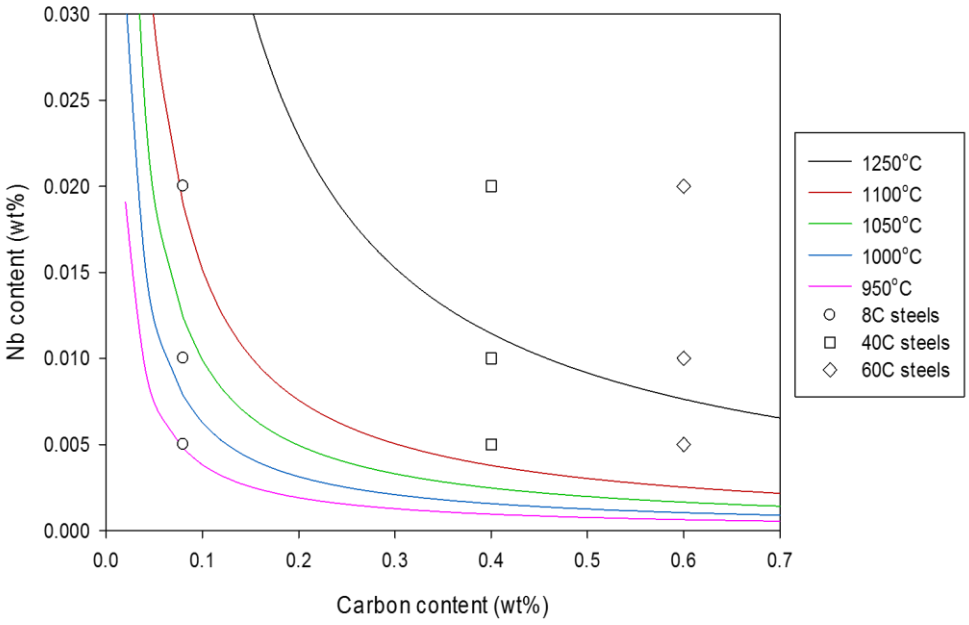

Figure 5-1 Solubility limits of Nb at homogenisation and deformation temperatures. Points showing the Nb contents of the steels in this study.

It is important to highlight that there is no unique solubility equation which could calculate the dissolved Nb content in austenite for different steel compositions. Even though Palmiere's equation is considered to be the most accurate solubility product, it has its own limitations.

As it can be seen from Figure 5-1, for the 60C steels, the Nb solubility limit is 0.008 wt%, and as such 60C10Nb and 60C20Nb should have identical Nb in solution which is 0.008 wt%. However, the experimental results showed considerable difference between 60C10Nb and 60C20Nb steels. It is not hard to understand that to predict Nb content in solution in the magnitude of 10ppm could be a challenge. The Nb in solution in 60C20Nb steel after homogenisation might be higher than the calculated value. Nevertheless, a margin of error is inevitable in any equation obtained from experimental observation and the solubility product equation by Palmiere serves well to quantitatively interpret the results observed in this study.

5.2 Influence of Nb and C on rough rolling behaviour

5.2.1 Flow curves and microstructure analyses

The flow curves for rough rolling were part of the flow curves shown in Section 4.2. The flow curves of rough rolling for 8C steels shown in Figure 4-7 were taken as an example. For the Nb microalloyed steels, the flow curves reached a plateau at the end of rough rolling. This indicated strain hardening was balanced by the dynamic softening. The plain carbon steel 8C0Nb showed substantial dynamic softening, a peak stress around the strain of 0.2 was observed. As it has been discussed in Section 2.1.2.2, even though the peak stress is a clear indication of dynamic recrystallisation, the actual onset of dynamic recrystallisation happens before the occurrence of peak stress [177,178].

A method to determine the onset of dynamic recrystallisation based on the irreversible thermodynamics process was proposed by Poliak and Jonas [179]. In their method, due to an additional degree of restoration, the work hardening rate (θ=$\partial\sigma/\partial\varepsilon$) is decreased. Therefore, the deflection point in the work hardening rate vs stress curve (θ-σ curve) or a stationary point of the $(-\partial\theta/\partial\sigma)$ – σ curve is considered to be the beginning of dynamic recrystallisation.

The application of this method requires numerical differentiation of the original flow curves. The inevitable noise from the original load data recorded by the testing machine is amplified by the differentiation calculation and leads to substantial noise for the θ data. In order to eliminate the influence of the noise, a method proposed by Najafizadeh and Jonas [180] was used. They reported that the θ-σ curve can be interpreted by a third order polynomial fit of the original data. The equation is given by:

$$\theta = a\sigma^3 + b\sigma^2 + c\sigma + d \tag{5.3}$$

where θ=$\partial\sigma/\partial\varepsilon$, a, b, c and d are constants dependent on deformation condition and materials composition.

$\theta = -0.0304\sigma^3 + 5.5063\sigma^2 - 343.18\sigma + 7523.1$, $R^2 = 0.8218$

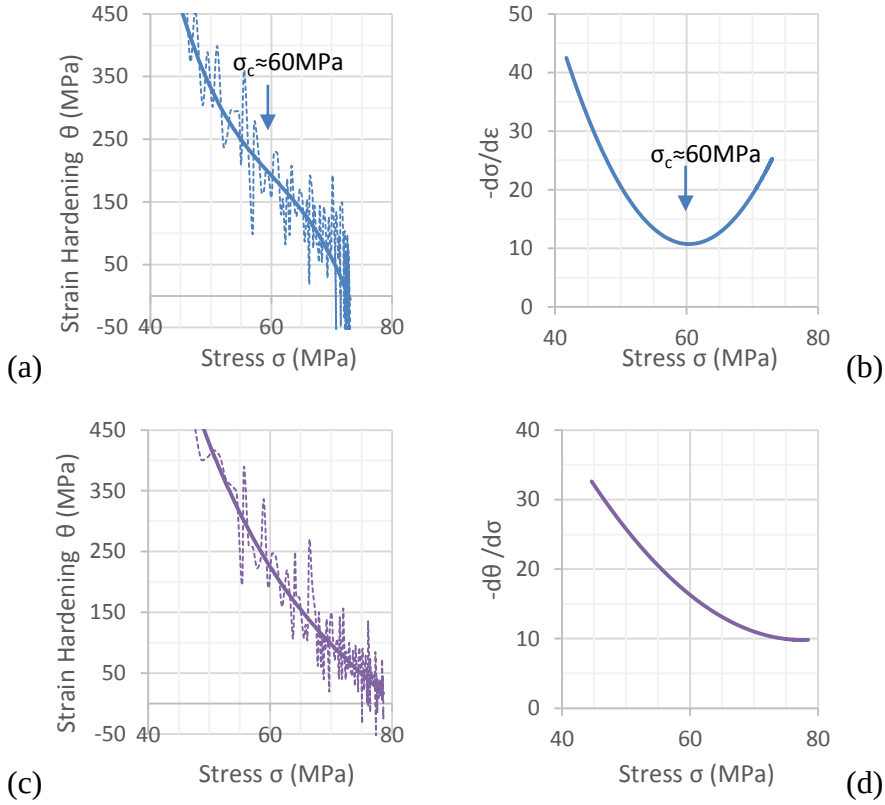

$\theta = -0.007\sigma^3 + 1.6288\sigma^2 - 136.15\sigma + 4032.8$, $R^2 = 0.8897$

Figure 5-2 Work hardening rate with respect to flow stress during rough rolling (a) 8C0Nb; (c) 8C20Nb; The critical stress for dynamic recrystallisation is indicated by the stationary point on the derivative curve of work hardening rate plotted against flow stress (b) 8C0Nb; (d) 8C20Nb

The experimental θ-σ curve data of 8C0Nb and 8C20Nb during rough rolling, and the best fit curve including the corresponding third order polynomial equation is shown in Figure 5-2 (a) and (c) as an example. The critical stress for dynamic recrystallisation was determined by the double-differentiation method, i.e. the stationary point on the derivative curve of work hardening rate plotted against flow stress, see Figure 5-2 (b) and (d). The θ-σ curve data and critical stress for dynamic recrystallisation for all the steels during rough rolling are shown in Appendix III.

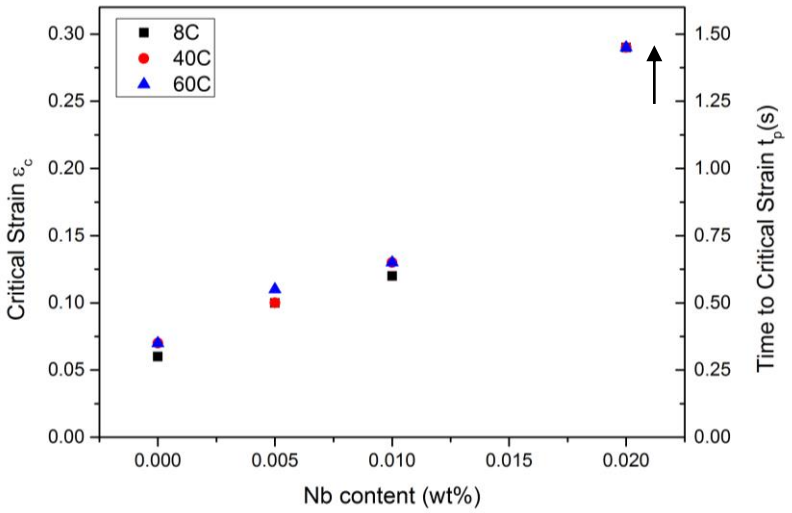

Figure 5-3 Critical strain (ε_c) and time to critical strain (t_p) for dynamic recrystallisation for various steels during rough rolling.

Using the critical stress, the critical strain of dynamic recrystallisation can be determined correspondingly on the stress-strain curves. The evolution of critical strain of dynamic recrystallisation with Nb and C content is shown in Figure 5-3. The increase of Nb content continuously increased the critical strain of dynamic recrystallisation. The critical strains for the 20Nb steels were larger than the strain for rough rolling (0.3) as the stationary point of the derivative curve was not shown (Figure 5-2 (d)).

The prior-austenite microstructural observation corresponds well with the impact Nb exerts on the critical strain of dynamic recrystallisation. The percent recrystallisation decreases with the increase of Nb content in all three steels of varying carbon content at the end of rough rolling, see Figure 4-26. Increasing the Nb content leads to an increase of the critical strain to initiate dynamic recrystallisation, therefore a longer time was required to start dynamic recrystallisation in a constant strain rate deformation. The critical times for dynamic recrystallisation were about 0.3s, 0.5s, 0.6s and >1.5s for 0Nb, 5Nb, 10Nb and 20Nb steels, respectively (Figure 5-3). The early start of the recrystallisation resulted in a greater fraction of recrystallisation. However, the microstructures of the 20Nb steels at the end of rough rolling showed inconsistent results with the critical strain data. The microstructures of the 20Nb steels showed clear evidence of recrystallisation (see Figure 4-20(d), Figure 4-22(d),

and Figure 4-24(d)). This inconsistent result can be attributed to two reasons. First, at the end of rough rolling, the decreasing rate of $-d\sigma/d\varepsilon - \sigma$ dramatically reduced to near zero which suggested the critical strain was similar to the rough rolling strain of around 0.3. Second, there is a delay between the end of deformation and the start of quenching which is less than 0.5s. During this time, recrystallisation may have happened.

5.2.2 Influence of Nb on dynamic recrystallisation behaviour

At this stage, the Nb in austenite exists in two forms; which consisted either of Nb in solid solution or any Nb present as undissolved particles. The influence from both needs to be considered. A number of studies [89,181,182] have reported that the undissolved particles have no influence on recovery and recrystallisation due to their large size, low quantity and wide inter-particle spacing. Therefore, it is believed that there was no influence from the large undissolved NbC particles to the recrystallisation and grain growth behaviour of austenite throughout this study.

Numerous works [94,183–188] have revealed the effect of solute Nb on the dynamic recrystallisation behaviour of austenite. A similar effect was observed, even though larger in magnitude compared with the current study due to the larger Nb contents used in the previous studies. For example, Zhang *et al* [184] observed the addition of 0.03 wt% Nb into a 0.2 wt% C plain carbon steel, raise both ε_c and ε_p values at various deformation temperatures and strain rates. Ouchi *et al* [189] studied the dynamic recrystallisation behaviour with plain carbon steel and three Nb microalloyed steels with Nb content from 0.03 – 0.12 wt% and reported the critical strain ε_c for dynamic recrystallisation increases with the increase of Nb contents.

The ε_c and ε_p values of Nb microalloyed steels are constantly higher than that of the plain carbon steels. In these studies, the influence of Nb is explained quantitatively through their influence on the activation energy of deformation. A summary of the activation energy values is shown in Table 5-2.

Table 5-2 The influence of Nb on deformation activation energy from literature.

Steel composition (wt%)	Q_{def} value	Reference
0.04C, 0.22Mn	265	Poliak *et al* [183]
0.04C, 0.22Mn, 0.03Nb	319	
0.085C, 0.95Mn	230	Cho *et al* [94]
0.085C, 0.95Mn,0.045Nb	314	
0.2C, 1.2Mn	359	Zhang *et al* [184]
0.2C, 1.2Mn, 0.03Nb	419	
0.11C, 1.23Mn, 0.041Nb	287	Medina *et al* [185]
0.11C, 1.32Mn, 0.093Nb	294	
0.06C, 1.85Mn, 0.08Nb	365	Niu *et al* [186]
0.05C, 1.75Mn, 0.095Nb	395	
0.36C, 1.42Mn	278	Wei *et al* [187]
0.35C, 1.41Mn, 0.044Nb	347	

Medina *et al* [185] performed multiple regression calculations on the activation energy of a number of steels and proposed a regression equation of the activation energy as a function of the chemical compositions:

$$\begin{aligned} Q_{def}(J \cdot mol^{-1}) = {} & 267000 - 2535.52(C\%) + 1010(Mn\%) + \\ & 33620.76(Si\%) + 35651.28(Mo) + \\ & 93680.52(Ti\%)^{0.5919} + 31673.46(V\%) + \\ & 70729.85(Nb\%)^{0.5649} \end{aligned} \tag{5.4}$$

The trend of Nb increasing the activation energy is clear.

Therefore, in this study, the increase of the critical strain for dynamic recrystallisation is attributed to the solute drag effect from the solute Nb. The dislocations have high energy and they are the preferred sites for the solute atoms. In the case of the Nb microalloyed steels, solute Nb is enriched at the dislocations, which leads to a decrease in both interfacial energy and dislocation mobility. This effect leads to a delay on the annihilation and rearrangement of dislocations by which the nucleation of recrystallisation grains are delayed. As a result, a higher energy is needed to induce the recrystallisation process [189].

5.2.3 Influence of C on dynamic recrystallisation behaviour

The C content has a complicated influence on the hot deformation behaviour of steels, and there is disagreement in the literature about its influence.

Some studies [185,190,191] have reported a decreasing activation energy with the increase of C content. Mead *et al* [192] reported that this is due to the high diffusivity of iron atoms caused by the increase of C content. As an interstitial solute atom, C expands the austenite lattice and the diffusivity of iron and carbon atoms both increase. However, some other researchers [193,194] suggested otherwise. A possible explanation for this is that C as interstitial solute in steels, provides solute drag on dislocation movement. Therefore, a higher C content leads to an increase in deformation activation energy [195].

In this study, differences in C content showed no influence on the critical strain of dynamic recrystallisation, or the influence was too small to be detected. As it is shown in Figure 5-3, the critical strain is the same for three different C contents in both plain carbon steel and Nb microalloyed steels. This shows good agreement with the work done by Beladi *et al* [104,196,197], in which they reported C has no specific effect on the hot deformation behaviour of austenite. Additionally, Collinson *et al* [198] reported that C has very little influence on the hot deformation behaviour of plain carbon steel.

5.3 Influence of Nb and C on the recrystallisation behaviour after finish rolling

5.3.1 Microstructural analysis after finish rolling

As shown in Figure 4-46, the C content did not show any noticeable influence on the percent recrystallisation. The reason for this has been explained in Section 5.2.3 through the influence of the C on the deformation activation energy.

The percent recrystallisation reduced with increasing Nb content in steels with each of the C contents, see Figure 4-46. Since the C content did not make any influence on recrystallisation behaviour, the difference in recrystallisation was attributed to Nb. Nb can influence the recrystallisation behaviour in the form of solute Nb and/or strain-induced Nb precipitation. Immediately after the first finish rolling, the precipitation cannot happen for two reasons. First, the supersaturation ratio was too small. Second, the time was too short for precipitation to occur. So the reduction in percent recrystallisation after finish rolling was only attributed to the solute drag effect of solute Nb.

The renowned work regarding the influence of Nb solute drag effect on austenite recrystallisation was presented by Yamamoto *et al* [104]. In their work, a series Nb contents up to 1.71wt% were added into decarburized steels containing 0.002wt% C and 0.0025wt% N. They found that 0.05wt% Nb slowed the recrystallisation by an order of magnitude. An even stronger retarding effect was found for 0.097wt% and 0.171wt% Nb where the recrystallisation was slowed by two orders compared with a similar steel without Nb.

Furthermore, Speer *et al* [89] homogenised the steel (0.007wt%C and 0.26wt% Nb) in the deformation temperature (954°C) for 5 hours to make sure that any Nb content beyond the Nb solubility limit at the deformation temperature was precipitated and there was no driving force for further precipitation during or after the deformation.

They reported that solute Nb did provide a drag effect to recrystallisation, but it was much smaller compared with the pinning forces generated by Nb precipitation.

Owing to the much higher Nb content in these studies, compared to the current study, their observation showed similar but stronger Nb solute drag effect on recrystallisation. Yamamoto *et al* [104] reported that the effect of solute Nb was remarkable within the 20% softening region at all temperatures, although at higher temperatures the retarding force became smaller. And in the region above 20% softening, the recrystallisation did not seem to be influenced by solute Nb. Therefore, the solute Nb only influenced the recovery and then the onset of recrystallisation. Similar results were also reported by other researchers [162,199].

In conclusion, it is believed that the continuous decrease in percent recrystallisation after finish rolling with the increase of Nb contents was due to the retardation of Nb on the recovery and hence the onset of recrystallisation, but not from the retardation on the progress of recrystallisation itself.

5.3.2 Semi-empirical equation to predict recrystallisation behaviour and $T_{5\%}$, $T_{95\%}$ for steels with various Nb contents

In order to predict the hot deformation behaviour of Nb microalloyed steels, a semi-empirical equation was proposed. A mathematical fit was performed using Sigmaplot and the fitting procedure is briefly explained as following.

Previous works [75,124,200] have shown that the evolution of austenite recrystallisation fraction with deformation temperature exhibits a classic sigmoidal shape. So in this study, a three parameters sigmoidal equation was used to fit the data. As it can be seen in Figure 5-4 (a), the fitting was first tried out on the experimental determined percent recrystallisation data of 40C10Nb. The fitting cannot represent the recrystallisation behaviour because the software automatically defined the upper and lower data point, which are 76.2% and 0%, as the upper and lower limit of percent recrystallisation.

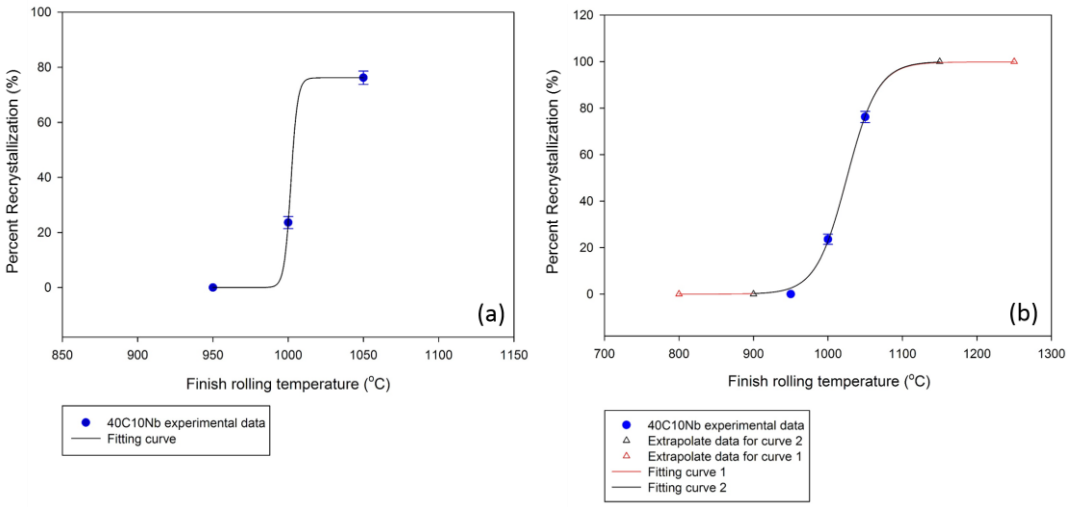

Figure 5-4 (a) fitting using experimental data only. (b) fitting using experimental data and two separate sets of extrapolated data points. No error is introduced from the extrapolated data.

Subsequently, two more extrapolated data points were added to determine the limit of percent recrystallisation, which are 0% and 100%. The 0% and 100% recrystallisation extrapolated data were placed at the deformation temperature where recrystallisation would not have started and would have finished, respectively. In order to investigate any possible influence from the extrapolated data points, two sets of extrapolated data were added and compared, as it is shown in Figure 5-4 (b). The two fitting curves overlap with each other which means the fitting was only determined by the experimental data, i.e. the extrapolated data will not introduce error to the fitting.

So the method was applied to all the samples and the results are shown in Figure 5-5. The fitting curves can be described using the following equation:

$$f_{RXN} = a/(1+\exp(-(T-x_0)/b)) \quad (5.5)$$

where f_{RXN} is the percent recrystallisation, T is the rolling temperature in Celsius, a, b and x_0 are coefficients. Coefficients a, b and x_0 for various steels are summarised in Table 5-3. The fitting curves fit the experimental data points well as for all the steels (R^2>0.99).

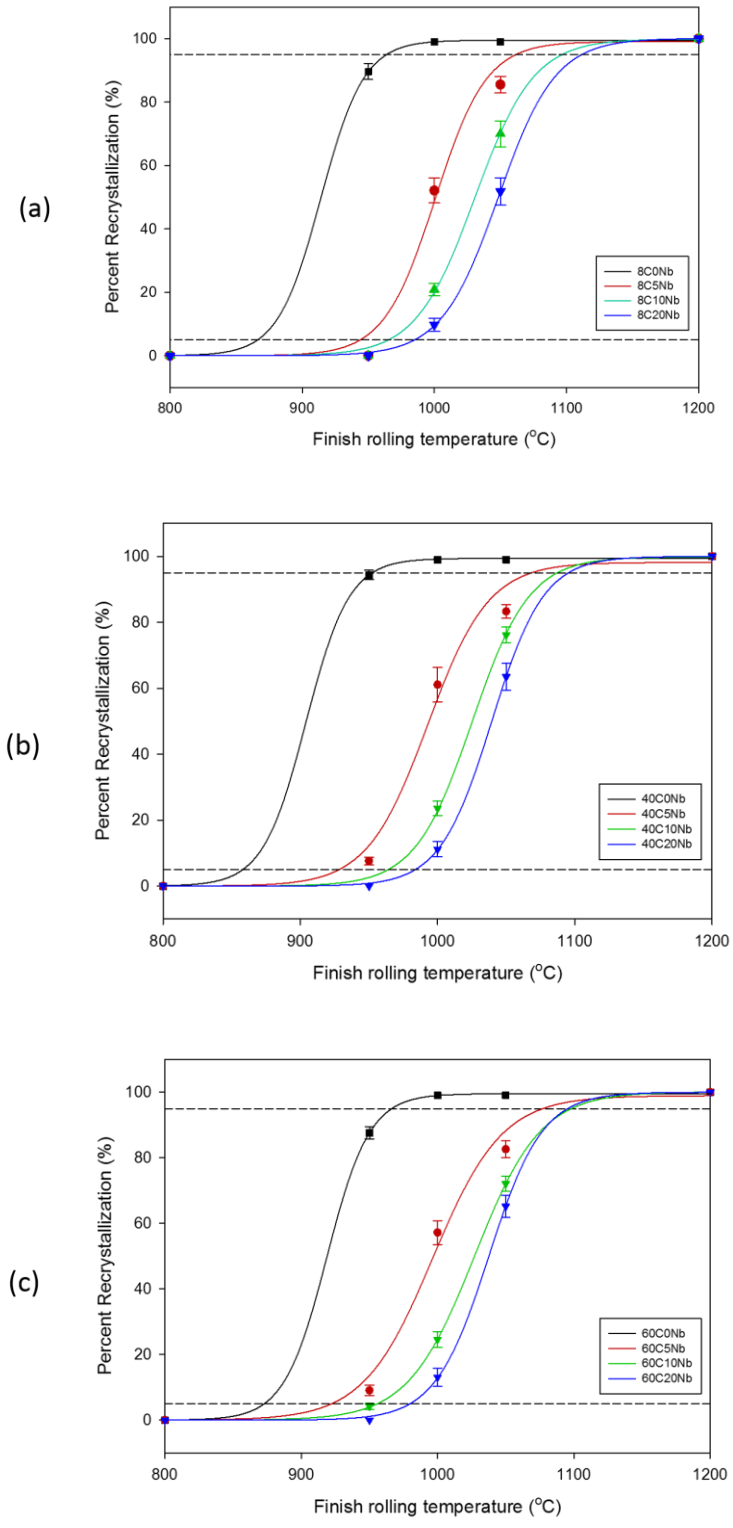

Figure 5-5 Sigmoidal fitting to the percent recrystallisation data of all the steels after finish rolling. (a) 8C steels (b) 40C steels (c) 60C steels.

Table 5-3 Summary of the coefficients of the semi-empirical equation to predict percent recrystallisation of various steels

	a	*b*	x_0	R^2
8C0Nb	99.5±0.3	16.3±5.4	914.1±11.6	0.9999
8C5Nb	99.0±1.8	19.4±3.5	1000.7±3.2	0.9904
8C10Nb	99.9±1.9	22.3±1.5	1030.7±2.0	0.9981
8C20Nb	100.1±0.8	21.5±0.8	1048.4±0.7	0.9999
40C0Nb	99.4±0.3	15.6±6.2	904.1±17.9	0.9999
40C5Nb	98.2±2.9	22.1±4.5	992.9±4.7	0.9901
40C10Nb	99.8±1.9	20.8±1.4	1025.2±2.0	0.9991
40C20Nb	100.0±0.6	18.9±0.5	1039.5±0.6	0.9998
60C0Nb	99.5±0.4	15.7±5.2	918.8±10.1	0.9999
60C5Nb	98.9±2.4	25.4±3.9	996.5±4.2	0.9934
60C10Nb	100.1±0.2	24.3±0.1	1027.1±0.2	0.9999
60C20Nb	100.0±0.8	19.7±0.6	1037.6±0.8	0.9997

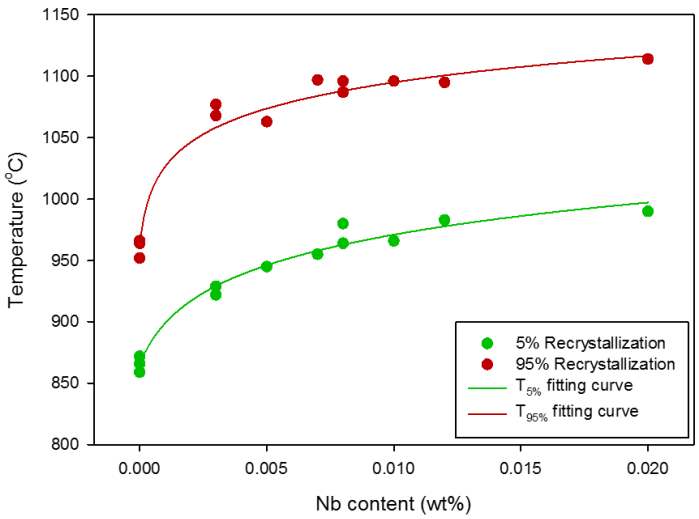

Figure 5-6 Evolution of $T_{5\%}$ and $T_{95\%}$ after finish rolling of steels with various Nb contents in solution (irrespective of C content change from 0.08 wt% to 0.6 wt%).

As it has been discussed, when solute drag is the mechanism suppressing the progress of recrystallisation, the C content cannot make noticeable influence and the change in recrystallisation behaviour is due to Nb in solution. The evolution of $T_{5\%}$

and $T_{95\%}$ with the change of Nb in solution after finish rolling is shown in Figure 5-6. $T_{5\%}$ and $T_{95\%}$ of all steels were calculated using the semi-empirical equation (Figure 5-5). The mathematical fitting for $T_{5\%}$ and $T_{95\%}$ are also shown in Figure 5-6. The relationships between solute Nb and $T_{5\%}$ and $T_{95\%}$ were found.

$$T_{5\%} = 1151.7 + 39.9\ln([Nb] + 0.0008) \quad (5.6)$$

$$T_{95\%} = 1239.2 + 31.4\ln([Nb] + 0.0001) \quad (5.7)$$

where *[Nb]* is the solute Nb content. The two equations describe the data well (R^2>0.97).

5.4 Influence of Nb and C on recrystallisation behaviour during the 20s holding period

5.4.1 Softening behaviour analysis after the 20s holding period

The influence of Nb on the softening behaviour of steels was studied by the means of interrupted double hit deformation. The fractional softening of the steels was calculated using the 2% offset method.

It is noteworthy that the percent softening represents the total softening during the 20s holding period, which includes softening caused by both recovery and recrystallisation. As it is shown in Section 2.1.2.1, the recovery process contributes 15-20% of the overall softening. The criterion that 20% of softening is due to recovery has been widely used [28,35,37,81,124].

Previous work [28,124] done using the same experimental equipment to the present research have reported that the $T_{95\%}$ temperature was correlated to approximately 60% of the total softening.

Adopting these criteria in this study, a great consistency was found between the fractional softening behaviour and the microstructural observation, as shown in

Figure 5-7. The fractional softening behaviour further supports the microstructural observation.

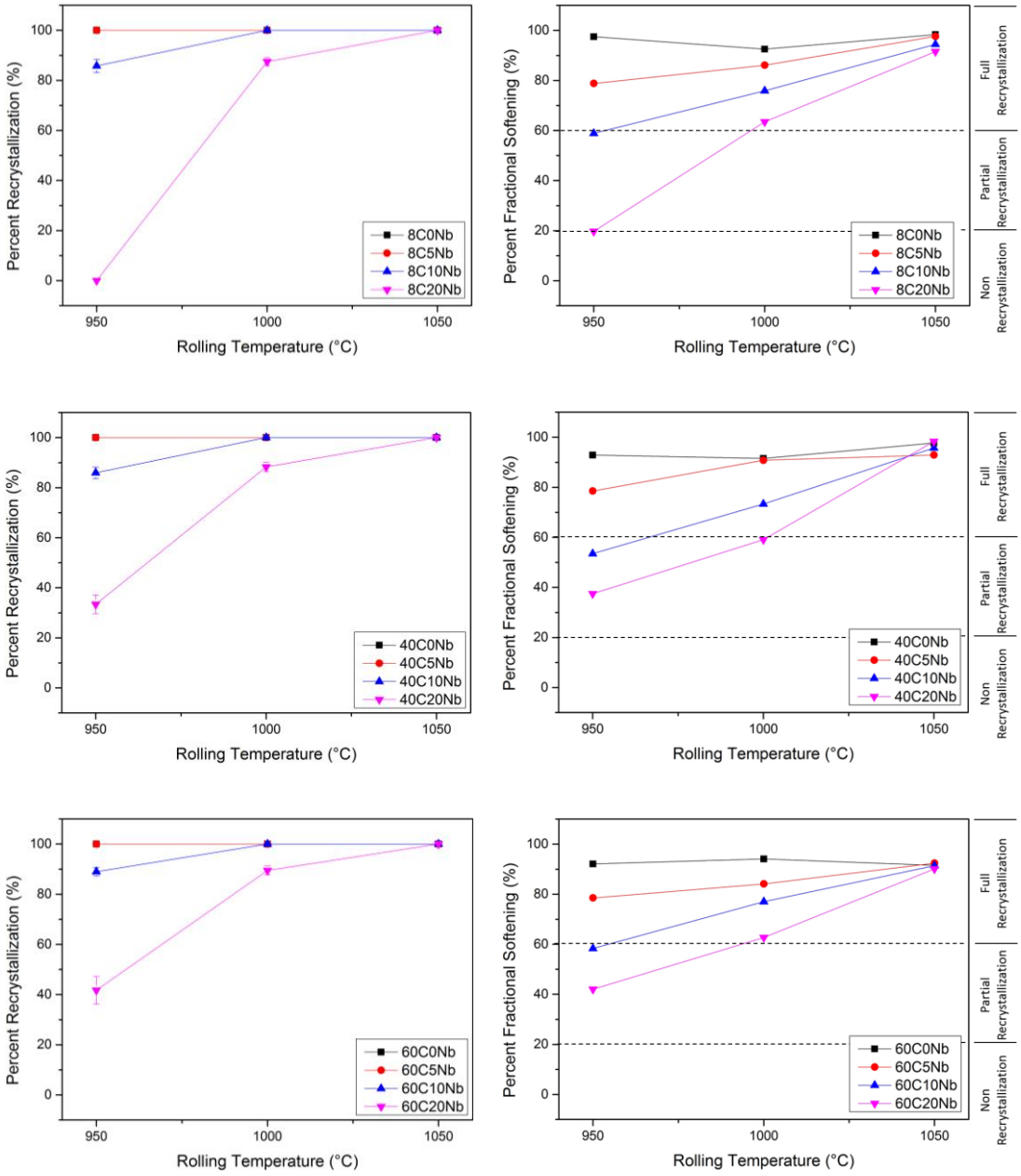

Figure 5-7 Comparison between recrystallisation fraction after the 20s holding period and the fractional softening behaviour.

5.4.2 Microstructural analysis after the 20s holding period

The microstructures of prior-austenite grain after the 20s holding period were shown in Section 4.5. As it can be seen from Figure 4-63, the C content did not show any influence on the recrystallisation behaviour of any of the steels except the 20Nb steels being rolled at the finish rolling temperature of 950°C. This is due to the relatively high Nb contents and low rolling temperature, such that precipitation happened during the isothermal holding. The difference in percent recrystallisation was attributed to the difference in precipitation which is further discussed in Section 5.4.3.

For all other steels, the precipitation did not happen and substantial recrystallisation was achieved during the holding period. For example, when the finish rolling temperature was 1000°C, 20Nb steels exhibited a partially recrystallised microstructure whereas all the other steels were fully recrystallised. Similar behaviour was observed at 950°C, where 10Nb steels showed a partially recrystallised microstructure whereas 0Nb and 5Nb steels showed a fully recrystallised microstructure. Higher Nb contents showed larger retardation for each of the rolling temperatures. This was believed to be a subsequent result from the delay of the onset of recrystallisation.

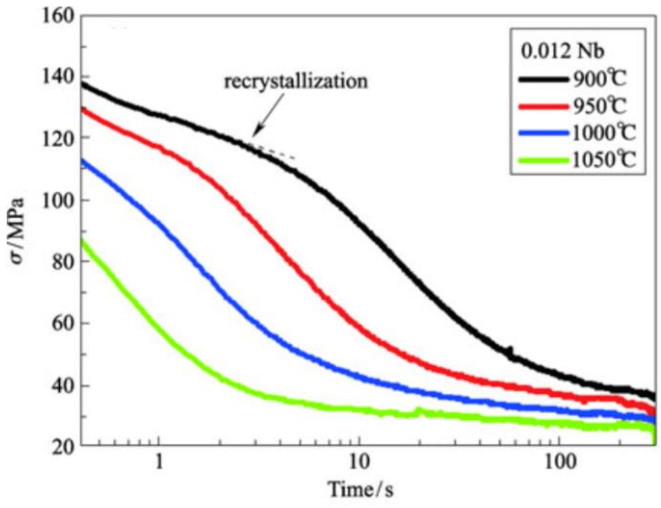

Figure 5-8 The stress relaxation curves for low carbon steel with 0.012 wt% Nb after deformation with 25% strain and 1/s strain rate at various deformation temperatures [201].

The recrystallisation behaviour during the 20s holding period can be illustrated using stress relaxation tests by Miao *et al* [123,201]. One of the Nb microalloyed steels they used (0.04 wt% C and 0.012 wt% Nb) is very similar to 8C10Nb steel in this study. The stress relaxation curves after strain of 25% with a strain rate of 1/s is shown in Figure 5-8. Good agreement in austenite recrystallisation behaviour is found. In Miao's work, recrystallisation was finished within 2s and 9s after deformation at 1050°C and 1000°C, respectively. In this study, after the 20s holding period, 8C10Nb showed fully recrystallised prior-austenite microstructures at 1050°C and 1000°C. In our study, 8C10Nb contains 85.8±2.6% recrystallised prior-austenite after the 20s holding period at 950°C, which is consistent with result in Figure 5-8 where recrystallisation completed in over 20s after deformation. No precipitation was found in their study, which supports our argument that the delay in recrystallisation is due to the retardation of solute Nb on the onset of recrystallisation.

Comparing the three rolling temperatures, it was found that the influence of solute Nb on suppression recrystallisation was more profound at low rolling temperatures. For example, 20Nb steels after the 20s holding period were partially recrystallised at 1000°C whereas it showed full recrystallisation at 1050°C. This is because recovery and recrystallisation are thermally activated processes. The intrinsic mobility of dislocation and grain boundary is low at low temperatures. Thus, for the same Nb content, recrystallisation needs more time to complete at lower temperature.

5.4.3 Influence of NbC precipitation on the recrystallisation behaviour

5.4.3.1 Quantitative comparison between F_{RXN} and F_{PIN}

For the 20Nb steels being rolled at 950°C, a substantial difference in percent recrystallisation was observed after the 20s holding period due to the difference in precipitation behaviour.

In Section 4.7, clear precipitation particles were found at the end of the 20s holding period. The precipitation particle size distribution was shown in Figure 4-68. The

average particle sizes of the strain-induced precipitates in each of these three steels were about 5 nm. This is in good agreement with numerous works [35,37,63,93,139]. However, the number density of the particles showed a decreasing trend with the increase in the C content, where a weaker pinning force was provided to retard recrystallisation. Therefore, the F_{RXN} and F_{PIN} were calculated and compared as following.

The driving force for recrystallisation is the stored energy from deformation. The F_{RXN} were determined using the area under the flow curve of the first finish rolling. As it has been reviewed in Section 2.1.1, the stored energy provides the driving force for both recovery and recrystallisation [23,24]. Adopting the criterion that 20% of the stored energy is consumed by recovery [28,35,37,81,124], the F_{RXN} is calculated and shown in Table 5-4. The F_{RXN} is calculated using the area below the first rolling and deducting the 20% caused by recovery.

The precipitate particle sizes measured from the TEM images were shown in Table 5-5. The number densities of the precipitates were also calculated (Table 5-5). Then the volume fraction of the NbC precipitates were determined using the following equation proposed by Ashby and Ebeling [202], which has been adopted in a number of studies [35,37,93,139,203].

$$f_v = \frac{\pi}{6} N_s(\bar{x}^2 + \sigma^2) \tag{5.8}$$

In the equation, $\bar{x}$ and σ are the mean and standard deviation of the precipitates. *Ns* is the particle number density (particles per unit area).

It is worth noticing that the precipitation volume fraction calculated may not be the true value. This is because the efficiency of the extraction is always less than 100%, especially with very fine particles. However, assuming extraction efficiencies were similar for all steels, the calculated volume fraction served well for comparison purposes.

Table 5-4 Driving force for recrystallisation (F_{RXN}) measured from the area under the flow curve of the first finish rolling at 950°C ($MN \cdot m^{-2}$)

Steel	8C20Nb	40C20Nb	60C20Nb
Area under flow curve of the first finish rolling	26.5	25.5	22.8
F_{RXN} (80% of area under flow curve)	21.2	20.4	18.2

Table 5-5 Precipitation size, number density, volume fraction and F_{PIN} in austenite grain boundaries of 20Nb steels after 20s isothermal holding at 950°C

Steel	r (nm)	$N_s(\mu m^2)$	$f_v\ (10^{-4})$	$F_{PIN}(MN \cdot m^{-2})$
8C20Nb	2.62	44.7	6.99	19.5
40C20Nb	2.51	30.7	4.27	12.9
60C20Nb	2.64	24.0	3.68	10.1

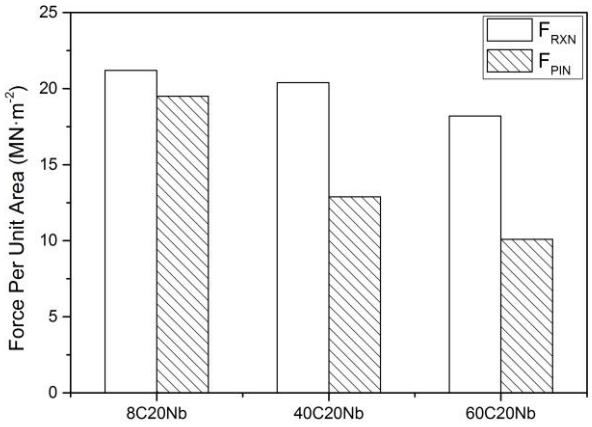

Figure 5-9 Comparison between F_{RXN} and F_{PIN} of 8C20Nb, 40C20Nb and 60C20Nb after finish rolling and 20s isothermal holding period at deformation temperature of 950°C.

The pinning forces F_{PIN} were then calculated using Hansen *et al* [93]'s subgrain boundary model (Equation 2.23). In the equation, the precipitate particle radius and volume fraction were measured (Table 5-5), the interfacial energy of austenite grain boundary is taken as $0.8J/m^2$ [37,121], the subgrain size is 0.5μm [37,93]. The calculated F_{PIN} were summarized in Table 5-5.

A direct comparison between the recrystallisation driving force F_{RXN} and pinning force F_{PIN} was made in Figure 5-9. For 40C20Nb and 60C20Nb steels, the F_{PIN} was substantially less than F_{RXN}. In such cases, the precipitation cannot fully retard the recrystallisation process and thus result in a partially recrystallised microstructure. For 8C20Nb steel, F_{RXN} (21.2 $MN \cdot m^{-2}$) was of the same magnitude as F_{PIN} (19.5 $MN \cdot m^{-2}$). It is important to note that this calculated F_{PIN} value was expected to be smaller than the actual F_{PIN} value as the efficiency of extraction is always less than 100%. Therefore, the actual F_{PIN} is believed to be larger than F_{RXN} such that the recrystallisation was fully retarded.

This comparison between F_{RXN} and F_{PIN} further validates the microstructural observation.

5.4.3.2 Quantitative description of NbC precipitates in austenite of 20Nb steels

From the microstructural observation and calculation above, the $T_{5\%}$ was clearly decreased with the increase of C in the present study (For 8C20Nb, $T_{5\%}$>950°C whereas for 40C20Nb and 60C20Nb, $T_{5\%}$<950°C). This seems to be contrary to what is reported in other research. For example, Beladi *et al* [197] reported a raise of 40-60°C in $T_{5\%}$ of a 0.03 wt% Nb microalloyed steel when the carbon content was increased from 0.04 to 0.11 and then 0.16 wt%. Furthermore, Speer *et al* [89] showed that the recrystallisation was suppressed by two orders of magnitude when the carbon content was increased from 0.008 to 0.10 wt% in 0.05 wt% Nb microalloyed steels. This is due to the larger pinning force provided by the increasing amount of Nb(CN) caused by the increase in C content.

It is worthy to note in the work by Beladi *et al* [197] and Speer *et al* [89], that even though the C content was raised, the Nb dissolution temperatures were still lower than their homogenisation temperature. In other words, the Nb were still fully dissolved during homogenisation. At the deformation temperatures in their study, higher C content lead to a smaller Nb solubility. Consequently, the Nb supersaturation ratio was increased.

As it is reviewed in Section 2.3.2, the supersaturation ratio is the degree of Nb supersaturation, which is closely related to the precipitation potential, and hence the suppression of recrystallisation. A critical supersaturation ratio of 5-7.5 to fully retard recrystallisation was first reported by Hansen *et al* [93]. However, later Cuddy [58] showed that the supersaturation ratio is not constant but falls within the range of 5-40 due to the considerable difference in the solubility products used to calculate the supersaturation ratios. Nonetheless, a general trend of increasing $T_{5\%}$ with increasing supersaturation ratios was shown in these studies. However, this is contrary to the observation in the present study (see Table 5-6). 8C20Nb showed a higher $T_{5\%}$ (>950°C) but a smaller Nb supersaturation ratio (4.5).

In the present study, even though the 40C20Nb and 60C20Nb possess higher supersaturation ratios compared with 8C20Nb, a smaller precipitation potential could be generated due to the higher degree of deviation away from stoichiometric austenite composition. The austenite composition was lacking Nb atoms so that the amount of supersaturated Nb atoms was the controlling factor to the precipitation potential.

To calculate Nb supersaturation in austenite, the following equation was used [35,37],

$$[Nb]_{ss} = [Nb]_{\gamma} - [Nb]_{\varepsilon} \tag{5.9}$$

where $[Nb]_{ss}$ is the Nb supersaturation, and $[Nb]_{\gamma}$ and $[Nb]_{\varepsilon}$ are the amounts of Nb in solution at homogenisation and deformation temperatures, respectively. The Nb supersaturations at 950°C along with other parameters are summarized in Table 5-6. A direct comparison between Nb supersaturation, precipitation number density and the corresponding recrystallisation fractions is also made between 8C20Nb, 40C20Nb and 60C20Nb, see Figure 5-10. As it is shown, the decrease in Nb supersaturation results in lower precipitation number densities and higher recrystallisation fractions.

Table 5-6 Comparison of parameters measured from 20Nb steels

	8C20Nb	40C20Nb	60C20Nb
Bulk Nb concentration (wt%)	0.02	0.017	0.018
Nb in solution in austenite at 1250°C (wt%)	0.02	0.012	0.008
Nb in solution in austenite at 950°C (wt%)	0.004	0.001	0.001
Nb supersaturation at 950°C (wt%)	0.016	0.011	0.007
Nb supersaturation ratio at 950°C	4.5	12.0	12.0
Nb precipitation number density (/μm^2)	44.7	30.7	24.0
Recrystallisation fraction after 20s holding period at 950°C (%)	0%	33.4±3.7%	41.7±5.5%
$T_{5\%}$ after 20s holding period (°C)	>950	<950	<950

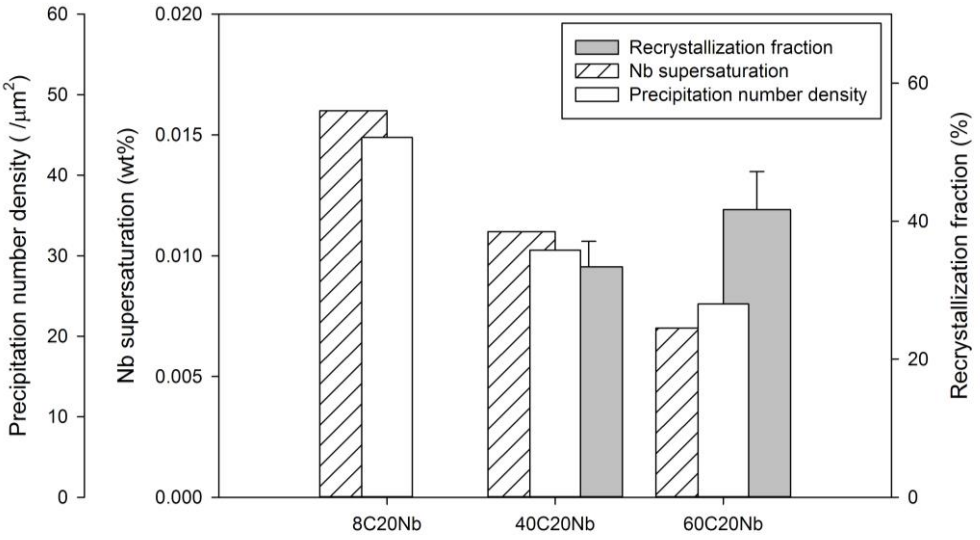

Figure 5-10 Comparison of Nb supersaturation, precipitation number density and recrystallisation fractions between 8C20Nb, 40C20Nb and 60C20Nb after the 20s holding period at finish rolling temperature of 950°C.

The different recrystallisation behaviours after the 20s holding period at the deformation temperature of 950°C can be interpreted in two parts.

First is the influence of different Nb content in solution to the solute drag effect before recrystallisation. It has been illustrated that the recrystallisation can only be fully suppressed when the solute drag retarded the recrystallisation sufficiently until the onset of precipitation [104,204]. The wide distribution of C contents in this study exerts an influence on the Nb contents which can be dissolved after homogenisation (Figure 5-1 and Table 5-1). For the higher C steels, namely 40C and 60C steels, only 0.012 wt% and 0.008 wt% of Nb can be dissolved after homogenisation. In this study, the lower Nb in solution led to a smaller solute drag effect to retard recrystallisation and consequently a shorter incubation time for recrystallisation.

The second is the effect of the difference in Nb supersaturation on the precipitation behaviour. Nb supersaturation is the driving force for precipitation. A higher Nb supersaturation promoted the strain-induced precipitation [205]. Palmiere *et al* [35] showed that $T_{5\%}$ is increased from 942°C to 971°C and 1030°C with the increase of Nb supersaturation from 0.0194wt% to 0.0384 wt% and 0.0455 wt%, respectively. Furthermore, Cao *et al* [181] reported that with the increase of Nb supersaturation, Nb precipitation could happen at higher temperatures and with a shorter incubation time.

In this study, at the same deformation temperature, a higher Nb supersaturation (0.016 wt% from 8C20Nb steel) yielded higher precipitation potential, hence a larger precipitation number density was observed (Figure 4-69 and Figure 5-10). Even though there was no direct observation of the incubation time of the onset of precipitation, an indirect explanation might be given through the precipitation particles diameter distribution (Figure 4-68). The more even precipitation particle diameter distribution, and the higher frequency of the larger precipitation (>8nm) from 8C20Nb, might suggest the early onset of precipitation. Because the early precipitated particles had a longer particle growth time, this led to larger particle diameters.

The combination of these two effects results in the difference of the recrystallisation behaviour, and the recrystallisation in this study can be interpreted using the general RPTT diagram, as shown in Figure 2-24.

For 40C20Nb and 60C20Nb steels, the weaker Nb solute drag effect cannot halt deformed austenite long enough for precipitation to occur. Recrystallisation happened before the onset of precipitation. Before the finish of recrystallisation, precipitation happened in the remaining unrecrystallised regions. Therefore, a partially recrystallised microstructure was obtained for 40C20Nb and 60C20Nb steels. Comparing 40C20Nb and 60C20Nb, 60C20Nb steel showed a slightly higher percent recrystallisation due to the lower Nb solute drag and Nb supersaturation. This behaviour from 40C20Nb and 60C20Nb corresponds well with regime II behaviour.

For the 8C20Nb steel, the higher Nb in solution led to a shorter incubation time for precipitation and longer incubation time for recrystallisation, thus the precipitation happened prior to recrystallisation. Therefore, the recrystallisation was fully retarded which showed the typical regime III behaviour.

5.4.4 $T_{5\%}$ and $T_{95\%}$ for steels with various Nb contents after the 20s holding period

After the 20s isothermal holding at the three deformation temperatures, the recrystallisation in all the steels other than 8C20Nb being rolled at 950°C has started. Due to the lack of deformation in the fully unrecrystallised region for 40C20Nb and 60C20Nb steels, and lack of deformation in both partially recrystallised and fully unrecrystallised region in the case of 0Nb and 5Nb steels, a relationship between $T_{5\%}$, $T_{95\%}$ and the Nb in solution (like which was shown in Section 5.3.2) cannot be established. However, based on the microstructural observation, $T_{5\%}$ and $T_{95\%}$ were superimposed on the deformation map as it can be seen in Figure 5-11. Due to the partial dissolution of the 0.02 wt% Nb in 40C20Nb and 60C20Nb steels after homogenisation, their actual positions on the deformation map according to the

calculation shown in Figure 5-1 were highlighted. Further study can be conducted at lower temperatures to establish the relationship between $T_{5\%}$, $T_{95\%}$ and the Nb in solution.

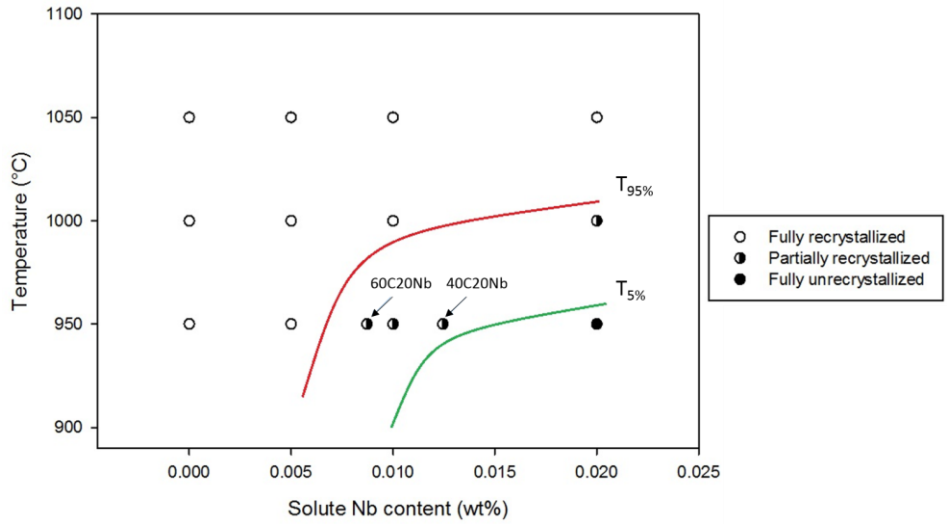

Figure 5-11 Deformation map showing various austenite microstructures after the 20s holding period with different solute Nb contents. $T_{5\%}$ and $T_{95\%}$ were superimposed on the map.

5.5 Influence of Nb and C on austenite grain growth behaviour during the 20s holding period

After recrystallisation was finished, the recrystallised austenite grains continued to grow during the isothermal holding. Unfortunately, the time needed to complete recrystallisation at the three deformation temperatures was not available. So the study on the influence of Nb and C on the grain growth behaviour was conducted on the steels deformed and isothermally held at 1050°C.

The reason is that immediately after the finish rolling at 1050°C, i.e. before the isothermal holding, more than 50% of recrystallisation had already happened in all the microalloyed steels and the plain carbon steels were fully recrystallised (Figure 4-32, Figure 4-38 and Figure 4-44). Therefore, within less than a second the

recrystallisation should have finished in all the steels. This enables us to eliminate the influence from different time needed to finish recrystallisation. So the brief time for recrystallisation to finish was ignored and the corresponding time for grain growth at 1050°C was assumed to be 20s.

Another assumption was made on the recrystallised grain sizes for the microalloyed steels. At the end of finish rolling, only the plain carbon steels completed the recrystallisation process. Since homogenised prior-austenite grain sizes with different Nb contents for each of the C content were similar (Figure 4-4), it was assumed that the recrystallised austenite grain sizes with various Nb content were the same before the isothermal holding. For example, the austenite grain sizes for 8C5Nb, 8C10Nb and 8C20Nb were assumed to be the same with 8C0Nb which is 61.9μm.

5.5.1 Influence of Nb on austenite grain growth behaviour

As it is reviewed in Section 2.4.3, solute atoms exert a retarding force on austenite grain growth through the solute drag effect on the motion of austenite grain boundaries. The grain boundaries, which have higher energy, attract the Nb atoms to segregate in the vicinity of grain boundaries. Through this, both the interfacial energy and grain boundary mobility reduces.

The Nb solute drag effect on grain coarsening behaviour is shown in a number of studies [74,120–123,206]. Gong *et al* [74] studied the dissolution behaviour of NbCN precipitation and its influence on the austenite grain growth behaviour at a high reheating temperature of 1200°C. They reported that the solute drag effect from solute Nb cannot be neglected. In fact, it became the dominant contribution on retarding austenite grain growth as NbCN particles were dissolved. Additionally, Miao *et al* [122] showed 0.1 wt% Nb in solution provided an intensive solute drag effect, which resulted in an very slow austenite grain growth rate. The prior-austenite grain sizes after deformation and holding at 1000°C for 3s, 60s and 240s were 13.3μm, 20 μm and 28.0 μm, respectively.

In current study, there was not any observed NbC precipitation for the steels after 20s holding period at the finishing temperature of 1050°C. The difference in the isothermal grain growth behaviour was attributed to the Nb and C in solution.

For the low carbon 8C steels, compared with the plain carbon steel 8C0Nb, the microalloyed steels showed a smaller tendency on isothermal austenite grain growth. With the increase in the amount of Nb in solution, the prior-austenite grain size gradually reduced after the 20s holding period (Figure 4-70). This is because of the stronger solute drag forces provided by the higher Nb contents.

For the 40C steels, the low Nb content up to 0.01wt% seems to have no influence on the grain growth behaviour. The prior-austenite grain sizes of 40C0Nb, 40C5Nb and 40C10Nb showed no noticeable difference after the 20s holding period at 1050°C, whereas the 40C20Nb steel showed smaller prior-austenite grain size (Figure 4-71).

For the 60C steels, all the steels showed similar prior-austenite grain sizes after the holding period (Figure 4-72).

In order to explain the difference in the influence of Nb exerted on the isothermal grain growth behaviour, the influence of C on grain growth was investigated.

5.5.2 Influence of C on austenite grain growth behaviour

Compared with the influence of the microalloying elements in retarding grain growth, the studies on the influence of C to the austenite grain growth behaviour are limited. In the present study, it is obvious that the change in the C content had a distinguishable effect on the isothermal grain growth behaviour of austenite (Figure 4-4).

Like Nb, C atoms are not uniformly distributed in solid solution but tend to segregate to the grain boundaries. Hondros *et al* [207] reported that the tendency of segregation is related to the solubility of the elements. A lower solubility leads to a greater enrichment of the solute at grain boundaries. Therefore, C can be highly enriched at the austenite grain boundaries [151]. The enrichment of C on the prior-austenite

grain boundaries was directly observed using atom probe microscopy [208,209]. A study by Kostryzhev *et al* [209] is shown in Figure 5-12 as an example.

The C solute drag effect on the austenite grain boundary migration was observed in a number of studies [210–212]. For example, Uhm *et al* [210] studied the austenite isothermal grain growth behaviour with a series of plain carbon steels containing 0.08 wt% to 0.32 wt% carbon with the isothermal holding time up to 10 mins. They found out that the tendency for grain growth is reduced with the increase of C content, which indicates that the C segregation on the grain boundaries exert a solute drag effect on the grain boundary migration. Moreover, Maity *et al* [211] studied the kinetics of isothermal austenite grain growth with long holding periods (1-6 hours) using two plain carbon steels with dramatic change in C contents (0.35 wt% and 1.0 wt%). Compared with Uhm *et al* [210]'s results, a more profound solute drag effect was observed from the steel with 1.0 wt% C due to the higher degree of C segregation on the grain boundaries.

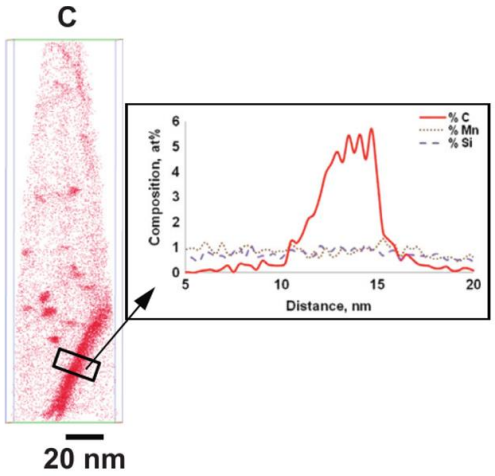

Figure 5-12 C concentration profile across a prior-austenite grain boundary from an Nb-Ti microalloyed steel being quenched after deformation at 1075°C [209].

In the present study, the 40C and 60C steels had a smaller tendency for austenite grain growth (around 55μm to 75μm) during the isothermal holding compared with the 8C steels (around 62μm to 95μm) because the larger C segregation on austenite grain boundaries provided larger solute drag effect on austenite grain boundary migration.

However, the difference between 40C (52µm to 76µm) and 60C (58µm to 77µm) steels was not obvious. This might be due to the very short holding period of 20s in the current study. A similar behaviour was observed in the work by Uhm *et al* [210]. At short holding period, the differences in prior-austenite grain sizes with different C contents were small and hard to distinguish. The prior-austenite grain sizes differences were more obvious with longer holding periods (up to 10mins). The prior-austenite grain sizes after homogenisation for the 60C steels were smaller than that of the 40C steels (Figure 4-4), which further supported this explanation.

5.5.3 The effectiveness of the dilute Nb on refining austenite grain

In this study, since the large undissolved particles in the 40C20Nb and 60C20Nb steels after homogenisation cannot influence austenite grain growth behaviour during the 20s holding period, the difference in the austenite grain growth behaviour is only attributed to the solute Nb and C atoms in solution.

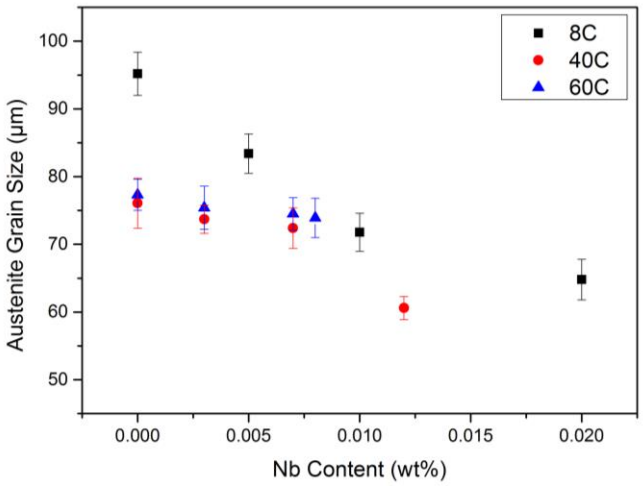

Figure 5-13 Evolution of prior-austenite grain size against Nb in solution after the 20s isothermal holding period at the finish rolling temperature of 1050°C. Carbon contents are shown in the legend.

As it can be seen from Figure 5-13, for 8C steels the dilute Nb additions slow austenite grain growth resulting in smaller prior-austenite grain sizes. The refinement is obvious even with Nb content as low as 0.005 wt%. On the other hand, with the increase of the C content from 0.08 wt% (8C) to 0.4 wt% (40C), the effect from Nb

contents up to 0.007 wt% on the refinement of prior-austenite grain sizes are vanished. Only the 40C20Nb steel (0.012 wt% Nb in solution) shows a refinement on prior-austenite grain size compared with 40C0Nb. Additionally, when the C content is 0.6 wt% (60C), none of the microalloyed steels shows noticeable refinement on the prior-austenite grain size after 20s isothermal holding period.

As discussed previously in Section 5.5.2, the C content clearly showed the solute drag effect on the grain boundary motion, and that the solute drag effect is increased with the increase in the C content. A plausible explanation on the effectiveness of Nb on retarding austenite grain growth is given as follows.

With the 8C (0.08 wt% C) steels, the solute drag effect from C solutes is small, therefore the solute drag from Nb atoms is the dominant retarding force on austenite grain growth. As a result, the influence of solute drag effect from as low as 0.005 wt% Nb is obvious.

For the 40C and 60C steels, higher C contents provide larger retarding force. This retarding force might be much larger than the retarding force caused by up to 0.008 wt% solute Nb. As a result, the retarding force caused by C solutes is dominant, so that Nb contents up to 0.008wt% show no noticeable influence on austenite grain growth for 40C and 60C steels. When the Nb in solution is 0.012 wt% (40C20Nb steel), the retarding force on austenite grain growth might be comparable with the retarding force caused by C atoms. An additional retarding force is provided by Nb atoms, therefore an obvious refinement is observed in 40C20C steels compared with the other 40C steels, as shown in Figure 5-13. Accordingly, the critical solute Nb content to make a noticeable refinement on austenite grain size for 40C steel is between 0.008 wt% to 0.0012wt%.

5.5.4 Semi-empirical equation to predict austenite grain growth behaviour under the influence of Nb solute drag

In a recent study, Gong *et al* [74] investigated the strain-induced NbCN dissolution behaviour and their influence on the austenite grain growth behaviour. They found

that both the Zener pinning effect from the precipitates and the solute drag effect from the Nb in solution retard the austenite grain growth at short reheating times, up to 100s in their case. For longer reheating times, with vast majority NbCN precipitates being dissolved back into solution, the solute drag effect become the dominant effect.

They compared their experimental data with the theories proposed by Fan [213], Cahn [116], Feltham [214] and Hellman & Hillert [215] and found that Fan's theory fitted well with the experimental data especially at longer holding times (100s and 1000s) where solute drag was the dominant retarding force on grain growth. Therefore, Fan *et al*'s theory was used to propose a semi-empirical equation to predict the austenite grain growth behaviour with various Nb contents.

In Fan *et al*'s theory, they proposed a power law for grain growth as follows,

$$R_t{}^m - R_0{}^m = kt \tag{5.10}$$

where R_0 is the starting grain size, R_t is the grain size at time t, k is the kinetic coefficient, and m is the growth exponent. The exponent m for a pure material is 2. When the solute drag exists, the exponent m can be any value between 2 and 3, dependent on the ratio between lattice diffusion and the mobility of grain boundary.

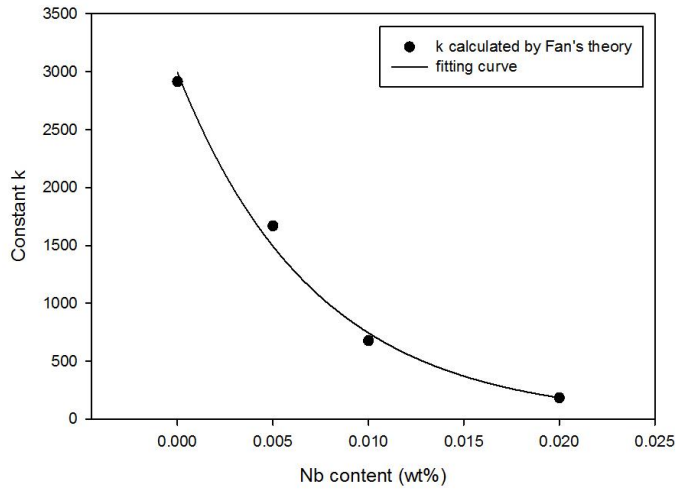

Figure 5-14 Calculated *k* value in Fan's theory and the regression fitting curve showing the evolution of *k* value with Nb contents.

Taking *m* as 2.5[74] and using the prior-austenite grain sizes for 8C steels at 0s and 20s, the constant *k* was calculated to be 2914.1, 1668.7, 676.9 and 182.8 for 8C0Nb, 8C5Nb, 8C10Nb and 8C20Nb, respectively. Regression fitting was performed on the calculated *k* value and a relationship between Nb content and *k* was found, as shown in Figure 5-14.

$$k = 2993.1\exp(-139.2[Nb]) \tag{5.11}$$

where *[Nb]* is the Nb content in solution. Therefore, the semi-empirical equation to predict austenite grain growth of 8C steels at the temperature of 1050°C is proposed by substitution of Equation 5.11 into Equation 5.10.

$$R_t{}^{2.5} - R_0{}^{2.5} = 2993.1\exp(-139.2[Nb])t \tag{5.12}$$

A comparison between the experimental prior-austenite grain size and the predicted austenite grain size is shown in Figure 5-15.

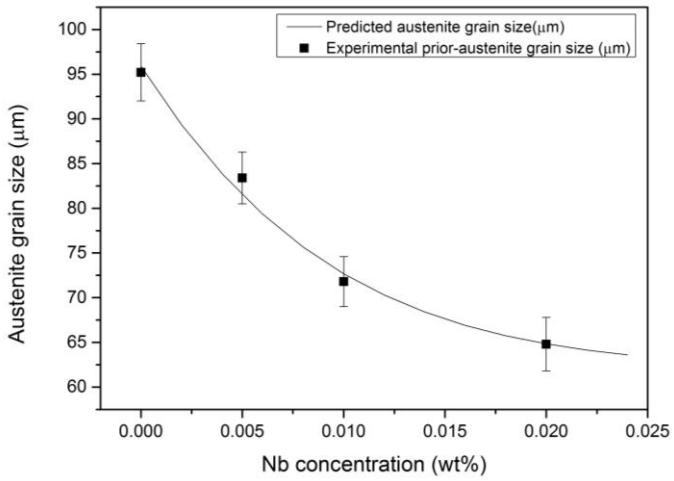

Figure 5-15 Experimental determined and predicted austenite grain size for 8C steels after the holding period of 20s.

5.6 Influence of strain accumulation on the rolling load

In the current study, it was found that the flow stress was influenced by the recrystallisation behaviour during the holding period. When complete recrystallisation happened during the 20s holding period, the flow stress showed no influence from the addition of Nb, see flow stress curves in Section 4.2. This indicates that if the rolling process is conducted at temperatures above $T_{95\%}$, the dilute Nb in solution will not increase the rolling load to the rolling equipment.

However, for all the steels whose recrystallisation process were not finished during the holding period, the increase in flow stress (compared with the flow stress of the reference steel with the same deformation temperature) at the end of the second finish rolling was summarised in Figure 5-16. The strain accumulation was calculated using the equation proposed by Hodgson and Gibbs [216].

$$\varepsilon_r = A(1-x)\varepsilon \tag{5.13}$$

where ε_r is the strain accumulation, A is a coefficient, x is the percent recrystallisation and ε is the pass strain. Taking A as 1, the strain accumulation was calculated. From Figure 5-16, it can be seen strain accumulation led to an increase in the flow stress and hence the rolling loads.

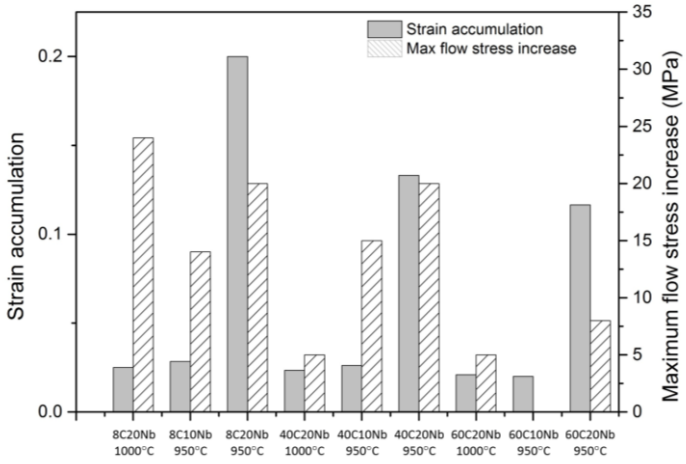

Figure 5-16 Increase in flow stress caused by strain accumulation. X axis shows the test ID which is identified by the steel and finish rolling temperature.

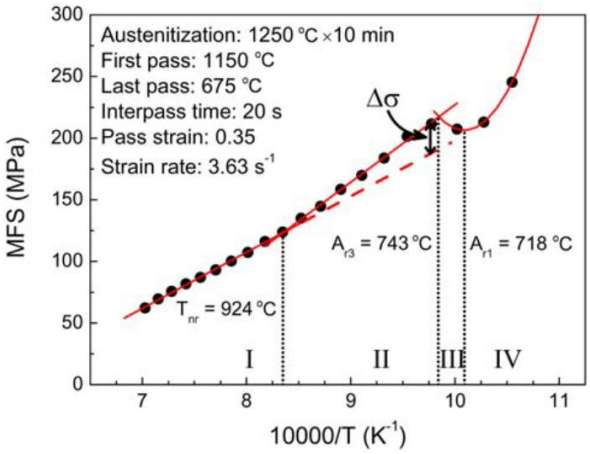

Figure 5-17 Mean flow stress evolution with the inverse of absolute temperature in a multipass hot torsion test of a steel with 0.2 wt% C and 0.007 wt% Nb. The rolling parameters are shown in the graph [134].

The flow stress increase values were between 5-25MPa. No particular relationship can be established between the strain accumulation and the increase in flow stress. This might be because the inevitable margin of error in the data recording process during the macroscopic PSC tests. Nevertheless, the stress increase caused by strain accumulation was widely reported in the literature [129,134,165,217–219]. A multipass torsion test by Gomez *et al* [134] is shown in Figure 5-17 as an example. In region II, the deformation was performed below the $T_{95\%}$, where the pass strain was partially or fully accumulated. The strain accumulation led to an increase in the mean flow stress ($\Delta\sigma$).

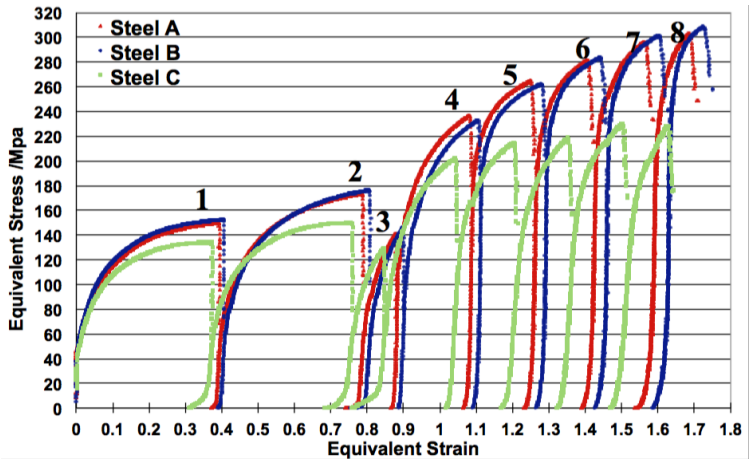

Figure 5-18 Comparison between the flow stress curves of the steels under the same multipass PSC tests (three rough rolling and five finish rolling). Steel A: Nb microalloyed steel; Steel B: Nb-Ti microalloyed steel; Steel C: plain carbon steel. [165].

Another study conducted by Bin [165] using multipass PSC tests on Nb microalloyed steel, Nb-Ti microalloyed steel and plain carbon steel is shown in Figure 5-18. In his study, the five finish rolling passes was conducted below $T_{5\%}$ (started at 880°C and finished at 840°C with an interpass time of 12s). A continuous increase in flow stress with the increase in the accumulated strain was shown. The greatest increase in the flow stress was observed in the final finish rolling due to the largest accumulated strain, where an 80 MPa increase was found.

It is worth noticing that compared all these studies, even though the various strain accumulation and deformation parameters led to different absolute values in the flow stress increase, the percent flow stress increase accounted for no more than around 30%.

Therefore, it is concluded that due to the strain accumulation up to 0.2, an increase in the maximum flow stress of 5-25 MPa (about 4-18%) was found with the processing parameter used in this study.

5.7 Industrial application

As it has been shown in the previous results and discussion, the dilute Nb provides clear benefits which could potentially be used in the industrial processing.

In steel plants with low capacity, i.e. old or small plants, in order to reduce the rolling load, the rolling process start and finish at high temperatures. The rolling load might be just below the load capacity of the rolling mills. Therefore, rolling below $T_{5\%}$ might be a problem for them due to the raise in the rolling load and the rolling process has to be conducted above $T_{95\%}$. In this case, the addition of dilute Nb can be beneficial in two ways, precipitation/solid solution strengthening and refinement of grain size in the final product.

For the medium carbon steels 40C and 60C (apart from 40C20Nb steel) being rolled above $T_{95\%}$, even though dilute Nb do not seem to have influence on austenite grain coarsening during the rolling process, it is still beneficial to apply. Jansto [16]

reported that in actual steel production operations, poor homogeneity of austenite grain size could be obtained due to the fluctuation in the reheating temperature. With a dilute Nb addition of 0.005-0.02 wt% being added, the Nb atomic cluster and/or precipitates delayed austenite grain growth in the overheated regions of the slab. Therefore, the occurrence of inhomogeneous grain size distribution caused by the reheating temperature fluctuation during slab reheating was reduced. Moreover, Nb in solution at the end of finish rolling provides precipitation potential during the following cooling process. Nb has the potential to increase the strength of final product through either precipitation strengthening or/and solid solution strengthening. Yu *et al* [220] has reported that 0.013 wt% Nb lead to an increase of 55MPa in the tensile strength of a low carbon steel at two coiling temperatures. For low carbon 8C steels, due to the retardation force that solute Nb exert on the austenite grain growth during interval time between passes, recrystallisation controlled rolling (RCR) can be performed. Compared with plain carbon steels, finer austenite grains before transformation lead to finer transformed microstructure. This provides another increase in both strength and toughness through grain refinement strengthening.

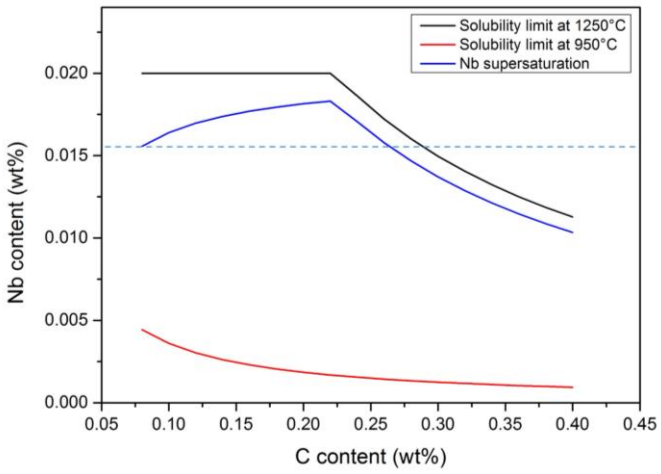

Figure 5-19 Calculated solubility limit at homogenisation temperature of 1250°C, deformation temperature of 950°C and the corresponding Nb supersaturation at 950°C.

For high capacity steel plants where the rolling can be performed at relatively low temperatures. 20Nb can be added to increase $T_{5\%}$. With the proper design of the rolling process, the whole finish rolling or several passes of the finish rolling can be

performed below $T_{5\%}$. Therefore, final product with much finer grains can be achieved which could yield large increase in the final properties.

In the early discussion, it is found that the $T_{5\%}$ was related to the Nb supersaturation. Using the same homogenisation temperature 1250°C, a calculation of Nb supersaturation was performed on the steels with 0.02 wt% Nb and up to 0.4 wt% C as shown in Figure 5-19. The supersaturations for steels with C content between 0.08 wt% and 0.26 wt% at 950°C are higher than the Nb supersaturation of 8C20Nb steel (0.016 wt%). As a result, steels with 0.02 wt% Nb and 0.08-0.26 wt% C are expected to have a $T_{5\%}$ higher than 950°C and a similar deformation behaviour with 8C20Nb steels. For steels with 0.02 wt% Nb and >0.26 wt% C, and steels with <0.02 wt% Nb, $T_{5\%}$ are expected to be lower than 950°C due to the smaller Nb supersaturation. Therefore, a lower finish rolling temperature is required to fully retard the austenite recrystallisation.

Chapter 6 Conclusions

From the findings in current study, the following concluding remarks can be made:

6.1 Homogenisation behaviour

- The as homogenised prior-austenite grains showed finer grain size with the increase in the C contents.
- Dilute Nb contents did not make a noticeable influence on the homogenised prior-austenite grain size.
- The dramatic increase in C content influenced the dissolution behaviour of Nb. Undissolved NbC particles were found in the 40C20Nb and 60C20Nb as homogenised samples.
- The Nb dissolution behaviour was compared with the calculation from published solubility products. It was found that the solubility product proposed by Palmiere *et al* [72] best predicted the dissolution behaviour of NbC.
- At homogenisation temperature of 1250°C, Nb solubility limit was 0.057 wt%, 0.012 wt% and 0.08 wt% for 8C, 40C and 60C steels, respectively. Therefore, the Nb in solution after homogenisation at 1250°C for 1 hour was 0.02 wt%, 0.012 wt% and 0.08 wt% for 8C20Nb, 40C20Nb and 60C20Nb steels, respectively.

6.2 Dynamic recrystallisation behaviour during rough rolling

- The critical strain of dynamic recrystallisation was investigated by analysing the flow stress curves. The critical strain was determined by the inflection point of the work hardening rate – flow stress (θ-σ) curve or alternatively and probably

more accurately, the stationary point of the derivative of work hardening rate – flow stress ($(-\partial\theta/\partial\sigma) - \sigma$) curve.

- C content showed no detectable influence on the critical strain of dynamic recrystallisation.
- Nb in solution increased the critical strain of dynamic recrystallisation. With the strain rate of 0.2/s and temperature of 1100°C, the critical strain for dynamic recrystallisation was 0.07, 0.1, 0.13 and > 0.3 for steels with 0 wt%, 0.005 wt%, 0.01 wt% and 0.02 wt% Nb, respectively.

6.3 Recrystallisation behaviour after finish rolling

- The flow stress curves for finish rolling showed continuously work hardening. No dynamic recrystallisation was found during finish rolling in any of the steels.
- C content did not show any noticeable influence on the austenite recrystallisation behaviour after finish rolling.
- The recrystallisation was delayed by Nb in solution at all three deformation temperatures due to its retardation on the recovery and hence the onset of recrystallisation, but not from the retardation on the progress of recrystallisation.
- The evolution of austenite recrystallisation with deformation temperature exhibited a classic sigmoidal shape. A three parameter sigmoidal equation was proposed, which fitted well with the experimental data,

$$f_{RXN} = a/(1+\exp(-(T-x_0)/b))$$

where f_{RXN} is the percent recrystallisation, T is the rolling temperature in Celsius, a, b and x_0 are coefficients dependent on various steels.

- Applying this method to all the steels, and relationships between Nb content in solution and $T_{5\%}$ and $T_{95\%}$ after finish rolling were found, as follows:

$$T_{5\%} = 1151.7 + 39.9\ln([Nb] + 0.0008)$$

$$T_{95\%} = 1239.2 + 31.4\ln([Nb] + 0.0001)$$

where *[Nb]* is the solute Nb content. It is worth noticing that the evolution of T5% and T95% were irrespective of C content.

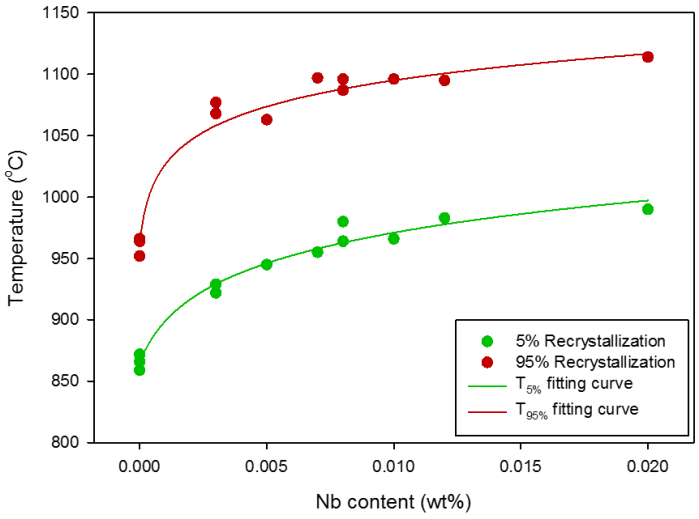

Figure 6-1 Evolution of $T_{5\%}$ and $T_{95\%}$ after finish rolling of steels with various Nb contents in solution (irrespective of C content change from 0.08 wt% to 0.6 wt%).

6.4 Recrystallisation behaviour after 20s isothermal holding period

- The fractional softening behaviour obtained from the double-hit PSC tests was used to determine critical temperatures associated with recrystallisation behaviour of the steels. 20% and 60% softening between passes were associated with $T_{5\%}$ and $T_{95\%}$ of recrystallisation.
- The quantitative metallography corresponds well with the fractional softening behaviour of austenite.
- Nb supersaturation was the critical parameter which determined whether Nb precipitation can happen.
- For all steels apart from steels with 0.02 wt% Nb (20Nb steels) being finish rolled at the finish rolling temperature of 950°C, precipitation did not happen due to the low Nb supersaturation. In those cases, substantial recrystallisation

happened after the 20s isothermal holding period as a result of a small retarding force on recrystallisation provided by the dilute Nb content in solution.

At the finish rolling temperatures of 1000°C and 950°C, higher Nb content led to smaller percent recrystallisation. This is believed to be a subsequent result from the delay of recovery and hence the onset of recrystallisation.

- For steels with 0.02 wt% Nb (20Nb steels) being finish rolled at the finish rolling temperature of 950°C, precipitation occurred. The precipitation pinning effect provided much larger retarding force on recrystallisation compared with the solute drag effect from the solute Nb.

  The precipitation particle size for all three steels was similar, which was around 5nm. However, the number density of the precipitates was increased with the increase of Nb supersaturation. The difference in Nb supersaturation was mainly attributed to the influence of C content on the Nb dissolution behaviour after homogenisation.

  The precipitation pinning force F_{PIN} was calculated using the subgrain boundary pinning mechanism [93]. The recrystallisation driving force was determined from the flow curves of the PSC tests. F_{RXN} was calculated based on the area under the flow stress curve of the first finish rolling. The quantitative comparison between F_{PIN} and F_{REX} showed great correspondence with fractional softening and the recrystallisation behaviours.

- Base on the microstructural observation, $T_{5\%}$ and $T_{95\%}$ for steels with various Nb contents in solution after finish rolling and the 20s holding period were superimposed on the deformation map, as shown in Figure 6-2.

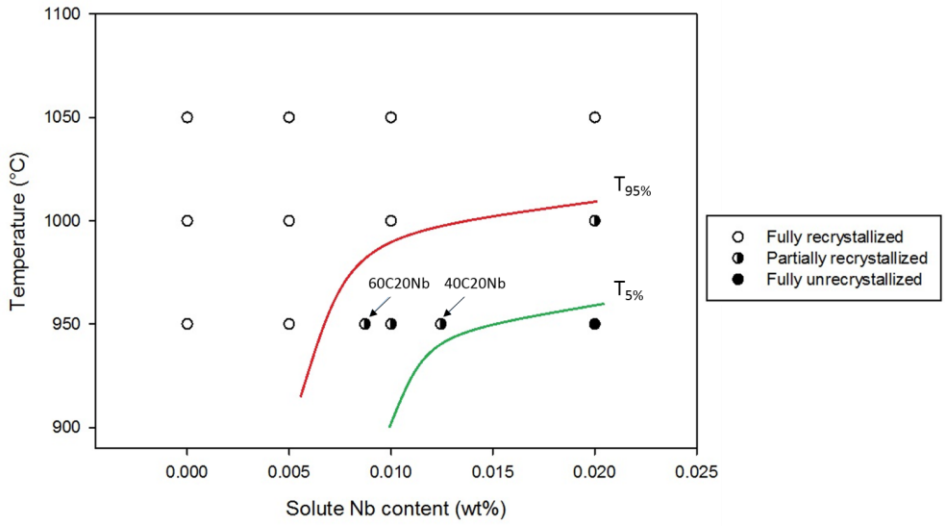

Figure 6-2 Deformation map showing various austenite microstructures after the 20s holding period with different solute Nb contents. $T_{5\%}$ and $T_{95\%}$ were superimposed on the map.

6.5 Grain growth behaviour during the 20s holding period

- The austenite grain growth behaviour was conducted on the steels deformed and isothermally held at the deformation temperature of 1050°C. There was no NbC precipitation at the end of the holding period at the deformation temperature of 1050°C. Therefore, the difference in austenite grain growth behaviour was attributed to the solute Nb and C.
- The austenite grain growth was slowed by both Nb and C in solution due to their solute drag effect on the grain boundary motion.
- For 8C steels, the prior-austenite grain size at the end of 20s holding period continuously decreased with the increase in dilute Nb contents.

  The solute drag effect from Nb was the dominant retarding force on grain growth due to the relatively low C content. As a result, Nb content as low as 0.005 wt% led to a clear refinement in the prior-austenite grain size.

  A semi-empirical equation to predict the austenite grain growth behaviour of 8C

steels as a function of solute Nb content was proposed based on Fan's [213] solute drag theory, as follows:

$$R_t^{2.5} - R_0^{2.5} = 2993.1\exp(-139.2[Nb])t$$

where R_0 is the starting grain size, R_t is the grain size at time t and $[Nb]$ is the Nb content in solution.

- For 40C steels, the prior-austenite grain size was similar for 40C0Nb, 40C5Nb and 40C10Nb steels. A clear refinement in prior-austenite grain size was observed for 40C20Nb steel.
- For 60C steels, the prior-austenite grain sizes were all similar and the dilute Nb additions did not make a difference on the prior-austenite grain sizes after the 20s holding period.
- There was a threshold Nb content (0.007-0.012 wt% for 40C steels and >0.008 wt% for 60C steels) to suppress the austenite grain growth. Below the threshold Nb content, the C contents provided the dominant retarding force. No refinement on austenite grain size from Nb was found. Whereas above the threshold Nb content, the retarding force from Nb was comparable with the retarding force provided by C. Therefore, an additional retarding force from solute Nb contributed to slow austenite grain growth. As a result, a further refinement in austenite grain size was found.

6.6 Industrial applications

- Fractional softening behaviour of austenite using the double hit compression can be a quick way to determine $T_{5\%}$ and $T_{95\%}$ of recrystallisation without the microstructural analysis.
- For steel plants with low capacity, where the rolling load is conducted at high temperature (>$T_{95\%}$), the dilute Nb addition is applicable since it will not increase the rolling load. For Nb content below the threshold content to slow austenite

grain growth in 40C and 60C steels, the dilute Nb additions have the potential to increase the strength of final product through either precipitation strengthening or/and solid solution strengthening. For steels where Nb additions slow the austenite grain growth (Nb in 8C steels and Nb content above the threshold in 40C and 60C steels), another contribution from grain refinement is expected to increase strength and toughness through the refinement of austenite grain size.

- For steel plants with high capacity, the finish rolling can be performed below $T_{5\%}$ through which much finer grains of final products can be achieved. An increase of around 30% of the rolling load needs to be taken into consideration.

Chapter 7 Future Work

According to the findings in the current study, areas of future research are suggested as follows:

- It is worth conducting the finish rolling at lower temperatures (800-950°C), through which the relationship between $T_{5\%}$, $T_{95\%}$ and Nb contents after 20s holding period could be established (Figure 5-11). Precipitation behaviour can be studied in steels with various dilute Nb additions being rolled below $T_{5\%}$.
- The $T_{5\%}$ and $T_{95\%}$ is influenced by the strain per pass (Figure 2-6). Therefore, the influence of strain on the $T_{5\%}$ and $T_{95\%}$ in steels with various dilute Nb additions can be studied.

  Combined with the influence of various Nb additions to the $T_{5\%}$ and $T_{95\%}$ (Figure 5-6 and Figure 5-11), a 3D map for $T_{5\%}$ and $T_{95\%}$ with the various strain per pass and Nb content could be generated as illustrated in Figure 7-1. This 3D map could be a powerful tool to tailor the steel composition and rolling parameters in different steel plants for various final properties.

- Various isothermal holding periods could be conducted to further validate and/or refine the austenite grain growth kinetics under the solute drag effect of Nb in 8C steels (Equation 5-11).
- The threshold Nb contents to slow austenite grain growth in 40C and 60C steels can be investigated in more detail. Higher solute Nb can be achieved through increasing the homogenisation temperature for 40C20Nb and 60C20Nb steels.

  The influence of various dilute Nb addition on austenite grain growth behaviour

during the holding period can be studied further in steels with 0.2 wt% C. This could provide more evidence to support our explanation on the influence of C on the effectiveness of dilute Nb to refine austenite grains. The relationship between C content and the threshold Nb content to slow austenite grain growth might also be established.

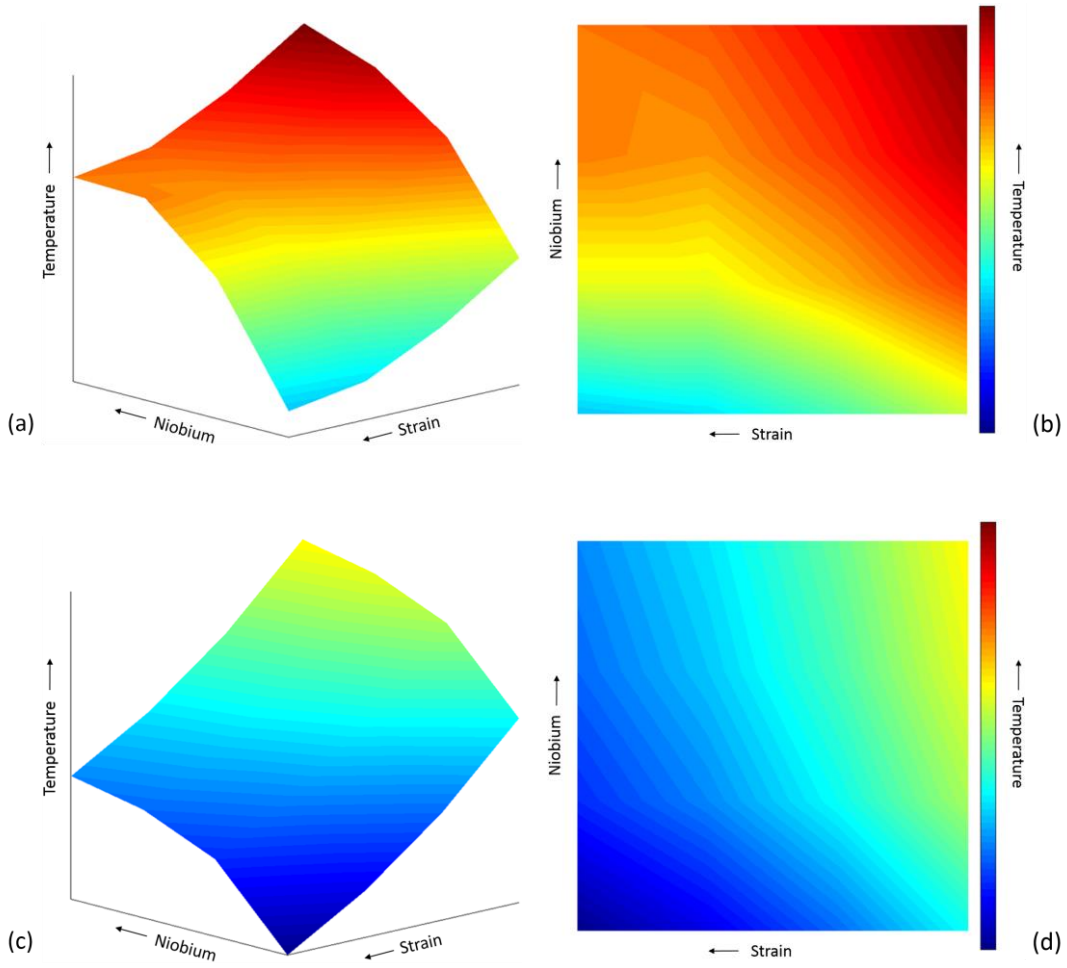

Figure 7-1 3D processing map, (a) and (c), illustrates the evolution of $T_{5\%}$ and $T_{95\%}$ with the change in strain per pass and Nb content. (b) and (d) are the corresponding contour maps to (a) and (c).

- The influence of dilute Nb additions to the phase transformation behaviours during the following cooling process can be investigated by cooling the steels with various Nb contents at selective cooling rates.

- Since the TMC machine has the capability to conduct multi-pass PSC tests with

accurate control of the deformation parameters, it is worth simulating the whole industrial rolling process on selective steels with representative cooling process after deformation. The mechanical properties of the steels can be tested and studied afterwards. This could provide the quantitative information on the benefits from dilute Nb to the austenite before transformation, transformed microstructure and the final mechanical properties of steels in industrial practice level.

References

[1] F. Grimpe, S. Meimeth, C. Heckmann, A. Liessem, A. Gehrke, Development, Production and Application of Heavy Plates in Grades up to X120, Super-High Strength Steels. (2005) 1–10.

[2] A.J. DeArdo, M.J. Hua, K.G. Cho, C.I. Garcia, On Strength of Microalloyed Steels: an interpretive review, Mater. Sci. Technol. 25 (2009) 1074–1082.

[3] L.J. Cuddy, J.J. Bauwin, J.C. Raley, Recrystallization in Austenite, Metall. Trans. A. 11 (1980) 381–386.

[4] H. de Boer, H. Masumoto, Niobium in Rail Steel, in: Niobium Sci. Technol., Niobium 2001 Ltd, Bridgeville, 2001: pp. 821–844.

[5] T. Kimura, Y. Kurebayashi, Niobium in Microalloyed Engineering steels, Wire Rods and Case Carburized Products., in: Int. Symp. Niobium 2001, 2001: pp. 801–819.

[6] Y. Zhang, A. Guo, S.G. Jansto, Q. Wang, Application Research of Nb Microalloying on Medium and High Carbon Long Products, in: HSLA Steels 2015, Microalloying 2015 Offshore Eng. Steels 2015, John Wiley & Sons, Inc., 2015: pp. 903–908.

[7] D.K. Matlock, J.G. Speer, Microalloying Concepts and Application in Long Products, Mater. Sci. Technol. 25 (2009) 1118–1125.

[8] M. Wright, Benefits of High Strength Microalloyed Rebar, in: HSLA Steels 2015, Microalloying 2015 Offshore Eng. Steels 2015, John Wiley & Sons, Inc., 2015: pp. 881–886.

[9] S. Hashimoto, M. Nakamura, Effects of Microalloying Elements on Mechanical Properties of Reinforcing Bars, Isij Int. 46 (2006) 1510–1515.

[10] H. Masumoto, K. Sugino, H. Hayashida, Development of Wear Resistant and Anti-Shelling High Strength Rails, in: Heavy Haul Railw. Conf. Proceeding, Institution of Engineers, Perth, Western Australia, 1978: pp. 1–8.

[11] W. Heller, R. Schweitzer, Microstructure and Wear Behaviour of Rail Steels, in: Proc. 2nd Int. Conf. Heavy Haul Railw., Association of American Railroads and American Society of Mechanical Engineers (1982), Colorado Springs, 1982: pp. 282–286.

[12] H.H. Cornell, Improvement in Carbon Rail Steels by the Addition of Niobium, 22 (1983) 347–351.

[13] U.P. Singh, R. Singh, S. Jha, Influence of Microalloying on Fracture Toughness and Wear Resistance of Rail Steel, Scand. J. Metall. 24 (n.d.) 180–186.

[14] A. Nolasco, E. Oliveira, G. Leonardos, P.J.. Bordignon, Niobium in Si-Mn rail steel, in: Proceeding Int. Symp. Niobium 81, San Francisco, 1981: pp. 1041–1060.

[15] C. Liu, Y. Huang, H. Liu, M. Jiang, Effects and Mechanisms of Niobium on the Fracture Toughness of Heavy Rail Steel, Adv. Mater. Res. 163–167 (2010) 110–116.

[16] S.G. Jansto, MicroNiobium Alloy Approach in Medium and High Carbon Steel Bar, Plate and Sheet Products, Metall. Mater. Trans. B. (2013).

[17] R.D.K. Misra, S. Shanmugam, T. Mannering, D. Panda, S.G. Jansto, Some Process and Physical Metallurgy Aspects of Niobium Microalloyed Steels for Heavy Structural Beams, in: Int. Conf. New Dev. Long Prod., 2006: pp. 179–187.

[18] U.P. Singh, A.M. Popli, D.K. Jain, B. Roy, S. Jha, Influence of Microalloying on Mechanical and Metallurgical Properties of Wear Resistant Coach and Wagon Wheel Steel, J. Mater. Eng. Perform. 12 (2003) 573–580.

[19] S.G. Jansto, Applied Metallurgy of the MicroNiobium ® Alloy Approach in Long and Plate Products, (2012).

[20] S.G. Jansto, MicroNiobium Steelmaking Alloy Approach in Eutectoid 1080 Wire Rod, in: AISTech - Iron Steel Technol. Conf. Proc., Indianapolis, 2014: pp. 43–47.

[21] World Steel Association, Buildings and infrastructure, Worldsteel Assoc. Steel Mark. Reports. (2016).

[22] F.J. Humphreys, M. Hatherly, Recrystallization and Related Annealing Phenomena, in: Elesvier, Oxford, 2004: pp.628.

[23] F.J. Humphreys, M. Hatherly, Recrystallization and Related Annealing Phenomena, in: Elsevier, Oxford, 2004: pp 12-14.

[24] L.A. Reza Abbaschian Robert E. Reed-Hill, Physical Metallurgy Principles, Cengage Learning, 2010.

[25] H.J. McQueen, J.J. Jonas, Recovery and Recrystallization during High Temperature Deformation, Treatise Mater. Sci. Technol. 6 (1975) 393–493.

[26] F.J. Humphreys, M. Hatherly, Recrystallization and Related Annealing Phenomena,

in: Elsevier, Oxford, 2004: pp. 169–171.

[27] D. Hull, J.D. Bacon, Introduction to Dislocations, Butterworth-Heinemann, 2011.

[28] B. Dutta, E.J. Palmiere, Effect of Prestrain and Deformation Temperature on the Recrystallization Behavior of Steels Microalloyed with Niobium, Metall. Mater. Trans. A. 34 (2003) 1237–1247.

[29] P.J. Hurley, P.D. Hodgson, B.C. Muddle, A Study of Deformation Substructures in Austenite Using a Model Ni-30 wt.% Fe Alloy, Scr. Mater. 45 (2001) 25–32.

[30] J.G. Lenard, M. Pietrzyk, L. Cser, Mathematical and Physical Simulation of the Properties of Hot Rolled Products, 1999.

[31] J.G. Lenard, Primer on Flat Rolling, 2014.

[32] W. Roberts, B. Ahlblom, A Nucleation Criterion for Dynamic Recrystallization during Hot Working, Acta Metall. 26 (1978) 801–813.

[33] R.A. Petković, M.J. Luton, J.J. Jonas, Recovery and Recrystallization of Carbon Steel between Intervals of Hot Working, Can. Metall. Q. 14 (1975) 137–145.

[34] E.J. Palmiere, C.I. Garcia, A.J. DeArdo, The Influence of Niobium Supersaturation in Austenite on the Static Recrystallization Behavior of Low Carbon Microalloyed Steels, in: R. Asfahani, G. Tither (Eds.), Int. Symp. “Low-Carbon Steel 90’s,” TMS, Pittsburgh, PA, 1993: pp. 121–130.

[35] E.J. Palmiere, C.I. Garcia, A.J. DeArdo, The Influence of Niobium Supersaturation in Austenite on the Static Recrystallization Behavior of Low Carbon Microalloyed Steels, Metall. Mater. Trans. A. 27 (1996) 951–960.

[36] A.J. DeArdo, Fundamental Aspects of the Physical Metallurgy of Thermomechanical Processing of Steel, in: Int. Conf. Phys. Metall. Thermomechanical Process. Steels Other Met. THERMEC-88., 1988: pp. 20–29.

[37] E.J. Palmiere, PhD Thesis: Suppression of Recrystallization during the Hot Deformation of Microalloyed Austenite, University of Pittsburgh, 1992.

[38] C. Zener, J.H. Hollomon, Effect of Strain Rate upon Plastic Flow of Steel, J. Appl. Phys. 15 (1944) 22–32.

[39] C.M. Sellars, W.J. McTegart, On the Mechanism of Hot Deformation, Acta Metall. 14 (1966) 1136–1138.

[40] F.J. Humphreys, M. Hatherly, Recrystallization and Related Annealing Phenomena,

in: Elsevier, Oxford, 2004: pp. 1–10.

[41] C.M. Sellars, From Trial and Error to Computer Modelling of Thermomechanical Processing, Ironmak. Steelmak. 38 (2011) 250–257.

[42] N. Hansen, Hall-Petch Relation and Boundary Strengthening, Scr. Mater. 51 (2004) 801–806.

[43] A.J. DeArdo, C.I. Garcia, E.J. Palmiere, Thermomechanical Processing of Steel, in: Met. Handb., ASM International, 1991: pp. 237–255.

[44] R.W.K. Honeycombe, H.K.D.H. Bhadeshia, H. Bhadeshia, Steels: Microstructure and Properties, E. Arnold, 1995.

[45] H.-G. Hillenbrand, M. Graf, C. Kalwa, Development and Production of High Strength Pipeline Steels, Int. Symp. Niobium. (2002) 543–569.

[46] M. Cohen, S.S. Hansen, On the Fundamentals of HSLA Steels, HSLA Steels Metall. Appl. (1985) 61–71.

[47] L.J.Cuddy, G.R. Speich C.R. Gordon, A.J. DeArdo, International Conference on Phase Tranformation In Ferrous Alloys, in: J.I.G. A.R. Marder (Ed.), Int. Conf. Phase Tranformation Ferr. Alloy., TMS-AIME, Warrendale, PA, 1984: pp. 341–389.

[48] L. Cuddy, Grain Refinement of Nb Steels by Control of Recrystallization during Hot Rolling, Metall. Mater. Trans. A. 15 (1984) 87–98.

[49] J.M.Gray, A.J. DeArdo L. Meyer, in Niobium, in: H. Stuart (Ed.), TMS-AIME, Warrendale, PA, 1984: p. 685.

[50] A.J. Deardo, Metallurgical Basis for Thermomechanical Processing of Microalloyed Steels, Ironmak. Steelmak. 28 (2001) 138–144.

[51] S. Vervynckt, K. Verbeken, B. Lopez, J.J. Jonas, Modern HSLA Steels and Role of Non-Recrystallisation Temperature, Int. Mater. Rev. 57 (2012) 187–207.

[52] T. Siwecki, A. Sandberg, W. Roberts, R. Lagneborg, The Influence of Processing Route and Nitrogen Content on Microstructure Development and Precipitation Hardening in Vanadium-Microalloyed HSLA-Steels, in: A.J. DeArdo, G.A. Ratz, P.J. Weay (Eds.), Thermomechanical Process. Microalloyed Austenite, AIME, Pittsburgh, PA, 1981: pp. 163–194.

[53] G.R. Speich, Formation of Ferrite From Controlled Rolled Austenite, Proc. Phase Transform. Ferr. Alloy. PA TMS-AIME, 1984). pp: 341–390.

[54] C. Ouchi, T. Ssmpei, I. Kozasu, The Effect of Hot Rolling Condition and Chemical Composition on the Onset Temperature of γ-α Transformation after Hot Rolling, Trans. Iron Steel Inst. Japan. 22 (1982) 214–222.

[55] A. Thorvaldsen, The Intercept Method—2. Determination of Spatial Grain Size, Acta Mater. 45 (1997) 595–600.

[56] C. Ouchi, T. Okita, S. Yamamoto, Effects of Interrupted Accelerated Cooling after Controlled Rolling on the Mechanical Properties of Low Alloy Steels, Trans. Iron Steel. 67 (1982) 608–616.

[57] S. Yue, Thermomechanical Processing of Ferrous Alloys, in: ASM Handbook, Vol. 14A - Metalwork. Bulk Form., ASM International, 2005: pp. 286–296.

[58] L.J. Cuddy, The Effect of Microalloy Concentration on the Recrystallisation of Austenite during Hot Deformation, in: A.J. DeArdo, G.A. Ratz, P.J. Wray (Eds.), Thermomechanical Process. Microalloyed Austenite, 1981: pp. 129–140.

[59] T. Gladman, The Physical Metallurgy of Microalloyed Steels, 2nd ed., Institute of Materials London, London, 1997.

[60] A.J. Deardo, Niobium in Modern Steels, Int. Mater. Rev. 48 (2003) 371–402.

[61] Z. Patel, K. Khul'ka, Niobium for Steelmaking, Metallurgist. 45 (2001) 477–480.

[62] R.D.K. Misra, H. Nathani, J.E. Hartmann, F. Siciliano, Microstructural Evolution in a New 770 MPa Hot Rolled Nb-Ti Microalloyed Steel, Mater. Sci. Eng. A. 394 (2005) 339–352.

[63] W.M. Rainforth, M.P. Black, R.L. Higginson, E.J. Palmiere, C.M. Sellars, I. Prabst, P. Warbichler, F. Hofer, Precipitation of NbC in a Model Austenitic Steel, Acta Mater. 50 (2002) 735–747.

[64] K. Nishioka, K. Ichikawa, Progress in Thermomechanical Control of Steel Plates and Their Commercialization, Sci. Technol. Adv. Mater. 13 (2012) 23001.

[65] R. Lagneborg, T. Siwecki, S. Zajac, B. Hutchinson, The Role of Vanadium in Microalloyed Steels, Scand. J. Metall. 28 (1999) 186–241.

[66] H. Gondoh, T. Osuka, Applications of Niobium Microalloyed Ferrite Pearlite Steels to Line Pipe and Plate, (1984).

[67] L. Meyer, F. Heisterkamp, W. Mueschenborn, Columbium, Titanium, and Vanadium in Normalized, Thermo-Mechanically Treated and Cold-Rolled Steels, in: J. Crane

(Ed.), Microalloying 75, Union Carbide Corporation, New York, NY, 1977: pp. 153–167.

[68] M.J.Spanraft, T.M. Hoogendoorn, Quantifying the Effect of Microalloying Elements on Structures during Processing, in: J. Crane (Ed.), Microalloying 75, Union Carbide Corporation, New York, NY, 1977: pp. 75–85.

[69] M.A. Altuna, B. Pereda, I. Gutie, M. Society, Precipitation of Nb in Ferrite After Austenite Conditioning. Part I: Microstructural Characterization, (2012).

[70] R.W.K. Honeycombe, Fundamental Aspects of Precipitation in Microalloyed Steels, HSLA Steels Metall. Appl. (1985) 243–250.

[71] D.P. Dunne, Review: Interaction of Precipitation with Recrystallisation and Phase Transformation in Low Alloy Steels, Mater. Sci. Technol. 26 (2010) 410–420.

[72] E.J. Palmiere, C.I. Garcia, A.J. DeArdo, Compositional and Microstructural Changes which Attend Reheating and Grain Coarsening in Steels Containing Niobium, Metall. Mater. Trans. A. 25 (1994) 277–286.

[73] Z. Cui, J. Patel, E.J. Palmiere, Thermomechanical Processing of Structural Steels with Dilute Niobium Additions, in: HSLA Steels 2015, Microalloying 2015 Offshore Eng. Steels 2015, John Wiley & Sons, Inc., 2015: pp. 281–287.

[74] P. Gong, E.J. Palmiere, W.M. Rainforth, Dissolution and Precipitation Behaviour in Steels Microalloyed with Niobium during Thermomechanical Processing, Acta Mater. 97 (2015) 392–403.

[75] B. Dutta, E.J. Palmiere, C.M. Sellars, Modelling the Kinetics of Strain Induced Precipitation in Nb Microalloyed Steels, Acta Mater. 49 (2001) 785–794.

[76] H. Nordberg, B. Aronsson, Solubility of Niobium Carbide in Austenite, J Iron Steel Inst. 206 (1968) 1263–1266.

[77] P.R. Smith, The Solubility of Niobium Carbide in Gramma Iron, Trans. Metall. Scoiety AIME. 236 (1966) 220.

[78] K. Narita, Physical Chemistry of the Group IVa (Ti, Zr), Va (V, Nb, Ta) and the Rare Earth Elements in Steel, Trans. Iron Steel Inst. Japan. 15 (1975) 145.

[79] T.H. Johansen, N. Christensen, B. Augland, The Solubility of Niobium (Columbium) Carbide in Gamma Iron., Technical University of Norway, Trondheim, 1967.

[80] T. Mori, M. Tokizane, K. Yamaguchi, E. Sunami, Y. Nakazima, Thermodynamic

Properties of Niobium Carbides and Nitrides in Steels, Tetsu-to-Hagane. 54 (1968) 763–776.

[81] H.L. Andrade, M.G. Akben, J.J. Jonas, Effect of Molybdenum, Niobium, and Vanadium on Static Recovery and Recrystallization and on Solute Strengthening in Microalloyed Steels, Metall. Trans. A. 14 (1983) 1967–1977.

[82] R.C. Sharma, V.K. Lakshmanan, J.S. Kirkaldy, Solubility of Niobium Carbide and Niobium Carbonitride in Alloyed Austenite and Ferrite, Metall. Trans. A. 15, 545–553.

[83] K. Balasubramanian, J.S. Kirkaldy, Themodynamics of Fe-Ti-C and Fe-Nb-C Austenite and Nonstoichiometric Titanium and Niobium Carbides, in: J.D. Embury, G.R. Purdy (Eds.), Adv. Phase Transitions, Pergamon Press, Ontario, 1987: p. 37.

[84] R.P. Smith, The Solubility of Niobium Nitride in Gamma Iron, Trans. Metall. Scoiety AIME. 224 (1962) 190.

[85] M.L. Santella, PhD Thesis: Grain Growth and High-temperature Hot Rolling Behavior of Low-alloy Steel Austenite, University of Pittsburgh, 1981.

[86] K.J. Irvine, F.B. Pickering, T. Gladman, Grain-refined C-Mn steels, Iron Steel Inst J. 205 (1967) 161–182.

[87] A.J. DeArdo, Metals Handbook, in: Met. Handb., 8th ed., ASM International, Materials Park, Ohio, 1991: p. 237.

[88] A. Chamisa, PhD thesis: Development of Ultra High Strength Steels for Reduced Carbon Emission in Automotive Vehicles, University of Sheffield, 2014.

[89] J.G. Speer, S.S. Hansen, Austenite Recrystallization and Carbonitride Precipitation in Niobium Microalloyed Steels, Metall. Trans. A. 20 (1989) 25–38.

[90] D.Q. Bai, S. Yue, W.P. Sun, J.J. Jonas, Effect of Deformation Parameters on the No-Recrystallization Temperature in Nb-Bearing Steel, Metall. Trans. A. 24 (1993) 2151–2159.

[91] B. Dutta, C.M. Sellars, Effect of Composition and Process Variables on Nb(C, N) Precipitation in Niobium Microalloyed Austenite, Mater. Sci. Technol. 3 (1987) 197–206.

[92] B. Dutta, E. Valdes, C.M. Sellars, Mechanism and Kinetics of Strain Induced Precipitation of Nb(C,N) in Austenite, Acta Metall. Mater. 40 (1992) 653–662.

[93] S.S. Hansen, J.B. Vander Sande, M. Cohen, Niobium Carbonitride Precipitation and Austenite Recrystallization in Hot-Rolled Microalloyed Steels, Metall. Trans. A. 11 (1980) 387–402.

[94] S.H. Cho, K.B. Kang, J.J. Jonas, The Dynamic, Static and Metadynamic Recrystallization of a Nb-microalloyed Steel, Isij Int. 41 (2001) 63–69.

[95] R. Abad, A.I. Fernandez, B. Lopez, J.M. Rodriguez-Ibabe, Interaction between Recrystallization and Precipitation during Multipass Rolling in a Low Carbon Niobium Microalloyed Steel, Isij Int. 41 (2001) 1373–1382.

[96] E. Valdes, C.M. Sellars, Influence of Roughing Rolling Passes on Kinetics of Strain Induced Percipitation of Nb(C,N), Mater. Sci. Technol. 7 (1991) 622–630.

[97] J. Wadsworth, J. Woodhead, S. Keown, The Influence of Stoichiometry upon Carbide Precipitation, Met. Sci. 10 (1976) 342–348.

[98] D.A. Porter, K.E. Easterling, Phase Transformations in Metals and Alloys, Chapman & Hall, 1992.

[99] L.J. Cuddy, J.C. Raley, Austenite Grain Coarsening in Microalloyed Steels, Metall. Trans. A. 14 (1983) 1989–1995.

[100] T. Gladman, in: Recryst. Grain Growth Multiph. Part. Contain. Mater., Riso National Laboratories, 1980: pp. 183–192.

[101] T. Gladman, in: HSLA Steels, TMS, Warrendale, PA, 1992: pp. 3–14.

[102] I. Weiss, J.J. Jonas, Dynamic Precipitation and Coarsening of Niobium Carbonitrides during the Hot Compression of HSLA Steels, Metall. Trans. A. 11 (1980) 403–410.

[103] T. Gladman, On the Theory of the Effect of Precipitate Particles on Grain Growth in Metals, Proc. R. Soc. A Math. Phys. Eng. Sci. 294 (1966) 298–309.

[104] S. Yamamoto, C. Ouchi, T. Osuka, The Effect of Microalloying Elements on the Recovery and Recrystallization in Deformed Austenite, in: Thermomechanical Process. Microalloyed Austenite, 1981: pp. 613–639.

[105] F.B. Pickering, High-Strengh, Low-Alloy Steels - A Decade of Progress, in: Microalloying 75, Union Carbide Corporation, New York, NY, 1977: pp. 9–31.

[106] T. Gladman, D. Dulieu, Grain Size Control in Steels, Met. Sci. (1974) 167–176.

[107] B.K. Panigrahi, Processing of Low Carbon Steel Plate and Hot Strip—An Overview, Bull. Mater. Sci. 24 (2001) 361–371.

[108] G. Krauss, Steels: Processing, Structure, and Performance, ASM International, 2015.

[109] R.D. Doherty, D.A. Hughes, F.J. Humphreys, J.J. Jonas, D.J. Jensen, M.E. Kassner, W.E. King, T.R. McNelley, H.J. McQueen, A.D. Rollett, Current Issues in Recrystallization: A review, Mater. Today. 1 (1998) 14–15.

[110] S. Zajac, T. Siwecki, B. Hutchinson, M. Attlegård, Recrystallization Controlled Rolling and Accelerated Cooling for High Strength and Toughness in V-Ti-N steels, Metall. Trans. A. 22 (n.d.) 2681–2694.

[111] M. Hillert, On the Theory of Normal and Abnormal Grain Growth, Acta Metall. 13 (1965) 227–238.

[112] S. Yamamoto, C. Ouchi, T. Osuka, Thermomechanical Processing of Microalloyed Austenite, in: TMS, Warrendale, 1982: pp. 613–639.

[113] L.J. Cuddy, Thermomechanical Processing of Microalloyed Austenite, ed. by AJ DeArdo, GH Ratz PJ Wray, TMS-AIME, Warrendale, PA. 129 (1982).

[114] L.J. Cuddy, Microstructures Developed during Thermomechanical Treatment of HSLA Steels, Metall. Trans. A. 12 (1981) 1313–1320.

[115] Y. Zheng, G. Fitzsimons, A.J. DeArdo, Achieving Grain Refinement Through Recrystallization Controlled Rolling, in: M. Korchynsky (Ed.), HSLA Steels Technol. Appl., ASM International, Metals Park, OH, 1984: p. 85.

[116] J.W. Cahn, The Impurity-Drag Effect in Grain Boundary Motion, Acta Metall. 10 (1962) 789–798.

[117] K. Lücke, K. Detert, A Quantitative Theory of Grain-Boundary Motion and Recrystallization in Metals in the Presence of Impurities, Acta Metall. 5 (1957) 628–637.

[118] K. Lucke, H.P. Stuwe, in: L. Himmel (Ed.), Recover. Recryst. Met., Interscience, New York, 1963: p. 171.

[119] F.J. Humphreys, M. Hatherly, Recrystallization and Related Annealing Phenomena, in: Elsevier, Oxford, 1996: p. 114.

[120] L. Fu, A. Shan, Effect of Nb Solute Drag and NbC Precipitate Pinning on the Recrystallisation Grain Growth in Low Carbon Nb-Microalloyed Steel, (2010) 832–837.

[121] L.M. Fu, H.R. Wang, W. Wang, A.D. Shan, Austenite Grain Growth Prediction

Coupling with Drag and Pinning Effects in Low Carbon Nb Microalloyed Steels, Mater. Sci. Technol. 27 (2011) 996–1001.

[122] C.L. Miao, C.J. Shang, G.D. Zhang, S.V Subramanian, Recrystallization and Strain Accumulation Behaviors of High Nb-Bearing Line Pipe Steel in Plate and Strip Rolling, Mater. Sci. Eng. A. 527 (2010) 4985–4992.

[123] C.L. Miao, C.J. Shang, H.S. Zurob, G.D. Zhang, S. V Subramanian, Recrystallization, Precipitation Behaviors, and Refinement of Austenite Grains in High Mn, High Nb Steel, Metall. Mater. Trans. A. 43 (2012) 665–676.

[124] L. Sun, Phd Thesis: The Effects of Strain Path Reversal on Austenite Grain Subdivision, Recrystallisation and Phase Transformations in Microalloyed Steel, (2012).

[125] C.M. Sellars, Options and Constraints for Thermomechanical Processing of Microalloyed Steel, ASM Int. (1986) 73–81.

[126] S. Vervynckt, K. Verbeken, P. Thibaux, Y. Houbaert, Recrystallization–Precipitation Interaction during Austenite Hot Deformation of a Nb Microalloyed Steel, Mater. Sci. Eng. A. 528 (2011) 5519–5528.

[127] Y. Houbaert, K. Verbeken, S. Vervynckt, P. Thibaux, M. Liebeherr, Control of the Austenite recrystallization in Niobium Microalloyed steels, in: Mater. Sci. Forum, Trans Tech Publ, 2010: pp. 3567–3572.

[128] R.L. Bodnar, R.O. Adebanjo, S.S. Hansen, Determination of the TR and Ar3 Temperatures from Roll Force Measurements, in: Mech. Work. Steel Process. Conf. Proc., Iron and Steel Society of AIME, 1996: pp. 743–758.

[129] M. Gómez, L. Rancel, B.J. Fernández, S.F. Medina, Evolution of Austenite Static Recrystallization and Grain Size during Hot Rolling of a V-Microalloyed Steel, Mater. Sci. Eng. A. 501 (2009) 188–196.

[130] F. Boratto, R. Barbosa, S. Yue, J.J. Jonas, Effect of Chemical Composition on the Critical Temperatures of Microalloyed Steels, in: Int. Conf. Phys. Metall. Thermomechanical Process. Steels Other Met. THERMEC-88., 1988: pp. 383–390.

[131] T.M. Maccagno, J.J. Jonas, S. Yue, B.J. McCrady, R. Slobodian, D. Deeks, Determination of Recrystallization Stop Temperature from Rolling Mill Logs and Comparison with Laboratory Simulation Results., ISIJ Int. 34 (1994) 917–922.

[132] A.I. Zaky, Determinations of the Non-Recrystallization Temperature for X52 steel Produced by Compact Slab Process Combined with Direct Hot Rolling, J. Mater. Eng. Perform. 15 (2006) 651–655.

[133] W.P. Sun, M. Militzer, D.Q. Bai, J.J. Jonas, Measurement and Modelling of the Effects of Precipitation on Recrystallization under Multipass Deformation Conditions, Acta Metall. Mater. 41 (1993) 3595–3604.

[134] M. Gómez, L. Rancel, S.F. Medina, Assessment of Austenite Static Recrystallization and Grain Size Evolution During Multipass Hot Rolling of a Niobium-Microalloyed Steel, Met. Mater. Int. 15 (2009) 689–699.

[135] M. Gómez, S.F. Medina, A. Quispe, P. Valles, Static Recrystallization and Induced Precipitation in a Low Nb Microalloyed Steel, Isij Int. 42 (2002) 423–431.

[136] S.F. Medina, Determination of No-Recrystallisation Temperature in Nb-V-Ti Microalloyed Steel and Discussion of its Definition, Mater. Sci. Technol. 14 (1998) 217–221.

[137] F.H. Samuel, S. Yue, J.J. Jonas, K.R. Barnes, Effect of Dynamic Recrystallization on Microstructural Evolution during Strip Rolling, Isij Int. 30 (1990) 216–225.

[138] Y.B. Xu, Y.M. Yu, B.L. Xiao, Z.Y. Liu, G.D. Wang, Modelling of Microstructure Evolution during Hot Rolling of a High-Nb HSLA Steel, J. Mater. Sci. 45 (2010) 2580–2590.

[139] O. Kwon, A.J. DeArdo, Interactions between Recrystallization and Precipitation in Hot-Deformed Microalloyed Steels, Acta Metall. Mater. 39 (1991) 529–538.

[140] S. Vervynckt, Phd Thesis: Control of the Non-Recrystallization Temperature in High Strength Low Alloy (HSLA) Steels., DISS, Ghent University, 2010.

[141] A.B. LeBon, L.N. de Saint-Martin, Using Laboratory Simulations to Improve Rolling Schedules and Equipment, in: Microalloying 75, Union Carbide Corporation, New York, NY, 1977: pp. 90–98.

[142] H.J. McQueen, Review of Simulations of Multistage Hot-Forming of Steels, Can. Metall. Q. 21 (1982) 445–460.

[143] G. Li, T.M. Maccagno, D.Q. Bai, J.J. Jonas, Effect of Initial Grain Size on the Static Recrystallization Kinetics of Nb Microalloyed Steels, ISIJ Int. 36 (1996) 1479–1485.

[144] T. Siwecki, Modelling of Microstructure Evolution during Recrystallization

Controlled Rolling, ISIJ Int. 32 (1992) 368–376.

[145] T. Siwecki, G. Engberg, Recrystallization Controlled Rolling of Steels, Thermo-Mechanical Process. Theory. (1996) 121–144.

[146] T. Siwechi, G. Engberg, Recrystallisation Controlled Rolling of Steels, in: Thermomechanical Process. Theory, Model. Pract., 1997: pp. 121–143.

[147] T. Tanaka, T. Enami, M. Kimura, Y. Saito, T. Hatomura, Formation Mechanism of Mixed Austenite Grain Structure Accompanying Controlled-Rolling of Niobium-Bearing Steel, in: Thermomechanical Process. Microalloyed Austenite, 1981: pp. 195–215.

[148] M.G. Akben, I. Weiss, J.J. Jonas, Dynamic Precipitation and Solute Hardening in a V Microalloyed Steel and Two Nb Steels Containing High Levels of Mn, Acta Metall. 29 (1981) 111–121.

[149] A. Le Bon, J. Rofes-Vernis, C. Rossard, Recrystallization and Precipitation during Hot Working of a Nb-Bearing HSLA Steel, Met. Sci. 9 (1975) 36–40.

[150] J.E. Bailey, P.B. Hirsch, The Recrystallization Process in Some Polycrystalline Metals, Proc. R. Soc. London A Math. Phys. Eng. Sci. 267 (1962) 11–30.

[151] W.C. Leslie, The Physical Metallurgy of Steels, Hempisphere Pub. Corp., 1981.

[152] R.W.K. Honeycombe, The Plastic Deformation of Metals, Edward Arnold, 1984.

[153] O. Nino, D. Martinez, C. Lizcano, M. Guerrero-Mata, R. Colas, Study of the Tempcore Process for the Production of High Resistance Reinforcing Rods, Mater. Sci. Forum. 537–38 (n.d.) 533–540.

[154] S.G. Jansto, Metallurgical Mechanism and Niobium Effects on Improved Mechanical Properties in High Carbon Steels, in: HSLA Steels 2015, Microalloying 2015 Offshore Eng. Steels 2015, John Wiley & Sons, Inc., 2015: pp. 981–986.

[155] J. Patel, Technical report, CBMM Suisse.

[156] M.S. Loveday, G.J. Mahon, B. Roebuck, A.J. Lacey, E.J. Palmiere, C.M. Sellars, M.R. van der Winden, Measurement of Flow Stress in Hot Plane Strain Compression Tests, Mater. High Temp. 23 (2006) 85–118.

[157] J.S. Hinton, TMC Manual: Testing on the IMMPETUS Thermomechanical Compression (TMC) Test Machine, University of Sheffield, 2009.

[158] J. Hinton, PhD thesis: Laboratory Simulation of Microstructural Evolution in AISI

430 Ferritic Stainless Steel during the Steckel Mill Process, University of Sheffield, 2006.

[159] S.M. Byon, S.I. Kim, Y. Lee, Predictions of Roll Force under Heavy-Reduction Hot Rolling Using a Large-Deformation Constitutive Model, Proc. Inst. Mech. Eng. Part B J. Eng. Manuf. 218 (2004) 483–494.

[160] P. Uranga, I. Gutiérrez, B. López, Determination of Recrystallization Kinetics from Plane Strain Compression Tests, Mater. Sci. Eng. A. 578 (2013) 174–180.

[161] C. Garcia-Mateo, B. Lopez, J.M. Rodriguez-Ibabe, Effect of Deformation Temperature on Microstructure and Mechanical Behaviour of Warm Working Vanadium Microalloyed Steels, J. Mater. Sci. 46 (2011) 3725–3737.

[162] L. Bäcke, Modeling the Microstructural Evolution during Hot Deformation of Microalloyed Steels, 2009.

[163] M.J. Thomas, M. Rainforth, PhD thesis: The Effect of Thermomechanical Process Parameters on the Microstructure and Crystallographic Texture Evolution of Near-α Aerospace Alloy Timetal®834, Thesis, University of Sheffield, 2007.

[164] F.H. Samuel, S. Yue, J.J. Jonas, B.A. Zbinden, Modeling of Flow Stress and Rolling Load of a Hot Strip Mill by Torsion Testing, Isij Int. 29 (1989) 878–886.

[165] B. Xiao, PhD thesis: Multipass Laboratory Simulation of Steel Plate Hot Rolling for Improved Productivity, University of Sheffield, 2013.

[166] P.R. Krahe, M. Desnoues, Revealing the Former Austenite Grain Boundaries of High-Purity Iron-Carbon Alloys, Metallography. 4 (1971) 171–175.

[167] J.R. Vilella, Metallographic Technique for Steel, in: Society for Metals, 1938: p. 38.

[168] D.R. Barraclough, Etching of Prior Austenite Grain Boundaries in Martensite, Metallography. 6 (1973) 465–472.

[169] J. Reiter, C. Bernhard, H. Presslinger, Austenite Grain Size in the Continuous Casting Process: Metallographic methods and evaluation, Mater. Charact. 59 (2008) 737–746.

[170] M. Mirza, C. Sellars, Modelling the Hot Plane Strain Compression Test Part 3 – Effect of asymmetric conditions, Mater. Sci. Technol. 23 (2007) 567–576.

[171] A.S. E112-12, Standard Test Methods for Determining Average Grain Size, ASTM Int. West Consh (2014) 1–27.

[172] R.L. Higginson, C.M. Sellars, Worked Examples in Quantitative Metallography,

Maney, London, 2003.

[173] Astm, Standard Test Method for Determining Volume Fraction by Systematic Manual Point Count, Practice. (2011) 1–7.

[174] D.B. Williams, C.B. Carter, Transmission Electron Microscopy, Second Edi, Springer, 2009.

[175] P.J. Goodhew, J. Humphreys, R. Beanland, Electron Microscopy and Analysis, Third Edit, CRC Press, 2000.

[176] E.J. Palmiere, C.I. Garcia, A.J. DeArdo, Compositional and Microstructural Changes Which Attend Reheating and Grain Coarsening in Steels Containing Niobium, Metall. Mater. Trans. A. 25A (1994) 277–286.

[177] M.J. Luton, C.M. Sellars, Dynamic Recrystallization in Nickel and Nickel-Iron Alloys during High Temperature Deformation, Acta Metall. 17 (1969) 1033–1043.

[178] C.M. Sellars, Dynamic Recrystallization, Met. Forum. 4 (1-2) (1981) 75–80.

[179] E.I. Poliak, J.J. Jonas, A One-Parameter Approach to Determining the Critical Conditions for the Initiation of Dynamic Recrystallization, Acta Mater. 44 (1996) 127–136.

[180] A. Najafizadeh, J.J. Jonas, Predicting the Critical Stress for Initiation of Dynamic Recrystallization, ISIJ Int. 46 (2006) 1679–1684.

[181] Y.B. Cao, F.R. Xiao, G.Y. Qiao, C.J. Huang, X.B. Zhang, Z.X. Wu, B. Liao, Strain-Induced Precipitation and Softening Behaviors of High Nb Microalloyed Steels, Mater. Sci. Eng. A. 552 (2012) 502–513.

[182] C.R. Hutchinson, H.S. Zurob, C.W. Sinclair, Y.J.M. Brechet, The Comparative Effectiveness of Nb Solute and NbC Precipitates at Impeding Grain-Boundary Motion in Nb Steels, Scr. Mater. 59 (2008) 635–637.

[183] E.I. Poliak, J.J. Jonas, Initiation of Dynamic Recrystallization in Constant Strain Rate Hot Deformation, ISIJ Int. 43 (2003) 684–691.

[184] Z.H. Zhang, Y.N. Liu, X.K. Liang, Y. She, The Effect of Nb on Recrystallization Behavior of a Nb Microalloyed Steel, Mater. Sci. Eng. A. 474 (2008) 254–260.

[185] S.F. Medina, C.A. Hernandez, General Expression of the Zener-Hollomon Parameter as a Function of the Chemical Composition of Low Alloy and Microalloyed Steels, Acta Mater. 44 (1996) 137–148.

[186] T. Niu, Y.L. Kang, H.W. Gu, Y.Q. Yin, M.L. Qiao, J.X. Jiang, Effect of Nb on the Dynamic Recrystallization Behavior of High-Grade Pipeline Steels, Int. J. Miner. Metall. Mater. 17 (2010) 742–747.

[187] H.L. Wei, G.Q. Liu, Effect of Nb and C on the Hot Flow Behavior of Nb Microalloyed Steels, Mater. Des. 56 (2014) 437–444.

[188] L. Bäcke, Modeling the Effect of Solute Drag on Recovery and Recrystallization during Hot Deformation of Nb Microalloyed Steels, ISIJ Int. 50 (2010) 239–247.

[189] C. Ouchi, T. Okita, Dynamic Recrystallization Behavior of Austenite in Nb-bearing High Strength Low Alloy Steels and Stainless Steel, Trans. ISIJ. 22 (1982) 543–551.

[190] S. Serajzadeh, A.K. Taheri, An Investigation on the Effect of Carbon and Silicon on Flow Behavior of Steel, Mater. Des. 23 (2002) 271–276.

[191] H.L. Wei, G.Q. Liu, H.T. Zhao, M.H. Zhang, Effect of Carbon Content on Hot Deformation Behaviors of Vanadium Microalloyed Steels, Mater. Sci. Eng. A. 596 (2014) 112–120.

[192] H.W. Mead, C.E. Birchenall, Self-Diffusion of Iron in Austenite, J. Met. 8 (1956) 1336–1339.

[193] P. Feltham, The Plastic Flow of Iron and Plain Carbon Steels above the A3-Point, Proc. Phys. Soc. 66B (1953) 865.

[194] D.N. Crowther, B. Mintz, Influence of Carbon on Hot Ductility of Steels, Mater. Sci. Technol. 2 (1986) 671–676.

[195] A.M. Elwazri, P. Wanjara, S. Yue, Effect of Carbon Content on Dynamic Recrystallization Behaviour of Plain Carbon Steels, Can. Metall. Q. 43 (2004) 507–

[196] H. Beladi, P.D. Hodgson, Effect of Carbon on the Hot Deformation Behaviour in Nb Steels, in: Mater. FORUM, 2007.

[197] H. Beladi, P.D. Hodgson, Effect of Carbon Content on the Recrystallization Kinetics of Nb-Steels, Scr. Mater. 56 (2007) 1059–1062.

[198] D.C. Collinson, P.D. Hodgson, C.H.J. Davies, The Effect of Carbon on the Hot Deformation and Recrystallisation of Austenite, in: T. Chandra, T. Sakai (Eds.), Thermec' 97, TMS, 1997: pp. 483–490.

[199] Y.B. Cao, F.R. Xiao, G.Y. Qiao, X.B. Zhang, B. Liao, Quantitative Research on Effects of Nb on Hot Deformation Behaviors of High-Nb Microalloyed Steels, Mater.

Sci. Eng. A. 530 (2011) 277–284.

[200] A. Schmitz, J. Neutjens, J.C. Herman, V. Leroy, New Thermomechanical Hot Rolling Schedule for the Processing of High Strength Fine Grained Multiphase Steels, in: Mech. Work. STEEL Process. Conf. Proc., Citeseer, 1998: pp. 295–310.

[201] C.L. Miao, C.J. Shang, G.D. Zhang, G.H. Zhu, H. Zurob, S. Subramanian, Studies on Softening Kinetics of Niobium Microalloyed Steel Using Stress Relaxation Technique, Front. Mater. Sci. China. 4 (2010) 197–201.

[202] M.F. Ashby, R. Ebeling, On the Determination of the Number, Size, Spacing, and Volume Fraction of Spherical Second-Phase Particles from Extraction Replicas, AIME Met Soc Trans. 236 (1966) 1396–1404.

[203] M. Gomez, S.F. Medina, P. Valles, Determination of Driving and Pinning Forces for Static Recrystallization during Hot Rolling of a Niobium Microalloyed Steel, Isij Int. 45 (2005) 1711–1720.

[204] J.J. Jonas, I. Weiss, Effect of Precipitation on Recrystallization in Microalloyed Steels, Met. Sci. 13 (1979) 238–245.

[205] S.G. Hong, K.B. Kang, C.G. Park, Strain-Induced Precipitation of NbC in Nb and Nb–Ti Microalloyed HSLA Steels, Scr. Mater. 46 (2002) 163–168.

[206] Q. Yu, Y. Sun, Abnormal Growth of Austenite Grain of Low-Carbon Steel, Mater. Sci. Eng. A. 420 (2006) 34–38.

[207] E.D. Hondros, M.P. Seah, Segregation to Interfaces, Int. Mater. Rev. 22 (1977) 262–301.

[208] K.Y. Xie, T. Zheng, J.M. Cairney, H. Kaul, J.G. Williams, F.J. Barbaro, C.R. Killmore, S.P. Ringer, Strengthening from Nb-rich Clusters in a Nb-Microalloyed Steel, Scr. Mater. 66 (2012) 710–713.

[209] A.G. Kostryzhev, A.A. Shahrani, C. Zhu, S.P. Ringer, E.V Pereloma, Effect of Deformation Temperature on Niobium Clustering, Precipitation and Austenite Recrystallisation in a Nb–Ti Microalloyed Steel, Mater. Sci. Eng. A. 581 (2013) 16–25.

[210] S. Uhm, J. Moon, C. Lee, J. Yoon, B. Lee, Prediction Model for the Austenite Grain Size in the Coarse Grained Heat Affected Zone of Fe-C-Mn Steels: Considering the Effect of Initial Grain Size on Isothermal Growth Behavior, ISIJ Int. 44 (2004) 1230–

1237.

[211] J. Maity, D.K. Mondai, Isothermal Grain Growth of Austenite in Hypoeutectoid and Hypereutectoid Plain Carbon Steels, J. Iron Steel Res. Int. 17 (2010) 38–43.

[212] S.J. Lee, Y.K. Lee, Prediction of Austenite Grain Growth during Austenitization of Low Alloy Steels, Mater. Des. 29 (2008) 1840–1844.

[213] D. Fan, S.P. Chen, L.Q. Chen, Computer Simulation of Grain Growth Kinetics with Solute Drag, J. Mater. Res. 14 (2011) 1113–1123.

[214] P. Feltham, Grain Growth in Metals, Acta Mater. 5 (1957) 97–105.

[215] P. Hellman, M. Hillert, On the Effect of Second-Phase Particles on Grain Growth, Scand. J. Metall. 4 (1975) 211–219.

[216] P.D. Hodgson, R.K. Gibbs, A Mathematical Model to Predict the Mechanical Properties of Hot Rolled C-Mn and Microalloyed Steels, ISIJ Int. 32 (1992) 1329–1338.

[217] M. Gomez, S.F. Medina, A. Quispe, P. Valles, Static Recrystallization and Induced Precipitation in a Low Nb Microalloyed Steel, Isij Int. 42 (2002) 423–431.

[218] X. Liu, J.K. Solberg, R. Gjengedal, A.O. Kluken, Modelling of Interaction between Recrystallisation and Precipitation during Multipass Rolling of Niobium Microalloyed Steels, Mater. Sci. Technol. 11 (1995) 469–473.

[219] J.M. Rodriguez-Ibabe, B. López, Thermomechanical Processing and Role of Microalloying in Eutectoid SteelsAdvanced Steels, in: Y. Weng, H. Dong, Y. Gan (Eds.), Springer Berlin Heidelberg, 2011: pp. 475–484.

[220] Q. Yu, Z. Wang, X. Liu, G. Wang, Effect of Microcontent Nb in Solution on the Strength of Low Carbon Steels, Mater. Sci. Eng. A. 379 (2004) 384–390.

[221] G.F. Vander Voort, Metallography, Principles and Practice, in: ASM International, 1984: pp. 219–223.

[222] G.F. Vander Voort, Metallography, Principles and Practice, in: ASM International, 1984: pp. 435–440.

[223] E.S. Richter, Experiences with Etching Reagents to Show Former Austenite Grain Boundaries in Steels, Prakt. Metallogr. 35 (1998) 384–394.

[224] A. Brownrigg, P. Curcio, R. Boelen, Etching of Prior Austenite Grain Boundaries in Martensite, Metallography. 8 (1975) 529–533.

[225] G.F. Vander Voort, Wetting Agents in Metallography, Mater. Charact. 35 (1995) 135–137.

[226] J.A. Nelson, The Use of Wetting Agents in Metallographic Etchants, Prakt. Metallogr. 4 (1967) 192–198.

[227] M.W. Lui, I.L. May, Etching of Prior Austenite Grain Boundaries in AISI 4140 Steel, Metallography. 4 (1971) 443–450.

[228] C. García de Andrés, M.. Bartolomé, C. Capdevila, D. San Martín, F.. Caballero, V. López, Metallographic Techniques for the Determination of the Austenite Grain Size in Medium-Carbon Microalloyed Steels, Mater. Charact. 46 (2001) 389–398.

Appendix I TMC setting considerations for successful tests

To successfully conduct the PSC tests, the correct setting of many parameters is required such as the temperature for the test furnace, the effective strain for each pass.

The TMC machine is a cutting-edge machine by which many parameters can be controlled and recorded during a test. There are a large number of components involved in a single test. Even if all the settings are correctly set in a test, there will still be the possibility to fail a PSC test. For instance, PSC sample could hit one of the tools and then fall off the robot arms; the tools could loosen and become misaligned; the sample could stick to the tool after deformation etc. Some problems encountered and solved during PSC tests are discussed as follows.

I.1 PSC tools misalignment

Unlike axisymmetric test tools, which are two flat surfaces, the deformation sections on the PSC tools are protruded out. And the deformation sections on the top and bottom tools need to be parallel and aligned. The misaligned tools may cause asymmetrical deformation as illustrated by the Z-shaped sample after deformation, as seen in Figure I-1, which leads to two detrimental influences. First, the strain in the deformation area might be changed due to the possible shear stress. Second, due to the Z shape, the possibility of the sample hitting the tools is increased.

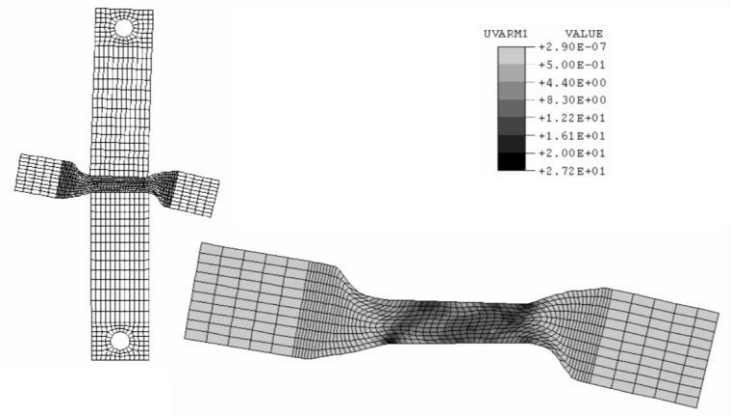

Figure I-1 Sample shows Z shape after deformation due to the misalignment of the tools [156].

The tools were aligned well every time when the tools were changed. However, since the PSC tests were conducted in extreme environments, i.e. high temperature (test furnace temperature above 900°C), high pressure, fast movement of the tools and most importantly the heating up and cooling down during days, the bolts, which attached the tools to the posts, could become loose. As a result, the tools could become misaligned during tests.

Before every test, it was important to check the tools were aligned and tightly attached to the posts. The alignment was checked visually. A metal stick was also used to touch the tools to check whether they were loose.

Once the misalignment happens, the tools need to be re-aligned manually before conducting any more tests. It needs to be done at room temperature, but cooling down and heating up the machine is time-consuming. Therefore, any issue that could possibly lead to the misalignment of the tools needs to be avoided. The main problem is the sample hitting the tool.

I.2 Sample hit the tool

As the sample is carried in and out the test furnace by the robot arms into the position in the middle of the tools, the relative position to both the upper and bottom tools is a very important factor to be considered before running a PSC test. As

explained in Chapter 3, the ideal position for the sample is about 2mm above the bottom tool.

An illustration of the relative position of the robot arm and tools is shown in Figure I-2 [158]. Possible problems related to the unsatisfactory robot arm position are shown too.

If the sample position is too low, the possibility of the sample hitting the bottom tool when it is carried in the test furnace is greatly increased. Hitting the tool causes two main problems. The first is the testing sample being wasted because the sample drops off from the robot arms into the test furnace. The second problem is tools misalignment as explained above. The reason why this is happening is the slight dipping of the sample due to the fast acceleration of the robot arms into the test furnace.

However, simply lifting the sample position up to have a bigger clearance between the sample and the bottom tool causes other problems. If the sample position is too high, the sample needs to move a long way after being contacted with the upper tool to be deformed. And when the load is removed, there will be a large vibration, as can be seen in Figure I-2. This excessive vibration combined with the fast movement of the robot arm will increase the chance of the sample dropping off the specimen holder.

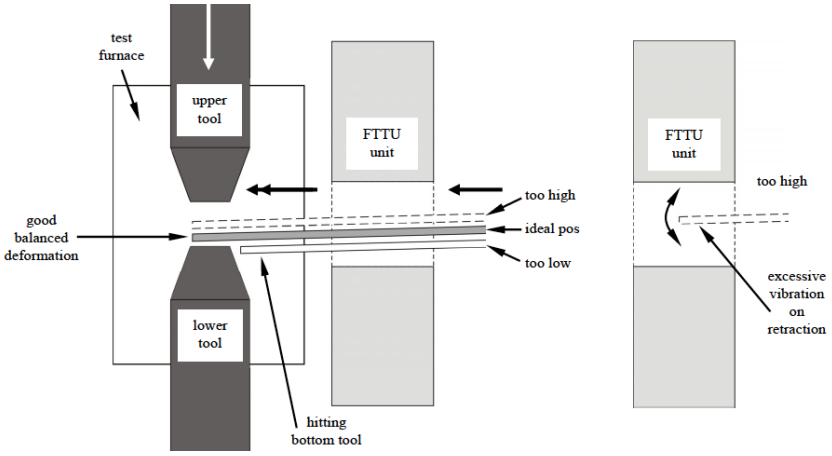

Figure I-2 An illustration of relative positions of the robot arm to the tools and the possible problems induced by the unsatisfactory positions [158].

I.3 Sample stuck on the tool

As explained in the deformation route in Chapter 3, the deformation simulation consists of both rough rolling and finish rolling. The rough rolling was conducted at high temperature 1100°C and with a low strain rate of 0.2/s and strain of 0.3. Due to the low strain rate, the deformation time for rough rolling was relatively long, about 1.5s.

Deforming the sample with high load at high temperature 1100°C for a long time 1.5s caused the sample to stick on the tools. Even though boron nitride lubricant was sprayed on both sides of the sample to play the role of anti-welding agent, a high percentage of the samples was stuck on one of the tools after rough rolling. This caused the failure of the test immediately as the thermocouple was broken when the robot arm retracted into the FTTU. The TMC automatically aborted the test due to the missing temperature reading.

The stuck sample was immediately removed by a long arm clamp from the test furnace. It was found that the sample was not firmly stuck on the tool, a small force was enough to remove it. A stronger bond between the sample and robot arms was considered to be the potential solution for this problem. The stronger bond was provided by binding the sample and robot arms together.

In order to bind them, two small holes were drilled on the non-deformation shoulder area of the PSC samples. Correspondingly, two holes were drilled on the robot arms too. Nickel-chrome wire was chosen as the string due to its high melting point (1400°C) and stability at high temperatures. The sample was bound carefully with two circles of nickel-chrome wire on both side to the robot arms, as can be seen in Figure I-3.

This attempt proved to be successful. After conducting this method, the sample never dropped off from the robot arms again and only one sample was attached to the tool after deformation.

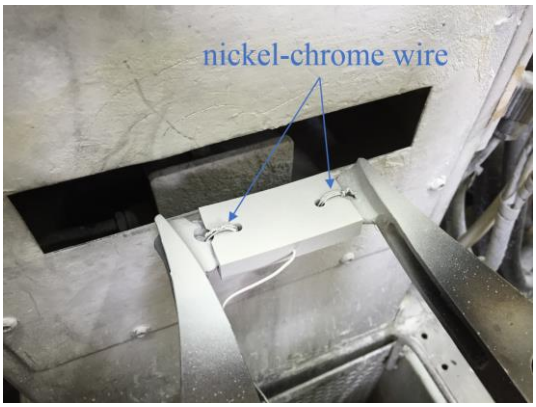

Figure I-3 PSC sample bound on the robot arms by nickel-chrome wire through the pre-drilled holes on both PSC sample and holder.

Appendix II Prior-austenite grain boundary etching

There is no doubt that to clearly reveal the prior-austenite grain boundaries is critical to the research focusing on austenite grain growth or the recrystallisation behaviour of austenite. In the current study, the quantitative analysis on the recrystallisation behaviour and grain growth behaviour would not be possible without the successful etching to reveal prior-austenite grain boundaries.

The etching methods in the literature failed to give satisfactory results for the steels used in this project. After large number of trial and error attempts, a new etching technique was found as explained in Section 3.4.3.2. In this new etching technique, there are some crucial influential factors comparing with the saturated picric acid aqueous solution etching reported by others [124,165–168,221–224]. The importance of each of the influential factors are discussed as follows.

II.1 Influential factors

II.1.1 Influence of the wetting agent

A wetting agent is the chemical which is added into etching solution in relatively small amount to change the surface energy of the solution and/or the sample so that the etching speed could be modified to have the best etching [225].

A study by D.R. Barraclough [168] in 1973 reported the successful delineation of prior-austenite grain boundaries by picric acid ethereal solutions with the tempered samples. He reported that variation of wetting agent showed little influence on the results which is contrary to the work done by J.A. Nelson [226]. J.A. Nelson [226] found in his work that the wetting agent played an important role. Sodium tridecyl benzene sulfonate used as a wetting agent suppressed the general inner structural etching and revealed the prior-austenite grain boundaries whereas none of the other

four wetting agents was as effective.

G.F. Vander Voort [225] has also reported in his review article that the wetting agent could be very critical to the etching process. Different wetting agents are reported to be effective in different steels with different chemical compositions and heat treatment conditions. The most widely used wetting agent in saturated picric acid aqueous solution for revealing prior-austenite grain boundaries is sodium dodecyl benzene sulfonate [227] or sodium alkylate sulfonate, which is also known as 'Teepol' [124,165,166,224].

In this study, the results show that the wetting agent plays a critical role on the etching results. According to the similar work done by other researchers [124,165], Teepol was tried first as the wetting agent. Sodium dodecyl benzene sulfonate was also tried due to its successful application reported in the literature. In addition, different etching parameters such as etching temperatures, amount of wetting agent, amount of HCl etc. were attempted. However, no good result was obtained. Teepol and sodium dodecyl benzene sulfonate have been proved to be unsatisfactory wetting agents in etching the high purity steels in this study.

During trial and error attempts of various wetting agents, another anionic surfactant sodium dodecyl sulfate, which has not previously been reported anywhere, was found to have excellent influence on revealing prior-austenite grain boundaries of the high purity steels in this study.

Figure II-1 shows an example of etching results on the 40C0Nb sample after finish rolling with Teepol and the sodium dodecyl sulfate. As can be seen in Figure II-1 (a), the martensitic microstructure has been revealed and the prior-austenite grain boundaries cannot be distinguished when Teepol was used as the wetting agent. The arrows in the images show etched prior-austenite grain boundaries.

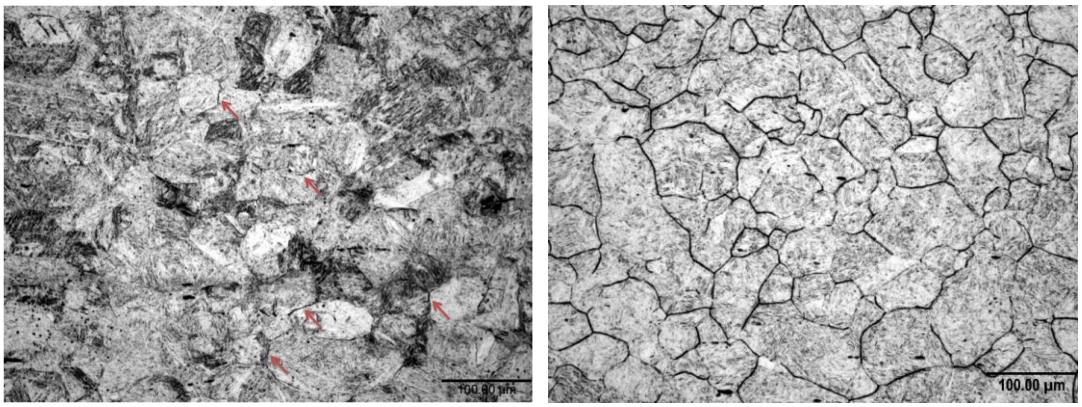

Figure II-1 Optical microscopy image of 40C0Nb steel after finish rolling at 1050°C (a) etched in saturated picric acid aqueous solution with three drops of hydrochloric and Teepol as wetting agent. Arrows show the etched prior-austenite grain boundaries (b) etched using the new etching technique.

By using sodium dodecyl sulfate as a new wetting agent, and following the etching procedure explained in Section 3.4.3.2, the etching of martensitic microstructure was greatly suppressed. At the same time, the etching of prior-austenite grain boundaries was enhanced. Hence, a clear and detailed result was obtained for the same sample, as shown in Figure II-1 (b).

II.1.2 Influence of the solution condition

In almost all the work done on etching so far, the attention has been focused on the chemical compositions of the solution. However, in this study, it was found that the condition of the solution also played a significant role.

From the observation during etching, an interesting trend was found. When the solution was first used when it was freshly made, see Figure 3-10 (a), unsatisfactory results were obtained, as can be seen in Figure II-2 (a). The prior-austenite grain boundaries were not delineated properly. Only small amounts of the prior-austenite grain boundaries were etched, as indicated by the arrows in Figure II-2 (a).

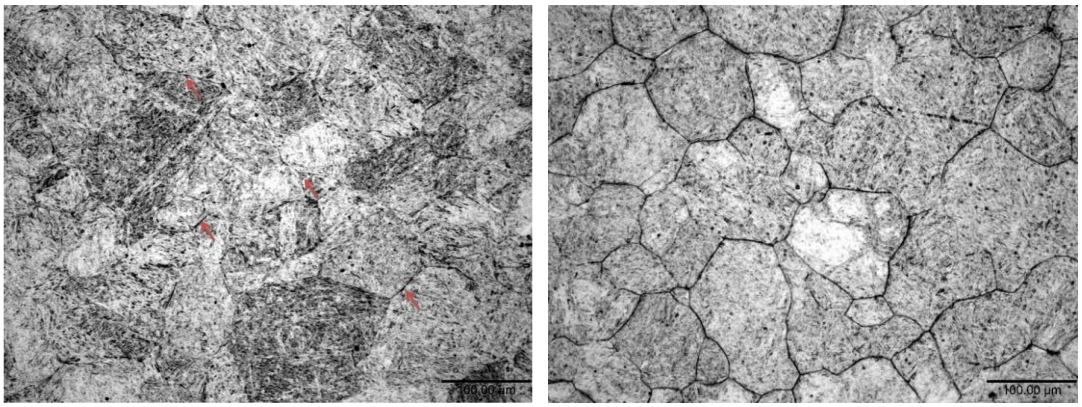

Figure II-2 Optical microscopy image of 60C20Nb steel after 20s holding period at 1050°C (a) etched in 'un-mature' solution. Arrows show the etched prior-austenite grain boundaries (b) etched in the mature solution.

However, when the etching went on, the colour of the solution became darker because the solution kept on reacting with the sample, as can be seen in Figure II-2 (b). The etching result became better as the solution got darker. The etching time for successful etching was consistently reduced by increasing the number of samples etched. This indicates that the solution became stronger as it reacted with the samples.

So the condition of the solution which gave the best etching was defined as 'mature' solution. It was found that after about 15 mins etching time the solution gave clear prior-austenite grain boundaries. Hence, to avoid the unsuccessful etching within the first 15 mins, three dummy samples were etched 5 mins each when a fresh solution was made. As a result, the solution was matured to give good etching. Figure II-2 shows the comparison of the same 60C20Nb steel being etched with unmature solution (Figure II-2 (a)) and mature solution (Figure II-2(b)).

To investigate whether good etching would be obtained if the fresh solution was made stronger, more picric acid powder was put in the solution. It gave unsatisfactory results and after a short time it started to form pits on the sample.

II.1.3 Influence of swabbing

When the solution reacted with the sample, etching product was produced on the

surface of the sample. Some researches [37,168] have reported that slightly swabbing the sample with cotton during etching generated better results. Putting the sample vertically or placing the beaker into the ultrasonic bath has the same purpose as swabbing the sample with cotton. The purpose of these is to remove the etching product from the sample surface when it is generated, so that the solution could keep reacting with the fresh surface of the sample.

In this study, swabbing the sample by cotton during etching was also tried. Other than the swabbing, everything was kept the same with the successful etching technique. The result shows removing the etching product from the surface of the sample is detrimental to the etching result.

Figure II-3 shows the optical microstructure of 40C20Nb steel after 20s holding period at 1050°C. As can be seen in Figure II-3 (a), when the etching product was constantly removed by swabbing, no prior-austenite grain boundaries were revealed. Instead, the martensitic microstructure was heavily revealed. The reason for this will be explained by the etching mechanism proposed in the next section.

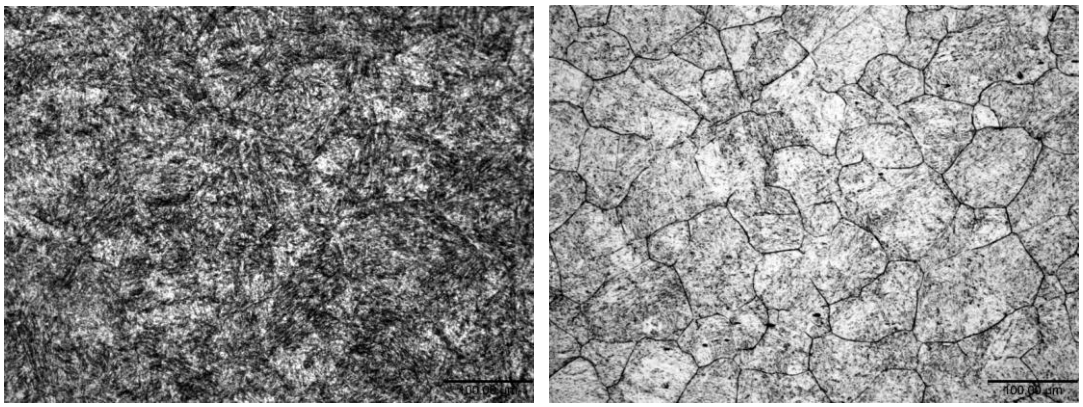

Figure II-3 Optical microscopy image of 40C20Nb steel after 20s holding period at 1050°C (a) etched by the successful etching technique with etching product being removed by cotton swabbing (b) etched by the successful etching technique

II.2 Mechanism of the new etching technique

Based on the observation during both successful and unsuccessful etching, the mechanism of the new etching technique is proposed as follows.

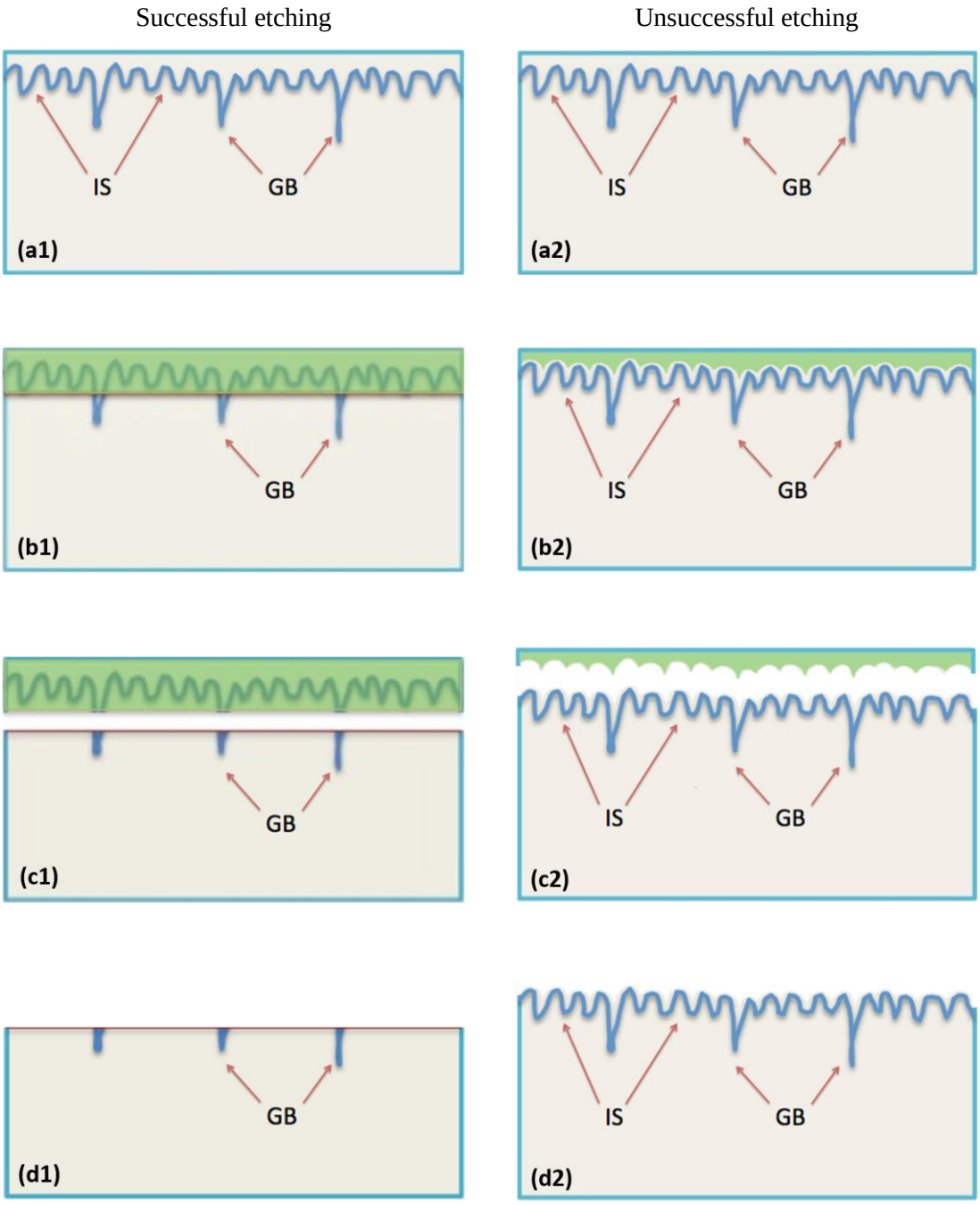

Figure II-4 Left column: Sketch illustration of the mechanism of the new etching technique Right column: Sketch illustration of the etching process of unsuccessful etching. IS: martensitic inner structure, GB: prior-austenite grain boundaries. (a1) and (a2): sectional view of the sample to be etched; (b1) and (b2): etching of the sample with the green area being the etching product; (c1) and (c2): etching product being removed from the sample surface after etching; (d1) and (d2): sectional view of the etched sample.

The successful etching process can be illustrated by the left column in Figure II-4. Figure II-4 (a1) shows the sectional view of the sample to be etched. The top surface is the polished surface to react with the etching solution. The curved lines in the sample show the potential microstructures to be observed after etching. As can be seen, the transformed martensitic inner structures within prior-austenite grains and the prior-austenite grain boundaries are both there potentially to be etched.

During etching, the solution keeps reacting with the sample. As explained above, the etching product was generated on the reacting surface. Because of the strong solution concentration of the matured solution and a proper etching time (2-4.5 mins depending on the condition of the solution), a certain depth of the sample was etched and transformed into the etching product. By keeping the sample still, i.e. no swabbing or ultrasonic bath, the etching product stayed on top of the reacting surface. As can be seen in Figure II-4 (b1), the green box indicates the etching product.

This etching product layer was considered to be the key of this new etching technique. The existence of this etching product layer made it harder for the solution to penetrate and react with the sample. So on the front line of etching reaction, which is the red line shown in Figure II-4 (b1), a natural shield was formed.

At this point, the solution was able to react with the prior-austenite grain boundaries but the reaction with the martensitic inner structure was prevented. This is because of the higher chemical potential the prior-austenite grain boundaries possess compared with the martensitic inner structure [228]. The chemical potential of prior-austenite grain boundaries was high enough to trigger the etching reaction and yet that of the inner structure was not enough. This was supported by the observation of the over-etched sample. As can be seen in Figure II-5, the majority of the etching pits were on the grain boundaries.

After etching, the sample was cleaned by running water and wiped with a wet cotton with washing liquid. The etching product layer was removed by the cotton, see Figure II-4 (c1). The existence of the etching product layer and the removal of it by

the cotton can be seen in Figure II-6. In Figure II-6 (a), it can be seen that the black product layer was on the surface of the sample. After it was removed, it revealed a shiny surface (shown in Figure II-6 (b)). The black mark on the cotton shows that the black product layer had been removed by the cotton.

After the etching product layer was removed, a microstructure with only nicely etched prior-austenite grain boundaries was obtained, as can be seen in Figure II-4 (d1).

The reasons for the unsuccessful etching can also be explained by the mechanism. The illustration of the unsuccessful etching process is shown in the right column in Figure II-4.

It has been discussed in Section I.1.1 that the wetting agent modifies the etching speed and sensitivity. The solution concentration plays the same role. When an unsatisfactory wetting agent was used or the solution concentration was not strong enough, only a thin layer of the sample was etched as shown in Figure II-4 (b2). The etching product layer was lack in depth to prevent the reaction between the solution and the lower chemical potential inner structure. Hence the natural shield of etching product layer could not be formed. The solution reacted with both the prior-austenite grain boundaries and the martensitic inner structures. So the messy microstructures were obtained, as shown in Figure II-1 (a) and Figure II-2 (a).

The failure of etching with the sample being swabbed, put vertically or ultrasonic bathed during etching can also be explained using this mechanism. The formation of the etching product with a certain depth needs a relatively long time. By conducting swabbing, the etching product was removed before the natural shield of thick etching product was formed. The etching process became the repetition of the process shown in the right column in Figure II-4 after each swabbing. Therefore, the microstructure with heavily etched martensitic structure was obtained, as shown in Figure II-3 (a).

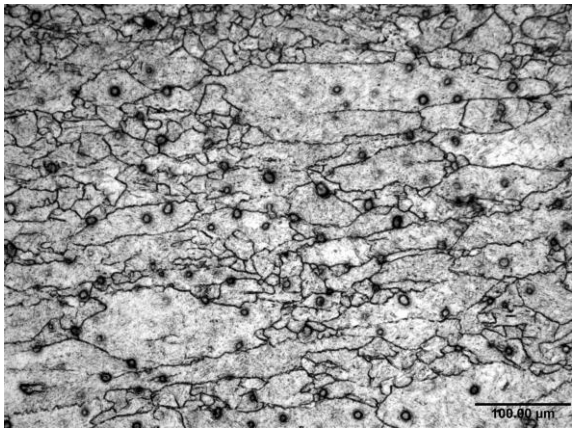

Figure II-5 Optical microscopy image of 60C10Nb sample after second rolling at 950°C, the sample is over-etched. The black dots are the etching pits.

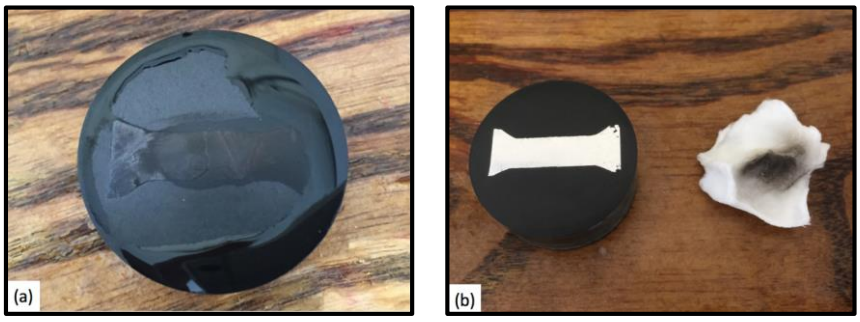

Figure II-6 (a) Sample after etching with the black etching product layer on the surface (b) Etching product layer removed by the cotton.

Appendix III Work hardening rate with respect to flow stress during rough rolling

$\theta = -0.0304\sigma^3 + 5.5063\sigma^2 - 343.18\sigma + 7523.1$, $R^2 = 0.8218$

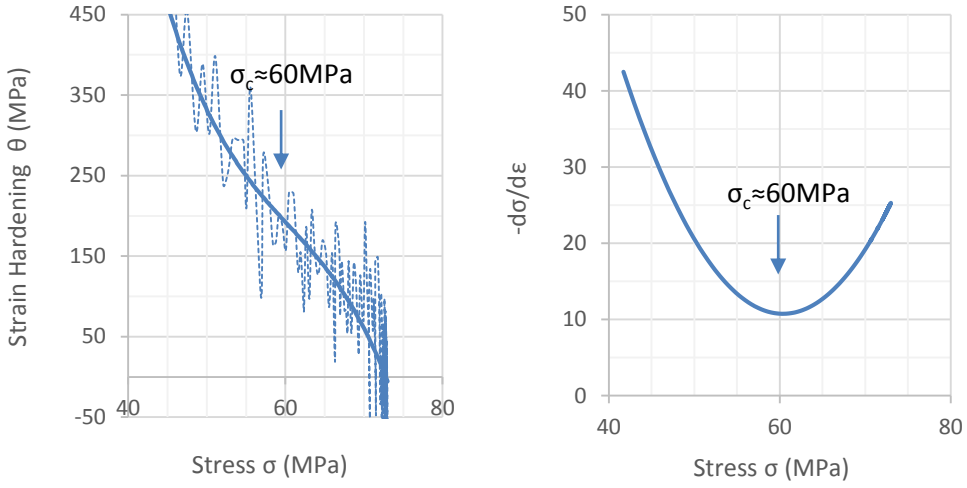

(a) (b)

Figure III-1 (a) Work hardening rate with respect to flow stress during rough rolling for 8C0Nb; (b) The critical stress for dynamic recrystallisation is indicated by the stationary point on the derivative curve of work hardening rate plotted against flow stress for 8C0Nb.

$\theta = -0.023\sigma^3 + 4.3503\sigma^2 - 283.81\sigma + 6480.3$, $R^2 = 0.8167$

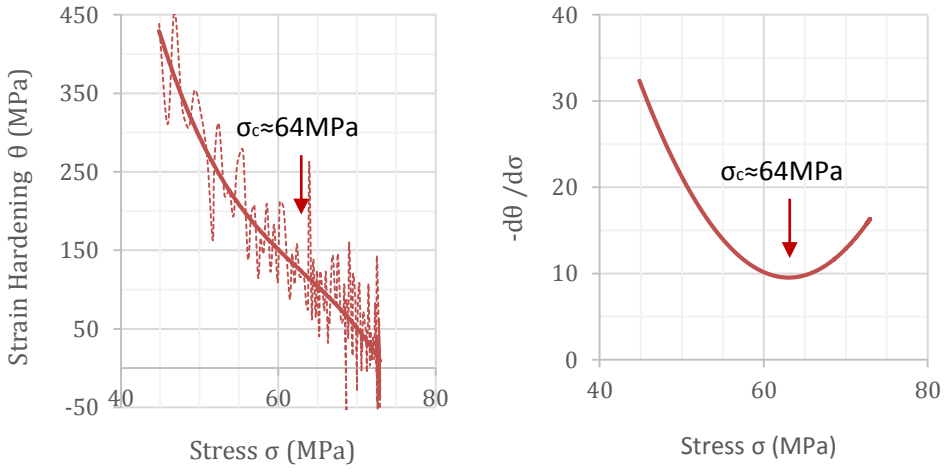

(a) (b)

Figure III-2 (a) Work hardening rate with respect to flow stress during rough rolling for 8C5Nb; (b) The critical stress for dynamic recrystallisation is indicated by the stationary point on the derivative curve of work hardening rate plotted against flow stress for 8C5Nb.

$\theta = -0.0071\sigma^3 + 1.4347\sigma^2 - 106.98\sigma + 2967.8$, $R^2 = 0.7529$

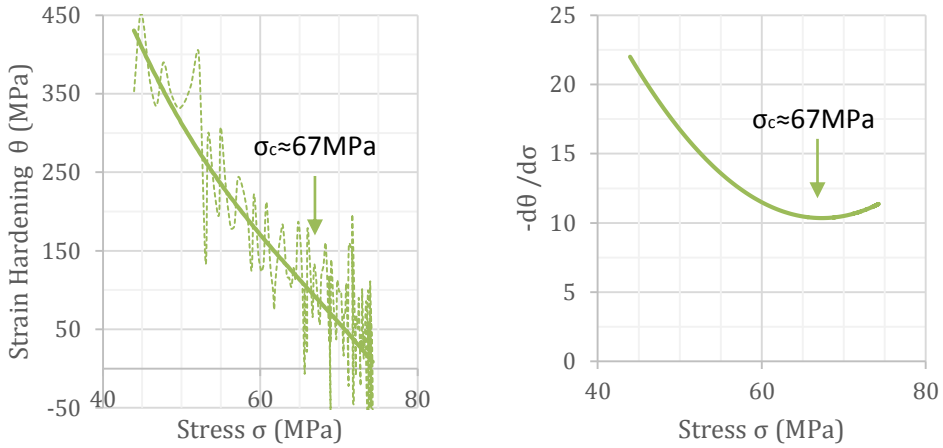

(a) (b)

Figure III-3 (a) Work hardening rate with respect to flow stress during rough rolling for 8C10Nb; (b) The critical stress for dynamic recrystallisation is indicated by the stationary point on the derivative curve of work hardening rate plotted against flow stress for 8C10Nb.

$\theta = -0.007\sigma^3 + 1.6288\sigma^2 - 136.15\sigma + 4032.8$, $R^2 = 0.8897$

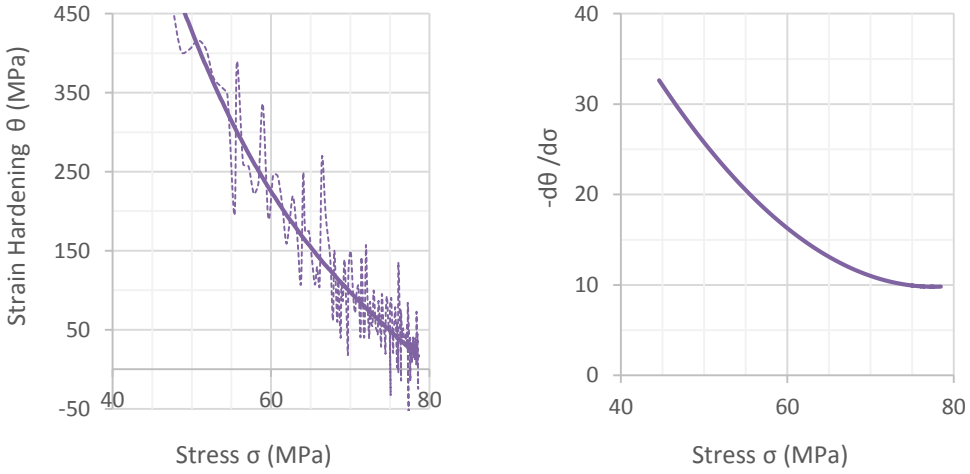

(a) (b)

Figure III-4 (a) Work hardening rate with respect to flow stress during rough rolling for 8C20Nb; (b) The critical stress for dynamic recrystallisation is indicated by the stationary point on the derivative curve of work hardening rate plotted against flow stress for 8C20Nb.

$\theta = 0.047\sigma^3 + 7.0282\sigma^2 - 362.63\sigma + 6568.2$, $R^2 = 0.8109$

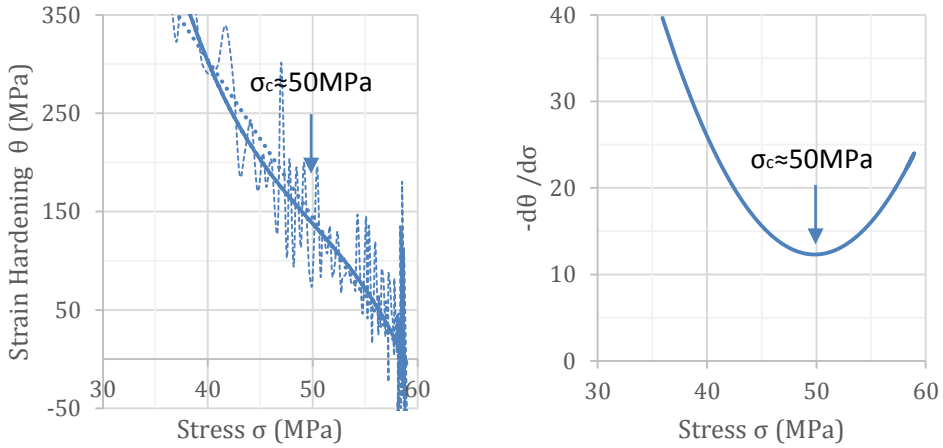

(a) (b)

Figure III-5 (a) Work hardening rate with respect to flow stress during rough rolling for 40C0Nb; (b) The critical stress for dynamic recrystallisation is indicated by the stationary point on the derivative curve of work hardening rate plotted against flow stress for 40C0Nb.

$\theta = -0.0261\sigma^3 + 4.0374\sigma^2 - 217.75\sigma + 4177.5$, $R^2 = 0.8792$

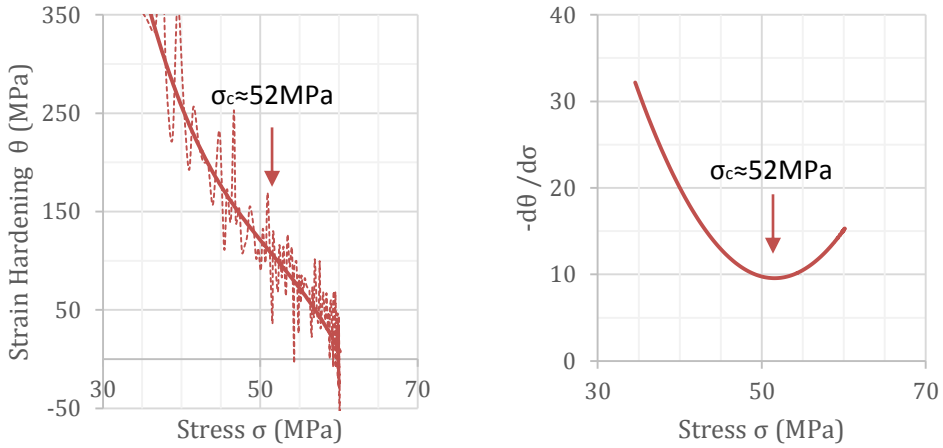

(a) (b)

Figure III-6 (a) Work hardening rate with respect to flow stress during rough rolling for 40C5Nb; (b) The critical stress for dynamic recrystallisation is indicated by the stationary point on the derivative curve of work hardening rate plotted against flow stress for 40C5Nb.

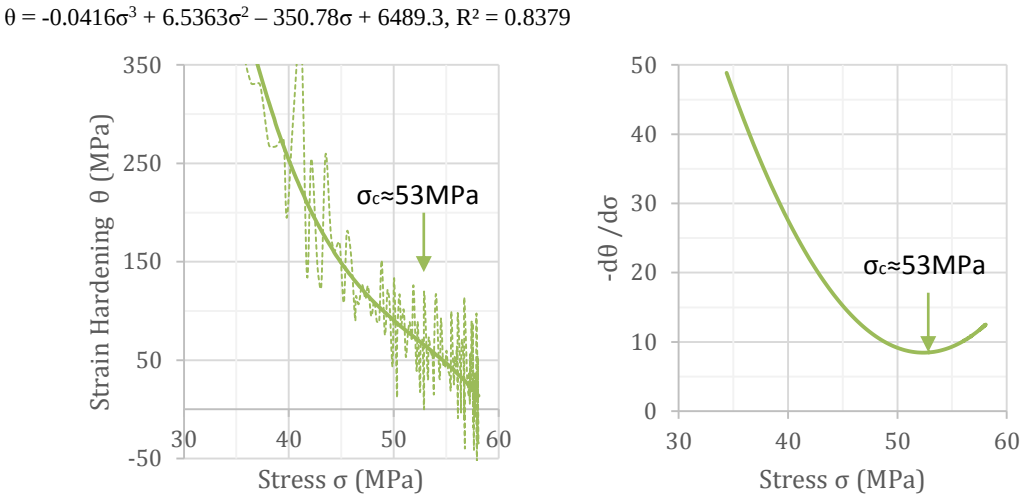

Figure III-7 (a) Work hardening rate with respect to flow stress during rough rolling for 40C10Nb; (b) The critical stress for dynamic recrystallisation is indicated by the stationary point on the derivative curve of work hardening rate plotted against flow stress for 40C10Nb.

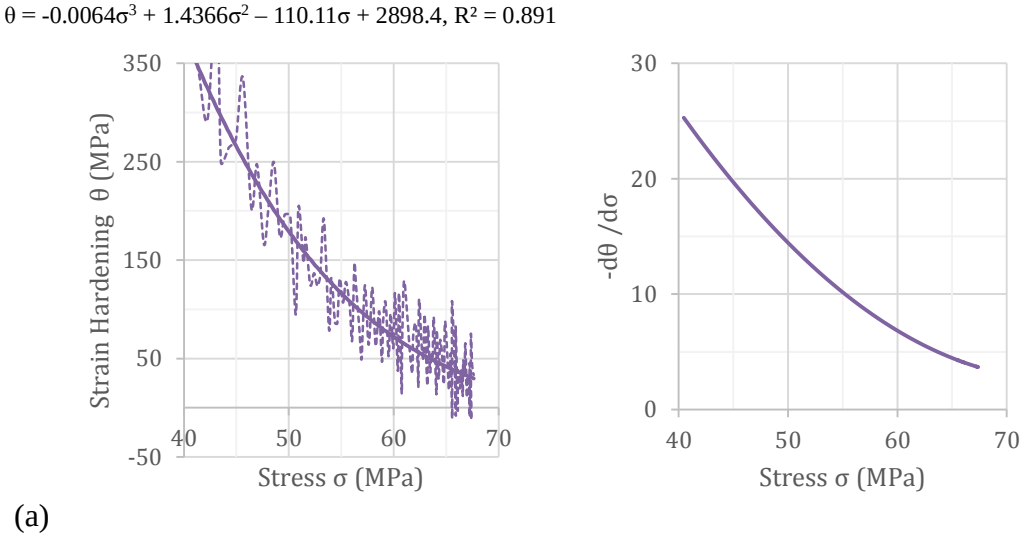

Figure III-8 (a) Work hardening rate with respect to flow stress during rough rolling for 40C20Nb; (b) The critical stress for dynamic recrystallisation is indicated by the stationary point on the derivative curve of work hardening rate plotted against flow stress for 40C20Nb.

$\theta = -0.0917\sigma^3 + 13.338\sigma^2 - 657.61\sigma + 11087$, $R^2 = 0.7823$

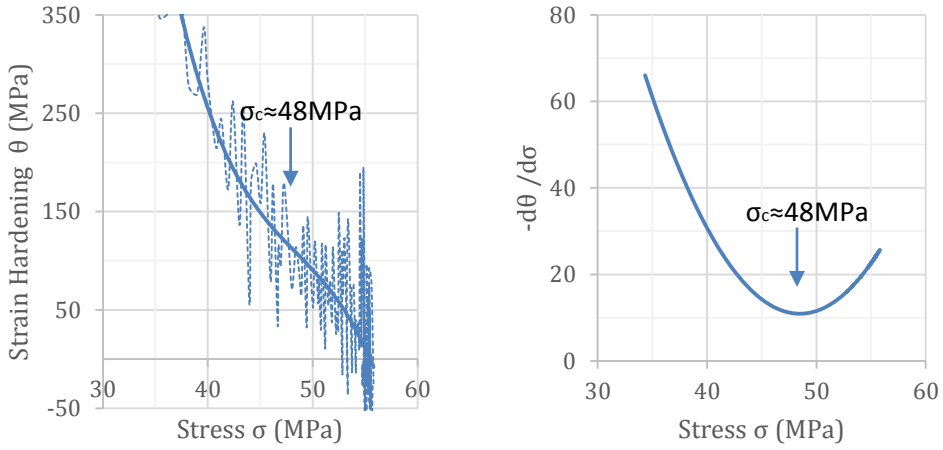

(a) (b)

Figure III-9 (a) Work hardening rate with respect to flow stress during rough rolling for 60C0Nb; (b) The critical stress for dynamic recrystallisation is indicated by the stationary point on the derivative curve of work hardening rate plotted against flow stress for 60C0Nb.

$\theta = -0.0417\sigma^3 + 6.2776\sigma^2 - 323.75\sigma + 5774.2$, $R^2 = 0.9274$

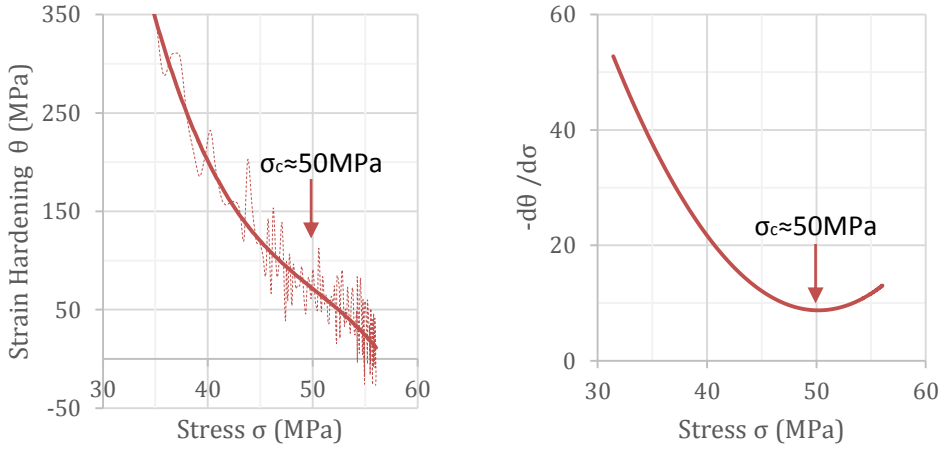

(a) (b)

Figure III-10 (a) Work hardening rate with respect to flow stress during rough rolling for 60C5Nb; (b) The critical stress for dynamic recrystallisation is indicated by the stationary point on the derivative curve of work hardening rate plotted against flow stress for 60C5Nb.

$\theta = -0.0381\sigma^3 + 6.1694\sigma^2 - 341.54\sigma + 6522.5$, $R^2 = 0.9104$

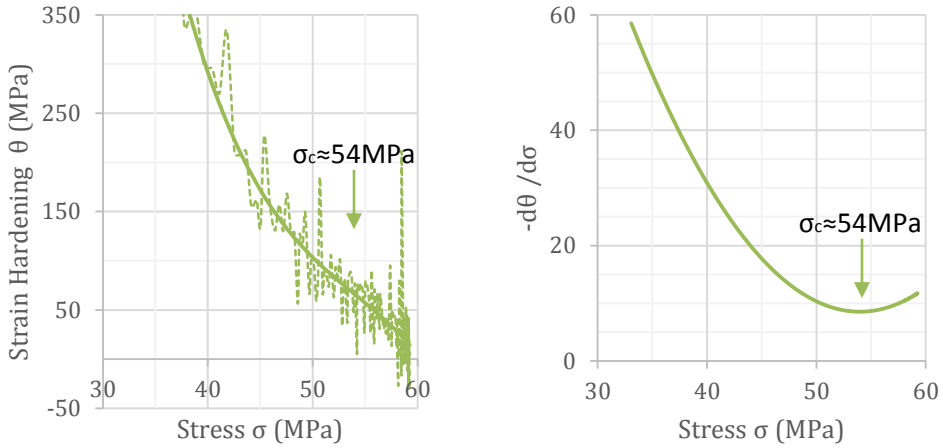

(a) (b)

Figure III-11 (a) Work hardening rate with respect to flow stress during rough rolling for 60C10Nb; (b) The critical stress for dynamic recrystallisation is indicated by the stationary point on the derivative curve of work hardening rate plotted against flow stress for 60C10Nb.

$\theta = -0.013\sigma^3 + 2.305\sigma^2 - 143.56\sigma + 3141.6$, $R^2 = 0.8587$

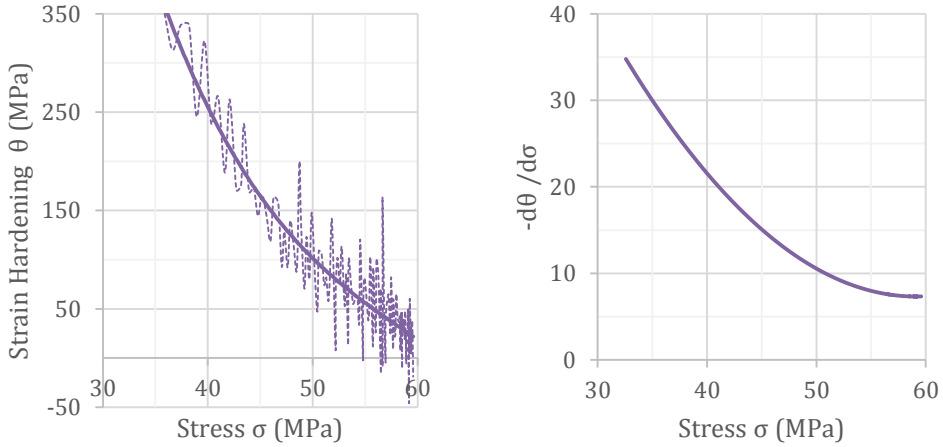

(a) (b)

Figure III-12 (a) Work hardening rate with respect to flow stress during rough rolling for 60C20Nb; (b) The critical stress for dynamic recrystallisation is indicated by the stationary point on the derivative curve of work hardening rate plotted against flow stress for 60C20Nb.